Développement d'un schéma aux volumes finis centré lagrangien pour la résolution 3D des équations de l'hydrodynamique et de l'hyperélasticité

Gabriel Georges

université de BORDEAUX

THÈSE de DOCTORAT

PRÉSENTÉE À

L'UNIVERSITÉ DE BORDEAUX

ÉCOLE DOCTORALE DE MATHÉMATIQUES ET D'INFORMATIQUE

Spécialité : Mathématiques Appliquées et Calcul Scientifique

Par **Gabriel GEORGES**

Développement d'un schéma aux Volumes Finis centré Lagrangien pour la résolution 3D des équations de l'hydrodynamique et de l'hyperélasticité

Development of a 3D cell-centered Lagrangian scheme for the numerical modeling of the gas dynamics and hyperelasticity systems

---

Soutenue le : 19 Septembre 2016

Après avis des rapporteurs :

Rémi Abgrall	Professeur, Zürich University
Michael Dumbser	Professeur, Trento University

Devant la commission d'examen composée de :

Rémi Abgrall	Professeur, Zürich University	Rapporteur
Jérôme Breil	Ingénieur-Chercheur, CEA	Directeur
Bruno Després	Professeur, Université Paris VI	Examinateur
Michael Dumbser	Professeur, Trento University	Rapporteur
Sergey Gavrilyuk	Professeur, Université Aix-Marseille III	Examinateur
Patrick Le Tallec	Professeur, Ecole Polytechnique	Président
Pierre-Henri Maire	Directeur de Recherche, CEA	Directeur
Guillaume Puigt	Chercheur Senior, Cerfacs	Examinateur
Vladimir Tikonchuk	Professeur, Université Bordeaux	Invité

– 2016 –

Remerciements

Je souhaiterais bien entendu remercier mes directeurs, Pierre-Henri et Jérôme, de m'avoir donné l'opportunité de faire cette thèse, de m'avoir formé durant ces 3 années et surtout... de m'avoir supporté. La rigueur à toute épreuve de Pierre-Henri ainsi que les idées folles de Jérôme ont été d'une grande aide. Merci aussi à Jérôme de m'avoir incité à aller à toutes ces conférences qui me laisseront de très bons souvenirs.

Un grand merci à Manue et Édouard pour leur oreille attentive à tous les petits problèmes de ma vie de thésard. Désolé, j'adore me plaindre !

Merci également à toutes les personnes du Celia pour ces moments autour d'un café (ou d'un thé pour moi) à base de mots fléchés et de bonne humeur.

Merci à Luce d'avoir si bien géré l'EDMI et d'avoir offert à tous les thésards le template LaTex d'une thèse. Tu nous as épargné quelques jours (semaines ?) de recherche sur internet.

Merci à Pascal de m'avoir offert les bases d'un code MPI avec git qui rocks ça maman. Sans lui je serais encore en train d'attendre les résultats du Chapitre 3 !

Merci à Léo pour les soirées 'juste une bière' après une bonne journée de travail.

À mon binôme, Seb: t'as qu'à travailler plus, fainéant !

Spéciale dédicace à mes proches (famille ou amis considérés comme de la famille). Merci à la famille donc ! Restez aussi fous que vous l'êtes, je me sens moins seul ! Merci pour votre soutien.

Développement d'un schéma aux Volumes Finis centré Lagrangien pour la résolution 3D des équations de l'hydrodynamique et de l'hyperélasticité

Résumé :

La Physique des Hautes Densités d'Énergies (HEDP) est caractérisée par des écoulements multi-matériaux fortement compressibles. Le domaine contenant l'écoulement subit de grandes variations de taille et est le siège d'ondes de chocs et de détente intenses. La représentation Lagrangienne est bien adaptée à la description de ce type d'écoulements. Elle permet en effet une très bonne description des chocs ainsi qu'un suivit naturel des interfaces multi-matériaux et des surfaces libres. En particulier, les schémas Volumes Finis centrés Lagrangiens GLACE (Godunov-type LAgrangian scheme Conservative for total Energy) et EUCCLHYD (Explicit Unstructured Cell-Centered Lagrangian HYDrodynamics) ont prouvé leur efficacité pour la modélisation des équations de la dynamique des gaz ainsi que de l'élasto-plasticité. Le travail de cette thèse s'inscrit dans la continuité des travaux de Maire et Nkonga [JCP, 2009] pour la modélisation de l'hydrodynamique et des travaux de Kluth et Després [JCP, 2010] pour l'hyperelasticité. Plus précisément, cette thèse propose le développement de méthodes robustes et précises pour l'extension 3D du schéma EUCCLHYD avec une extension d'ordre deux basée sur les méthodes MUSCL (Monotonic Upstream-centered Scheme for Conservation Laws) et GRP (Generalized Riemann Problem). Une attention particulière est portée sur la préservation des symétries et la monotonie des solutions. La robustesse et la précision du schéma seront validées sur de nombreux cas tests Lagrangiens dont l'extension 3D est particulièrement difficile.

Mots clés :

Méthodes aux Volumes Finis - Formalisme Lagrangien - Hydrodynamique - Hyperélasticité - Schémas centrés (colocalisé) - Méthodes de Godunov - Méthode MUSCL - Limiteurs de pente - Problème de Riemann Généralisé (GRP) - Multi-dimensionel - Maillages non-structurés

Development of a 3D cell-centered Lagrangian scheme for the numerical modeling of the gas dynamics and hyperelasticity systems

Abstract:

High Energy Density Physics (HEDP) flows are multi-material flows characterized by strong shock waves and large changes in the domain shape due to rarefaction waves. Numerical schemes based on the Lagrangian formalism are good candidates to model this kind of flows since the computational grid follows the fluid motion. This provides accurate results around the shocks as well as a natural tracking of multi-material interfaces and free-surfaces. In particular, cell-centered Finite Volume Lagrangian schemes such as GLACE (Godunov-type LAgrangian scheme Conservative for total Energy) and EUCCLHYD (Explicit Unstructured Cell-Centered Lagrangian HYDrodynamics) provide good results on both the modeling of gas dynamics and elastic-plastic equations. The work produced during this PhD thesis is in continuity with the work of Maire and Nkonga [JCP, 2009] for the hydrodynamic part and the work of Kluth and Després [JCP, 2010] for the hyperelasticity part. More precisely, the aim of this thesis is to develop robust and accurate methods for the 3D extension of the EUCCLHYD scheme with a second-order extension based on MUSCL (Monotonic Upstream-centered Scheme for Conservation Laws) and GRP (Generalized Riemann Problem) procedures. A particular care is taken on the preservation of symmetries and the monotonicity of the solutions. The scheme robustness and accuracy are assessed on numerous Lagrangian test cases for which the 3D extensions are very challenging.

Keywords :

Finite Volume methods - Lagrangian formalism - Hydrodynamics - Hyperelasticity - Cell-centered schemes - Godunov methods - MUSCL procedure - Slope limiting - Generalized Riemann Problem - Multi-dimensional - Unstructured meshes

Développement d'un schéma aux Volumes Finis centré Lagrangien pour la résolution 3D des équations de l'hydrodynamique et de l'hyperélasticité

Résumé substantiel en français:

Cette thèse s'est déroulée au Laboratoire CELIA (CEntre des Lasers Intenses et Applications) sous la direction de Pierre-Henri Maire et Jérôme Breil.

Le CELIA est une Unité Mixte de Recherche sous la tutelle du CEA (Commissariat à l'Energie Atomique), l'Université de Bordeaux et le CNRS (Centre National de la Recherche Scientifique). Au sein de ce laboratoire, le groupe IFCIA (Interaction - Fusion par Confinement Inertiel - Astrophysique) étudie la Physique des Hautes Densités d'Énergie (HEDP) comprenant, par exemple, les écoulements de type Fusion par Confinement Inertiel (ICF) et l'astrophysique de laboratoire. Ce groupe est notamment impliqué dans le projet du Laser Méga Joule (LMJ) consistant à produire de l'énergie à partir de réactions de fusion nucléaire. Pour ce faire, la matière est très fortement comprimée par des lasers. Ce procédé est qualifié d'attaque direct (direct drive ICF). Les expériences nécessaires à la compréhension de tous les phénomènes physiques intervenant lors d'un écoulement HEDP et leur interaction sont complexes et onéreuses. C'est pourquoi la simulation numérique est un outil très important, permettant de concevoir et interpréter ces expériences.

La Physique HEDP est caractérisée par des écoulements multi-matériaux fortement compressibles. Le domaine contenant l'écoulement subit de grandes variations de taille et est le siège d'ondes de chocs et de détente intenses. La représentation Lagrangienne est bien adaptée à la description de ce type d'écoulements. Elle permet en effet une très bonne description des chocs ainsi qu'un suivit naturel des interfaces multi-matériaux et des surfaces libres. Depuis 2003, Guy Schurtz, Pierre-Henri Maire et Jérôme Breil ont développé le code CHIC (Code d'Hydrodynamique et d'Implosion du Celia) pour résoudre l'hydrodynamique Lagrangienne combinée à de nombreux modules physiques, tels que le transport d'énergie et le ray-tracing par exemple, afin de modéliser des expériences de type ICF [17, 92].

Dans le code CHIC, l'hydrodynamique Lagrangienne est modélisée numérique-

ment par un schéma aux Volumes Finis centré Lagrangien. Pendant de nombreuses années, ce type de schéma a souffert d'une incompatibilité entre la vitesse de l'écoulement et le déplacement des nœuds du maillage. Ce problème a été résolu par Després et Mazeran dans [34] où ils proposent un solveur nodal permettant le calcul d'une vitesse de nœud respectant la GCL (Geometric Conservation Law) et assurant la conservation du volume lors de l'écoulement. Le schéma de Després a été nommé GLACE pour Godunov-type LAgrangian scheme Conservative for total Energy. Dans leur papier [93] Maire et al. ont proposé une variante de ce schéma permettant de supprimer la dépendance du schéma GLACE au rapport d'aspect des mailles. Ce dernier a été nommé EUCCLHYD pour Explicit Unstructured Cell-Centered Lagrangian HYDrodynamics et est actuellement implémenté dans le code CHIC. Dans sa version actuelle, le code CHIC modélise des écoulements à géométrie plane et axi-symétrique. Cependant, si les expériences tentent de reproduire une symétrie axiale, les écoulements 3D sont impossibles à éviter. Par exemple, des instabilités hydrodynamiques apparaissent à la surface de la cible ICF à cause des imperfections de la cible et de la distribution surfacique des lasers. Ces instabilités sont des phénomènes purement 3D qu'il n'est pas possible de modéliser avec un code 2D axi-symétrique et il y a une réelle nécessité de développer des schémas 3D [130]. L'extension 3D des schémas GLACE et EUCCLHYD a donc été proposée respectivement dans [28] et [95], ce dernier papier étant le point de départ de cette thèse. Plus particulièrement, le travail de cette thèse consiste à développer des méthodes précises et robustes pour le schéma EUCCLHYD 3D et son extension à l'ordre deux pour la résolution des systèmes de l'hydrodynamique et de l'hyperelasticité.

Le Chapitre 1 de cette thèse se concentre sur le développement, à l'ordre un, du solveur EUCCLHYD en 3D. Sous formalisme Lagrangien, le maillage suis l'écoulement du fluide et il se déforme donc au cours du temps. Une principale difficulté lors du développement d'un schéma Lagrangien est donc la compatibilité avec la GCL. En effet, il existe deux façons de calculer la variation de volume : un calcul explicite du volume de la maille à chaque instant à partir des coordonnées de ses nœuds ou la résolution discrète de la GCL. Le schéma sera dit compatible avec la GCL si les deux méthodes sont complètement équivalentes. Dans ce premier chapitre, une méthode est développée afin d'assurer la compatibilité du schéma EUCCLHYD avec la GCL pour un maillage polyédrique quelconque. Cette procédure est basée sur un principe de découpage des faces polygonales en triangles et est faite de façon à n'introduire aucune nouvelle inconnue. Le schéma EUCCLHYD est ensuite dérivé de façon classique [95]. En particulier, le solveur nodal est construit à partir des deux hypothèses d'inégalité entropique et de conservation du moment autour de chaque nœud. Le traitement des conditions aux limites est détaillé dans les cas des conditions de pression imposée, vitesse imposée et symétrie. Enfin, étendant au contexte 3D le travail fait par Vilar et al. [126, 127], le pas de temps est calculé de façon à garantir la positivité de l'énergie interne au cours du calcul. Ce critère permet, entre autre, de définir un critère CFL pour un maillage polyédrique quelconque.

Le Chapitre 2 présente l'extension à l'ordre deux de ce schéma en temps et en

espace. L'ordre deux en espace est obtenu par une méthode de type MUSCL (Monotonic upstream-centered Scheme for Conservation Laws) qui est entièrement détaillée. Cette procédure consiste à reconstruire linéairement les champs de pression et vitesse afin d'améliorer la précision du solveur nodal. Cependant, le contexte 3D de cette étude fait que certaines étapes de la méthode MUSCL peuvent être effectuées de différentes façon. Ainsi, les gradients de la reconstruction linéaire peuvent être approchés par une méthode de moindres carrés ou encore par la formule de Green. De plus, il n'y a pas unicité du critère de monotonie et deux variantes sont étudiées ici. Au final, ce sont trois limiteurs qui sont proposés dans ce chapitre : l'extension classique de la méthode MUSCL en multi-dimension, soit une limitation composante par composante des champs reconstruits (CW-limiter pour Component-Wise limiter), une limitation des champs de vitesses permettant de préserver la symétrie de la reconstruction (SP-limiter pour Symmetry Preserving limiter) et un limiteur basé sur l'extension multi-dimensionnelle du limiteur minmod (MM-limiter pour Multi-dimensional Minmod limiter). En particulier, le SP-limiteur est construit de façon à éviter les problèmes liés à la limitation des champs de vitesse. En effet, tel qu'il est proposé dans [90] avec le limiteur VIP, il faut utiliser l'enveloppe convexe d'un groupe de vecteurs pour pouvoir définir un critère de monotonie. Or les enveloppes convexes sont très complexes à construire en 3D et très difficilement utilisable dans le cas de tenseurs. De son côté, le MM-limiteur est construit de façon à stabiliser les écoulements à symétrie sphérique et à réduire l'effet de mesh printing. Concernant l'ordre deux en temps, les méthodes Prédicteur-Correcteur et Generalized Riemann Problem (GRP) sont toutes les deux détaillées. En particulier, la procédure GRP détaillée dans cette thèse est très similaire à celle proposée par Maire et al. dans [96] à la différence près que la variation temporelle du maillage est prise en compte ici. Les algorithmes correspondants à chacune de ces méthodes sont détaillés au fil du chapitre.

Dans le Chapitre 3, le schéma EUCCLHYD 3D est validé sur de nombreux cas test classiques au formalisme Lagrangien. En particulier, ce sont des cas tests difficiles qui permettent de valider et comparer les différentes méthodes proposées au Chapitre 2. Le cas test de Sod permet de voir l'impact de la méthode de reconstruction des gradients et du stencil de monotonie sur la stabilité de la solution. Ainsi, il apparaît que des gradients obtenus à partir d'une méthode de moindres carrés mènent à une solution présentant de forts overshoots au niveau du choc alors que la solution est beaucoup plus régulière en utilisant la formule de Green. De la même façon, le stencil de monotonie étendu permet d'améliorer la qualité de la solution autour des ondes de choc et de détente. L'ordre de convergence du schéma est évalué sur le cas test du Vortex de Taylor-Green. Un ordre de 1.97 est obtenu en utilisant une intégration en temps de type Prédicteur-Correcteur combinée aux limiteurs CW ou SP. Cependant, lorsqu'une méthode GRP est activée, des différences apparaissent. L'ordre de convergence est légèrement détérioré avec le CW-limiteur alors qu'il reste inchangé avec le SP-limiteur. Cette dernière perte de précision est probablement dû au fait que la méthode GRP nécessite elle aussi l'utilisation des gradients approchés. Les erreurs sont ainsi cumulées avec la méthode MUSCL. Le

problème de Saltzmann permet d'évaluer l'impact du maillage sur la solution finale. Dans cette étude, des résultats tout à fait comparables avec ceux de la littérature sont obtenus. Les limiteurs sont mis à défaut sur le cas test de Noh. En effet, sur ce problème à géométrie sphérique présentant un fort taux de compression, les deux limiteurs CW et SP échouent à l'obtention d'une solution monotone et de très fort overshoots apparaissent au niveau du choc. Des pertes de symétrie sont également notable dans le cas du CW-limiteur à cause des changements de base. Seul le MM-limiteur permet d'obtenir des résultats acceptables sur le maillage le plus fin. De la même façon, les limiteurs CW et SP sont mis à défaut sur le cas test de Sedov où une perte de symétrie sphérique ainsi que des mailles non convexes sont observables. Le MM-limiteur permet de palier à ces deux problèmes sur ce cas test également. Finalement, le schéma est évalué sur le cas très difficile de Kidder. Cette implosion de coquille en 3D est un problème instable en soi car le maillage ne respecte pas la symétrie sphérique et que ce problème présente une croissance exponentielle des défauts. Sur ce cas test encore, seul le MM-limiteur permet d'obtenir une solution qui n'est pas complètement détériorée par le mesh printing.

Le Chapitre 4 propose d'étudier le développement d'instabilités de type Rayleigh-Taylor (RTI) dans les restes d'une supernova soufflés par un pulsar interne. C'est une étude qui a été menée en collaboration avec d'autre chercheurs du laboratoire Celia. En particulier dans cette étude, la supernova est modélisée par une coquille de gaz soufflée par une loi de pression interne. Le cas test est d'abord validé sans perturbation grâce à la solution analytique du problème. Des perturbation en harmoniques sphériques sont ensuite introduite. Le schéma 3D est d'abord comparé au code CHIC sur une perturbation 2D-axisymétrique pour s'assurer que les résultats sont identiques. Plusieurs modes de perturbation sont ensuite étudiés de façon à valider numériquement l'hypothèse supposant que le mode azimutal n'impacte pas le taux de croissance des défauts.

Enfin, le Chapitre 5 étend le schéma EUCCLHYD 3D à la modélisation de l'hyper-élasticité. La loi constitutive du matériau est construite en utilisant la procédure de Coleman-Noll qui assure la consistance thermodynamique ainsi que l'indifférence matérielle. Cette dernière propriété est primordiale et assure notamment que les propriétés du solide ne varient pas lors d'un changement de référentiel. Plus précisément, les matériaux sont décrits par une loi de type Néo-Hookéenne. Le solveur nodal EUCCLHYD est ensuite utilisé pour discrétiser ce système d'équations en se basant sur les mêmes propriétés de consistance thermodynamique et de conservation des moments autour des nœuds. Ce schéma est étendu à l'ordre deux en utilisant les méthodes MUSCL et GRP proposées au Chapitre 2. En particulier, le SP-limiteur est modifié de façon à pouvoir limiter des champs de tenseurs. Le schéma est finalement validé sur différents cas test présentant des déformations infinitésimales ou des déformation importantes afin de valider le comportement du schéma dans différents régimes.

Introduction

My PhD thesis took place at the CELIA Laboratory (CEntre des Lasers Intenses et Applications) under the co-supervision of Pierre-Henri Maire and Jérome Breil.

The CELIA Laboratory is a Mixed Research Unit shared by the CEA (Commissariat à l'Energie Atomique), the University of Bordeaux and the CNRS (Centre National de la Recherche Scientifique). Within this laboratory, the group IFCIA (Interaction-Inertial Confinement Fusion-Astrophysics) aims at studying High Energy Density Physics (HEDP) flows such as Inertial Confinement Fusion (ICF) and laboratory astrophysics. In particular, this group works on the LMJ (Laser Mega Joule) program aiming at producing energy from nuclear fusion by heating a target with lasers also referred to as direct drive ICF. The experiments required to understand all the physical phenomena and their interactions during HEDP experiments are very challenging from a technological point of view and are very expensive. In this sense, the numerical simulation is a key tool for designing and interpreting such experiments.

HEDP flows are compressible multi-material fluid flows presenting strong shocks and strong changes in the domain shape due to rarefaction waves. The Lagrangian formalism is well suited to the modeling of such flows since the computational grid follows the fluid motion. In this way, a Lagrangian scheme provides a natural tracking of multi-material interfaces, free-surfaces and an accurate resolution of shocks. Since 2003, Guy Schurtz, Pierre-Henri Maire and Jérôme Breil have developed the CHIC code (Code d'Hydrodynamique et d'Implosion du Celia) for solving the Lagrangian hydrodynamics in combination of multiple physical modules such as energy transport modeling and laser ray tracing in order to model ICF experiments [17, 92].

In the CHIC code, the Lagrangian hydrodynamics is solved using a cell-centered Finite Volume Lagrangian scheme. For decades, this type of schemes were subject to an incompatibility between the grid displacement and the fluid motion. This problem has been solved by Després and Mazeran in [34] who proposed a nodal solver leading to the respect of the Geometric Conservation Law (GCL). This scheme is referred to as GLACE for Godunov-type LAgrangian scheme Conservative for total Energy. A variant of this scheme has then been developed by Maire et al. in [93] in order to remove the scheme dependency to the cell aspect ratio. This second scheme is called EUCCLHYD for Explicit Unstructured Cell-Centered Lagrangian HYDrodynamics and is the scheme implemented in the CHIC code. In its actual version,

the EUCCLHYD scheme can handle 2D and 2D-axisymmetric flows. However, in real experiments, a perfect symmetry is impossible and 3D effects are unavoidable. For example, one can mention the hydrodynamics instabilities appearing at the surface of the ICF target due to manufacturing imperfections and laser imprint. In particular, these 3D effects cannot be modeled by 2D or 2D-axisymmetric codes and there is a real necessity for developing 3D schemes [130]. The 3D extensions of the GLACE and EUCCLHYD schemes were respectively proposed in [28] and [95], the latter being the starting point of this PhD thesis. The aim of this thesis is to develop robust and accurate methods to improve the 3D scheme and its extension to second order using a MUSCL procedure (Monotonic Upstream-centered Scheme for Conservation Laws) which is a complex task in the 3D context. The extension of the scheme to the hyperelasticity system is also investigated to allow the modeling of solids under large stress. This work is structured as follows:

In Chapter 1, the complete derivation of the 3D EUCCLHYD scheme is detailed. The discretization of the Lagrangian gas dynamics equations on a moving grid is complex, especially in 3D. In particular, an important requirement is to ensure that the volume computed from the mesh is equivalent to the volume computed from the Geometric Conservation Law (GCL) which is referred to as GCL compatibility. In this first Chapter, a systematic and symmetric discretization of the cells is proposed in order to ensure the GCL compatibility on any unstructured polyhedral mesh. The velocity of the grid nodes, required to move the computational grid with respect to the fluid motion, is computed thanks to a nodal solver based on two assumptions. First, a momentum conservation condition around the nodes and second, an entropy inequality. The treatment of the boundary conditions as well as the computation of the time step are detailed for the sake of completeness. In particular, the latter is computed in such a way that the positivity of the internal energy is ensured at each time step following the work of Vilar et al. [126, 127].

The Chapter 2 studies the second order extension of this scheme using a MUSCL procedure. This procedure consists in linearly reconstructing the flow variables in order to improve the accuracy of the nodal solver. The reconstructed fields must be limited in order to respect a monotonicity criterion which prevents spurious oscillations. This limiting step is easy to perform in the case of scalar fields but is more difficult in the case of vector fields for which the definition of extrema becomes unclear. This Chapter recalls the classic 3D extension of the MUSCL procedure and proposes two new limiting procedures in order to improve the monotonicity and preserve the symmetry of the numerical solution. In the second part of this Chapter, second order time discretization procedures are presented. In particular, a classic Predictor-Corrector scheme is compared to a Generalized Riemann Problem (GRP) approach. Algorithms are detailed throughout the chapter to summarize the different procedures.

In Chapter 3, the scheme is validated on classic Lagrangian test cases. For example, the smooth and stationary problem of the Taylor-Green Vortex is used to

compute the order of accuracy of the scheme. Moreover, the scheme robustness and symmetry are assessed on the difficult problems of Noh, Sedov and Kidder that are particularly challenging in 3D. In this sense, they are a good tool to compare the advantages and the limits of the second-order procedures proposed in Chapter 2.

In Chapter 4, the study of Rayleigh-Taylor Instability (RTI) in supernova remnants blown up by a central pulsar is proposed. In this study, performed in collaboration with researchers of the CELIA Laboratory, the inner face of the supernova is perturbed by use of the spherical harmonics function. In particular, the 3D scheme is compared to the CHIC Code on a 2D-axisymmetric problem to ensure that the same results are found. Then a 3D problem is proposed: investigate the impact of the azimuthal mode on the perturbation growth.

Finally, the Chapter 5 presents the extension of the scheme to the modeling of hyperelasticity. As proposed in [76, 80, 96, 111], the Finite Volume Lagrangian schemes are an interesting alternative to the Finite Element formalism classically used for studying deforming solids. In this PhD thesis, the solids are described by the hyperelastic model which ensures the frame-indifference as well as the thermodynamic consistency by construction. With such a formalism, the constitutive law defines the Cauchy stress tensor as the derivative of the free-energy with respect to the deformation gradient which enables, for example, the use of Neo-Hookean materials. The nodal solver proposed in the EUCCLHYD scheme is extended to this problem using the same assumptions of momentum conservation and entropy criterion. The MUSCL and GRP procedures are used for the second-order extension of this hyperelasticity system. Finally, the scheme is validated on several test cases presenting both small and large deformations.

The work done during this PhD thesis lead to three articles in international peer-reviewed journals and communications in international conferences that are listed below:

Publications

- G.Georges, J.Breil, P.-H.Maire. *A 3D Finite Volume scheme for solving the updated Lagrangian form of hyperelasticity*, International Journal for Numerical Methods in Fluids, Accepted September 2016.

- G.Georges, J.Breil, P.-H.Maire. *A 3D GCL compatible cell-centered Lagrangian scheme for solving gas dynamics equations*, Journal of Computational Physics, 305 (2016) 921-941.

- G.Georges, J.Breil, X.Ribeyre, E. Le Bel. *A 3D cell-centered Lagrangian scheme applied to the simulation of 3D non-stationary Rayleigh-Taylor Instability in supernova remnants*, High Energy Density Physics, 17 (2015) 151-156.

Talks

- *A cell-centered Finite Volume method for solving 3D hyper-elasticity equations written under updated Lagrangian form*, 7^{th} International Conference on Numerical Methods for Multi-Material Fluid Flow, Würzburg (2015).

- *A cell-centered Lagrangian scheme for solving the 3D hyperelasticity*, 13^{th} US National Congress on Computational Mechanics, San Diego (2015).

- *A multi-dimensional minmod limiter based on nodal gradients for a GCL conservative cell-centered Lagrangian scheme*, Congrès SMAI Les Karellis (2015).

- *A 3D symmetric cell-centered Lagrangian scheme based on a multi-dimensional minmod limiter*, 5^{th} European Conference on Computational Mechanics at Barcelona (2014).

Posters

- *A 3D Lagrangian scheme applied to the simulation of Hyperelasticity*, 28^{th} seminar on the Numerical Fluid Mechanics at IHP, Paris (2016).

- *A 3D Lagrangian scheme applied to the simulation of non-stationary Rayleigh-Taylor instabilities in a supernova remnants*, HEDLA 10th International Conference on High Energy Density Laboratory Astrophysics, Bordeaux (2014).

- *A 3D symmetric cell-centered Lagrangian scheme based on a multi-dimensional minmod limiter*, 42^{th} CANUM National Congress of Numerical Analysis, Marseille (2014).

Contents

Chapter 1

Cell-centered Lagrangian scheme for multi-dimensional hydrodynamics

1.1 Introduction

There are two ways of representing the kinematics of a fluid, namely the Eulerian and the Lagrangian formalims. Under the Eulerian formalism, the computational grid is fixed and one can observe the fluid moving through the cells. This is possible thanks to mass fluxes at the cell faces which enable mass, momentum and total energy exchanges between two neighboring cells. Roughly speaking, this formalism enables to model any kind of flow on any kind of mesh. However, it also introduces strong numerical diffusion due to the discretization of the convection terms. Naturally, the second possible formalism, the Lagrangian formalism, is the one enabling the computational grid to follow the fluid motion. In this way, there is no mass flux through the cell faces and thus no diffusion due to the advection of the fluid. In particular, this property enables an exact tracking of multi-material interfaces and free-surface flows. However, since the quality of a numerical approximation is inherent to the quality of the computational grid, it is easily understood that such a formalism is limited to certain type of flows. For example, the Lagrangian formalism is particularly effective to compute compression problems but is quickly disadvantageous if the flow presents vorticity since it leads to mesh entanglement. In particular, the Lagrangian formalism is well suited to the simulation of High Energy Density Physics (HEDP) flows such as Inertial Confinement Fusion (ICF) and laboratory astrophysics since these flows are characterized by large changes in the domain shape due to strong shocks and rarefaction waves. Moreover, the absence of mass flux makes the Lagrangian formalism a very good candidate for multi-material interface tracking. Numerous works can be found in the literature on Lagrangian schemes nowadays. The interested reader is referred to the review of Benson [11], the introduction of [14] and the work of Maire [92] for more information.

The first Lagrangian scheme was proposed by Von Neumann and Richtmyer in 1950 for the numerical treatment of problems involving shocks [128]. This 1D scheme is staggered in the sense that the velocity is defined at the mesh nodes, whereas the

thermodynamic quantities, such as internal energy, pressure and density, are defined at the cell centers. This formalism is natural since it directly provides the velocity of the grid nodes which is required to move the grid. In their paper, Von Neumann and Richtmyer proposed the concept of artificial viscosity in order to transform kinetic energy into internal energy through shock waves which renders the scheme consistent with the Second Law of thermodynamics and enables a robust treatment of shock waves. The 2D extension of this scheme was proposed by Wilkins in his seminal work [132] devoted to the simulation of elastic-plastic flows. In particular, the 2D context highlighted two main drawbacks of the staggered methods: the non-conservation of total energy (referred to as compatibility) and the presence of spurious numerical modes (known as hourglass motion and spurious vorticity). Innovative cures have been introduced by Caramana et al. respectively in [19, 25] and [24, 27]. In these papers, they introduced the concept of subcell forces to remove the hourglass motion and used the method of support operators to perform a compatible discretization of both momentum and internal energy conservation equations which enables to recover the conservation of total energy. There is numerous ways of defining the artificial viscosity. In particular, one can refer to [23, 85, 131] for the construction of artificial viscosity using mimetic methods, to [87, 88, 101] for an artificial viscosity based on approximate Riemann solvers and [79] for a high-order Finite Element artificial viscosity. More recently, numerous work have been done in order to extend the good properties of compatibility and symmetry preservation in the 2D-axisymmetric context [6, 121, 122], and in the 3D context [26, 88].

The Lagrangian formalism has also been studied using the Finite Element formalism. In their work [115, 116], Scovazzi et al. proposed a variational multi-scale (VMS) approach to stabilize a piecewise linear approximation of the variables. In particular, this work extends the computation of Lagrangian hydrodynamics to triangular meshes. The 3D extension of the VMS procedure was performed in [113] and provides impressive results on tetrahedral meshes. In [5], Barlow showed the natural compatibility of Finite Element Lagrangian schemes using the adjointness of the discrete operators under an Arbitrary Lagrangian-Eulerian (ALE) formalism in the same way as in [25]. High-order extensions are quite natural under a Finite Element formalism thanks to the use of high-order interpolation basis. In this way, Dobrev et al. proposed in successive works [36, 37, 38] a high-order approximation of 2D and 2D axi-symmetric Lagrangian hydrodynamics using curvilinear finite elements and quadrangular meshes. The 3D extension of their scheme was also proposed in ALE [35, 39].

The cell-centered schemes, or collocated schemes, are different from the staggered schemes in the fact that they consider all the variables located at the cell centers. They were first studied by Godunov [56, 60] who proposed to compute the interface fluxes by mean of approximate Riemann solvers. In particular, the natural dissipation of approximate Riemann solvers simplifies the treatment of shock waves making the artificial viscosity unnecessary. Another difference with the staggered schemes is that cell-centered schemes solve the Euler equations under its conserva-

tive form leading to naturally conservative schemes. The main difficulty when using such schemes in the multi-dimensional context lies in the computation of the grid velocity. In [2] the attempt was made to design an algorithm computing the node velocity from the interface velocity fluxes using a weighted least squares procedure. However, this procedure leads to an artificial grid motion not in accordance with the flow due to the fact that the Geometric Conservation Law (GCL) is not respect. The GCL compatibility criterion means that volume variation due to the mesh motion is strictly identical to the volume variation expected by the GCL. In their seminal work [33, 34], Després and Mazeran developed a nodal solver providing a grid velocity compatible with the GCL leading to a scheme conservative in momentum and total energy and which respects an entropy inequality. It was called GLACE for Godunov-type LAgrangian scheme Conservative for total Energy. In particular, this nodal solver can be interpreted as the extension to cell-centered schemes of the notion of subcell forces introduced by Caramana et al. [24] in the context of staggered schemes. In [93, 94], Maire et al. proposed an alternative version of the GLACE scheme by introducing multiple pressure fluxes at the grid nodes. In particular, this feature enables to remove the scheme dependency to the cell aspect ratio. This scheme was called EUCCLHYD for Explicit Unstructured Cell-Centered Lagrangian HYDrodynamics. Both GLACE and EUCCLHYD schemes are based on a Lagrangian Finite Volume approach. Recently, their 3D extension were respectively proposed in [28] and [95]. Let mention the works [7, 129] where the authors propose alternative Godunov-type cell-centered schemes. The Discontinuous Galerkin (DG) formalism is also well suited to the cell-centered Lagrangian formalism as can be seen in the works [1, 84, 86, 89, 124, 125]. Let also mention the recent work [49] aiming at reducing the mesh printing effects in cell-centered schemes by working on the nodal solver.

As previously said, since the mesh follows the flow motion, if the flow presents shearing or vorticity then the mesh will tangle. Moreover, the quality of the numerical solution is directly impacted by the quality of the mesh since the latter depends on the numerical solution at the previous time. This flaw is referred to as mesh printing. It is inherent to Lagrangian schemes and is very strong in the 3D context due to the incapacity of designing meshes perfectly aligned with the flow under any circumstance. This is why most of the actual literature deals with Arbitrary Lagrangian Eulerian (ALE) procedures. Such a procedure takes advantage of both Eulerian and Lagrangian formalisms by authorizing the grid velocity to be different from the fluid velocity. As 3D ALE Lagrangian schemes, one can cite [14, 16, 18, 43, 50] for schemes under the Finite Volume formalism, [5, 35, 102] for the Finite Element formalism and [14] under the DG formalism.

The work produced during this PhD thesis consisted in the development of a purely Lagrangian cell-centered scheme in 3D. In particular this study is in continuity with the work of Maire and Nkonga [95]. This first Chapter is structured as follows: the Section 1.2 presents the compressible Euler equations under their Lagrangian form. The spatial discretization is then described in Section 1.3. In

particular, a procedure is proposed to ensure the GCL compatibility on any unstructured polyhedral mesh. Then, the cell-centered Lagrangian scheme EUCCLHYD is derived in Section 1.4. Finally, the Section 1.5 presents the different criteria used for computing the time step. In particular, the work of Vilar et al. [126, 127] on the time step monitoring is extended to the 3D context in order to ensure the positivity of the internal energy.

1.2 The compressible Euler equations under the Lagrangian formalism

In this section, we introduce the compressible Euler equations written under their Lagrangian form. This system of conservation laws is the basis of any Lagrangian scheme and is thus used to derive our scheme. In particular, this system expresses the conservation of mass, momentum and total energy of a convecting moving volume of fluid. The complete description of the Lagrangian formalism can be complex, especially if one wants to make the distinction between the updated and total Lagrangian formalisms. In this Chapter, only the updated Lagrangian form of the Euler system is described. Complete derivations of the total and updated Lagrangian formalisms can be found in [61, 86, 92, 98, 124, 125].

1.2.1 From the Eulerian to the Lagrangian forms

Let $\omega(t)$ be a domain of fluid moving with time in the $\mathbb{R}^3$ space. The time and spatial dependencies of the variables are not written explicitly for the sake of simplicity. For example, the fluid velocity at point $\boldsymbol{x}$ and time t, $\boldsymbol{V}(\boldsymbol{x},t)$, is simply written $\boldsymbol{V}$. Then, if ρ denotes the fluid density, P its pressure and E its specific total energy, the compressible Euler equations, also called gas dynamics equations, are written

$$\begin{aligned}
&\frac{\partial \rho}{\partial t} + \nabla \cdot (\rho \boldsymbol{V}) = 0, \\
&\frac{\partial (\rho \boldsymbol{V})}{\partial t} + \nabla \cdot (\rho \boldsymbol{V} \otimes \boldsymbol{V}) + \nabla P = \boldsymbol{0}, \\
&\frac{\partial (\rho E)}{\partial t} + \nabla \cdot (\rho E \boldsymbol{V}) + \nabla \cdot (P \boldsymbol{V}) = 0.
\end{aligned} \tag{1.1}$$

These three conservation laws respectively state for the conservation of mass, momentum and total energy of the fluid during its motion.

Let the scalar $\varphi = \varphi(\boldsymbol{x},t)$ and the vector $\boldsymbol{\psi} = \boldsymbol{\psi}(\boldsymbol{x},t)$ be fluid variables. Defining the fluid velocity as $\boldsymbol{V} = d\boldsymbol{x}/dt$ and using the chain rule enables to define the material derivatives of these variables as

$$\begin{aligned}
&\frac{d\varphi}{dt} = \frac{\partial \varphi}{\partial t} + \boldsymbol{V} \cdot \nabla \varphi, \\
&\frac{d\boldsymbol{\psi}}{dt} = \frac{\partial \boldsymbol{\psi}}{\partial t} + (\nabla \boldsymbol{\psi}) \boldsymbol{V},
\end{aligned} \tag{1.2}$$

where $\nabla\varphi$ and $\nabla\boldsymbol{\psi}$ are the spatial gradients of the variables and $\partial/\partial t = \partial/\partial t|_{\boldsymbol{x}}$ the time derivative holding $\boldsymbol{x}$ fixed. Let mention that in this multi-dimensional context, $\nabla\varphi$ is a vector and $\nabla\boldsymbol{\psi}$ is a tensor.

Assuming the flow variables are sufficiently smooth, we develop the divergence terms and using the definition of the material derivative (1.2), system (1.1) becomes

$$\begin{aligned} &\frac{d\rho}{dt} + \rho\nabla\cdot\boldsymbol{V} = 0, \\ &\frac{d(\rho\boldsymbol{V})}{dt} + (\rho\boldsymbol{V})\nabla\cdot\boldsymbol{V} + \nabla P = \boldsymbol{0}, \\ &\frac{d(\rho E)}{dt} + (\rho E)\nabla\cdot\boldsymbol{V} + \nabla\cdot(P\boldsymbol{V}) = 0. \end{aligned} \tag{1.3}$$

Developing now the material derivatives by use of the chain rule and using the mass conservation equation, the system of compressible Euler equations is finally written under the compact form

$$\begin{aligned} &\rho\frac{d}{dt}\left(\frac{1}{\rho}\right) - \nabla\cdot\boldsymbol{V} = 0, \\ &\rho\frac{d\boldsymbol{V}}{dt} + \nabla P = \boldsymbol{0}, \\ &\rho\frac{dE}{dt} + \nabla\cdot(P\boldsymbol{V}) = 0. \end{aligned} \tag{1.4}$$

The total energy writes $E = \varepsilon + \frac{1}{2}\boldsymbol{V}^2$ where ε is the internal energy. This system is closed by linking the thermodynamic variables through the equation of state (EOS) $\varepsilon = \varepsilon(\rho, \eta)$ where η is the specific entropy. The temperature and pressure of the fluid are respectively defined as

$$\theta = \left(\frac{\partial\varepsilon}{\partial\eta}\right)_{\rho} \quad \text{and} \quad P = \rho^2\left(\frac{\partial\varepsilon}{\partial\rho}\right)_{\eta}, \tag{1.5}$$

leading to the Gibbs relation

$$\rho\theta\frac{d\eta}{dt} = \rho\frac{d\varepsilon}{dt} + \rho P\frac{d}{dt}\left(\frac{1}{\rho}\right). \tag{1.6}$$

The EOS can also be written as $P = P(\rho, \varepsilon)$ and one can define the speed of sound as $a^2 = (\partial P/\partial\rho)_{\eta} > 0$. The EOS is left under this general form to preserve the generality of the procedure. In practice, the fluids considered are perfect gas ruled by the gamma gas law (refer to Chapter 3).

It is well known that the system of gas dynamics might admit discontinuous solutions such as shock waves. The selection of physically relevant shock waves is ensured by enforcing the thermodynamic consistency $d\eta/dt \geq 0$.

Finally, using the definition of the internal energy and the Euler system, one can write the conservation equation for the internal energy as

$$\rho \frac{d\varepsilon}{dt} + P\nabla \cdot \boldsymbol{V} = 0, \tag{1.7}$$

which is equivalent to $\rho\theta d\eta/dt = 0$ for a smooth flow.

The system (1.4) is written under its local form. In the next section, we introduce the integral form of (1.4) more suited to the development of a Finite Volume scheme.

1.2.2 Integral form of the Euler equations

In order to facilitate the introduction of a Finite Volume discretization, let write the integral form of the system (1.4). Indeed, this system is true for any point $\boldsymbol{x}$ in $\omega(t)$ thus it is true over the whole domain $\omega(t)$ and it can be integrated over $\omega(t)$. However, since the domain $\omega(t)$ evolves in time with respect to the fluid motion, the integration of the time derivatives is not straightforward. In particular, it is not possible to simply switch the spatial integration with the time differentiation and one needs to use the Reynolds transport formula [61]. For an arbitrary scalar variable φ and a domain $\omega(t)$ moving with the velocity $\boldsymbol{V}$, this formula writes

$$\frac{d}{dt}\int_{\omega(t)} \varphi \,\mathrm{d}v = \int_{\omega(t)} \frac{d\varphi}{dt} + \varphi\nabla \cdot \boldsymbol{V} \,\mathrm{d}v. \tag{1.8}$$

In particular, substituting φ by $\rho\varphi$ enables to write

$$\frac{d}{dt}\int_{\omega(t)} \rho\varphi \,\mathrm{d}v = \int_{\omega(t)} \rho\frac{d\varphi}{dt} + \varphi\left(\frac{d\rho}{dt} + \rho\nabla \cdot \boldsymbol{V}\right) \mathrm{d}v. \tag{1.9}$$

One recognizes the mass conservation equation between brackets, thus the relation becomes

$$\int_{\omega(t)} \rho\frac{d\varphi}{dt} \,\mathrm{d}v = \frac{d}{dt}\int_{\omega(t)} \rho\varphi \,\mathrm{d}v. \tag{1.10}$$

In the same manner, for an arbitrary vector variable $\boldsymbol{\psi}$, one gets

$$\int_{\omega(t)} \rho\frac{d\boldsymbol{\psi}}{dt} \,\mathrm{d}v = \frac{d}{dt}\int_{\omega(t)} \rho\boldsymbol{\psi} \,\mathrm{d}v. \tag{1.11}$$

Substituting $\varphi = \rho$ in (1.8) leads to the conservation of mass

$$\frac{d}{dt}\int_{\omega(t)} \rho \,\mathrm{d}v = 0. \tag{1.12}$$

This result is the one expected since, under the Lagrangian formalism, the domain $\omega(t)$ follows the fluid motion and there is no mass flux through the boundary $\partial\omega(t)$. In other words, the mass of fluid in $\omega(t)$ is constant with respect to time.

Then, integrating the system (1.4) over $\omega(t)$ and using the formulas (1.10)-(1.11), one obtains the integral form of the compressible Euler equations under their Lagrangian form as

$$\begin{aligned}
&\frac{d}{dt}\int_{\omega(t)} \mathrm{d}v - \int_{\omega(t)} \nabla\cdot\boldsymbol{V}\,\mathrm{d}v = 0,\\
&\frac{d}{dt}\int_{\omega(t)} \rho\boldsymbol{V}\,\mathrm{d}v + \int_{\omega(t)} \nabla P\,\mathrm{d}v = \boldsymbol{0},\\
&\frac{d}{dt}\int_{\omega(t)} \rho E\,\mathrm{d}v + \int_{\omega(t)} \nabla\cdot(P\boldsymbol{V})\,\mathrm{d}v = 0.
\end{aligned} \tag{1.13}$$

Let mention that substituting $\varphi = 1$ in the Reynolds transport formulas (1.8), one recovers the first equation of this system. This equation states for the conservation of volume through the motion of $\omega(t)$ and is called the Geometric Conservation Law (GCL). Using the divergence theorem, the GCL is written

$$\frac{d}{dt}\int_{\omega(t)} \mathrm{d}v - \int_{\partial\omega(t)} \boldsymbol{V}\cdot\boldsymbol{n}\,\mathrm{d}s = 0. \tag{1.14}$$

Finally, applying the divergence theorem to the two last equations of system (1.13), one can write the momentum and total energy conservation equations as

$$\begin{aligned}
&\frac{d}{dt}\int_{\omega(t)} \rho\boldsymbol{V}\,\mathrm{d}v + \int_{\partial\omega(t)} P\boldsymbol{n}\,\mathrm{d}s = \boldsymbol{0},\\
&\frac{d}{dt}\int_{\omega(t)} \rho E\,\mathrm{d}v + \int_{\partial\omega(t)} P\boldsymbol{V}\cdot\boldsymbol{n}\,\mathrm{d}s = 0.
\end{aligned} \tag{1.15}$$

A last equation is needed to fully describe the motion of a volume of fluid with the Lagrangian formalism. Indeed, we have derived the compressible Euler equations under their Lagrangian form which enables to determine the volume, momentum and total energy of the moving domain $\omega(t)$ at each time t. However, the missing information is the shape of this domain with respect to time, namely its position in the $\mathbb{R}^3$ space. That is why we add to the system (1.14)-(1.12)-(1.15) the following trajectory equation which provides the position of a node $\boldsymbol{x} \in \partial\omega(t)$ with respect to time

$$\begin{cases}
\dfrac{d\boldsymbol{x}}{dt} = \boldsymbol{V},\\
\boldsymbol{x}(t=0) = \boldsymbol{X}.
\end{cases} \tag{1.16}$$

In this equation, $\boldsymbol{X}$ is the position of point $\boldsymbol{x}(t)$ at initial time $t = 0$. $\boldsymbol{X}$ is called the Lagrangian coordinate whereas $\boldsymbol{x}$ is the Eulerian coordinate.

In this section we have derived a system of equations that fully describes the motion and the thermodynamic state of a volume of fluid $\omega(t)$ moving in the $\mathbb{R}^3$

space. Since we aim at describing complex flows in the 3D context, a numerical approximation is necessary. In the next section we show how to discretize this system of equations using a Finite Volume approach. A particular care is taken for the discretization of the GCL equation (1.14) in order to define the discrete divergence and gradient operators.

1.3 Finite Volume discretization

In this section, we aim at discretizing the space using a Finite Volume formalism. In particular, any Lagrangian scheme is confronted to the difficulty of the face definition which is not unique in 3D. The present study follows the work of Maire and Nkonga [95] where a triangularization of the faces is proposed but one can also refer to [28] where the faces are parametrized. Here, a particular care is taken in order to make the spatial discretization compatible with any polyhedral unstructured mesh, symmetry preserving and compatible with the GCL (1.14).

1.3.1 Discretization of the spatial domain

The continuous domain $\omega(t)$ is divided into a set of cells denoted ω_c and defined such that neither overlap nor void is created between them. In this way one can write $\omega(t) = \bigcup_c \omega_c$. In the present study, each cell is supposed to be a polyhedron, which means that it is a volume delimited by polygonal faces. This simple assumption is already source of discussion since, in the 3D space, four or more points are not necessarily coplanar. This means that the cell faces are for the moment not well defined in the sense that there is non-unique definition of their normal and area. This is a non trivial difficulty since we have to define numerical methods compatible with a moving mesh and one has to define properly the cell geometry before going any further.

No general rule can be imposed for the definition of a polygonal face in the 3D space. In particular, it is dependent on the desired accuracy and complexity of the geometry. The only logical requirement is to define the faces in such a way that neither void nor overlapping is created between two neighboring cells. In other words, the definition of the face geometry must be unique and invariant if considered from one or the other of its neighboring cells. It is possible to derive high order approximations of the face geometry (curved faces) such as in [36]. This track is not followed in this study since it can lead to cumbersome geometrical constructions in the 3D context. Moreover, we are interested in second order approximations of the flow which do not require high order approximation of the geometry.

Simple methods exist to uniquely define a face in 3D, namely parametrizing the polygonal faces or splitting them into triangles.

The parametrization is not considered here since it is restricted to triangle or quadrangle faces only, for which reference elements can be defined. For example one can refer to [28] where the hexahedral cells are mapped onto the reference unit cube

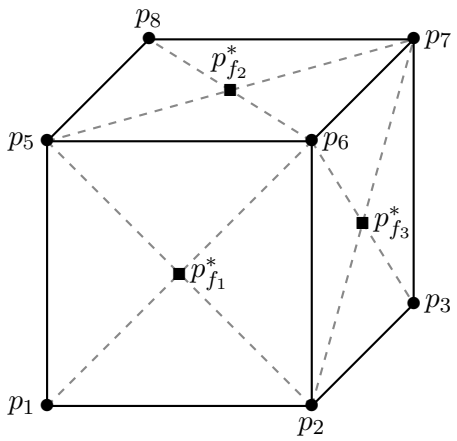

Figure 1.1 – Result of the splitting of the cell faces into triangles using the face barycenter p_f^*. Simple case of a hexahedral cell with square faces.

by an isoparametric transformation. This mapping is also detailed in [41].

The splitting of polygonal faces into triangles enables to define a unique area and outward normal for each resulting triangle. In [95], it is proposed to split the quadrangular faces into two triangles by using one of the diagonals. This methods was chosen for its simplicity since it does not introduce supplementary unknown (all the nodes of the triangle belong to the initial mesh). However, this procedure is not satisfactory since it is not symmetric and implies to choose between the two diagonals of the quadrangle. Moreover, this splitting is almost impossible to extend to the case of faces with more than four points. In [20], Burton introduced a splitting which is symmetric and systematic for any polyhedral cell. It is based on the face barycenter and the edges midpoint. This is cumbersome since it requires the construction of numerous points (one point per face and per edge of the mesh). This can quickly be disadvantageous when confronted to a 3D mesh with a large number of cells.

In this work, we propose a splitting halfway between the two splitting presented previously. As a matter of fact, the face barycenter p_f^* is a sufficient information to perform a symmetric and systematic splitting of any polygonal face. As shown in Figure 1.1, a triangle can be constructed with two points of the face and the new point p_f^*. The example is shown for a simple hexahedral cell with quadrangular faces but the procedure is identical for any polyhedral cell. This splitting still introduces a new point per face that requires to be dealt with. In the next section we will see how to limit the impact of this new unknown with a simple assumption.

An implicit difficulty of the spatial discretization in the 3D framework is the number of unknowns created. When the 3D mesh is refined, the number of unknowns drastically increases and some procedures can be numerically too costly. Keeping this in mind justifies to seek for simple methods, introducing few unknowns while keeping good properties.

Definition of the topological sets

We are interested in methods able to handle unstructured meshes, in the sense that it is not possible to find the neighbor of a cell simply from its global index. In particular, it is necessary to define the topology of the mesh, namely the neighboring relations between the different entities of the mesh (cells, faces, nodes, ...). Let us mention that even regular Cartesian meshes are considered to be unstructured in this study. In the sequel, the index c refers to the cell ω_c, f refers to a face and p to a node. The triangles created by the the face splitting are denoted t_r. Then, the following topological sets are defined:

- $\mathcal{P}^*(c)$ is the set of nodes p of cell c including the nodes p_f^*,
- $\mathcal{P}(c)$ is the set of nodes p of cell c without the nodes p_f^*,
- $\mathcal{P}(f)$ is the set of nodes p of face f without the node p_f^*,
- $\mathcal{P}^*(t_r)$ is the set of the three points of the triangle t_r (contains p_f^*),
- $\mathcal{F}(c,p)$ is the set of faces f of cell c and sharing point p,
- $\mathcal{C}(p)$ is the set of cells c holding node p,
- $\mathcal{T}(c)$ is the set of triangles t_r resulting from the splitting of all the faces of cell c,
- $\mathcal{T}(c,p)$ is the set of triangles t_r resulting from the splitting of the faces holding the node p on cell c,
- $\mathcal{T}(c,f)$ is the set of triangles t_r resulting from the splitting of face f on the cell c,
- $\mathcal{T}(c,f,p)$ is the set of triangles t_r resulting from the splitting of face f that holds node p on the cell c.

These sets are used throughout this manuscript and a special care has to be taken with them. For example, it is important to notice the difference between the sets $\mathcal{P}^*(c)$ and $\mathcal{P}(c)$.

Now that the methodology for discretizing the space and the topology of the mesh are defined, we are able to discretize the first equation of the system, namely the GCL (1.14).

1.3.2 GCL compatibility

The key feature of a Lagrangian scheme is the GCL compatibility. Let recall that under the Lagrangian formalism the mesh follows the fluid motion and there is two ways of computing the volume variation: an explicit computation from the coordinates of the cell nodes and the discretization of the GCL (1.14). The GCL compatibility then states that both methods are completely equivalent. Let denote by $\dot{v}_c$ the variation of cell volume due to the grid displacement during the time interval dt and by dv_c/dt the time rate of change of the cell volume imposed by the GCL. These notations are introduced to help differentiate the quantities evaluated geometrically from the one obtained by discretizing the GCL. In the sequel, it is shown that $\dot{v}_c \equiv dv_c/dt$.

Computation of the cell volume variation $\dot{v}_c$ from geometry

Starting from the previous face splitting, the polyhedral cell ω_c can be decomposed into tetrahedrons. Let $\mathscr{T}_{t_r}$ be the tetrahedron such that its basis is the triangle t_r and its remaining vertex is the space origin O (refer to Figure 1.2). The cell volume v_c is then computed geometrically as the sum of the tetrahedrons volume $v_{\mathscr{T}_{t_r}}$ as follows

$$v_c = \sum_{t_r \in \mathcal{T}(c)} v_{\mathscr{T}_{t_r}}. \tag{1.17}$$

Denoting now by p, p^+ and p^{++} the three points of the triangle t_r, and by O the space origin, all the tetrahedrons can be represented by the set $\mathscr{T}_{t_r} = \{O, p, p^+, p^{++}\}$. This supplementary node denomination (refer to Figure 1.3) is introduced in order to highlight cyclic simplifications in the calculations but one has to keep in mind that one of these node is p_f^*. Moreover, this denomination is chosen such that the triangle t_r has the same orientation than the face f it is related to where the orientation of f is chosen relatively to one of its neighboring cells.

Let $\boldsymbol{x}_p$ denote the position vector of node p, then the tetrahedron volume $v_{\mathscr{T}_{t_r}}$ writes

$$v_{\mathscr{T}_{t_r}} = \frac{1}{6}\boldsymbol{x}_p \cdot (\boldsymbol{x}_{p^+} \times \boldsymbol{x}_{p^{++}}). \tag{1.18}$$

The volume variation $\dot{v}_{\mathscr{T}_{t_r}}$ is computed by time differentiating this last relation. In particular, using the chain rule, one has

$$\dot{v}_{\mathscr{T}_{t_r}} = \frac{1}{6}\Big[\boldsymbol{V}_p \cdot (\boldsymbol{x}_{p^+} \times \boldsymbol{x}_{p^{++}}) + \boldsymbol{x}_p \cdot (\boldsymbol{V}_{p^+} \times \boldsymbol{x}_{p^{++}}) + \boldsymbol{x}_p \cdot (\boldsymbol{x}_{p^+} \times \boldsymbol{V}_{p^{++}})\Big], \tag{1.19}$$

where $\boldsymbol{V}_p = d\boldsymbol{x}_p/dt$ is the velocity of node p. Using a circular shift, this relation can be simplified into

$$\dot{v}_{\mathscr{T}_{t_r}} = \frac{1}{6}\sum_{p \in \mathcal{P}^*(t_r)} \boldsymbol{V}_p \cdot (\boldsymbol{x}_{p^+} \times \boldsymbol{x}_{p^{++}}). \tag{1.20}$$

Finally, using relation (1.17) and the linearity of the time derivative, the time rate of change of the cell volume $\dot{v}_c$ is written as

$$\dot{v}_c = \frac{1}{6}\sum_{t_r \in \mathcal{T}(c)} \sum_{p \in \mathcal{P}^*(t_r)} \boldsymbol{V}_p \cdot (\boldsymbol{x}_{p^+} \times \boldsymbol{x}_{p^{++}}). \tag{1.21}$$

This last relation can be rearranged into

$$\dot{v}_c = \sum_{p \in \mathcal{P}^*(c)} \boldsymbol{V}_p \cdot \left[\frac{1}{6}\sum_{t_r \in \mathcal{T}(c,p)} (\boldsymbol{x}_{p^+} \times \boldsymbol{x}_{p^{++}})\right], \tag{1.22}$$

where the term between brackets stands for the corner normal related to node p introduced by Caramana et al. in [25]. In the sequel, the GCL is discretized to show that the same result is obtained. In this way, the volume flux is completely determined by the GCL compatibility condition.

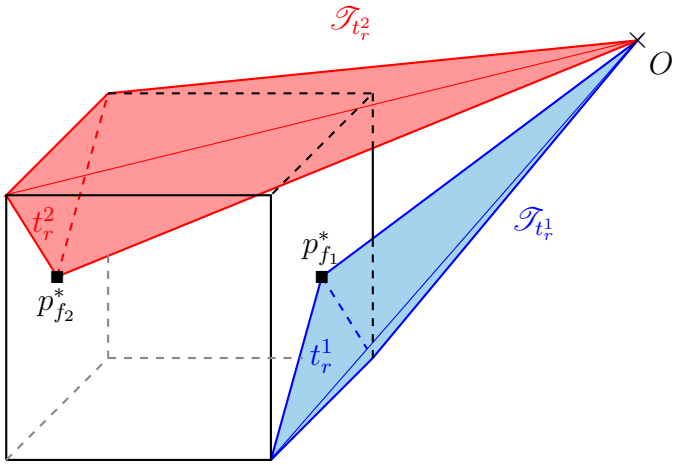

Figure 1.2 – Splitting of the cell into tetrahedrons $\mathscr{T}_{t_r}$. The basis of $\mathscr{T}_{t_r^1}$ in blue (respectively $\mathscr{T}_{t_r^2}$ in red) is the triangle t_r^1 (respectively t_r^2) and its remaining vertex is the space origin O. $\mathscr{T}_{t_r^1}$ has a negative volume and $\mathscr{T}_{t_r^2}$ has a positive one.

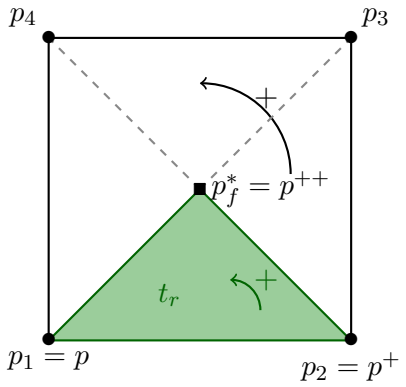

Figure 1.3 – Decomposition of the face f into triangle t_r. The nodes p, p^+ and p^{++} are indexed relatively to the counter clockwise ordering of the face f. Simple case of square face where $p^*_f = p^{++}$.

Computation of dv_c/dt from discretization of the GCL

Defining the cell volume in a Finite Volume way as $v_c = \int_{\omega_c} \mathrm{d}v$ and using the divergence theorem, the GCL (1.14) writes

$$\frac{dv_c}{dt} - \int_{\partial\omega_c} \boldsymbol{V}\cdot\boldsymbol{n}\,\mathrm{d}s = 0, \tag{1.23}$$

where $\boldsymbol{n}$ is the unit outward normal of $\partial\omega_c$, the boundary of ω_c. The splitting proposed previously consists in decomposing the cell boundary into triangles, thus one has $\partial\omega_c = \bigcup t_r$ and the GCL becomes

$$\frac{dv_c}{dt} - \sum_{t_r\in\mathcal{T}(c)} \left(\int_{t_r} \boldsymbol{V}\cdot\boldsymbol{n}\,\mathrm{d}s\right) = 0. \tag{1.24}$$

A triangle is supposed to remain a triangle during its motion which corresponds to suppose a linear mapping of the geometry between times t and $t + dt$. Hence,

the unit outward normal $\boldsymbol{n}$ is constant on the triangle t_r. It is denoted $\boldsymbol{n}_{t_r}$ and computed as

$$\boldsymbol{n}_{t_r} = \frac{1}{2s_{t_r}} \left(\boldsymbol{x}_{p^+} - \boldsymbol{x}_p\right) \times \left(\boldsymbol{x}_{p^{++}} - \boldsymbol{x}_p\right), \tag{1.25}$$

where $s_{t_r} = \frac{1}{2} \left\| \left(\boldsymbol{x}_{p^+} - \boldsymbol{x}_p\right) \times \left(\boldsymbol{x}_{p^{++}} - \boldsymbol{x}_p\right) \right\|$ is the area and $\{p, p^+, p^{++}\}$ the nodes of the triangle as shown in Figure 1.3. Moreover, using again the linearity assumption, the mean velocity of the triangle is defined as its barycentric velocity. One writes

$$\frac{1}{s_{t_r}} \left(\int_{t_r} \boldsymbol{V} \cdot \boldsymbol{n} \, \mathrm{d}s \right) = \frac{1}{3} \sum_{p \in \mathcal{P}^*(t_r)} \boldsymbol{V}_p, \tag{1.26}$$

and the relation (1.24) becomes

$$\frac{dv_c}{dt} - \frac{1}{3} \sum_{t_r \in \mathcal{T}(c)} \sum_{p \in \mathcal{P}^*(t_r)} \boldsymbol{V}_p \cdot s_{t_r} \boldsymbol{n}_{t_r} = 0. \tag{1.27}$$

Let show that this last form of the GCL is completely equivalent to (1.22). Expanding the relation (1.25) provides

$$s_{t_r} \boldsymbol{n}_{t_r} = \frac{1}{2} \Big[\left(\boldsymbol{x}_{p_+} \times \boldsymbol{x}_{p^{++}}\right) - \left(\boldsymbol{x}_{p_+} \times \boldsymbol{x}_p\right) - \left(\boldsymbol{x}_p \times \boldsymbol{x}_{p^{++}}\right) + \left(\boldsymbol{x}_p \times \boldsymbol{x}_p\right) \Big]. \tag{1.28}$$

Then using the cyclic notation, it is simplified into

$$s_{t_r} \boldsymbol{n}_{t_r} = \frac{1}{2} \sum_{p \in \mathcal{P}^*(t_r)} \left(\boldsymbol{x}_p \times \boldsymbol{x}_{p^+}\right). \tag{1.29}$$

Substituting this oriented area into (1.27) enables to write

$$\frac{dv_c}{dt} = \frac{1}{6} \sum_{t_r \in \mathcal{T}(c)} \left[\sum_{p \in \mathcal{P}^*(t_r)} \boldsymbol{V}_p \right] \cdot \left[\sum_{p \in \mathcal{P}^*(t_r)} \left(\boldsymbol{x}_p \times \boldsymbol{x}_{p^+}\right) \right]. \tag{1.30}$$

Let expand and denote by Π_1 the product between brackets. One has

$$\begin{aligned}
\Pi_1 = & \left[\sum_{p \in \mathcal{P}^*(t_r)} \boldsymbol{V}_p \right] \cdot \left[\sum_{p \in \mathcal{P}^*(t_r)} \left(\boldsymbol{x}_p \times \boldsymbol{x}_{p^+}\right) \right], \\
= & \quad \boldsymbol{V}_p \cdot \Big[\left(\boldsymbol{x}_{p^+} \times \boldsymbol{x}_{p^{++}}\right) + \left(\boldsymbol{x}_p \times \boldsymbol{x}_{p^+}\right) - \left(\boldsymbol{x}_p \times \boldsymbol{x}_{p^{++}}\right) \Big] \\
& + \boldsymbol{V}_{p^+} \cdot \Big[\left(\boldsymbol{x}_{p^{++}} \times \boldsymbol{x}_p\right) + \left(\boldsymbol{x}_{p^+} \times \boldsymbol{x}_{p^{++}}\right) - \left(\boldsymbol{x}_{p^+} \times \boldsymbol{x}_p\right) \Big] \\
& + \boldsymbol{V}_{p^{++}} \cdot \Big[\left(\boldsymbol{x}_p \times \boldsymbol{x}_{p^+}\right) + \left(\boldsymbol{x}_{p^{++}} \times \boldsymbol{x}_p\right) - \left(\boldsymbol{x}_{p^{++}} \times \boldsymbol{x}_{p^+}\right) \Big].
\end{aligned} \tag{1.31}$$

Now, the cyclic notation leads to

$$\Pi_1 = \sum_{p \in \mathcal{P}^*(t_r)} \boldsymbol{V}_p \cdot \Big[\left(\boldsymbol{x}_{p^+} \times \boldsymbol{x}_{p^{++}}\right) + \Big(\boldsymbol{x}_p \times \left(\boldsymbol{x}_{p^+} - \boldsymbol{x}_{p^{++}}\right)\Big) \Big], \tag{1.32}$$

and relation (1.30) becomes

$$\frac{dv_c}{dt} = \frac{1}{6} \sum_{t_r \in \mathcal{T}(c)} \sum_{p \in \mathcal{P}^*(t_r)} \boldsymbol{V}_p \cdot \Big[(\boldsymbol{x}_{p^+} \times \boldsymbol{x}_{p^{++}}) + \Big(\boldsymbol{x}_p \times (\boldsymbol{x}_{p^+} - \boldsymbol{x}_{p^{++}}) \Big) \Big]. \tag{1.33}$$

Finally, the double sum is rearranged as

$$\frac{dv_c}{dt} = \frac{1}{6} \sum_{p \in \mathcal{P}^*(c)} \sum_{t_r \in \mathcal{T}(c,p)} \boldsymbol{V}_p \cdot \Big[(\boldsymbol{x}_{p^+} \times \boldsymbol{x}_{p^{++}}) + \Big(\boldsymbol{x}_p \times (\boldsymbol{x}_{p^+} - \boldsymbol{x}_{p^{++}}) \Big) \Big]. \tag{1.34}$$

Briefly, we have replaced a sum over the triangles of the cell and then a sum over the triangle nodes by a sum over the cell nodes and then a sum over the triangles impinging on this node. In particular, since the index p is independent on the triangle t_r (on the contrary, t_r depends on p), the previous relation can be decomposed into

$$\begin{aligned} \frac{dv_c}{dt} = & \quad \frac{1}{6} \sum_{p \in \mathcal{P}^*(c)} \boldsymbol{V}_p \cdot \left[\sum_{t_r \in \mathcal{T}(c,p)} (\boldsymbol{x}_{p^+} \times \boldsymbol{x}_{p^{++}}) \right] \\ & + \frac{1}{6} \sum_{p \in \mathcal{P}^*(c)} \boldsymbol{V}_p \cdot \left[\boldsymbol{x}_p \times \sum_{t_r \in \mathcal{T}(c,p)} (\boldsymbol{x}_{p^+} - \boldsymbol{x}_{p^{++}}) \right]. \end{aligned} \tag{1.35}$$

Now, noticing that the sum

$$\Sigma_1 = \sum_{t_r \in \mathcal{T}(c,p)} (\boldsymbol{x}_{p^+} - \boldsymbol{x}_{p^{++}}), \tag{1.36}$$

defines a closed contour (refer to Figure 1.4), one has $\Sigma_1 = 0$ and

$$\frac{dv_c}{dt} = \sum_{p \in \mathcal{P}^*(c)} \boldsymbol{V}_p \cdot \left[\frac{1}{6} \sum_{t_r \in \mathcal{T}(c,p)} (\boldsymbol{x}_{p^+} \times \boldsymbol{x}_{p^{++}}) \right]. \tag{1.37}$$

This last relation is completely equivalent to (1.22), thus one has $\dot{v}_c \equiv dv_c/dt$ and the discretization is GCL compatible. In particular, this result ensures that computing the cell volume geometrically, from relation (1.17), is strictly equivalent to solve the semi-discrete GCL equation. In the sequel, we show how to deal with the supplementary node p_f^* introduced by the face splitting.

Definition of the face area vectors

Computing the semi-discrete form (1.22) of the GCL requires to know the position and velocity of all the nodes $p \in \mathcal{P}^*(c)$. As said previously, the cell ω_c moves with the fluid motion. It is thus intended to derive a solver for computing the velocity of the mesh nodes. However, the nodes p_f^*, which belongs to the set $\mathcal{P}^*(c)$, are supplementary unknowns and it would be valuable not to derive a supplementary solver for computing their velocity $\boldsymbol{V}_{p_f^*}$.

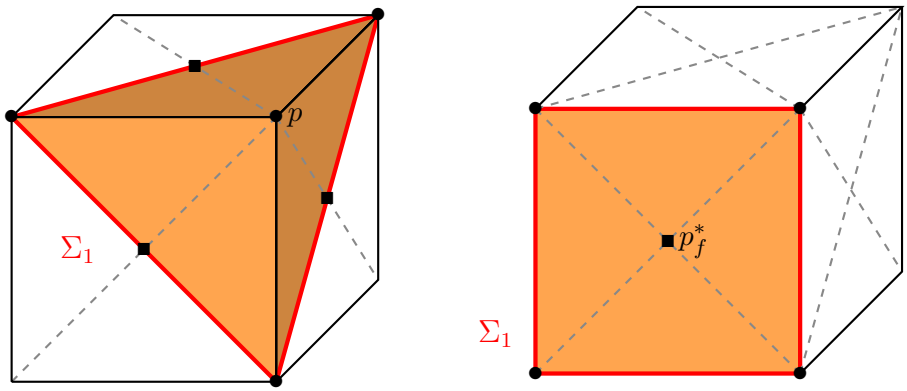

(a) (b)

Figure 1.4 – Representation of the set $\mathcal{T}(c,p)$ in the two possible cases: $p \in \mathcal{P}(c)$ (1.4a) and $p = p_f^*$ (1.4b). One can observe that the contour Σ_1 (red) is closed in both cases.

Let us recall that the node p_f^* is defined as the barycenter of face f. Moreover, the mapping linking the geometry between times t and $t + dt$ is supposed to be linear. This enables to preserve the simplex in the sense that a tetrahedron stays a tetrahedron after transformation. In this way, the barycenter of a triangular face moves with the barycentric velocity defined as

$$\boldsymbol{V}_{p_f^*} = \frac{1}{N_{p,f}} \sum_{q \in \mathcal{P}(f)} \boldsymbol{V}_q, \tag{1.38}$$

where $N_{p,f}$ is the number of nodes on the face f (without p_f^*). Let us rewrite relation (1.27) as

$$\frac{dv_c}{dt} = \frac{1}{3} \sum_{t_r \in \mathcal{T}(c)} \left(\boldsymbol{V}_p + \boldsymbol{V}_{p_+} + \boldsymbol{V}_{p_{++}} \right) \cdot s_{t_r} \boldsymbol{n}_{t_r}. \tag{1.39}$$

Recalling that the indexes p, p^+ and p^{++} are introduced in order to highlight cyclic simplifications, the index p can refer to any point of the triangle t_r. Let fix $p^{++} = p_f^*$ and substitute the velocity (1.38) in this last relation. One gets

$$\frac{dv_c}{dt} = \frac{1}{3} \sum_{t_r \in \mathcal{T}(c)} \left(\boldsymbol{V}_p + \boldsymbol{V}_{p_+} + \frac{1}{N_{p,f}} \sum_{q \in \mathcal{P}(f)} \boldsymbol{V}_q \right) \cdot s_{t_r} \boldsymbol{n}_{t_r}. \tag{1.40}$$

To facilitate a forthcoming sum rearrangement, let us rewrite this relation as

$$\frac{dv_c}{dt} = \frac{1}{3} \sum_{t_r \in \mathcal{T}(c)} \left(\sum_{q \in \mathcal{P}^*(t_r), q \neq p_f^*} \boldsymbol{V}_q + \frac{1}{N_{p,f}} \sum_{q \in \mathcal{P}(f)} \boldsymbol{V}_q \right) \cdot s_{t_r} \boldsymbol{n}_{t_r}. \tag{1.41}$$

Then, recalling that each triangle belongs to a face f of the cell, the first sum of this relation is split into a sum over the cell faces and then a sum over the triangles

related to this face, which leads to

$$\frac{dv_c}{dt} = \frac{1}{3} \sum_{f \in \mathcal{F}(c)} \sum_{t_r \in \mathcal{T}(c,f)} \left(\sum_{q \in \mathcal{P}^*(t_r), q \neq p_f^*} \boldsymbol{V}_q + \frac{1}{N_{p,f}} \sum_{q \in \mathcal{P}(f)} \boldsymbol{V}_q \right) \cdot s_{t_r} \boldsymbol{n}_{t_r}, \tag{1.42}$$

where $\mathcal{F}(c)$ is the set of faces f of cell c. The sums are then rearranged, starting by summing over the cell nodes. The previous relation is then written as

$$\begin{aligned} \frac{dv_c}{dt} = \frac{1}{3} \Bigg(& \sum_{p \in \mathcal{P}(c)} \sum_{f \in \mathcal{F}(c,p)} \sum_{t_r \in \mathcal{T}(c,f,p)} \boldsymbol{V}_p \cdot s_{t_r} \boldsymbol{n}_{t_r} \\ & + \frac{1}{N_{p,f}} \sum_{p \in \mathcal{P}(c)} \sum_{f \in \mathcal{F}(c,p)} \sum_{t_r \in \mathcal{T}(c,f)} \boldsymbol{V}_p \cdot s_{t_r} \boldsymbol{n}_{t_r} \Bigg). \end{aligned} \tag{1.43}$$

Now, noticing that the index p is independent on the triangle t_r, the previous relation is factorized into

$$\frac{dv_c}{dt} = \sum_{p \in \mathcal{P}(c)} \sum_{f \in \mathcal{F}(c,p)} \boldsymbol{V}_p \cdot \frac{1}{3} \left(\sum_{t_r \in \mathcal{T}(c,f,p)} s_{t_r} \boldsymbol{n}_{t_r} + \frac{1}{N_{p,f}} \sum_{t_r \in \mathcal{T}(c,f)} s_{t_r} \boldsymbol{n}_{t_r} \right). \tag{1.44}$$

For convenience, this relation is written under the compact form

$$\frac{dv_c}{dt} = \sum_{p \in \mathcal{P}(c)} \boldsymbol{V}_p \cdot \left[\sum_{f \in \mathcal{F}(c,p)} s_{pf} \boldsymbol{n}_{pf} \right]. \tag{1.45}$$

The term between brackets is the corner vector attached to node p. It is sum of terms relative to the faces around the node. These $s_{pf}\boldsymbol{n}_{pf}$ are called face area vectors and are defined as

$$s_{pf} \boldsymbol{n}_{pf} = \frac{1}{3} \left(\sum_{t_r \in \mathcal{T}(c,f,p)} s_{t_r} \boldsymbol{n}_{t_r} + \sum_{t_r \in \mathcal{T}(c,f)} \frac{1}{N_{p,f}} s_{t_r} \boldsymbol{n}_{t_r} \right). \tag{1.46}$$

One can remark that the face area vector is a linear combination of the oriented areas $s_{t_r}\boldsymbol{n}_{t_r}$ on the face f. This is a consequence of the linear mapping which induces a linear velocity field over the face f. The geometric representation of the face area vector is almost impossible for general case. However, it is possible to draw it for simple cases.

Case of a triangular face:
The face is necessarily planar and its barycenter p_f^* defines three triangles t_r of equal areas as shown in Figure 1.5a. In this way, $\boldsymbol{n}_{t_r} = \boldsymbol{n}_f$ and $s_{t_r} = \frac{1}{3} s_f$. Now, noticing that the set $\mathcal{T}(c,f,p)$ contains two elements and $\mathcal{T}(c,f)$ three, the relation (1.46) provides (refer to Figure 1.5b)

$$s_{pf} \boldsymbol{n}_{pf} = \frac{1}{3} s_f \boldsymbol{n}_f. \tag{1.47}$$

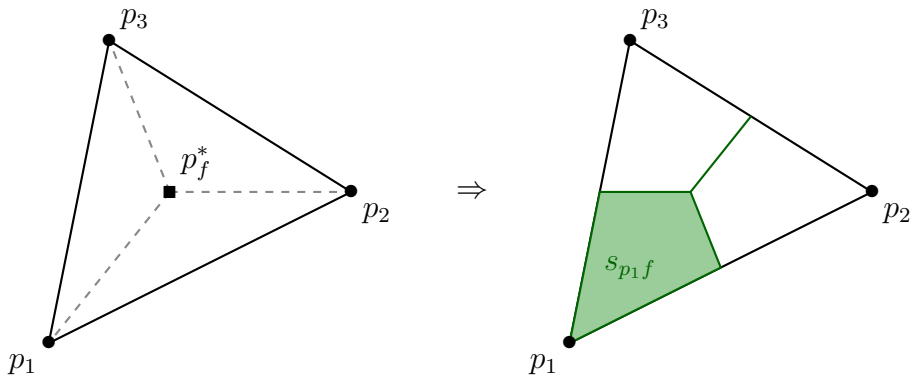

(a) (b)

Figure 1.5 – Representation of the splitting (1.5a) and the corresponding face area vectors (1.5b) in the simple case of a triangular face. Only the areas are drawn since all the normal are identical.

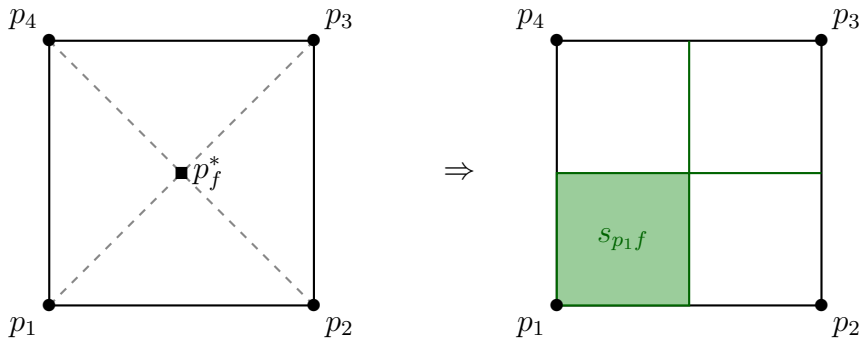

(a) (b)

Figure 1.6 – Representation of the splitting (1.6a) and the corresponding face area vectors (1.6b) in the simple case of a planar square face. Only the areas are drawn since all the normal's are identical.

Case of a planar square face:
The barycenter of a planar square defines four triangles of equal area (refer to Figure 1.6a), thus one has $\boldsymbol{n}_{t_r} = \boldsymbol{n}_f$ and $s_{t_r} = \frac{1}{4} s_f$. Now, noticing that the set $\mathcal{T}(c, f, p)$ contains two elements and $\mathcal{T}(c, f)$ four, relation (1.46) provides (refer to Figure 1.6b)

$$s_{pf} \boldsymbol{n}_{pf} = \frac{1}{4} s_f \boldsymbol{n}_f. \tag{1.48}$$

The face area vectors are the cornerstone of this study. Using the cell splitting presented at the beginning of this section, they are the geometric quantity on which to construct the numerical scheme in order to preserve the symmetry and respect the GCL. In the sequel, we show that the face area vectors lead to the definition of discrete operators which enable the discretization of the Euler equations in a compatible way with the discretization of the GCL.

Discrete divergence and gradient operators

The comparison between the integral form of the GCL (1.14) and its semi-discrete form (1.45) enables the identification of a discrete divergence operator. Indeed, defining the discrete divergence of the velocity in the cell ω_c as

$$\mathcal{DIV}_c(\boldsymbol{V}) = \frac{1}{v_c}\frac{dv_c}{dt} = \frac{1}{v_c}\int_{\partial\omega_c} \boldsymbol{V}\cdot\boldsymbol{n}\,\mathrm{d}s, \tag{1.49}$$

the following identification is made

$$\mathcal{DIV}_c(\boldsymbol{V}) = \frac{1}{v_c}\sum_{p\in\mathcal{P}(c)}\sum_{f\in\mathcal{F}(c,p)} s_{pf}\boldsymbol{V}_p\cdot\boldsymbol{n}_{pf}. \tag{1.50}$$

Now, extending this definition to an arbitrary vector $\boldsymbol{\psi}$, the discrete divergence operator of $\boldsymbol{\psi}$ is defined by

$$\mathcal{DIV}_c(\boldsymbol{\psi}) = \frac{1}{v_c}\sum_{p\in\mathcal{P}(c)}\sum_{f\in\mathcal{F}(c,p)} s_{pf}\boldsymbol{\psi}_p\cdot\boldsymbol{n}_{pf}, \tag{1.51}$$

where $\boldsymbol{\psi}_p$ is the value of $\boldsymbol{\psi}$ at node p. The discrete gradient operator of a scalar φ in the cell ω_c can be defined in different ways. In particular, this is one difference between the GLACE [34] and the EUCCLHYD [93] schemes. The GLACE scheme uses the discrete gradient

$$\mathcal{GRAD}_c^G(\varphi) = \frac{1}{v_c}\sum_{p\in\mathcal{P}(c)}\varphi_{cp}\boldsymbol{n}_p, \tag{1.52}$$

where φ_{cp} is the value of φ at node p relative to cell c and $\boldsymbol{n}_p = \sum_{f\in\mathcal{F}(c,p)} s_{pf}\boldsymbol{n}_{pf}$ is the corner normal, whereas the EUCCLHYD scheme uses

$$\mathcal{GRAD}_c(\varphi) = \mathcal{GRAD}_c^E(\varphi) = \frac{1}{v_c}\sum_{p\in\mathcal{P}(c)}\sum_{f\in\mathcal{F}(c,p)}\varphi_{cfp}s_{pf}\boldsymbol{n}_{pf}, \tag{1.53}$$

where φ_{cfp} is the value of the variable φ at node p on the face f relative to cell c. This difference comes from the number of quadrature points chosen for approximating the integral $\int_{\partial\omega_c} P\boldsymbol{n}\,\mathrm{d}s$. In this sense, the GLACE scheme uses one pressure flux P_{cp} per node whereas the EUCCLHYD scheme requires as many pressure flux P_{cfp} as the number of faces f impinging on node p. This is illustrated in Figure 1.7 in the 2D case for simplicity. In particular, it is shown in Appendix A that these discrete operators preserve linear fields.

1.4 Scheme construction

In this section we use the discrete operators (1.51) and (1.53) to perform the discretization of the Euler equations in their Lagrangian form (1.12)-(1.15)-(1.16). The nodal fluxes introduced by this discretization are then computed by use of the nodal solver taken from EUCCLHYD [93] and its 3D extension [95]. The treatment of the boundary conditions is also detailed for the sake of completeness.

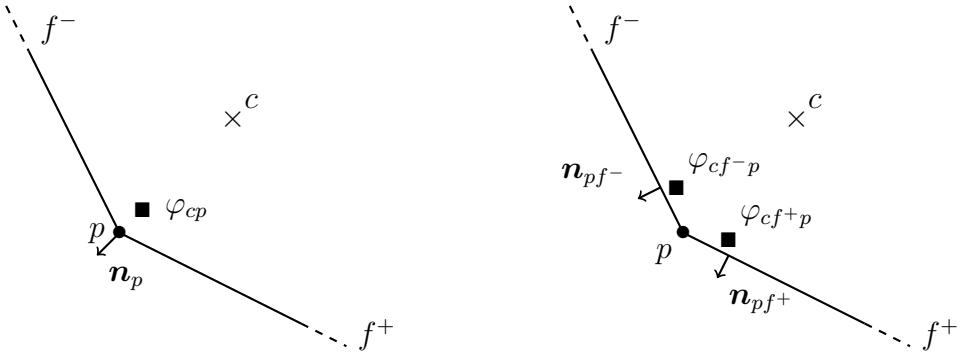

Figure 1.7 – Representation of the pressure flux localization in the case of the GLACE scheme (1.7a) and the EUCCLHYD scheme (1.7b). Portion of a 2D cell with two faces f^- and f^+ impinging on node p.

1.4.1 Discretization of the Euler equations

The mass conservation equation (1.12) is easily discretized. Denoting by m_c the mass of fluid present in the cell ω_c, this mass writes

$$m_c = \int_{\omega_c} \rho \, \mathrm{d}v, \tag{1.54}$$

and equation (1.12) becomes $dm_c/dt = 0$. The mass m_c is thus constant over time, there is no mass flux a the cell interfaces.

Using a cell-centered Finite Volume formalism, all the variables are located at the center of the cells. Let define the mass averaged value φ_c of the physical variable φ over the cell ω_c as

$$\varphi_c = \frac{1}{m_c} \int_{\omega_c} \rho\varphi \, \mathrm{d}v. \tag{1.55}$$

In particular, using this last formula to define the velocity $\boldsymbol{V}_c$ and specific total energy E_c in the cell c enables to write the system (1.15) as

$$\begin{aligned} m_c \frac{d\boldsymbol{V}_c}{dt} + \int_{\partial\omega_c} P\boldsymbol{n} \, \mathrm{d}s = \boldsymbol{0}, \\ m_c \frac{dE_c}{dt} + \int_{\partial\omega_c} P\boldsymbol{V} \cdot \boldsymbol{n} \, \mathrm{d}s = 0. \end{aligned} \tag{1.56}$$

Now, using the definition of the discrete operators (1.51)-(1.53), one writes

$$\begin{aligned} \mathcal{GRAD}_c(P) &= \frac{1}{v_c} \int_{\partial\omega_c} P\boldsymbol{n} \, \mathrm{d}s, \\ \mathcal{DIV}_c(P\boldsymbol{V}) &= \frac{1}{v_c} \int_{\partial\omega_c} P\boldsymbol{V} \cdot \boldsymbol{n} \, \mathrm{d}s. \end{aligned} \tag{1.57}$$

and the semi-discrete system writes

$$\begin{aligned} m_c \frac{d\boldsymbol{V}_c}{dt} + \sum_{p\in\mathcal{P}(c)} \sum_{f\in\mathcal{F}(c,p)} s_{pf} P_{cfp} \boldsymbol{n}_{pf} &= \boldsymbol{0}, \\ m_c \frac{dE_c}{dt} + \sum_{p\in\mathcal{P}(c)} \sum_{f\in\mathcal{F}(c,p)} s_{pf} P_{cfp} \boldsymbol{V}_p \cdot \boldsymbol{n}_{pf} &= 0. \end{aligned} \tag{1.58}$$

The system (1.58) is referred to as the semi-discrete form of the Euler equations since the discretization has only been performed in space whereas the time derivatives are still continuous. In the same way as at the continuous level, this semi-discrete system is closed using the EOS linking the pressure to the other variables. One writes $P_c = P(\rho_c, \varepsilon_c)$, where the specific internal energy of the cell ε_c is computed as

$$\varepsilon_c = E_c - \frac{1}{2}\boldsymbol{V}_c^2, \tag{1.59}$$

and the cell density is equal to $\rho_c = m_c/v_c$. Finally, the trajectory equation, which enables to move the mesh nodes, is discretized as follows

$$\frac{d\boldsymbol{x}_p}{dt} = \boldsymbol{V}_p. \tag{1.60}$$

In the sequel, the nodal solver used for computing the nodal fluxes P_{cfp} and $\boldsymbol{V}_p$ is described. This solver is composed of two steps, an entropy criterion and a momentum conservation condition.

1.4.2 Entropy inequality

In order to describe flows with shock waves, it is proposed in this section to derive the semi-discrete Gibbs relation. Denoting by η_c and θ_c the entropy and the temperature in cell c respectively, the Gibbs relation writes

$$m_c \theta_c \frac{d\eta_c}{dt} = m_c \frac{d\varepsilon_c}{dt} + m_c P_c \frac{d}{dt}\left(\frac{1}{\rho_c}\right). \tag{1.61}$$

Differentiating equation (1.59), the time rate of change of internal energy writes as

$$m_c \frac{d\varepsilon_c}{dt} = m_c \left(\frac{dE_c}{dt} - \boldsymbol{V}_c \cdot \frac{d\boldsymbol{V}_c}{dt}\right). \tag{1.62}$$

Substituting dE/dt and $d\boldsymbol{V}/dt$ by the relations of system (1.58), this relation becomes

$$m_c \frac{d\varepsilon_c}{dt} = \sum_{p\in\mathcal{P}(c)} \sum_{f\in\mathcal{F}(c,p)} s_{pf} P_{cfp} \left(\boldsymbol{V}_c - \boldsymbol{V}_p\right) \cdot \boldsymbol{n}_{pf}. \tag{1.63}$$

Now, writing the semi-discrete GCL equation (1.45) as

$$m_c \frac{d}{dt}\left(\frac{1}{\rho_c}\right) = \frac{dv_c}{dt} = \sum_{p\in\mathcal{P}(c)} \sum_{f\in\mathcal{F}(c,p)} s_{pf} \boldsymbol{V}_p \cdot \boldsymbol{n}_{pf}, \tag{1.64}$$

and using the fact that the contour of the cell ω_c is closed, i.e.

$$\sum_{p\in\mathcal{P}(c)}\sum_{f\in\mathcal{F}(c,p)} s_{pf}\boldsymbol{n}_{pf} = \boldsymbol{0}, \tag{1.65}$$

one writes

$$m_c P_c \frac{d}{dt}\left(\frac{1}{\rho_c}\right) = \sum_{p\in\mathcal{P}(c)}\sum_{f\in\mathcal{F}(c,p)} s_{pf} P_c \left(\boldsymbol{V}_c - \boldsymbol{V}_p\right)\cdot\boldsymbol{n}_{pf}. \tag{1.66}$$

Finally, the semi-discrete entropy production is written

$$m_c\theta_c\frac{d\eta_c}{dt} = \sum_{p\in\mathcal{P}(c)}\sum_{f\in\mathcal{F}(c,p)} s_{pf}\left(P_{cfp} - P_c\right)\left(\boldsymbol{V}_c - \boldsymbol{V}_p\right)\cdot\boldsymbol{n}_{pf}. \tag{1.67}$$

The Second Law of thermodynamics ensures that the entropy production is positive or null, that is to say $d\eta_c/dt \geq 0$. A sufficient condition to respect this at the semi-discrete level is to link the pressure jump across the face f to the velocity jump by the relation

$$P_{cfp} - P_c = Z_c\left(\boldsymbol{V}_c - \boldsymbol{V}_p\right)\cdot\boldsymbol{n}_{pf}, \tag{1.68}$$

where $Z_c = \rho_c a_c$ is the acoustic impedance and a_c the isentropic speed of sound in cell c. This relation can also be interpreted as the conservation of the half Riemann invariant $P + Z\boldsymbol{V}\cdot\boldsymbol{n}$ along the direction $\boldsymbol{n}_{pf}$.

As a conclusion, the relation (1.68) expresses the nodal pressure P_{cfp} as a function of the nodal velocity $\boldsymbol{V}_p$. In this way, the semi-discrete scheme for the entropy variation can be written as

$$m_c\theta_c\frac{d\eta_c}{dt} = \sum_{p\in\mathcal{P}(c)}\sum_{f\in\mathcal{F}(c,p)} s_{pf} Z_c\left[\left(\boldsymbol{V}_c - \boldsymbol{V}_p\right)\cdot\boldsymbol{n}_{pf}\right]^2, \tag{1.69}$$

which ensures that the entropy production is positive or null. In particular, the entropy production is proportional to the square of the velocity jump between the cell and the node. In this way, strong discontinuities in the velocity field lead to a strong production of entropy which is the case for example in shocks. Moreover, one observes that entropy is not conserved in smooth regions of the flow unless the flow is constant.

1.4.3 Local momentum balance and nodal velocity

The second step of the nodal solver consists in invoking the total momentum conservation. Following the work [95], the nodal velocity $\boldsymbol{V}_p$ is computed by imposing the momentum balance around the node p. The mathematical steps are completely detailed in [95] and are thus not recalled here for the sake of conciseness. As shown in Figure 1.8, represented in the 2D context for simplicity, numerous pressure fluxes are acting around the node p. More precisely, there is two pressures per face impinging on the node. Imposing the momentum balance around node p corresponds in fact

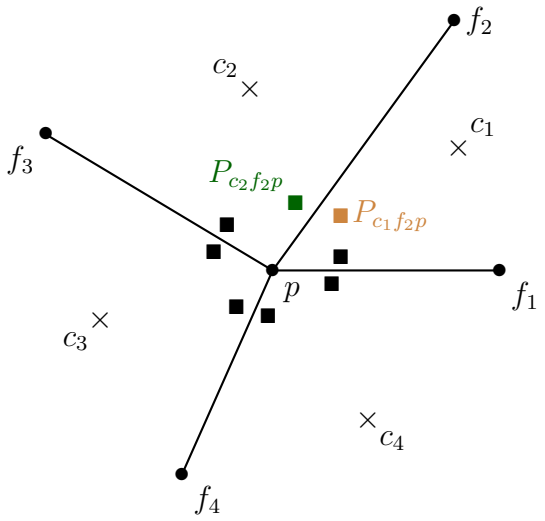

Figure 1.8 – Representation, in the 2D case, of the pressure fluxes acting around a node p.

to balance all the pressure fluxes in competition around this node. Mathematically, this condition writes

$$\sum_{c\in\mathcal{C}(p)}\sum_{f\in\mathcal{F}(c,p)} s_{pf}P_{cfp}\boldsymbol{n}_{pf} = \boldsymbol{0}. \tag{1.70}$$

Now, substituting P_{cfp} by the relation (1.68) gives

$$\sum_{c\in\mathcal{C}(p)}\sum_{f\in\mathcal{F}(c,p)} s_{pf}\Big(P_c + Z_c\left(\boldsymbol{V}_c - \boldsymbol{V}_p\right)\cdot\boldsymbol{n}_{pf}\Big)\boldsymbol{n}_{pf} = \boldsymbol{0}. \tag{1.71}$$

Using formula (D.1), this relation can be written under the compact form

$$\mathbb{M}_p\boldsymbol{V}_p = \boldsymbol{B}_p, \tag{1.72}$$

where

$$\begin{aligned}
\mathbb{M}_p &= \sum_{c\in\mathcal{C}(p)}\sum_{f\in\mathcal{F}(c,p)} s_{pf}Z_c\left(\boldsymbol{n}_{pf}\otimes\boldsymbol{n}_{pf}\right),\\
\boldsymbol{B}_p &= \sum_{c\in\mathcal{C}(p)}\sum_{f\in\mathcal{F}(c,p)} s_{pf}\Big[P_c\boldsymbol{n}_{pf} + Z_c\boldsymbol{V}_c\left(\boldsymbol{n}_{pf}\otimes\boldsymbol{n}_{pf}\right)\Big].
\end{aligned} \tag{1.73}$$

The relation (1.72) is sufficient to determine the nodal velocity since the matrix $\mathbb{M}_p$ is symmetric positive definite thus invertible (refer to Appendix D.3). The nodal velocity is thus given by $\boldsymbol{V}_p = \mathbb{M}_p^{-1}\boldsymbol{B}_p$ and the pressure flux P_{cfp} is easily computed by substituting $\boldsymbol{V}_p$ into relation (1.68).

1.4.4 Global momentum and total energy conservation

Here we show that condition (1.70) enables to recover the global conservation of momentum and total energy. The complete proof can also be found in [92, 95].

Recalling the semi-discrete momentum conservation equation in the cell ω_c is

$$m_c \frac{d\boldsymbol{V}_c}{dt} + \sum_{p\in\mathcal{P}(c)} \sum_{f\in\mathcal{F}(c,p)} s_{pf} P_{cfp} \boldsymbol{n}_{pf} = \boldsymbol{0}, \tag{1.74}$$

the global momentum variation $\delta\left(m\boldsymbol{V}\right)_{\omega(t)}$ is defined as

$$\begin{aligned} \delta\left(m\boldsymbol{V}\right)_{\omega(t)} = & \sum_c \left(m_c \frac{d\boldsymbol{V}_c}{dt} \right), \\ = & -\sum_c \sum_{p\in\mathcal{P}(c)} \sum_{f\in\mathcal{F}(c,p)} s_{pf} P_{cfp} \boldsymbol{n}_{pf}. \end{aligned} \tag{1.75}$$

Now, rearranging the sums, this last relation is written

$$\delta\left(m\boldsymbol{V}\right)_{\omega(t)} = -\sum_p \left(\sum_{c\in\mathcal{C}(p)} \sum_{f\in\mathcal{F}(c,p)} s_{pf} P_{cfp} \boldsymbol{n}_{pf} \right). \tag{1.76}$$

The term between parenthesis is nothing but the relation (1.70) which ensures the balance of momentum around node p. In this way, the momentum is globally conserved, i.e. $\delta\left(m\boldsymbol{V}\right)_{\omega(t)} = \boldsymbol{0}$, provided that relation (1.70) is respected for every node of the domain. In particular, work has to be done in order to respect this relation at the boundary nodes. This is detailed in the next section.

A very similar proof can be written for the global conservation of total energy. Starting from the semi-discrete total energy conservation equation

$$m_c \frac{dE_c}{dt} + \sum_{p\in\mathcal{P}(c)} \sum_{f\in\mathcal{F}(c,p)} s_{pf} P_{cfp} \boldsymbol{V}_p \cdot \boldsymbol{n}_{pf} = 0, \tag{1.77}$$

and summing over all the cells of the domain leads to

$$\begin{aligned} \delta\left(mE\right)_{\omega(t)} = & \sum_c \left(m_c \frac{dE_c}{dt} \right), \\ = & -\sum_c \sum_{p\in\mathcal{P}(c)} \sum_{f\in\mathcal{F}(c,p)} s_{pf} P_{cfp} \boldsymbol{V}_p \cdot \boldsymbol{n}_{pf}. \end{aligned} \tag{1.78}$$

Then, performing the same sum rearrangement enables to factorize the nodal velocity as

$$\delta\left(mE\right)_{\omega(t)} = -\sum_p \boldsymbol{V}_p \cdot \left(\sum_{c\in\mathcal{C}(p)} \sum_{f\in\mathcal{F}(c,p)} s_{pf} P_{cfp} \boldsymbol{n}_{pf} \right). \tag{1.79}$$

Using once again the relation (1.70), the global conservation of total energy is straightforward and one writes

$$\delta\left(mE\right)_{\omega(t)} = 0. \tag{1.80}$$

In the next section we show how to take into account the boundary conditions in a consistent manner with (1.70).

1.4.5 Boundary condition treatment

The treatment of boundary conditions is crucial for implementing a numerical scheme. Looking at the integrated equations (1.14)-(1.15) one understands that the boundary of the domain $\partial\omega(t)$ can only be constrained by a pressure or a normal velocity. In this way, the treatment of pressure, velocity and symmetry boundary conditions is presented. In the sequel, $\mathcal{F}^b(p)$ is the set of boundary faces f around node p.

Pressure boundary condition

The pressure boundary conditions are easily implemented. Indeed, since the nodal solver consists in balancing the pressure forces acting around a node p, one has to add the pressure force resulting from the pressure boundary condition in the relation (1.72). Let P^b be the pressure prescribed at the boundary face $f \in \mathcal{F}^b(p)$, then the momentum balance at the boundary node becomes

$$\mathbb{M}_p \boldsymbol{V}_p = \boldsymbol{B}_p - \sum_{f \in \mathcal{F}^b(p)} s_{pf} P^b \boldsymbol{n}_{pf}. \tag{1.81}$$

Velocity boundary condition

The velocity boundary conditions are more complex to handle and have to be taken into account properly in the momentum balance condition (1.72). In the present study, we always consider a single velocity boundary condition V^b applied to a set of boundary faces $f \in \mathcal{F}^b(p)$ defining a plane around node p. Such a configuration corresponds, for example, to a moving flat wall. This configuration is geometrically simple, but not trivial from a mathematical point of view. Indeed, one has to compute the pressure force equivalent to the prescribed velocity boundary condition and add its contribution to the momentum balance (1.72) as proposed in [92]. Let write this pressure force $\Pi_p^b \boldsymbol{d}_p$, where $\boldsymbol{d}_p$ is the corner normal at node p

$$\boldsymbol{d}_p = \sum_{f \in \mathcal{F}^b(p)} s_{pf} \boldsymbol{n}_{pf}, \tag{1.82}$$

and Π_p^b an unknown scalar. Then, the momentum balance at node p writes

$$\mathbb{M}_p \boldsymbol{V}_p = \boldsymbol{B}_p - \Pi_p^b \boldsymbol{d}_p. \tag{1.83}$$

Since all the boundary faces are coplanar, the projection of the node velocity along the normal direction $\boldsymbol{d}_p$ gives

$$\boldsymbol{V}_p . \boldsymbol{d}_p = \sum_{f \in \mathcal{F}^b(p)} s_{pf} V^b. \tag{1.84}$$

Performing the same projection on the relation (1.83) enables to compute the scalar Π_p^b as

$$\Pi_p^b = \frac{\mathbb{M}_p^{-1} \boldsymbol{B}_p \cdot \boldsymbol{d}_p - \sum_{f \in \mathcal{F}^b(p)} s_{pf} V^b}{\mathbb{M}_p^{-1} \boldsymbol{d}_p \cdot \boldsymbol{d}_p}. \tag{1.85}$$

This relation always has a solution since $\mathbb{M}_p^{-1}$ is symmetric positive definite and thus $\mathbb{M}_p^{-1}\boldsymbol{d}_p \cdot \boldsymbol{d}_p > 0$. Finally, $\boldsymbol{V}_p$ is computed by substituting this expression of Π_p^b into relation (1.83).

Symmetry boundary conditions

The symmetry boundary conditions are computed by making geometric considerations on the node velocity $\boldsymbol{V}_p$. Three types of symmetry boundary conditions can be observed in 3D as sketched in Figure 1.9. The three cases are:

• **Symmetry plane** of orthonormal basis $(\boldsymbol{\tau}_1, \boldsymbol{\tau}_2)$ (refer to Figure 1.9a). The node is constrained to evolve in the symmetry plane and its velocity writes

$$\boldsymbol{V}_p = \alpha_1 \boldsymbol{\tau}_1 + \alpha_2 \boldsymbol{\tau}_2. \tag{1.86}$$

The unknowns to be computed are now the two scalars α_1 and α_2. This is done by substituting (1.86) into (1.72) which gives

$$\mathbb{M}_p \left(\alpha_1 \boldsymbol{\tau}_1 + \alpha_2 \boldsymbol{\tau}_2\right) = \boldsymbol{B}_p. \tag{1.87}$$

Then, performing successive projections on $\boldsymbol{\tau}_1$ and $\boldsymbol{\tau}_2$ leads to a 2×2 system which writes as follows

$$\begin{aligned} \alpha_1 M_1 + \alpha_2 M_2 &= B_1, \\ \alpha_1 M_2 + \alpha_2 M_3 &= B_2, \end{aligned} \tag{1.88}$$

where

$$\begin{aligned} M_1 &= \mathbb{M}_p \boldsymbol{\tau_1} \cdot \boldsymbol{\tau_1}, \\ M_2 &= \mathbb{M}_p \boldsymbol{\tau_1} \cdot \boldsymbol{\tau_2} = \mathbb{M}_p \boldsymbol{\tau_2} \cdot \boldsymbol{\tau_1}, \\ M_3 &= \mathbb{M}_p \boldsymbol{\tau_2} \cdot \boldsymbol{\tau_2}, \\ B_1 &= \boldsymbol{B} \cdot \boldsymbol{\tau_1}, \\ B_2 &= \boldsymbol{B} \cdot \boldsymbol{\tau_2}. \end{aligned} \tag{1.89}$$

• **Symmetry line** of director vector $\boldsymbol{\tau}_1$ also defined as the intersection of two symmetry planes (refer to Figure 1.9b). The node is constrained to evolve along this line, its velocity becomes $\boldsymbol{V}_p = \alpha_1 \boldsymbol{\tau}_1$, and the relation (1.72) becomes

$$\alpha_1 \mathbb{M}_p \boldsymbol{\tau}_1 = \boldsymbol{B}_p. \tag{1.90}$$

The scalar α_1 is then easily determined by projecting this last relation on $\boldsymbol{\tau}_1$. One finds

$$\alpha_1 \mathbb{M}_p \boldsymbol{\tau_1} \cdot \boldsymbol{\tau_1} = \boldsymbol{B}_p \cdot \boldsymbol{\tau_1}, \tag{1.91}$$

and finally

$$\alpha_1 = \boldsymbol{B}_p \cdot \boldsymbol{\tau_1} \left(\mathbb{M}_p \boldsymbol{\tau_1} \cdot \boldsymbol{\tau_1}\right)^{-1}. \tag{1.92}$$

• **Symmetry point** which is the intersection of three symmetry planes (refer to Figure 1.9c). The node stays fixed, that is to say $\boldsymbol{V}_p = \boldsymbol{0}$.

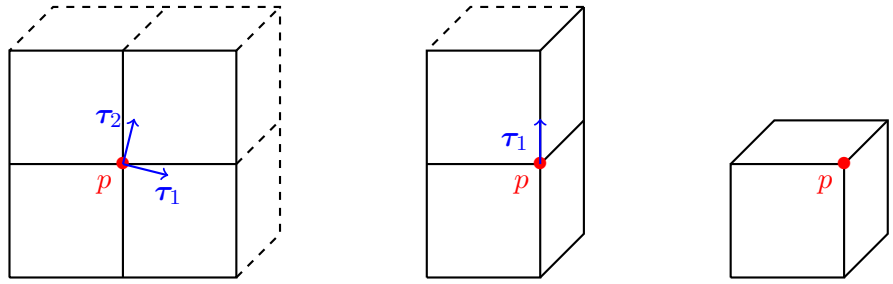

(a) (b) (c)

Figure 1.9 – Representation of the three possible symmetry boundary conditions. Symmetry plane (1.9a), symmetry line (1.9b) and symmetry point (1.9c).

1.5 Time step monitoring

In this section, we consider the time discretization of the numerical scheme using a first order Explicit Euler integration. The semi discrete system (1.45)-(1.58) is written under the general form

$$\frac{d\mathcal{U}_c}{dt} = \mathcal{F}(t, \mathcal{U}_c(t)), \tag{1.93}$$

where $\mathcal{U}_c = (v_c, \boldsymbol{V}_c, E_c)$ is the vector of unknowns and $\mathcal{F}(t, \mathcal{U}_c(t))$ is the flux function such that

$$\mathcal{F}(t, \mathcal{U}_c(t)) = \sum_{p \in \mathcal{P}(c)} \sum_{f \in \mathcal{F}(c,p)} \left(s_{pf} \boldsymbol{V}_p \cdot \boldsymbol{n}_{pf}, \quad s_{pf} P_{cfp} \boldsymbol{n}_{pf}, \quad s_{pf} P_{cfp} \boldsymbol{V}_p \cdot \boldsymbol{n}_{pf} \right)^t. \tag{1.94}$$

Then, a classic Explicit Euler time integration writes as

$$\begin{aligned} \mathcal{U}_c^{n+1} &= \mathcal{U}_c^n + \Delta t \mathcal{F}\left(t^n, \mathcal{U}^n\right), \\ t^{n+1} &= t^n + \Delta t, \end{aligned} \tag{1.95}$$

where the superscript n indicates that the approximation is made at time t^n and Δt is the time step of the scheme. The different criteria imposed for computing the time step Δt are detailed in the sequel.

1.5.1 Volume variation criterion

A first constraint is applied to the time step in order to control the variation of the cell volume [93, 95]. Approximating $(v_c^{n+1} - v_c^n)$ by $\Delta t_c (dv_c/dt)^n$ thanks to the GCL equation (1.45), one can impose the volume variation to be less than a fixed value $C_v \in [0, 1]$. This criterion writes

$$\Delta t \frac{|(dv_c/dt)^n|}{v_c^n} \leq C_v, \tag{1.96}$$

hence

$$\Delta t \leq C_v \frac{v_c^n}{|(dv_c/dt)^n|}. \tag{1.97}$$

In this way, introducing the time step

$$\Delta t_v = \min_c \left\{ \frac{v_c^n}{|(dv_c/dt)^n|} \right\}, \tag{1.98}$$

the condition $\Delta t \leq C_v \Delta t_v$ ensures that the volume variation is lower than C_v for each cell.

1.5.2 Positivity of the internal energy

A second constraint is imposed on the time step to ensure that the new internal energy, ε_c^{n+1}, is positive in every cell. Here we follow the procedure proposed in [126, 127]. Starting from the discrete system

$$\begin{aligned}
&m_c \left(\frac{1}{\rho_c^{n+1}} - \frac{1}{\rho_c^n} \right) - \Delta t \sum_{p \in \mathcal{P}(c)} \sum_{f \in \mathcal{F}(c,p)} s_{pf} \boldsymbol{V}_p \cdot \boldsymbol{n}_{pf} = 0, \\
&m_c \left(\boldsymbol{V}_c^{n+1} - \boldsymbol{V}_c^n \right) + \Delta t \sum_{p \in \mathcal{P}(c)} \sum_{f \in \mathcal{F}(c,p)} s_{pf} P_{cfp} \boldsymbol{n}_{pf} = \boldsymbol{0}, \\
&m_c \left(E_c^{n+1} - E_c^n \right) + \Delta t \sum_{p \in \mathcal{P}(c)} \sum_{f \in \mathcal{F}(c,p)} s_{pf} P_{cfp} \boldsymbol{V}_p \cdot \boldsymbol{n}_{pf} = 0,
\end{aligned} \tag{1.99}$$

let write the discrete Gibbs relation. The discrete kinetic energy variation is computed as

$$m_c \left(\frac{(\boldsymbol{V}_c^{n+1})^2}{2} - \frac{(\boldsymbol{V}_c^n)^2}{2} \right) = \frac{m_c}{2} \left(\boldsymbol{V}_c^{n+1} - \boldsymbol{V}_c^n \right) \left(\boldsymbol{V}_c^{n+1} + \boldsymbol{V}_c^n \right). \tag{1.100}$$

Using then the discrete momentum equation of system (1.99), one writes the half-time velocity $\boldsymbol{V}_c^{n+\frac{1}{2}}$ as

$$\boldsymbol{V}_c^{n+\frac{1}{2}} = \frac{1}{2} \left(\boldsymbol{V}_c^{n+1} + \boldsymbol{V}_c^n \right) = \boldsymbol{V}_c^n - \frac{\Delta t}{2 m_c} \sum_{p \in \mathcal{P}(c)} \sum_{f \in \mathcal{F}(c,p)} s_{pf} P_{cfp} \boldsymbol{n}_{pf}. \tag{1.101}$$

Multiplying this velocity by the discrete momentum equation of system (1.99), the relation (1.100) becomes

$$\begin{aligned}
m_c \left(\frac{(\boldsymbol{V}_c^{n+1})^2}{2} - \frac{(\boldsymbol{V}_c^n)^2}{2} \right) &= m_c \left(\boldsymbol{V}_c^{n+1} - \boldsymbol{V}_c^n \right) \boldsymbol{V}_c^{n+\frac{1}{2}}, \\
&= -\Delta t \sum_{p \in \mathcal{P}(c)} \sum_{f \in \mathcal{F}(c,p)} s_{pf} P_{cfp} \boldsymbol{V}_c^n \cdot \boldsymbol{n}_{pf} \\
&+ \frac{\Delta t^2}{2 m_c} \left(\sum_{p \in \mathcal{P}(c)} \sum_{f \in \mathcal{F}(c,p)} s_{pf} P_{cfp} \boldsymbol{n}_{pf} \right)^2.
\end{aligned} \tag{1.102}$$

Subtracting this relation into the discrete total energy conservation relation of system (1.99) leads to the following relation for the discrete internal energy

$$\begin{aligned} m_c\left(\varepsilon_c^{n+1}-\varepsilon_c^n\right) = & -\Delta t \sum_{p\in\mathcal{P}(c)}\sum_{f\in\mathcal{F}(c,p)} s_{pf}P_{cfp}(\boldsymbol{V}_p^n-\boldsymbol{V}_c^n)\cdot\boldsymbol{n}_{pf} \\ & -\frac{\Delta t^2}{2m_c}\left(\sum_{p\in\mathcal{P}(c)}\sum_{f\in\mathcal{F}(c,p)} s_{pf}P_{cfp}\boldsymbol{n}_{pf}\right)^2. \end{aligned} \tag{1.103}$$

In this way, one can write

$$\begin{aligned} m_c\left(\varepsilon_c^{n+1}-\varepsilon_c^n\right)+ & m_cP_c^n\left(\frac{1}{\rho_c^{n+1}}-\frac{1}{\rho_c^n}\right) = \\ & -\Delta t \sum_{p\in\mathcal{P}(c)}\sum_{f\in\mathcal{F}(c,p)} s_{pf}(P_{cfp}-P_c)(\boldsymbol{V}_p^n-\boldsymbol{V}_c^n)\cdot\boldsymbol{n}_{pf} \\ & -\frac{\Delta t^2}{2m_c}\left(\sum_{p\in\mathcal{P}(c)}\sum_{f\in\mathcal{F}(c,p)} s_{pf}P_{cfp}\boldsymbol{n}_{pf}\right)^2, \end{aligned} \tag{1.104}$$

which states for the discrete form of the Gibbs relation (1.61). Using now the definition of the nodal pressure flux (1.68), the previous relation writes equivalently

$$\begin{aligned} \varepsilon_c^{n+1} = & \varepsilon_c^n - P_c^n\left(\frac{1}{\rho_c^{n+1}}-\frac{1}{\rho_c^n}\right) \\ & +\frac{\Delta t}{m_c}\sum_{p\in\mathcal{P}(c)}\sum_{f\in\mathcal{F}(c,p)} s_{pf}Z_c\Big[(\boldsymbol{V}_p^n-\boldsymbol{V}_c^n)\cdot\boldsymbol{n}_{pf}\Big]^2 \\ & -\frac{\Delta t^2}{2m_c^2}\left(\sum_{p\in\mathcal{P}(c)}\sum_{f\in\mathcal{F}(c,p)} s_{pf}Z_c\Big[(\boldsymbol{V}_p^n-\boldsymbol{V}_c^n)\cdot\boldsymbol{n}_{pf}\Big]\boldsymbol{n}_{pf}\right)^2. \end{aligned} \tag{1.105}$$

Let write this relation under the compact form

$$\varepsilon_c^{n+1} = A_c + \frac{\Delta t Z_c}{m_c}B_c, \tag{1.106}$$

where

$$\begin{aligned} A_c = & \ \varepsilon_c^n - P_c^n\left(\frac{1}{\rho_c^{n+1}}-\frac{1}{\rho_c^n}\right), \\ B_c = & \sum_{p\in\mathcal{P}(c)}\sum_{f\in\mathcal{F}(c,p)} s_{pf}\Big[(\boldsymbol{V}_p^n-\boldsymbol{V}_c^n)\cdot\boldsymbol{n}_{pf}\Big]^2 \\ & -\frac{\Delta t Z_c}{2m_c}\left(\sum_{p\in\mathcal{P}(c)}\sum_{f\in\mathcal{F}(c,p)} s_{pf}\Big[(\boldsymbol{V}_p^n-\boldsymbol{V}_c^n)\cdot\boldsymbol{n}_{pf}\Big]\boldsymbol{n}_{pf}\right)^2. \end{aligned} \tag{1.107}$$

Then, the positivity of ε_c^{n+1} is ensured if both A_c and B_c are positive.

Positivity of A_c

The positivity of A_c is straightforwardly ensured if

$$\varepsilon_c^n \geq P_c^n \left(\frac{1}{\rho_c^{n+1}} - \frac{1}{\rho_c^n} \right), \tag{1.108}$$

which is equivalent to

$$\left(\frac{1}{\rho_c^{n+1}} - \frac{1}{\rho_c^n} \right) \leq \frac{\varepsilon_c^n}{P_c^n}, \tag{1.109}$$

since $P_c > 0$. In particular, multiplied by m_c, this relation can be written as

$$\frac{|v_c^{n+1} - v_c^n|}{v_c^n} \leq \frac{\varepsilon_c^n \rho_c^n}{P_c^n} = \frac{1}{\gamma - 1}, \tag{1.110}$$

in the particular case of a fluid defined by a gamma gas law (refer to Chapter 3). One recognizes the criterion controlling the volume variation defined previously. In this way,

$$\text{if} \quad C_v \leq \frac{1}{\gamma - 1} \quad \text{then} \quad A_c \geq 0. \tag{1.111}$$

In particular, if $\gamma = \frac{5}{3}$ (monoatomic gas) or $\gamma = \frac{7}{5}$ (diatomic gas) one obtains respectively

$$C_v \leq 1.5 \quad \text{and} \quad C_v \leq 2.5, \tag{1.112}$$

which are not severe constraints.

Positivity of B_c

The positivity of B_c is more complex to control. Let introduce the variable $\delta V_{cfp} = (\boldsymbol{V}_p^n - \boldsymbol{V}_c^n) \cdot \boldsymbol{n}_{pf}$ and let use the change of variable

$$\begin{array}{c} (p,f) \\ \mathcal{P}(c) \times \mathcal{F}(c,p) \end{array} \mapsto \begin{array}{c} k \\ \mathcal{K}(c) = \mathcal{P}(c) \times \mathcal{F}(c,p). \end{array} \tag{1.113}$$

In this way, B_c can be simplified into

$$B_c = \sum_{k \in \mathcal{K}(c)} s_k (\delta V_{ck})^2 - \frac{\Delta t Z_c}{2 m_c} \left(\sum_{k \in \mathcal{K}(c)} s_k \delta V_{ck} \boldsymbol{n}_k \right)^2. \tag{1.114}$$

Developing this expression leads to

$$B_c = \sum_{k \in \mathcal{K}(c)} s_k (\delta V_{ck})^2 \left(1 - \frac{\Delta t Z_c}{2 m_c} s_k \right) - \frac{\Delta t Z_c}{2 m_c} \sum_{k \in \mathcal{K}(c)} \sum_{l \neq k} s_k s_l \delta V_{ck} \delta V_{cl} \boldsymbol{n}_k \cdot \boldsymbol{n}_l. \tag{1.115}$$

Now, this expression can be written under the following quadratic form

$$B_c = \mathbb{K}_c \boldsymbol{\delta V}_c \cdot \boldsymbol{\delta V}_c, \tag{1.116}$$

where $(\boldsymbol{\delta V}_c)_k = \delta V_{ck}$ and the matrix $\mathbb{K}_c$ is such that

$$(\mathbb{K}_c)_{k,l} = \begin{cases} s_k \left(1 - \dfrac{\Delta t Z_c}{2m_c} s_k\right), & \text{if } k = l, \\ -\dfrac{\Delta t Z_c}{2m_c} s_k s_l \boldsymbol{n}_k \cdot \boldsymbol{n}_l, & \text{if } k \neq l. \end{cases} \tag{1.117}$$

A sufficient condition for B_c to be positive is that the matrix $\mathbb{K}_c$ is symmetric diagonally dominant with non-negative diagonal terms which makes $\mathbb{K}_c$ positive semi-definite. The symmetry is trivial. Now, the term $(\mathbb{K}_c)_{k,k}$ is positive under the condition

$$\Delta t \leq \frac{2m_c}{s_k Z_c}. \tag{1.118}$$

Finally, it can be proved that the matrix is diagonally dominant, ie $(\mathbb{K}_c)_{k,k} \geq \sum_{l \neq k} (\mathbb{K}_c)_{k,l}$, under the condition

$$\Delta t \leq \frac{2m_c}{Z_c \sum_{l \neq k} s_l |\boldsymbol{n}_k \cdot \boldsymbol{n}_l|}. \tag{1.119}$$

Since $|\boldsymbol{n}_k \cdot \boldsymbol{n}_l| \leq 1$, both conditions (1.118) and (1.119) are respected if the time step is chosen, for example, such as

$$\Delta t \leq \frac{m_c}{Z_c \sum_k s_k} = \frac{v_c}{a_c \sum_k s_k}. \tag{1.120}$$

In this way, the condition

$$\Delta t \leq \Delta t_{CFL} = \min_c \left\{ \frac{v_c}{a_c \sum_k s_k} \right\}, \tag{1.121}$$

ensures that the internal energy at time t^{n+1} is positive in every cells. One can remark that its form is equivalent to a CFL criterion [30].

1.5.3 Final time step

The final time step is chosen as

$$\Delta t^n = \min(C_v \Delta t_v, \quad C_e \Delta t_{CFL}, \quad C_m \Delta t^{n-1}), \tag{1.122}$$

where $C_e = 0.45$, $C_v = 0.1$, $C_m = 1.1$ and Δt^{n-1} is the time step of the previous iteration. This last criterion is here to ensure that the increase or decrease of the time step is not to steep. Moreover, one can easily verify that for the perfect gas considered in this study, the condition $C_v \leq 1/(\gamma - 1)$ is respected when $C_v = 0.1$. This value corresponds to a maximum variation of 10% of the cell volume over a time step as proposed in [93, 95].

First order algorithm:

- The state $\mathcal{U}^n$ is completely known.
- Computation of the nodal fluxes P^n_{cfp} and $\boldsymbol{V}^n_p$ from (1.68) and (1.72).
- Computation of the time step Δt (1.122).
- Mesh update from the discrete trajectory equation:

$$\boldsymbol{x}^{n+1} = \boldsymbol{x}^n + \Delta t \boldsymbol{V}^n_p. \tag{1.123}$$

- Computation of the new velocity $\boldsymbol{V}^{n+1}_c$ and total energy E^{n+1}_c from (1.58):

$$\begin{aligned} \boldsymbol{V}^{n+1}_c &= \boldsymbol{V}^n_c - \frac{\Delta t}{m_c} \sum_{p\in\mathcal{P}(c)} \sum_{f\in\mathcal{F}(c,p)} s^n_{pf} P^n_{cfp} \boldsymbol{n}^n_{pf}, \\ E^{n+1}_c &= E^n_c - \frac{\Delta t}{m_c} \sum_{p\in\mathcal{P}(c)} \sum_{f\in\mathcal{F}(c,p)} s^n_{pf} P^n_{cfp} \boldsymbol{V}^n_p \cdot \boldsymbol{n}^n_{pf}. \end{aligned} \tag{1.124}$$

- Determination of the complete final state $\mathcal{U}^{n+1}$:

$$\begin{aligned} \rho^{n+1}_c &= m_c / v^{n+1}_c, \\ \varepsilon^{n+1}_c &= E^{n+1}_c - \frac{1}{2}\left(\boldsymbol{V}^{n+1}_c\right)^2, \\ P^{n+1}_c &= P(\rho^{n+1}_c, \varepsilon^{n+1}_c) \quad \text{(EOS)}, \\ a^{n+1}_c &= a(\rho^{n+1}_c, P^{n+1}) \quad \text{(EOS)}. \end{aligned} \tag{1.125}$$

Conclusion

In this Chapter, the first order 3D extension of the cell-centered Lagrangian scheme EUCCLHYD [93] is proposed. The Finite Volume spatial discretization is based on discrete operators that preserve symmetry and enable to solve exactly the GCL on any polyhedral unstructured mesh. The complete derivation of the scheme is detailed. It conserves globally the momentum and total energy and respects a local entropy inequality ensuring a positive entropy production through shock waves. The treatment of boundary conditions is also detailed for the sake of completeness. Finally, the different criteria imposed on the time step are detailed. One finds the classical volume variation criterion already proposed in [93]. Besides, the criterion proposed in [126, 127] ensuring the positivity of the internal energy is extended to this 3D scheme. In Chapter 2, the second order extension of this Finite Volume scheme is investigated in the 3D context using a MUSCL procedure.

Chapter 2

Second order extension in space and time

2.1 Introduction

First order schemes such as the one presented in Chapter 1 are quite diffusive. Their extension to second order accuracy is crucial to improve the accuracy of the numerical solution. Let mention however that accuracy can be improved in smooth regions only. Around a discontinuity, such as a shock wave, the numerical solution cannot be better than first order. Let also mention that the time accuracy of a scheme must be consistent with its spatial accuracy. In this way, work has to be done on both space and time approximations to improve the global accuracy of the scheme. This Chapter is dedicated to the second order extension since it introduces numerous difficulties linked to the Lagrangian formalism and the multi-dimensional context.

To improve the spatial accuracy of a scheme, one has to improve the order of approximation of the variables in the cells. Under a Finite Element (FE) or a Discontinuous-Galerkin (DG) formalism, the physical variables are projected on a basis of polynomial functions. The order of accuracy of the scheme is then linked to the order of the polynomials constituting this basis. In the particular case of Lagrangian schemes, one can refer to [38, 113] and to [89, 124, 125] for examples of second (or higher) order schemes under the FE and DG formalisms respectively. In the case of Finite Volume (FV) schemes, the physical variables are integrated over the cells which corresponds to a piecewise constant approximation of the unknowns. To improve the accuracy of the scheme, one has to reconstruct the variable fields. The order of accuracy is then linked to the order of the reconstruction. For example, a piecewise linear approximation of the variables leads to a second order accurate method. High order procedures (greater than 2) are not considered in this study since they require a high order approximation of the geometry (curved meshes) in addition to a high order approximation of the variables and curved geometries are particularly complex to compute in the 3D context.

In this study, the second order extension in space is performed using a MUSCL procedure (Monotonic Upstream-centered Scheme for Conservation Laws). This procedure was proposed by Van Leer in his seminal work [81, 82] and is very natural for Finite Volumes schemes. It consists in a piecewise linear reconstruction of the variables and a monotonicity criterion. This criterion ensures that a reconstructed value lies within the range of the neighbouring cell values in order to prevent oscillations and ensure the stability of the solution. In particular, the monotonicity is imposed by limiting the gradients of the linear reconstruction using slope limiters. Reviews of classic 1D slope limiters can be found in [12, 83]. The MUSCL procedure is complex to perform in the multi-dimensional context. For example, one can refer to [68, 105, 119] in the Eulerian context. However, in the case of Lagrangian schemes, since the mesh is moving with the flow, the approximations made during the MUSCL procedure impact immediately the mesh quality. In particular, spurious oscillations, overshoots and symmetry loss can be observed when using a Lagrangian scheme combined with limiting procedures that behave well on Eulerian simulations. Principally, the computation of accurate gradients on unstructured polyhedral meshes and the limiting of vector (or tensor) fields are the main difficulties of a multi-dimensional MUSCL procedure. The second one comes from the definition of extrema which is unclear for vector and tensor fields. In [65, 90], it is proposed to limit the vector fields using convex hulls. Indeed, if a reconstructed vector lies within the convex hull of the neighbouring vector values then one can show that the monotonicity is respected in every directions. This procedure has been successfully used in 2D studies. However, its extension to the 3D context is complex, especially due to the construction of convex hulls, and is thus not investigated here. In this study, simple modifications of the limiting procedure are proposed to improve the monotonicity of the solution and preserve the flow symmetries. Besides, a second limiter, based on the multi-dimensional extension of the minmod limiter, is proposed to provide a very strong limiting in the case of 1D radial flows. Concerning the second order extension in space, both the two-step Predictor-Corrector (PC) and the one-step Generalized Riemann Problem (GRP) integration procedures are detailed.

The Chapter is structured as follows. In Section 2.2, the multi-dimensional extension of the MUSCL procedure is described. In particular, it consists in a component-wise limiting of the fields. In Section 2.3, the SP-limiter (for Symmetry Preserving limiter) is presented. Then, the Section 2.4 presents the MM-limiter (for Multi-dimensional Minmod limiter) specially designed for spherical problems. Finally the Section 2.6 presents the second order time discretization of the scheme.

2.2 The MUSCL procedure

In this section we detail the classic multi-dimensional extension of the MUSCL procedure to the Lagrangian scheme presented in Chapter 1. In particular, the accuracy of the scheme is improved by using nodal extrapolated values in the nodal

solver (1.68)-(1.72) instead of cell-centered values. It is sufficient to reconstruct the pressure and velocity fields only, the cell impedance Z_c is supposed to remain constant for the sake of simplicity. Besides, let mention that the use of extrapolated values in the nodal solver has the good property of decreasing the entropy production by reducing the velocity jump in relation (1.69).

2.2.1 Piecewise linear reconstruction

The first step of the MUSCL procedure is to linearly reconstruct the variable fields within each cell. Let consider an arbitrary scalar field φ and a vector field $\boldsymbol{\psi}$. The linear reconstruction of these fields over the cell c writes

$$\begin{aligned} \widetilde{\varphi}_c(\boldsymbol{x}) &= \varphi_c + \nabla\varphi_c \cdot (\boldsymbol{x} - \boldsymbol{x}_c), \\ \widetilde{\boldsymbol{\psi}}_c(\boldsymbol{x}) &= \boldsymbol{\psi}_c + \nabla\boldsymbol{\psi}_c(\boldsymbol{x} - \boldsymbol{x}_c), \end{aligned} \tag{2.1}$$

where $\widetilde{\varphi}_c(\boldsymbol{x})$ (respectively $\widetilde{\boldsymbol{\psi}}_c(\boldsymbol{x})$) is the extrapolated value at point $\boldsymbol{x} \in \omega_c$ and $\nabla\varphi_c$ (respectively $\nabla\boldsymbol{\psi}_c$) is the gradient of φ (respectively $\boldsymbol{\psi}$) in the cell. In particular, $\nabla\varphi_c$ is a vector and $\nabla\boldsymbol{\psi}_c$ is a tensor. Finally, the point $\boldsymbol{x}_c$ is the point of reference of the cell ω_c. It can be defined as the cell centroid

$$\boldsymbol{x}_c = \frac{1}{v_c} \int_{\omega_c} \boldsymbol{x} \, \mathrm{d}v, \tag{2.2}$$

or the cell barycenter

$$\boldsymbol{x}_c = \frac{1}{N_{p,c}} \sum_{p \in \mathcal{P}(c)} \boldsymbol{x}_p, \tag{2.3}$$

where $N_{p,c}$ is the number of nodes composing cell c. The integral (2.2) can be numerically approximated, for example using the procedure proposed in [100] which is valid for any polyhedral cell. However, this procedure introduces round-off errors that are disadvantageous for the global accuracy of the scheme. In the sequel, $\boldsymbol{x}_c$ is defined as the cell barycenter since it is easily computed for any arbitrary polyhedron.

Remark:
Here, one can observe that the reconstruction step is not conservative. By definition, the reconstruction is said to be conservative if the mean value φ_c is recovered when integrating $\widetilde{\varphi}_c(\boldsymbol{x})$ over the cell c. In particular, this is easily proved to be true if and only if $\boldsymbol{x}_c$ is the cell centroid. For the Lagrangian scheme used in this study, the conservation of momentum and total energy are imposed by construction of the nodal solver through the use of relation (1.70) (refer to Section 1.4.3). In this way, the conservativity of the scheme is ensured regardless the definition of point $\boldsymbol{x}_c$. In particular, this property allows to define $\boldsymbol{x}_c$ as the cell barycenter. Moreover, let recall that the mass conservation is imposed by construction.

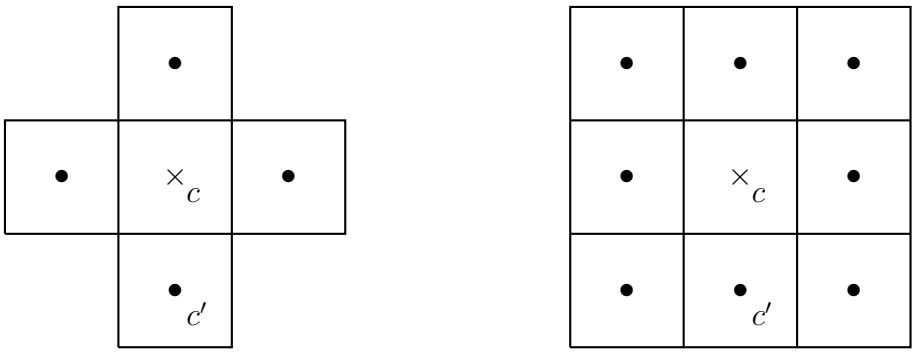

(a) (b)

Figure 2.1 – Representation of the two possible stencils $\mathcal{C}_f(c)$ (left) and $\mathcal{C}_p(c)$ (right) for a 2D Cartesian mesh. The neighboring cells c' are represented by black dots.

2.2.2 Gradient computation

Least squares (LS) procedure

The gradients introduced in relation (2.1) can be computed by a classical LS procedure [8]. This procedure is interesting since it enables to recover the analytic gradient in the case of linear fields and this independently of the mesh. It is detailed here for the sake of completeness. The first step is to impose the following condition on the linear fields $\widetilde{\varphi}_c$ and $\widetilde{\boldsymbol{\psi}}_c$

$$\begin{aligned} \widetilde{\varphi}_c(\boldsymbol{x}_{c'}) &= \varphi_{c'}, \\ \widetilde{\boldsymbol{\psi}}_c(\boldsymbol{x}_{c'}) &= \boldsymbol{\psi}_{c'}, \end{aligned} \tag{2.4}$$

which means that they must recover the mean values $\varphi_{c'}$ and $\boldsymbol{\psi}_{c'}$ in the neighboring cells c'. There is two possible neighborhoods, the face-based neighboring $\mathcal{C}_f(c)$ which contains all the cells c' sharing a face with cell c, and the node-based neighboring $\mathcal{C}_p(c)$ which contains all the cells c' sharing a node with cell c. These two stencils are sketched in Figure 2.1 in the simple case of a 2D Cartesian grid. There is no particular rule enabling to choose between these two stencils. In the foregoing computations, the stencil is arbitrarily denoted $\mathcal{C}_f(c)$.

The linear system resulting from (2.4) is over-determined thus we solve it in the least squares sense, seeking for the gradient minimizing the difference between the extrapolated value $\widetilde{\varphi}_c(\boldsymbol{x}_{c'})$ and the mean value $\varphi_{c'}$ (respectively $\widetilde{\boldsymbol{\psi}}_c(\boldsymbol{x}_{c'})$ and $\boldsymbol{\psi}_{c'}$) for all the cells $c' \in \mathcal{C}_f(c)$. Let detail the scalar case: introducing the residual $\mathcal{R}_{cc'} = \widetilde{\varphi}_c(\boldsymbol{x}_{\boldsymbol{c'}}) - \varphi_{c'}$, the functional is defined as

$$\mathcal{F}(\nabla\varphi_c) = \sum_{c'\in\mathcal{C}_f(c)} \mathcal{R}_{cc'}^2 = \sum_{c'\in\mathcal{C}_f(c)} \frac{1}{2}\big(\widetilde{\varphi}_c(\boldsymbol{x}_{\boldsymbol{c'}}) - \varphi_{c'}\big)^2, \tag{2.5}$$

and the minimizing condition

$$\frac{d\mathcal{F}}{d\nabla\varphi_c} = 0. \tag{2.6}$$

Substituting relation (2.1) into (2.5), the minimizing condition becomes

$$\frac{d\mathcal{F}}{d\nabla\varphi_c} = \frac{d}{d\nabla\varphi_c} \sum_{c'\in\mathcal{C}_f(c)} \frac{1}{2}\big(\varphi_c + \nabla\varphi_c \cdot (\boldsymbol{x}_{c'} - \boldsymbol{x}_c) - \varphi_{c'}\big)^2, \tag{2.7}$$

then using the chain rule and the formula (D.1), one gets

$$\mathbf{0} = \sum_{c'\in\mathcal{C}_f(c)} \big(\varphi_c - \varphi_{c'}\big)\big(\boldsymbol{x}_{c'} - \boldsymbol{x}_c\big) + \sum_{c'\in\mathcal{C}_f(c)} \nabla\varphi_c\big(\boldsymbol{x}_{c'} - \boldsymbol{x}_c\big) \otimes \big(\boldsymbol{x}_{c'} - \boldsymbol{x}_c\big). \tag{2.8}$$

This minimizing condition can then be written

$$\mathbb{M}_c \nabla\varphi_c = \sum_{c'\in\mathcal{C}_f(c)} \big(\varphi_{c'} - \varphi_c\big)\big(\boldsymbol{x}_{c'} - \boldsymbol{x}_c\big), \tag{2.9}$$

where $\mathbb{M}_c$ is the symmetric definite positive matrix

$$\mathbb{M}_c = \sum_{c'\in\mathcal{C}_f(c)} \big(\boldsymbol{x}_{c'} - \boldsymbol{x}_c\big) \otimes \big(\boldsymbol{x}_{c'} - \boldsymbol{x}_c\big). \tag{2.10}$$

This matrix is always invertible (refer to Appendix D.3) and the gradient finally writes

$$\nabla\varphi_c = \mathbb{M}_c^{-1} \left[\sum_{c'\in\mathcal{C}_f(c)} \big(\varphi_{c'} - \varphi_c\big)\big(\boldsymbol{x}_{c'} - \boldsymbol{x}_c\big) \right]. \tag{2.11}$$

In the case of a vector field, the same minimizing procedure leads to

$$\nabla\boldsymbol{\psi}_c \mathbb{M}_c = \sum_{c'\in\mathcal{C}_f(c)} \big(\boldsymbol{\psi}_{c'} - \boldsymbol{\psi}_c\big) \otimes \big(\boldsymbol{x}_{c'} - \boldsymbol{x}_c\big), \tag{2.12}$$

and finally, using relation (D.9),

$$\nabla\boldsymbol{\psi}_c = \left[\sum_{c'\in\mathcal{C}_f(c)} \big(\boldsymbol{\psi}_{c'} - \boldsymbol{\psi}_c\big) \otimes \big(\boldsymbol{x}_{c'} - \boldsymbol{x}_c\big) \right] \mathbb{M}_c^{-1}. \tag{2.13}$$

One has to take care that $\mathbb{M}_c^{-1}$ is right multiplied this time since the matrix between brackets is not symmetric.

The relations (2.11) and (2.13) suppose that the variables $\varphi_{c'}$ and $\boldsymbol{\psi}_{c'}$ are known in all the neighboring cells c'. However, this is not true at the boundaries of the domain. In particular, the main drawback of the LS procedure is that it is not possible to properly take into account the pressure and velocity boundary conditions. In the case of symmetry boundary conditions, it it possible to reconstruct the vector field in the neighboring ghost cells. However, the task quickly becomes complex when dealing with the node-based stencil $\mathcal{C}_p(c)$ as sketched in Figure 2.2. This Figure shows a 2D Cartesian mesh for simplicity, however we are interested in 3D unstructured meshes for which the problem is more complex. This problem is well known and in general the stencil $\mathcal{C}_f(c)$ is chosen for the sake of simplicity.

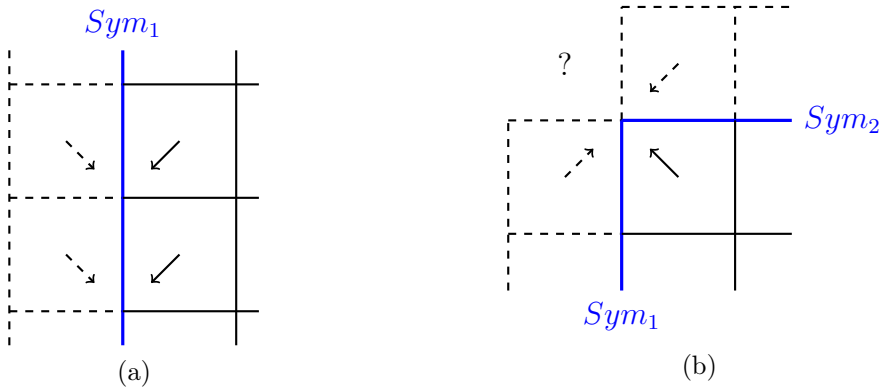

Figure 2.2 – Symmetrization of a vector field at the boundaries of the domain - Simple example of a 2D Cartesian mesh. Case of one symmetry boundary condition (left) and two symmetry boundary conditions (right).

Green formula

The LS procedure proposed previously presents two main drawbacks. First, the resulting gradients are dependent on the stencil chosen (refer to Figure 2.1). Second, information is missing to properly take into account the boundary conditions. This is why it is proposed to use the Green formula to compute the gradients ∇P_c and $\nabla \boldsymbol{V}_c$. Indeed, the discrete gradient operator introduced in Chapter 1 provides, by definition, a first order accurate approximation of the gradient in cell c. In this way, the cell gradients are computed as

$$\nabla P_c \approx \mathcal{GRAD}_c(P) = \frac{1}{v_c} \sum_{p \in \mathcal{P}(c)} \sum_{f \in \mathcal{F}(c,p)} s_{pf} P_{cfp} \boldsymbol{n}_{pf}, \tag{2.14}$$

and

$$\nabla \boldsymbol{V}_c \approx \mathcal{GRAD}_c(\boldsymbol{V}) = \frac{1}{v_c} \sum_{p \in \mathcal{P}(c)} \sum_{f \in \mathcal{F}(c,p)} s_{pf} \boldsymbol{V}_p \otimes \boldsymbol{n}_{pf}. \tag{2.15}$$

These gradients provide the analytic solution in the case of linear fields as shown in Appendix A.2. Moreover, they are more interesting than the LS gradients in some points. They are compatible with the spatial discretization in the sense that they approximate the cell gradient with the same accuracy that the scheme does. They do not depend on one of the stencils introduced in Figure 2.1. Finally, they naturally take the boundary conditions into account since they use the nodal fluxes P_{cfp} and $\boldsymbol{V}_p$. In particular, since these gradients depend on the first order solver, different results will be found depending on the studied scheme. One can refer to [28, 124] where discrete operators are also used.

2.2.3 Monotonicity criterion

The gradients in relation (2.1) are numerically approximated. If these gradients are too steep, the linear reconstruction can create non physical extrema leading to

numerical oscillations. In particular, such oscillations are known to appear at the discontinuities such as the ones encountered in shocks. To avoid these non-physical oscillations and preserve the scheme stability, it is necessary to limit the gradients using a monotonicity criterion as first proposed in [31, 48]. In this study, we are interested in the discrete maximum principle defining the minimum and maximum values of the linear reconstructed field in the neighborhood of the cell.

Let detail the scalar case. The classic limiting procedure consists in applying a scalar $\alpha_c \in [0,1]$ to the gradient $\nabla\varphi_c$ in order that the limited reconstructed value $\widetilde{\varphi}_c^{lim}(\boldsymbol{x})$ lies within the range of the neighboring cell averaged values. Mathematically, for a point $\boldsymbol{x}$ in cell c, one writes

$$\widetilde{\varphi}_c^{lim}(\boldsymbol{x}) = \varphi_c + \alpha_c \nabla\varphi_c \cdot (\boldsymbol{x} - \boldsymbol{x}_c), \tag{2.16}$$

and

$$\varphi_c^{min} \leq \widetilde{\varphi}_c^{lim}(\boldsymbol{x}) \leq \varphi_c^{max}, \quad \boldsymbol{x} \in \omega_c. \tag{2.17}$$

where φ_c^{min} and φ_c^{max} are respectively the minimum and maximum values of the scalar field φ in the neighboring of cell c. This neighboring can be defined by both the face-based $\mathcal{C}_f(c)$ or the node-based $\mathcal{C}_p(c)$ stencils presented in Figure 2.1. The face-based stencil is classically chosen for simplicity for the same reasons as for the LS procedure. In this case the extrema are computed as

$$\varphi_c^{min} = \min\left\{\min_{c'\in\mathcal{C}_f(c)}(\varphi_{c'}), \varphi_c\right\} \quad \text{and} \quad \varphi_c^{max} = \max\left\{\max_{c'\in\mathcal{C}_f(c)}(\varphi_{c'}), \varphi_c\right\}. \tag{2.18}$$

The criterion (2.17) can be simplified since the extremum values of a linear field are reached at the boundary of the polyhedral cells, i.e. at the cell nodes. One thus writes

$$\varphi_c^{min} \leq \widetilde{\varphi}_c^{lim}(\boldsymbol{x}_p) \leq \varphi_c^{max}, \quad p \in \mathcal{P}(c). \tag{2.19}$$

The next subsection shows how to compute the limiting scalar α_c.

The notion of extrema is intuitive and easy to manipulate for a scalar fields, even in the 3D space. It is however more complex in the case of vector (or tensor) fields. A vector can be compared to its neighbors thanks to the convex hull defined by the resulting set of vectors as proposed in [90]. Indeed, if a reconstructed vector $\boldsymbol{\psi}_c(\boldsymbol{x})$ lies in the convex hull of its neighbour vectors then it writes as a convex combination

$$\boldsymbol{\psi}_c(\boldsymbol{x}) = \sum_{d\in\mathcal{C}_f(c)} \lambda_d \boldsymbol{\psi}_d, \text{ where } \sum_{d\in\mathcal{C}_f(c)} \lambda_d = 1 \text{ and } \lambda_d \geq 0. \tag{2.20}$$

Then, for any direction $\boldsymbol{n}$, one can write the following monotonicity criterion

$$\min\left(\boldsymbol{\psi}_d \cdot \boldsymbol{n}\right) \leq \boldsymbol{\psi}_c(\boldsymbol{x}) \cdot \boldsymbol{n} \leq \max\left(\boldsymbol{\psi}_d \cdot \boldsymbol{n}\right). \tag{2.21}$$

However, the construction of convex hulls in 3D is complex and its extension to the case of tensor fields is not clear. This is why convex hulls are not investigated in this

work. To simplify this problem, it is proposed to apply the monotonicity criterion to the components of the vector field expressed in a certain basis as done in [88, 92]. This basis must then be representative of the flow direction as detailed in the next subsection.

2.2.4 Slope limiters

Scalar case

The direct application of the monotonicity criterion (2.19) to a reconstructed scalar field leads to the Barth-Jespersen limiter [9]. This limiter consists in defining the limiting factor α_c in relation (2.16) as

$$\alpha_c = \min_{p \in \mathcal{P}(c)} (\alpha_{c,p}), \tag{2.22}$$

where

$$\alpha_{c,p} = \begin{cases} \min\left(\dfrac{\varphi_c^{max} - \varphi_c}{\widetilde{\varphi}_c(\boldsymbol{x}_p) - \varphi_c},\ 1 \right) & \text{if } \widetilde{\varphi}_c(\boldsymbol{x}_p) > \varphi_c, \\ \min\left(\dfrac{\varphi_c^{min} - \varphi_c}{\widetilde{\varphi}_c(\boldsymbol{x}_p) - \varphi_c},\ 1 \right) & \text{if } \widetilde{\varphi}_c(\boldsymbol{x}_p) < \varphi_c, \\ 1 & \text{if } \widetilde{\varphi}_c(\boldsymbol{x}_p) = \varphi_c. \end{cases} \tag{2.23}$$

The proof of the Barth-Jespersen limiter is easily computed by substituting (2.16) into (2.19). The great advantage of this limiter is that it writes under the exact same form independently on the space dimension. Many others slope limiters have been developed for MUSCL-type procedures. A review of these limiters can be found in [12, 83].

Vector case

Here it is proposed to extend to the 3D context a well-tried procedure in 2D consisting in limiting the velocity field along directions computed from the flow. These directions are chosen in order to constitute a basis and thus this procedure can be assimilated to a component-wise limiting after the change of basis [88, 92, 95, 124]. The difficulty lies in the definition of this basis, denoted $\mathcal{B}_\xi^c = (\boldsymbol{\xi}_1^c, \boldsymbol{\xi}_2^c, \boldsymbol{\xi}_3^c)$, which has to preserve the flow symmetries in cell c. In particular, the basis has to be frame-invariant in the sense that it must be dependent on the flow and not on the frame of reference (refer to Chapter 5 for the mathematical definition of frame-indifference).

In [88, 92], the attempt is made to reconstruct the basis from the flow direction $\boldsymbol{\xi}_1^c = \boldsymbol{V}_c / \|\boldsymbol{V}_c\|$. The difficulty then lies in the computation of the second basis vector since the third one is naturally computed as $\boldsymbol{\xi}_3^c = \boldsymbol{\xi}_1^c \times \boldsymbol{\xi}_2^c$. Such a procedure fails to preserve the flow symmetries in every cases since the second basis vector cannot be

computed properly. For example, if the flow is 1D radial, there is infinite solutions to construct $\boldsymbol{\xi}_2$. Moreover, the direction $\boldsymbol{\xi}_1^c = \boldsymbol{V}_c/\|\boldsymbol{V}_c\|$ is not Galilean invariant which is not satisfactory. Such a procedure is thus not considered here.

During this thesis, the attempt has been made to use the basis constructed upon the eigenvectors of two matrices

$$\begin{aligned} &\circ \text{ the deformation gradient} \quad \mathbb{D}_c = \frac{1}{2}\Big[\mathcal{GRAD}_c(\boldsymbol{V}) + \big(\mathcal{GRAD}_c(\boldsymbol{V})\big)^t\Big] \\ &\circ \text{ and the matrix} \qquad\qquad \mathbb{N}_c = \sum_{p\in\mathcal{P}(c)} (\boldsymbol{x}_p - \boldsymbol{x}_c)\otimes(\boldsymbol{x}_p - \boldsymbol{x}_c). \end{aligned} \tag{2.24}$$

In particular, the second matrix represents the deformation of the cell and is similar to the matrix $\mathbb{M}_c$ appearing in the Least Squares procedure (2.10).

For an arbitrary basis $\mathcal{B}_\xi^c$, the limited vector field is written

$$\widetilde{\boldsymbol{\psi}}_c^{lim}(\boldsymbol{x}) = \boldsymbol{\psi}_c + (\mathbb{B}_{\xi,c}\mathbb{A}_c\mathbb{B}_{\xi,c}^t)\nabla\boldsymbol{\psi}_c(\boldsymbol{x}-\boldsymbol{x}_c), \quad \boldsymbol{x}\in\omega_c, \tag{2.25}$$

where $\mathbb{B}_{\xi,c} = (\boldsymbol{\xi}_1^c|\boldsymbol{\xi}_2^c|\boldsymbol{\xi}_3^c)$ is the change of basis and the limiting matrix $\mathbb{A}_c$ writes

$$\mathbb{A}_c = \begin{pmatrix} \alpha_{\xi_1} & 0 & 0 \\ 0 & \alpha_{\xi_2} & 0 \\ 0 & 0 & \alpha_{\xi_3} \end{pmatrix}. \tag{2.26}$$

The limiting scalars α_{ξ_1}, α_{ξ_2} and α_{ξ_3} are computed using the Barth-Jespersen limiter (2.22) component-wise in the $\mathcal{B}_\xi^c$ basis. In the particular case where $\mathcal{B}_\xi^c$ is the Cartesian basis, one has $\mathbb{B}_{\xi,c} = \mathrm{Id}$.

Unfortunately, none of these basis provide convincing results on 1D radial flows (refer to Chapter 3). This is linked to the difficulty of defining a frame-invariant basis and its effective numerical computation in the 3D space. Let mention that the accuracy of the procedures used, in particular when computing the eigenvectors of a matrix, is a supplementary difficulty. Here the eigenvectors are computed using a Numerical Recipe routine based on the Jacobi method [107].

In this section, we have detailed the classic multi-dimensional extension of the MUSCL procedure. Its algorithm is summarized in Section 2.5. It is shown in Chapter 3 that this limiting procedure leads to spurious oscillations, strong overshoots and symmetry loss on classic Lagrangian test cases. An additional limiting factor is classically added to the gradients in order to reduce these flaws. However such a scalar is user-defined and problem dependent which is not satisfactory.

2.3 The Symmetry Preserving limiter (SP-limiter)

This section proposes a new limiting procedure to drastically reduce the spurious oscillations and overshoots observable with the classic MUSCL procedure (refer to

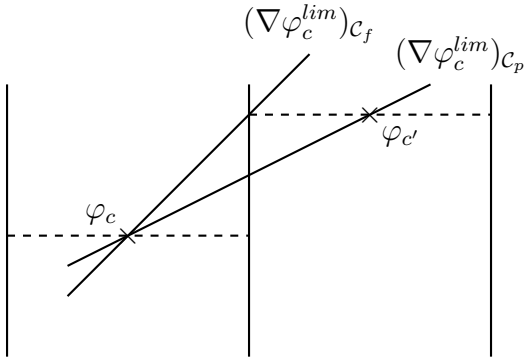

Figure 2.3 – Impact of the monotonicity stencil - Cell gradient limited on the face-based stencil $(\nabla\varphi_c^{lim})_{\mathcal{C}_f}$ and cell gradient limited on the node-based stencil $(\nabla\varphi_c^{lim})_{\mathcal{C}_p}$ - Schematic drawing in the 1D case.

Chapter 3). It seems indeed that the limited second order extension of a purely Lagrangian scheme is more difficult to control than in the case of ALE or Eulerian ones. This is due to the fact that the mesh motion is directly computed from the numerical solution of the gas dynamics equations. The main design principle of this limiter is the preservation of the flow symmetries. In this sense, it is referred to as SP-limiter for Symmetry Preserving limiter.

2.3.1 A different monotonicity stencil

To improve the monotonicity of the second order extension, it is proposed to modify the stencil used for the definition of the monotonicity criterion. Classically, the monotonicity is verified at the cell nodes thanks to relation (2.19). This criterion ensures that the monotonicity is respected everywhere in the cell since the field is linear, the maximum values are thus reached at the cell nodes. In this study it is proposed to extend the monotonicity stencil to the centers of the neighbouring cells such as

$$\varphi_c^{min} \leq \widetilde{\varphi}_c^{lim}(\boldsymbol{x}_{c'}) \leq \varphi_c^{max}, \qquad c' \in \mathcal{C}_p(c). \tag{2.27}$$

This modification is justifiable by the following arguments. First, the criterion (2.27) is completely equivalent to the criterion (2.19) for linear fields. Second, it ensures that the reconstructed field, extrapolated at the cells containing an extremum, respects this extremum which is not the case with criterion (2.19). This last argument is easily understood in 1D thanks to Figure 2.3. Moreover, this monotonicity stencil uses the node-based stencil $\mathcal{C}_p(c)$ since there is no reason why the extrema should have a face-based distribution as suggested by the stencil $\mathcal{C}_f(c)$. However, the boundary condition problem remains open: the pressure and velocity boundary conditions cannot be taken into account properly in the monotonicity criterion and the symmetry boundary conditions are taken into account by constructing the ghost cells in the $\mathcal{C}_f(c)$ neighbouring. However, nothing is done for ghost cells symmetric by one edge or one point.

2.3.2 Monotonicity criterion for a vector field

As explained previously, the change of basis classically proposed to limit the vector field component by component can lead to symmetry loss. In particular, it is worthwhile to seek for a scalar criterion representing the vector field in order to extend the scalar limiting procedure to the vector case. Few scalars can be representative of an arbitrary vector field. For example, one can consider the norm of the vector or its projection along a certain direction. All information about the vector direction is then lost.

Here, it is proposed to represent a vector field by its projection along a unique direction. This direction $\boldsymbol{\xi}_c$ is defined as the direction of the pressure gradient in the cell ω_c since it is colinear to the flow acceleration (thanks to the momentum conservation equation). Moreover, it is Galilean invariant, i.e. invariant by a uniform translation, whereas $\boldsymbol{V}_c/\|\boldsymbol{V}_c\|$ is not. One writes

$$\boldsymbol{\xi}_c = \begin{cases} \dfrac{(\nabla P)_c}{\|(\nabla P)_c\|}, & \text{if } \|(\nabla P)_c\| \neq 0, \\ \boldsymbol{e}_x, & \text{otherwise.} \end{cases} \tag{2.28}$$

In practice, the pressure gradient is approximated by relation (2.14). The corresponding monotonicity criterion then writes

$$\psi_c^{\xi,min} \leq \widetilde{\boldsymbol{\psi}}_c^{lim}(\boldsymbol{x}_{c'}) \cdot \boldsymbol{\xi}_c \leq \psi_c^{\xi,max}, \quad c' \in \mathcal{C}_p(c), \tag{2.29}$$

where the extrema are defined as

$$\begin{aligned} \psi_c^{\xi,min} &= \min \left\{ \min_{c' \in \mathcal{C}_p(c)} (\boldsymbol{\psi}_{c'} \cdot \boldsymbol{\xi}_c),\ \boldsymbol{\psi}_c \cdot \boldsymbol{\xi}_c \right\}, \\ \psi_c^{\xi,max} &= \max \left\{ \max_{c' \in \mathcal{C}_p(c)} (\boldsymbol{\psi}_{c'} \cdot \boldsymbol{\xi}_c),\ \boldsymbol{\psi}_c \cdot \boldsymbol{\xi}_c \right\}. \end{aligned} \tag{2.30}$$

It is possible to apply the classic Barth-Jespersen limiter (2.22) to the scalar criterion (2.29). The resulting limiting factor α_c is then applied to the whole tensor gradient $\nabla\boldsymbol{\psi}_c$ in order to preserve its inherent symmetries. Finally, the limited reconstructed field writes

$$\widetilde{\boldsymbol{\psi}}_c^{lim}(\boldsymbol{x}) = \boldsymbol{\psi}_c + \alpha_c \nabla\boldsymbol{\psi}_c(\boldsymbol{x} - \boldsymbol{x}_c), \quad \forall \boldsymbol{x} \in \omega_c. \tag{2.31}$$

Let mention that this limiting procedure is completely equivalent to the componentwise limiting in the case of 1D flows.

It is shown in Chapter 3 that the SP-limiter enables to remove the spurious oscillations and overshoots introduced by the classic componentwise limiting procedure. Nonetheless, the SP-limiter reaches its limits when confronted to spherical problems on strongly refined meshes. To deal with such flows, an other limiter is proposed in the following section.

2.4 Multi-dimensional Minmod limiter (MM-limiter)

The limiter proposed in this section is meant to deal with 1D radial symmetric problems involving strong shocks and mesh printing such as the Noh and Kidder problems (refer to Chapter 3). This limiter can be interpreted as the multi-dimensional extension of the classic 1D minmod limiter since it proposes to construct a cell gradient from nodal gradients, computed around each nodes of the cell, and the minmod function. The version presented in this section is very close to the limiter proposed in [53] with the difference that no change of basis is made here in order to preserve the flow symmetries. On the contrary, the nodal gradients are projected along a cell-relative direction. The cell gradient is then defined as the minmod value of the scalars resulting from these projections. The underlying idea is to filter the reconstructions that are not aligned with the flow in the cell. In this sense, this limiter is also well suited to 1D flows.

Considering a cell c, the first step of the MM-limiter consists in computing the nodal gradients with the Green formula. These gradients are denoted $\nabla\varphi_p$ and $\nabla\boldsymbol{\psi}_p$, $p \in \mathcal{P}(c)$ and are computed on the dual-cell ω_p around node p as sketched in Figure 2.4. In particular, one writes

$$\nabla\varphi_p = -\frac{1}{v_p} \sum_{c' \in \mathcal{C}(p)} \sum_{f \in \mathcal{F}(c',p)} s_{pf} \varphi_{c'} \boldsymbol{n}_{pf}, \tag{2.32}$$

and

$$\nabla\boldsymbol{\psi}_p = -\frac{1}{v_p} \sum_{c' \in \mathcal{C}(p)} \sum_{f \in \mathcal{F}(c',p)} s_{pf} \boldsymbol{\psi}_{c'} \otimes \boldsymbol{n}_{pf}, \tag{2.33}$$

where $\mathcal{C}(p)$ is the set of cells c' around node p. The volume v_p of the dual-cell ω_p is computed as

$$v_p = \sum_{c' \in \mathcal{C}(p)} \sum_{f \in \mathcal{F}(c',p)} v_{pf}, \tag{2.34}$$

where v_{pf} is the volume impinging on the face area vector $s_{pf}\boldsymbol{n}_{pf}$. By analogy with the construction of these face area vectors (refer to Section 1.3.2), this volume is computed as

$$v_p = \frac{1}{3} \left(\sum_{t_r \in \mathcal{T}(c,f,p)} v_{\mathscr{T}_{t_r}} + \sum_{t_r \in \mathcal{T}(c,f)} \frac{1}{N_{p,f}} v_{\mathscr{T}_{t_r}} \right), \tag{2.35}$$

where $v_{\mathscr{T}_{t_r}}$ is the volume of the tetrahedron $\mathscr{T}_{t_r}$ introduced in Section 1.3.2. For dual-cells on the boundary of the domain, it is possible to replace the values $\boldsymbol{\psi}_{c'}$ and $\varphi_{c'}$ in the ghost cell c' by the nodal fluxes on the face area vector.

The second step of the MM-limiter consists in defining a cell-relative direction $\boldsymbol{\xi}_c$ on which to perform the projections. In this study, $\boldsymbol{\xi}_c$ is defined as the direction

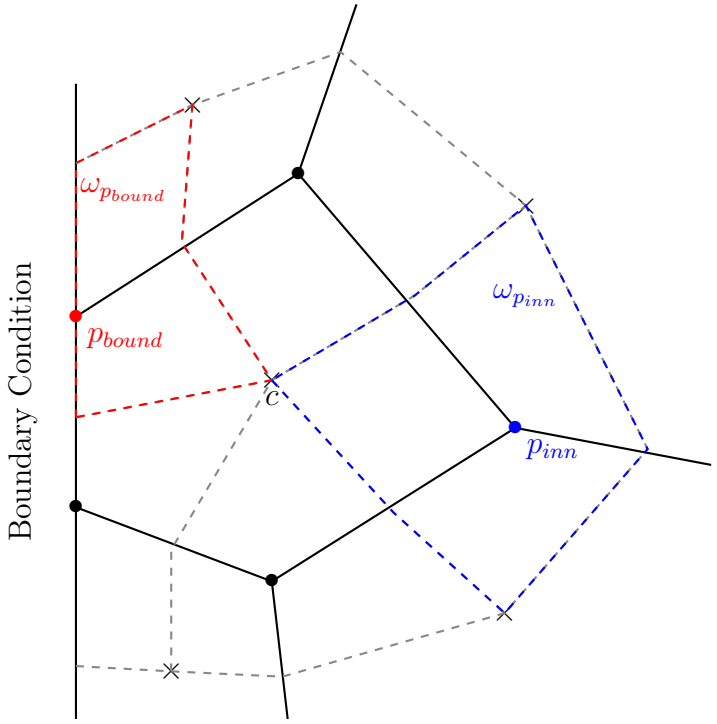

Figure 2.4 – Example of primal (solid lines) and dual meshes (dashed lines) in 2D - The dual-cell around the boundary node p_{bound} is denoted $\omega_{p_{bound}}$ (red) and the dual-cell around the inner node p_{inn} is denoted $\omega_{p_{inn}}$ (blue).

of the pressure gradient in the cell

$$\boldsymbol{\xi}_c = \begin{cases} \dfrac{(\nabla P)_c}{\|(\nabla P)_c\|}, & \text{if } \|(\nabla P)_c\| \neq 0, \\ \boldsymbol{e}_r, & \text{otherwise,} \end{cases} \tag{2.36}$$

where $\boldsymbol{e}_r = \boldsymbol{x}_c/\|\boldsymbol{x}_c\|$ is the radial direction in the cell and $(\nabla P)_c$ is approximated thanks to the relation (2.14). Let mention that in practice, setting $\boldsymbol{e}_r$ or $\boldsymbol{e}_x$ leads to equivalent results. Then the nodal gradients are projected along the $\boldsymbol{\xi}_c$ direction as follows

$$\begin{aligned} \nabla\varphi_p^{\xi} &= \nabla\varphi_p \cdot \boldsymbol{\xi}_c, \\ \nabla\psi_p^{\xi} &= (\nabla\boldsymbol{\psi}_p\boldsymbol{\xi}_c) \cdot \boldsymbol{\xi}_c. \end{aligned} \tag{2.37}$$

Finally, the limited cell gradients are constructed from the previous scalars as follows

$$\begin{aligned} \nabla\varphi_c &= \underset{p\in\mathcal{P}(c)}{\text{minmod}}\Big(\nabla\varphi_p^{\xi}\Big)\boldsymbol{\xi}_c, \\ \nabla\boldsymbol{\psi}_c &= \underset{p\in\mathcal{P}(c)}{\text{minmod}}\Big(\nabla\psi_p^{\xi}\Big)(\boldsymbol{\xi}_c \otimes \boldsymbol{\xi}_c), \end{aligned} \tag{2.38}$$

where the minmod function is defined as: let $(\alpha_p)_{p\in\{1,N\}}$ be a set of N scalar values,

then

$$\underset{p}{\text{minmod}}(\alpha_p) = \begin{cases} 0, & \text{if there exists } i \text{ and } j \text{ such that } \text{sign}(\alpha_i) \neq \text{sign}(\alpha_j), \\ \text{sign}(\alpha_i) \underset{i\in\{1,N\}}{\min} |\alpha_i|, & \text{otherwise.} \end{cases} \tag{2.39}$$

This limiter provides very satisfying results on 1D radial problems such as the Noh test case (refer to Chapter 3). In particular, it has the good property of not requiring an additive monotonicity criterion. This is due to the minmod function that automatically limits the gradient. It is well known that in the 1D case, the minmod limiter provides a monotonic second order solution. The proof is complex to derive in the 3D case, however, the results obtained on the Noh problem show that the reconstructed solution is monotonic. This good behavior is due to the symmetry of the spherical flows which are almost 1D around a cell. Another good property of this limiter is that it degenerates onto the classic minmod limiter in the 1D case.

2.5 Summary and algorithms

This section summaries the limiting procedures presented above and presents their respective algorithms.

A MUSCL procedure is proposed to improve the spatial accuracy of the Lagrangian scheme. To linearly reconstruct the pressure and velocity fields, the cell gradients can be computed with two methods: the LS procedure or the Green formula. Then, these gradients can be limiting in different ways. First, it is proposed to limit the fields component-wise in a certain basis. This limiting procedure is referred to as **CW-limiter** for Component-Wise limiter.

CW-limiter algorithm:

- Limit the pressure field with the Barth-Jespersen limiter (2.22) on the monotonicity stencil (2.19)
- Construct the basis $\mathcal{B}^c_{\boldsymbol{\xi}}$
- Limit the velocity field component-wise (2.25)

Second, a limiter is proposed to preserve the flow symmetries without resorting to a particular basis. The velocity field is projected along a cell-relative direction computed from the flow and a scalar limiter is computed from the resulting scalar field. This limiter is applied to the whole velocity gradient. Moreover, the stencil of the monotonicity criterion is extended to the centers of the neighboring cells. This new limiter is referred to as **SP-limiter** for Symmetry-Preserving limiter.

SP-limiter algorithm:

- Limit the pressure field with the Barth-Jespersen limiter (2.22) on the monotonicity stencil (2.27)
- Project the velocity field on the direction $\boldsymbol{\xi}_c$ (2.36)
- Limit the velocity field using a single scalar (2.31)

Third, a limiter is constructed for dealing with 1D and 1D-radial flows. This limiter is based on the multi-dimensional extension of the minmod limiter and nodal gradients computed with the Green formula on the dual mesh. It is referred to as **MM-limiter** for Multi-dimensional Minmod limiter.

MM-limiter algorithm:

- Compute the nodal pressure and velocity gradients from relations (2.32) and (2.33).
- Project these gradients along the $\boldsymbol{\xi}_c$ direction defined as the director vector of the pressure gradient in the cell (2.37).
- Construct the limited cell gradients ∇P_c and $\nabla \boldsymbol{V}_c$ from the gradient projections and the minmod function (2.38).

2.6 Second order extension in time

This section presents the second order extension in time of the scheme. Two different methods are presented here, the classic Predictor-Corrector (PC) scheme and the Generalized Riemann Problem (GRP) approach proposed by Ben-Artzi and Falcovitz [10].

2.6.1 Predictor-Corrector scheme (PC)

The PC scheme (as well as the second order Runge-Kutta (RK2) scheme) is widely used for reaching second order in time accuracy. It belongs to the family of two-steps time integration methods. Starting from a scheme written under the general semi-discrete form

$$\frac{d\mathcal{U}}{dt} = \mathcal{F}(t,\mathcal{U}), \tag{2.40}$$

the time integration is performed as

$$\begin{aligned}
&\mathcal{U}_c^{(1)} = \mathcal{U}_c^n + \alpha\Delta t\mathcal{F}\left(t^n,\mathcal{U}^n\right),\\
&\mathcal{U}_c^{n+1} = \mathcal{U}_c^{(1)} + \Delta t\left[\left(1-\frac{1}{2\alpha}\right)\mathcal{F}\left(t^n,\mathcal{U}^n\right) + \frac{1}{2\alpha}\mathcal{F}\left(t^{n+1},\mathcal{U}^{(1)}\right)\right],\\
&t^{n+1} = t^n + \Delta t,\\
&\alpha \in [0,1].
\end{aligned} \tag{2.41}$$

In particular, one recovers the PC scheme for $\alpha = 1$ and the RK2 scheme for $\alpha = 1/2$. The PC scheme is thus written

$$\begin{aligned}
&\mathcal{U}_i^{(1)} = \mathcal{U}_i^n + \Delta t \mathcal{F}\left(t^n, \mathcal{U}^n\right), \\
&\mathcal{U}_i^{n+1} = \mathcal{U}_i^{(1)} + \frac{1}{2}\Delta t \left[\mathcal{F}\left(t^n, \mathcal{U}^n\right) + \mathcal{F}\left(t^{n+1}, \mathcal{U}^{(1)}\right)\right], \\
&t^{n+1} = t^n + \Delta t.
\end{aligned} \tag{2.42}$$

The algorithm of the PC scheme is detailed in the sequel in the particular case of our Lagrangian scheme. The first step of this procedure, the **predictor step**, is nothing but an explicit Euler time integration such as the one presented at the end of Chapter 1. Starting from state $\mathcal{U}^n$, it computes an intermediate step $\mathcal{U}^{(1)}$. The new state $\mathcal{U}^{n+1}$ is then determined by the **corrector step**. This second step is less detailed since the stages are redundant.

Predictor step:

- The state $\mathcal{U}^n$ is completely known.
- If the flow is radial:
  - Call the MM-limiter algorithm

  Else:
  - Compute the pressure and velocity cell gradients
  - Call the SP-limiter algorithm

  EndIf
- Second order nodal solver:
  - computation of the nodal velocity $\boldsymbol{V}_p^n = \mathbb{M}_p^{-1}\boldsymbol{B}$ from relation (1.72) and the following right hand-side:

$$\boldsymbol{B} = \sum_{c\in\mathcal{C}(p)} \sum_{f\in\mathcal{F}(c,p)} s_{pf}^n \left[\widetilde{P}_c(\boldsymbol{x}_p^n)\boldsymbol{n}_{pf}^n + Z_c^n \widetilde{\boldsymbol{V}}_c(\boldsymbol{x}_p^n)\left(\boldsymbol{n}_{pf}^n \otimes \boldsymbol{n}_{pf}^n\right)\right], \tag{2.43}$$

  - computation of the nodal pressure P_{cfp} from the second order Riemann problem:

$$P_{cfp}^n = \widetilde{P}_c(\boldsymbol{x}_p^n) + Z_c^n \left(\widetilde{\boldsymbol{V}}_c(\boldsymbol{x}_p^n) - \boldsymbol{V}_p^n\right)\cdot \boldsymbol{n}_{pf}^n. \tag{2.44}$$

- Computation of the time step Δt (refer to Section 1.5).
- Mesh update from the discrete trajectory equation:

$$\boldsymbol{x}_p^{(1)} = \boldsymbol{x}_p^n + \Delta t \boldsymbol{V}_p^n. \tag{2.45}$$

- Computation of the intermediate velocity $\boldsymbol{V}_c^{(1)}$ and total energy $E_c^{(1)}$ from

the time discretization of (1.58):

$$\begin{aligned} \boldsymbol{V}_c^{(1)} &= \boldsymbol{V}_c^n - \frac{\Delta t}{m_c} \sum_{p\in\mathcal{P}(c)} \sum_{f\in\mathcal{F}(c,p)} s_{pf}^n P_{cfp}^n \boldsymbol{n}_{pf}^n, \\ E_c^{(1)} &= E_c^n - \frac{\Delta t}{m_c} \sum_{p\in\mathcal{P}(c)} \sum_{f\in\mathcal{F}(c,p)} s_{pf}^n P_{cfp}^n \boldsymbol{V}_p^n \cdot \boldsymbol{n}_{pf}^n. \end{aligned} \tag{2.46}$$

- Determination of the complete intermediate state $\mathcal{U}^{(1)}$ from relations (1.125) (EOS).

Corrector step:

- The state $\mathcal{U}^{(1)}$ is completely known.
- If the flow is radial:
  - Call the MM-limiter algorithm

  Else:
  - Compute the pressure and velocity cell gradients
  - Call the SP-limiter algorithm

  EndIf
- Second order nodal solver.
- Mesh update from the discrete trajectory equation and the mean nodal velocity

$$\boldsymbol{x}_p^{n+1} = \boldsymbol{x}_p^n + \frac{\Delta t}{2}\left(\boldsymbol{V}_p^n + \boldsymbol{V}_p^{(1)}\right). \tag{2.47}$$

- Computation of the new velocity $\boldsymbol{V}_c^{n+1}$ and total energy E_c^{n+1} using mean predicted fluxes:

$$\boldsymbol{V}_c^{n+1} = \boldsymbol{V}_c^n - \frac{\Delta t}{2m_c} \sum_{p\in\mathcal{P}(c)} \sum_{f\in\mathcal{F}(c,p)} \left[s_{pf}^n P_{cfp}^n \boldsymbol{n}_{pf}^n + s_{pf}^{(1)} P_{cfp}^{(1)} \boldsymbol{n}_{pf}^{(1)} \right], \tag{2.48}$$

$$E_c^{n+1} = E_c^n - \frac{\Delta t}{2m_c} \sum_{p\in\mathcal{P}(c)} \sum_{f\in\mathcal{F}(c,p)} \left[s_{pf}^n P_{cfp}^n \boldsymbol{V}_p^n \cdot \boldsymbol{n}_{pf}^n + s_{pf}^{(1)} P_{cfp}^{(1)} \boldsymbol{V}_p^{(1)} \cdot \boldsymbol{n}_{pf}^{(1)} \right]. \tag{2.49}$$

- Determination of the complete final state $\mathcal{U}^{n+1}$ from relation (1.125) (EOS).

The PC scheme can introduce a supplementary dissipation since it consists in solving the spatial discretization twice. The dissipation of the scheme is thus accumulated and the improvement of accuracy in time can be insufficient to compensate the loss of accuracy in space. The strength of this procedure remains its ease of implementation, however, it literally doubles the computation time. In the next

section, the one-step GRP integration procedure is described. This procedure is more complex to implement but is faster and less dissipative.

2.6.2 The Generalized Riemann Problem (GRP) approach

This section details the GRP procedure [10] used for the second order extension in time of the cell-centered Lagrangian scheme proposed throughout Chapters 1 and 2. Let mention that other efficient approaches exist such as the ADER approach used in [14]. The complete derivation of the GRP procedure can be found in [92] in the two-dimensional case. Here it is detailed in the 3D context. This procedure consists in performing a one-step time integration of the semi-discrete scheme

$$\begin{aligned}
&\frac{d\boldsymbol{x}_p}{dt} = \boldsymbol{V}_p, \\
&\frac{dv_c}{dt} - \sum_{p\in\mathcal{P}(c)} \sum_{f\in\mathcal{F}(c,p)} \boldsymbol{V}_p \cdot s_{pf}\boldsymbol{n}_{pf} = 0, \\
&m_c \frac{d\boldsymbol{V}_c}{dt} + \sum_{p\in\mathcal{P}(c)} \sum_{f\in\mathcal{F}(c,p)} P_{cfp} s_{pf}\boldsymbol{n}_{pf} = \boldsymbol{0}, \\
&m_c \frac{dE_c}{dt} + \sum_{p\in\mathcal{P}(c)} \sum_{f\in\mathcal{F}(c,p)} P_{cfp} \boldsymbol{V}_p \cdot s_{pf}\boldsymbol{n}_{pf} = 0,
\end{aligned} \tag{2.50}$$

where $\boldsymbol{V}_p$ is the second order node velocity computed from (1.72)-(2.43) and the second order pressure flux P_{cfp} (2.44). The integration of this system between times t^n and t^{n+1} is written

$$\begin{aligned}
&\boldsymbol{x}_p^{n+1} - \boldsymbol{x}_p^n = \int_{t^n}^{t^{n+1}} \boldsymbol{V}_p(t)\,\mathrm{d}t, \\
&v_c^{n+1} - v_c^n - \sum_{p\in\mathcal{P}(c)} \sum_{f\in\mathcal{F}(c,p)} \int_{t^n}^{t^{n+1}} \boldsymbol{V}_p(t) \cdot \big(s_{pf}\boldsymbol{n}_{pf}\big)(t)\,\mathrm{d}t = 0, \\
&m_c(\boldsymbol{V}_c^{n+1} - \boldsymbol{V}_c^n) + \sum_{p\in\mathcal{P}(c)} \sum_{f\in\mathcal{F}(c,p)} \int_{t^n}^{t^{n+1}} P_{cfp}(t)\big(s_{pf}\boldsymbol{n}_{pf}\big)(t)\,\mathrm{d}t = \boldsymbol{0}, \\
&m_c(E_c^{n+1} - E_c^n) + \sum_{p\in\mathcal{P}(c)} \sum_{f\in\mathcal{F}(c,p)} \int_{t^n}^{t^{n+1}} P_{cfp}(t)\boldsymbol{V}_p(t) \cdot \big(s_{pf}\boldsymbol{n}_{pf}\big)(t)\,\mathrm{d}t = 0.
\end{aligned} \tag{2.51}$$

At first order, these time integrals are approximated by a one-step integration procedure using the integrands at time t^n. To gain one order of accuracy in time, the GRP procedure consists in computing these integrals using a midpoint quadrature formula. The task is then to determine the integrands at the intermediate time

$$t^{n+\frac{1}{2}} = t^n + \frac{\Delta t}{2}. \tag{2.52}$$

In the sequel, the quantities evaluated at this intermediate time are written

$$\varphi^{n+\frac{1}{2}} = \varphi\left(t^{n+\frac{1}{2}}\right) = \varphi\left(t^n + \frac{\Delta t}{2}\right). \tag{2.53}$$

Time discretization of the trajectory equation

Considering the trajectory equation

$$\boldsymbol{x}_p^{n+1} - \boldsymbol{x}_p^n = \int_{t^n}^{t^{n+1}} \boldsymbol{V}_p(t)\,\mathrm{d}t, \tag{2.54}$$

the midpoint quadrature formula leads to

$$\boldsymbol{x}_p^{n+1} - \boldsymbol{x}_p^n = \Delta t \boldsymbol{V}_p^{n+\frac{1}{2}}, \tag{2.55}$$

where the intermediate node velocity is defined thanks to relation (2.53). In this way, the node position at the new time step $\boldsymbol{x}_p^{n+1}$ is second order accurate in time if and only if the node velocity is itself second order accurate. Let perform a Taylor expansion of the node velocity. One writes

$$\boldsymbol{V}_p^{n+\frac{1}{2}} = \boldsymbol{V}_p(t^n) + \frac{\Delta t}{2}\left(\frac{d\boldsymbol{V}_p}{dt}\right)(t^n) + O\left(\left(\frac{\Delta t}{2}\right)^2\right), \tag{2.56}$$

by definition of the intermediate quantities (2.53). This last relation is simplified into

$$\boldsymbol{V}_p^{n+\frac{1}{2}} = \boldsymbol{V}_p^n + \frac{\Delta t}{2}\left(\frac{d\boldsymbol{V}_p}{dt}\right)^n + O(\Delta t^2), \tag{2.57}$$

and the node position at the end of the time step is approximated by

$$\boldsymbol{x}_p^{n+1} = \boldsymbol{x}_p^n + \Delta t\left[\boldsymbol{V}_p^n + \frac{\Delta t}{2}\left(\frac{d\boldsymbol{V}_p}{dt}\right)^n\right]. \tag{2.58}$$

The time derivative of the nodal velocity $\left(d\boldsymbol{V}_p/dt\right)^n$, introduced in this relation, is a new unknown. Before investigating its computation, let discretize the rest of system (2.51).

Time discretization of the GCL

The GCL equation is recalled to be of the form

$$v_c^{n+1} - v_c^n = \sum_{p\in\mathcal{P}(c)}\sum_{f\in\mathcal{F}(c,p)} \int_{t^n}^{t^{n+1}} \boldsymbol{V}_p(t)\cdot(s_{pf}\boldsymbol{n}_{pf})(t)\,\mathrm{d}t. \tag{2.59}$$

Since the nodal velocity $\boldsymbol{V}_p^{n+\frac{1}{2}}$ is fixed during the time step Δt, $\boldsymbol{x}(t)$ is linear with respect to time and $(s_{pf}\boldsymbol{n}_{pf})(t)$ is thus quadratic. In this way, it would be possible to

perform an exact integration of the GCL using, for example, the Simpson quadrature rule. In the present study, the GCL is approximated at second order by the relation

$$v_c^{n+1} - v_c^n = \Delta t \sum_{p\in\mathcal{P}(c)} \sum_{f\in\mathcal{F}(c,p)} \boldsymbol{V}_p^{n+\frac{1}{2}} \cdot (s_{pf}\boldsymbol{n}_{pf})^{n+\frac{1}{2}}, \tag{2.60}$$

where the intermediate node velocity $\boldsymbol{V}_p^{n+\frac{1}{2}}$ is given by relation (2.57). In the same way as for the trajectory equation, one requires a second order in time approximation of the face area vector $(s_{pf}\boldsymbol{n}_{pf})^{n+\frac{1}{2}}$. This geometric quantity is recalled to be of the form (refer to Section 1.3.2)

$$\left(s_{pf}\boldsymbol{n}_{pf}\right)^{n+\frac{1}{2}} = \frac{1}{3}\left(\sum_{t_r\in\mathcal{T}(c,f,p)} \left(s_{t_r}\boldsymbol{n}_{t_r}\right)^{n+\frac{1}{2}} + \sum_{t_r\in\mathcal{T}(c,f)} \frac{1}{N_{p,f}} \left(s_{t_r}\boldsymbol{n}_{t_r}\right)^{n+\frac{1}{2}} \right), \tag{2.61}$$

with

$$\left(s_{t_r}\boldsymbol{n}_{t_r}\right)^{n+\frac{1}{2}} = \frac{1}{2}\left(\boldsymbol{x}_{p^+}^{n+\frac{1}{2}} - \boldsymbol{x}_p^{n+\frac{1}{2}}\right) \times \left(\boldsymbol{x}_{p^{++}}^{n+\frac{1}{2}} - \boldsymbol{x}_p^{n+\frac{1}{2}}\right). \tag{2.62}$$

Performing a Taylor expansion of the intermediate node position, defined by relation (2.53), one writes

$$\boldsymbol{x}_p^{n+\frac{1}{2}} = \boldsymbol{x}_p^n + \frac{\Delta t}{2}\boldsymbol{V}_p^n + O(\Delta t^2). \tag{2.63}$$

Hence,

$$\begin{aligned} \left(s_{t_r}\boldsymbol{n}_{t_r}\right)^{n+\frac{1}{2}} = \;& \frac{1}{2}\left(\boldsymbol{x}_{p^+}^n - \boldsymbol{x}_p^n\right) \times \left(\boldsymbol{x}_{p^{++}}^n - \boldsymbol{x}_p^n\right) \\ + \;& \frac{\Delta t}{4}\Big[\left(\boldsymbol{x}_{p^+}^n - \boldsymbol{x}_p^n\right) \times \left(\boldsymbol{V}_{p^{++}}^n - \boldsymbol{V}_p^n\right) \Big] \\ + \;& \frac{\Delta t}{4}\Big[\left(\boldsymbol{V}_{p^+}^n - \boldsymbol{V}_p^n\right) \times \left(\boldsymbol{x}_{p^{++}}^n - \boldsymbol{x}_p^n\right) \Big] \\ + \;& O(\Delta t^2), \end{aligned} \tag{2.64}$$

which can be simplified into

$$\left(s_{t_r}\boldsymbol{n}_{t_r}\right)^{n+\frac{1}{2}} = s_{t_r}^n\boldsymbol{n}_{t_r}^n + \frac{\Delta t}{2}\frac{d}{dt}\left(s_{t_r}\boldsymbol{n}_{t_r}\right)^n + O(\Delta t^2), \tag{2.65}$$

by introducing the time derivative

$$\frac{d}{dt}\left(s_{t_r}\boldsymbol{n}_{t_r}\right)^n = \frac{1}{2}\Big[\left(\boldsymbol{x}_{p^+}^n - \boldsymbol{x}_p^n\right) \times \left(\boldsymbol{V}_{p^{++}}^n - \boldsymbol{V}_p^n\right) + \left(\boldsymbol{V}_{p^+}^n - \boldsymbol{V}_p^n\right) \times \left(\boldsymbol{x}_{p^{++}}^n - \boldsymbol{x}_p^n\right) \Big]. \tag{2.66}$$

Then, by linearity of the time derivative, the face area vectors $(s_{pf}\boldsymbol{n}_{pf})^{n+\frac{1}{2}}$ are straightforwardly written

$$\left(s_{pf}\boldsymbol{n}_{pf}\right)^{n+\frac{1}{2}} = s_{pf}^n\boldsymbol{n}_{pf}^n + \frac{\Delta t}{2}\frac{d}{dt}\left(s_{pf}\boldsymbol{n}_{pf}\right)^n + O(\Delta t^2), \tag{2.67}$$

with

$$\frac{d}{dt}\left(s_{pf}\boldsymbol{n}_{pf}\right)^n = \frac{1}{3}\left(\sum_{t_r\in\mathcal{T}(c,f,p)}\frac{d}{dt}\left(s_{t_r}\boldsymbol{n}_{t_r}\right)^n + \sum_{t_r\in\mathcal{T}(c,f)}\frac{1}{N_{p,f}}\frac{d}{dt}\left(s_{t_r}\boldsymbol{n}_{t_r}\right)^n\right). \tag{2.68}$$

Finally, the dot product between relations (2.57) and (2.67) can be written under the compact form

$$\boldsymbol{V}_p^{n+\frac{1}{2}}\cdot\left(s_{pf}\boldsymbol{n}_{pf}\right)^{n+\frac{1}{2}} = \boldsymbol{V}_p^n\cdot s_{pf}^n\boldsymbol{n}_{pf}^n + \frac{\Delta t}{2}\frac{d}{dt}\left(\boldsymbol{V}_p\cdot s_{pf}\boldsymbol{n}_{pf}\right)^n + O(\Delta t^2), \tag{2.69}$$

by introducing the time derivative

$$\frac{d}{dt}\left(\boldsymbol{V}_p\cdot s_{pf}\boldsymbol{n}_{pf}\right)^n = \boldsymbol{V}_p^n\cdot\frac{d}{dt}\left(s_{pf}\boldsymbol{n}_{pf}\right)^n + \left(\frac{d\boldsymbol{V}_p}{dt}\right)^n\cdot s_{pf}^n\boldsymbol{n}_{pf}^n. \tag{2.70}$$

The second order in time discretization of the GCL is thus written

$$v_c^{n+1} - v_c^n = \Delta t\sum_{p\in\mathcal{P}(c)}\sum_{f\in\mathcal{F}(c,p)}\left[\boldsymbol{V}_p^n\cdot s_{pf}^n\boldsymbol{n}_{pf}^n + \frac{\Delta t}{2}\frac{d}{dt}\left(\boldsymbol{V}_p\cdot s_{pf}\boldsymbol{n}_{pf}\right)^n\right]. \tag{2.71}$$

Second order in time discrete operators

By analogy with the Section 1.3.2, a second order in time discrete divergence operator can be extracted from relation (2.71). For an arbitrary linearly reconstructed vector field $\widetilde{\boldsymbol{\psi}}$, this operator writes

$$\mathcal{DIV}_c^{O2}(\widetilde{\boldsymbol{\psi}}) = \sum_{p\in\mathcal{P}(c)}\sum_{f\in\mathcal{F}(c,p)}\left[\widetilde{\boldsymbol{\psi}}_p(\boldsymbol{x}_p^n)\cdot s_{pf}^n\boldsymbol{n}_{pf}^n + \frac{\Delta t}{2}\frac{d}{dt}\left(\widetilde{\boldsymbol{\psi}}_p(\boldsymbol{x}_p)\cdot s_{pf}\boldsymbol{n}_{pf}\right)^n\right]. \tag{2.72}$$

Similarly, the second order in time discrete gradient operator of the scalar field $\widetilde{\varphi}$ is defined as

$$\mathcal{GRAD}_c^{O2}(\widetilde{\varphi}) = \sum_{p\in\mathcal{P}(c)}\sum_{f\in\mathcal{F}(c,p)}\left[\widetilde{\varphi}_p(\boldsymbol{x}_p^n)s_{pf}^n\boldsymbol{n}_{pf}^n + \frac{\Delta t}{2}\frac{d}{dt}\left(\widetilde{\varphi}_p(\boldsymbol{x}_p)s_{pf}\boldsymbol{n}_{pf}\right)^n\right]. \tag{2.73}$$

Discrete scheme

Using the discrete operators introduced previously, the discrete momentum and total energy conservation equations are written as

$$\boldsymbol{V}_c^{n+1} = \boldsymbol{V}_c^n - \frac{\Delta t}{m_c}\sum_{p\in\mathcal{P}(c)}\sum_{f\in\mathcal{F}(c,p)}\left[P_{cfp}^n s_{pf}^n\boldsymbol{n}_{pf}^n + \frac{\Delta t}{2}\frac{d}{dt}\left(P_{cfp}s_{pf}\boldsymbol{n}_{pf}\right)^n\right], \tag{2.74}$$

$$E_c^{n+1} = E_c^n - \frac{\Delta t}{m_c}\sum_{p\in\mathcal{P}(c)}\sum_{f\in\mathcal{F}(c,p)}\left[P_{cfp}^n\boldsymbol{V}_p^n\cdot s_{pf}^n\boldsymbol{n}_{pf}^n + \frac{\Delta t}{2}\frac{d}{dt}\left(P_{cfp}\boldsymbol{V}_p\cdot s_{pf}\boldsymbol{n}_{pf}\right)^n\right], \tag{2.75}$$

where the time derivatives of the fluxes are naturally given by

$$\frac{d}{dt}\Big(P_{cfp}s_{pf}\boldsymbol{n}_{pf}\Big)^n = P^n_{cfp}\frac{d}{dt}\big(s_{pf}\boldsymbol{n}_{pf}\big)^n + \left(\frac{dP_{cfp}}{dt}\right)^n s^n_{pf}\boldsymbol{n}^n_{pf}, \tag{2.76}$$

and

$$\begin{aligned}\frac{d}{dt}\Big(P_{cfp}\boldsymbol{V}_p\cdot s_{pf}\boldsymbol{n}_{pf}\Big)^n = \;& P^n_{cfp}\boldsymbol{V}^n_p\cdot\frac{d}{dt}\big(s_{pf}\boldsymbol{n}_{pf}\big)^n \\ + \;& \left[\left(\frac{dP_{cfp}}{dt}\right)^n\boldsymbol{V}^n_p + P^n_{cfp}\left(\frac{d\boldsymbol{V}_p}{dt}\right)^n\right]\cdot s^n_{pf}\boldsymbol{n}^n_{pf}.\end{aligned} \tag{2.77}$$

Since the time derivative of the face area vector is known thanks to relation (2.68), only two new unknowns are introduced by this GRP procedure: the time derivative of the nodal velocity $(d\boldsymbol{V}_p/dt)^n$ (also required in relation (2.58)) and the time derivative of the nodal pressure $(dP_{cfp}/dt)^n$. It is thus necessary to design a solver to compute these new unknowns. In the same way as in Chapter 1, let invoke the momentum conservation condition.

Momentum conservation

The semi-discrete scheme (2.50) is proved to conserve globally the momentum and total energy in Section 1.4.3. It is now necessary that the fully discrete scheme preserves this property. Defining the total momentum in the domain at time t^n as $(m\boldsymbol{V})^n = \sum_c m_c\boldsymbol{V}^n_c$, the global variation of momentum during the time step writes

$$\delta(m\boldsymbol{V}) = (m\boldsymbol{V})^{n+1} - (m\boldsymbol{V})^n. \tag{2.78}$$

Then, substituting (2.74) in the previous relation leads to

$$\delta(m\boldsymbol{V}) = -\Delta t\sum_c\sum_{p\in\mathcal{P}(c)}\sum_{f\in\mathcal{F}(c,p)}\left[P^n_{cfp}s^n_{pf}\boldsymbol{n}^n_{pf} + \frac{\Delta t}{2}\frac{d}{dt}\Big(P_{cfp}s_{pf}\boldsymbol{n}_{pf}\Big)^n\right]. \tag{2.79}$$

Now, imposing the scheme to be globally conservative in momentum, i.e. $\delta(m\boldsymbol{V}) = \boldsymbol{0}$, enables to write the condition

$$\begin{aligned}\boldsymbol{0} = \;& \sum_c\sum_{p\in\mathcal{P}(c)}\sum_{f\in\mathcal{F}(c,p)}P^n_{cfp}s^n_{pf}\boldsymbol{n}^n_{pf} \\ + \;& \frac{\Delta t}{2}\sum_c\sum_{p\in\mathcal{P}(c)}\sum_{f\in\mathcal{F}(c,p)}\frac{d}{dt}\Big(P_{cfp}s_{pf}\boldsymbol{n}_{pf}\Big)^n.\end{aligned} \tag{2.80}$$

The first sum is null by construction of the pressure flux P^n_{cfp} (refer to Section 1.4.3). In this way, the previous condition simplifies into

$$\sum_c\sum_{p\in\mathcal{P}(c)}\sum_{f\in\mathcal{F}(c,p)}\frac{d}{dt}\Big(P_{cfp}s_{pf}\boldsymbol{n}_{pf}\Big)^n = \boldsymbol{0}. \tag{2.81}$$

Rearranging the sums, one can write

$$\sum_p \left[\sum_{c\in\mathcal{C}(p)} \sum_{f\in\mathcal{F}(c,p)} \frac{d}{dt}\Big(P_{cfp} s_{pf} \boldsymbol{n}_{pf}\Big)^n \right] = \mathbf{0}, \tag{2.82}$$

which provides a condition similar to (1.70). This condition writes

$$\sum_{c\in\mathcal{C}(p)} \sum_{f\in\mathcal{F}(c,p)} \frac{d}{dt}\Big(P_{cfp} s_{pf} \boldsymbol{n}_{pf}\Big)^n = \mathbf{0}, \tag{2.83}$$

and imposes the time derivatives of the pressure forces acting around a node to balance themselves. Now, developing the time derivative thanks to relation (2.76), one gets

$$\sum_{c\in\mathcal{C}(p)} \sum_{f\in\mathcal{F}(c,p)} \left[\left(\frac{dP_{cfp}}{dt}\right)^n s_{pf}^n \boldsymbol{n}_{pf}^n + P_{cfp}^n \frac{d}{dt}\big(s_{pf}\boldsymbol{n}_{pf}\big)^n \right] = \mathbf{0}. \tag{2.84}$$

This relation is a sufficient condition for the GRP procedure to globally preserve momentum and total energy. However, it introduces the new unknown $(dP_{cfp}/dt)^n$. Following the works [92, 96], it is proposed to time differentiate the relation (2.44) in order to write a nodal solver linking the two new unknowns $(dP_{cfp}/dt)^n$ and $(d\boldsymbol{V}_p/dt)^n$.

Time derivative of the pressure flux

Let write the linearly reconstructed Riemann problem (2.44) as

$$P_{cfp}^n = \widetilde{P}_c(\boldsymbol{x}_p^n) + \frac{Z_c^n}{s_{pf}^n}\Big(\widetilde{\boldsymbol{V}}_c(\boldsymbol{x}_p^n) - \boldsymbol{V}_p^n\Big)\cdot s_{pf}^n \boldsymbol{n}_{pf}^n, \tag{2.85}$$

where Z_c^n/s_{pf}^n can be interpreted as the surface impedance of face f_{pf} and is considered to be constant over the time step. Using the chain rule, the time derivation of this relation leads to

$$\begin{aligned}\left(\frac{dP_{cfp}}{dt}\right)^n = &\left(\frac{d\widetilde{P}_c(\boldsymbol{x}_p)}{dt}\right)^n + \frac{Z_c^n}{s_{pf}^n}\left[\left(\frac{d\widetilde{\boldsymbol{V}}_c(\boldsymbol{x}_p)}{dt}\right)^n - \left(\frac{d\boldsymbol{V}_p}{dt}\right)^n\right]\cdot s_{pf}^n\boldsymbol{n}_{pf}^n \\ &+ \frac{Z_c^n}{s_{pf}^n}\Big(\widetilde{\boldsymbol{V}}_c(\boldsymbol{x}_p^n) - \boldsymbol{V}_p^n\Big)\cdot\frac{d}{dt}\big(s_{pf}\boldsymbol{n}_{pf}\big)^n.\end{aligned} \tag{2.86}$$

This last expression provides the time derivative of the second order pressure flux P_{cfp}^n. However, it introduces two new unknowns in addition to the expected $(d\boldsymbol{V}_p/dt)^n$, namely $\Big(d\widetilde{P}_c(\boldsymbol{x}_p)/dt\Big)^n$ and $\Big(d\widetilde{\boldsymbol{V}}_c(\boldsymbol{x}_p)/dt\Big)^n$. These two derivatives will be computed latter. For the moment, let concentrate on the time derivative of the node velocity.

Time derivative of the node velocity

Let substitute relation (2.86) into the balance condition (2.84). Using the formula (D.1), one writes

$$\begin{aligned}
\mathbf{0} = & \sum_{c\in\mathcal{C}(p)}\sum_{f\in\mathcal{F}(c,p)} \left(\frac{d\widetilde{P}_c(\boldsymbol{x}_p)}{dt}\right)^n s_{pf}^n \boldsymbol{n}_{pf}^n \\
+ & \sum_{c\in\mathcal{C}(p)}\sum_{f\in\mathcal{F}(c,p)} \frac{Z_c^n}{s_{pf}^n}\left(s_{pf}^n\boldsymbol{n}_{pf}^n \otimes s_{pf}^n\boldsymbol{n}_{pf}^n\right)\left[\left(\frac{d\widetilde{\boldsymbol{V}}_c(\boldsymbol{x}_p)}{dt}\right)^n - \left(\frac{d\boldsymbol{V}_p}{dt}\right)^n\right] \\
+ & \sum_{c\in\mathcal{C}(p)}\sum_{f\in\mathcal{F}(c,p)} \frac{Z_c^n}{s_{pf}^n}\left[\frac{d}{dt}\left(s_{pf}\boldsymbol{n}_{pf}\right)^n \otimes s_{pf}^n\boldsymbol{n}_{pf}^n\right]\left(\widetilde{\boldsymbol{V}}_c(\boldsymbol{x}_p^n) - \boldsymbol{V}_p^n\right) \\
+ & \sum_{c\in\mathcal{C}(p)}\sum_{f\in\mathcal{F}(c,p)} P_{cfp}^n \frac{d}{dt}\left(s_{pf}\boldsymbol{n}_{pf}\right)^n.
\end{aligned} \tag{2.87}$$

This relation is equivalently written

$$\begin{aligned}
\mathbb{M}_p\left(\frac{d\boldsymbol{V}_p}{dt}\right)^n = & \sum_{c\in\mathcal{C}(p)}\sum_{f\in\mathcal{F}(c,p)} \left(\frac{d\widetilde{P}_c(\boldsymbol{x}_p)}{dt}\right)^n s_{pf}^n \boldsymbol{n}_{pf}^n \\
+ & \sum_{c\in\mathcal{C}(p)}\sum_{f\in\mathcal{F}(c,p)} \frac{Z_c^n}{s_{pf}^n}\left(s_{pf}^n\boldsymbol{n}_{pf}^n \otimes s_{pf}^n\boldsymbol{n}_{pf}^n\right)\left(\frac{d\widetilde{\boldsymbol{V}}_c(\boldsymbol{x}_p)}{dt}\right)^n \\
+ & \sum_{c\in\mathcal{C}(p)}\sum_{f\in\mathcal{F}(c,p)} \frac{Z_c^n}{s_{pf}^n}\left(\widetilde{\boldsymbol{V}}_c(\boldsymbol{x}_p^n) - \boldsymbol{V}_p^n\right)\left[\frac{d}{dt}\left(s_{pf}\boldsymbol{n}_{pf}\right)^n \otimes s_{pf}^n\boldsymbol{n}_{pf}^n\right] \\
+ & \sum_{c\in\mathcal{C}(p)}\sum_{f\in\mathcal{F}(c,p)} P_{cfp}^n \frac{d}{dt}\left(s_{pf}\boldsymbol{n}_{pf}\right)^n,
\end{aligned} \tag{2.88}$$

where

$$\mathbb{M}_p^n = \sum_{c\in\mathcal{C}(p)}\sum_{f\in\mathcal{F}(c,p)} \frac{Z_c^n}{s_{pf}^n} s_{pf}^n\boldsymbol{n}_{pf}^n \otimes s_{pf}^n\boldsymbol{n}_{pf}^n. \tag{2.89}$$

One recognizes the matrix $\mathbb{M}_p$ used in relation (1.72). This matrix is symmetric positive definite thus invertible, and the time derivative of the nodal velocity is always computable.

Computation of the pressure and velocity time derivatives

To conclude the derivation of this GRP procedure, let compute the time derivatives $\left(d\widetilde{P}_c(\boldsymbol{x}_p)/dt\right)^n$ and $\left(d\widetilde{\boldsymbol{V}}_c(\boldsymbol{x}_p)/dt\right)^n$. First, the time derivatives of the recon-

structed pressure and velocity writes as

$$\begin{aligned}\left(\frac{d\widetilde{P}_c(\boldsymbol{x}_p)}{dt}\right)^n &= \left(\frac{dP_c}{dt}\right)^n,\\ \left(\frac{d\widetilde{\boldsymbol{V}}_c(\boldsymbol{x}_p)}{dt}\right)^n &= \left(\frac{d\boldsymbol{V}_c}{dt}\right)^n,\end{aligned} \tag{2.90}$$

since the other terms introduced by relation (2.1) are of order $O(\Delta t^3)$. Then, as done in [92, 96], the derivatives $(d\boldsymbol{V}_c/dt)^n$ and $(dP_c/dt)^n$ are found by writing the gas dynamic equations under their non-conservative form, i.e. expressed with the variables $(P, \boldsymbol{V}, \eta)$. This system writes

$$\begin{aligned}\frac{dP}{dt} &= -\rho a^2(\nabla\cdot\boldsymbol{V}),\\ \frac{d\boldsymbol{V}}{dt} &= -\frac{1}{\rho}(\nabla P),\\ \frac{d\eta}{dt} &= 0,\end{aligned} \tag{2.91}$$

and leads to the following approximations

$$\begin{aligned}\left(\frac{dP_c}{dt}\right)^n &= -\rho_c^n(a_c^n)^2\mathcal{DIV}_c^n(\boldsymbol{V}),\\ \left(\frac{d\boldsymbol{V}_c}{dt}\right)^n &= -\frac{1}{\rho_c^n}\mathcal{GRAD}_c^n(P),\end{aligned} \tag{2.92}$$

where the divergence $\mathcal{DIV}_c^n(\boldsymbol{V})$ and the gradient $\mathcal{GRAD}_c^n(P)$ are the discrete operators (1.51) and (1.53) respectively.

Remark:
In the case where a source term is present in the total energy conservation equation, the time derivative of the pressure is modified. See for example the Taylor-Green vortex test case (refer to Chapter 3). The proof is made in Appendix B.

GRP algorithm:

- The complete state $\mathcal{U}^n$ is known.
- If the flow is radial:
  - Call the MM-limiter algorithm

  Else:
  - Compute the pressure and velocity cell gradients
  - Call the SP-limiter algorithm

  EndIf
- Computation of the second order fluxes: $\boldsymbol{V}_p^n$ from (1.72)-(2.43) and P_{cfp}^n from (2.44).

- Computation of the time step Δt (refer to Section 1.5).
- Time derivatives:
  - determination of the cell derivatives $\left(d\widetilde{P}_c(\boldsymbol{x}_p)/dt\right)^n$ and $\left(d\widetilde{\boldsymbol{V}}_c(\boldsymbol{x}_p)/dt\right)^n$ from (2.90),
  - determination of the geometry derivative $d(s_{pf}\boldsymbol{n}_{pf})^n/dt$ from (2.68),
  - determination of the nodal velocity derivative $(d\boldsymbol{V}_p/dt)^n$ from (2.88),
  - determination of the nodal pressure derivative $(dP_{cfp}/dt)^n$ from (2.86).
- Mesh update from to the trajectory equation (2.58).
- Computation of the new velocity $\boldsymbol{V}_c^{n+1}$ (2.74) and total energy E_c^{n+1} (2.75) in the cells.
- Determination of the complete final state $\mathcal{U}^{n+1}$ from relations (1.125) (EOS).

Conclusion

This Chapter details the second order extension in space and time of the cell-centered Lagrangian scheme presented in Chapter 1. The classic MUSCL procedure, consisting in a linear reconstruction and a limiting step, is proposed. Moreover, the gradients needed for the reconstruction step can be computed in multiple way. In this study, both the Least Squares (LS) gradients and the Green formula are compared. Concerning the limiting step, a particular care has to be taken for the limiting of vector fields. The more natural limiting procedure would be the use of convex hulls, as proposed in [90] with the VIP limiter. However, the computation of convex hulls in 3D is a complex task which is not investigated here. Instead, it is proposed to limit the vector fields componentwise in a basis representing the flow directions (referred to as CW-limiter). Three different basis are studied in Chapter 3, however, none of them lead to completely satisfactory results. This is why two new limiters are proposed:

- the SP-limiter based on an extended monotonicity criterion (monotonicity verified at the centers of the neighboring cells) and which limits the vector fields using a single scalar. Change of basis are thus avoided, however, one has to compute a frame-invariant direction of the flow. In particular, this limiter enables to preserve the flow symmetries.
- the MM-limiter defined as the multi-dimensional extension of the 1D-minmod limiter. It is based on nodal gradients and the minmod function and is well suited to spherical flows.

Concerning the time discretization of the scheme, the classic PC scheme is presented. However, since this method is computationally costly, especially in 3D, the one-step GRP procedure is proposed and completely detailed. Algorithms are detailed throughout the Chapter to summarize the different procedures.

In Chapter 3, the different limiters are tested against numerous classic Lagrangian test cases. Moreover, the MM-limiter is used to study the development of Rayleigh-Taylor instabilities in supernova remnants in Chapter 4.

Chapter 3

Validation on classic Lagrangian test cases

This Chapter presents the results obtained with the second order cell-centered Lagrangian scheme presented throughout Chapters 1 and 2. The test cases used are classic in Lagrangian studies and help validate the methods. They are 1D, 2D or 1D spherical problems for which the analytic solution is known. In particular, they enable to evaluate the robustness and accuracy of the scheme. For example, the smooth problem of the Taylor-Green vortex enables to compute the order of convergence of the scheme (refer to Section 3.2). All the test cases are run on 3D meshes in order to verify that the symmetry of the flow is respected. For example, all the 1D problems are run on 3D Cartesian meshes to show that no spurious motion is created in the $\boldsymbol{y}$ and $\boldsymbol{z}$ directions. Moreover, the three limiting procedures presented in Chapter 2, namely the CW-limiter, the SP-limiter and the MM-limiter, are compared on these test cases in order to highlight their drawbacks and advantages. The second order time discretization of the scheme is performed by a GRP procedure. Finally, unless stated, the spatial reconstruction is based on LS gradient in the case of the CW-limiter and with the Green formula for the SP-limiter.

All the test cases presented in this Chapter consider a perfect gas ruled by the gamma gas law

$$P = (\gamma - 1)\rho\varepsilon, \tag{3.1}$$

where γ is the polytropic index of the gas. One has $\gamma = \frac{5}{3}$ if the gas is monoatomic and $\gamma = \frac{7}{5}$ if the gas is diatomic. In this way, the isentropic sound speed in the cell ω_c becomes

$$a_c = \sqrt{\frac{\gamma_c P_c}{\rho_c}}. \tag{3.2}$$

The Chapter is organized as follows. The Section 3.1 presents the Sod test case. The order of convergence of the scheme is then evaluated on the Taylor-Green vortex in Section 3.2, and the 3D Saltzmann problem is presented in Section 3.3. Finally, the limiting procedures are compared on spherical problems such as the Noh problem

in Section 3.4, the Sedov problem in Section 3.5 and the Kidder problem in Section 3.6.

3.1 Sod shock tube

The Sod test case [117] considers a domain $(x, y, z) \in [0; 1]^3$ split in its middle $x = 0.5$ into two sub-regions filled with diatomic gas. The left region has higher pressure and density than the right one such that

$$\begin{aligned} (\rho_l,\ P_l,\ \boldsymbol{V}_l) &= (1.0,\ 1.0,\ \mathbf{0}), \qquad x \leq 0.5, \\ (\rho_r,\ P_r,\ \boldsymbol{V}_r) &= (0.125,\ 0.1,\ \mathbf{0}), \quad x \geq 0.5. \end{aligned} \tag{3.3}$$

At time $t = 0$, the interface separating the two sub-regions is removed, creating a shock wave that propagates in the direction $x > 0$. The contact discontinuity (initial jump in density) also propagates in this direction and a rarefaction wave propagates in the opposite direction. This test case is very interesting for this feature: the three type of waves are present and one can thus observe the scheme behavior on each of these waves. Symmetry boundary conditions are imposed on all the boundaries of the domain. In particular, the physical variables are observed at final time $t = 0.2$ in order that the shock has not yet reached the wall $x = 1$.

The first order solution for density, pressure, x-velocity and internal energy are plotted along the x-axis in Figure 3.1 in dashed lines. In particular, one can observe some wall heating effect at the contact discontinuity resulting in an overshoot in internal energy. One can refer to [109] for a study on the wall heating phenomenon. The computations are made on a $200 \times 5 \times 5$ cells mesh in order to prove that a 1D problem remains 1D on a 3D mesh. In this way, each Figure shows in fact 5×5 overlapped 1D plots. The second order results plotted in this Figures were obtained using the SP-limiters in combination with discrete gradients. In particular, one can observe a good improvement of the accuracy.

To study the second order procedures, let concentrate on the solution behind the shock. The corresponding zooming box is shown in Figure 3.1a. Let recall that on this 1D problem, the CW- and SP-limiters are completely equivalent in their approach to the velocity limiting. The difference appear thus in the gradient computation and the monotonicity stencil. Let recall that there is two possible gradients, the gradients obtained using the Least Squares (LS) procedure and the gradients obtained with the Green formula (discrete gradients). There is also two possible monotonicity stencils, the classic monotonicity stencil, i.e. monotonicity imposed at the cell nodes (used in the CW-limiter), and the new monotonicity stencil, i.e. monotonicity imposed in the neighbouring cells, (used in the SP-limiter).

The Figure (3.2a) compares the solutions obtained using the LS gradients and the discrete gradients on the classic monotonicity stencil (CW-limiter). One can observe that the LS gradients lead to spurious oscillations with the CW-limiter

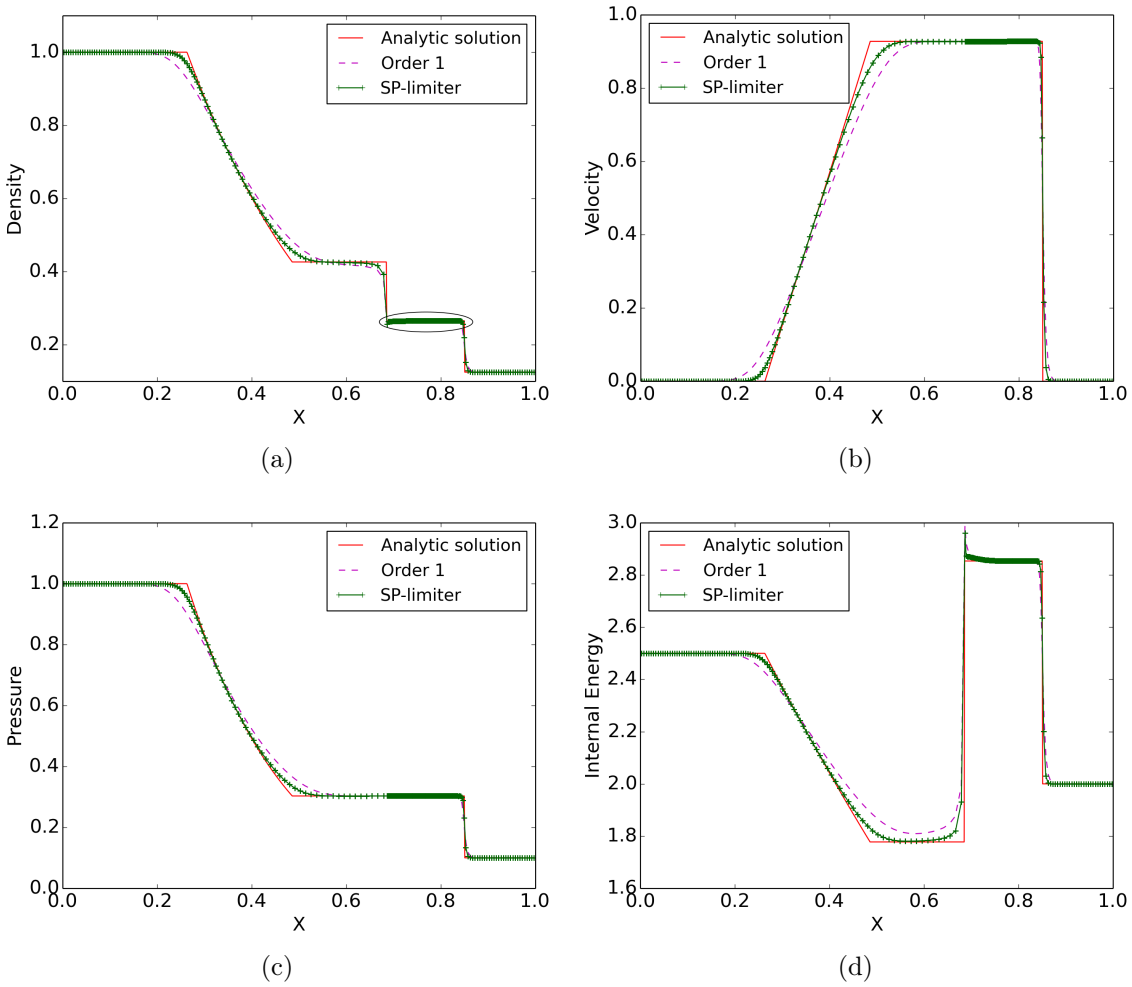

Figure 3.1 – Sod test case - First and second order solution using the SP-limiter with discrete gradients - Scatter plots of the density (3.1a), velocity (3.1b), pressure (3.1c) and internal energy (3.1d) at time $t = 0.2$ along the x axis on a $200 \times 5 \times 5$ cells mesh.

whereas the solution is smooth with discrete gradients. Using the new monotonicity stencil (SP-limiter) enables to remove these oscillations as shown in Figure (3.2b). The solution obtained with the MM-limiter is also shown in this last Figure since this limiting procedure computes its own gradients. In particular, one can observe that the resulting solution is very similar to the one obtained with LS gradients on the extended monotonicity stencil. Finally, the second order solution obtained with discrete gradients and the SP-limiter is compared to the first order one in Figure 3.1. One can observe a good gain of accuracy around the shock as well as in the rarefaction fan.

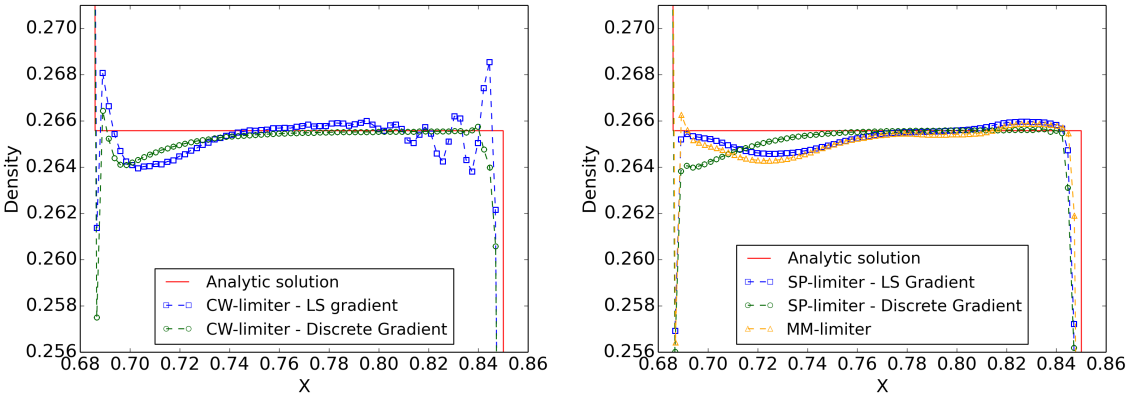

(a) (b)

Figure 3.2 – Sod test case - Second order solution - Comparison between the Least Squares Gradient (blue) and the Discrete Gradients (green) (3.2a) - Solutions using the new monotonicity stencil (3.2b) - Density at time $t = 0.2$ along the x axis on a $200 \times 5 \times 5$ cells mesh - Zoom behind the shock.

3.2 Taylor-Green vortex

The Taylor-Green Vortex is classically used for evaluating the order of convergence of a Lagrangian method. It has been proposed by Dobrev et al. in [38] and consists in simulating a 2D stationary vortex flow applied to a domain $(x, y, z) \in [0; 1]^3$ filled with a perfect diatomic gas. Symmetry boundary conditions are applied to all boundaries of the domain. The vortex is modelled by a divergence free velocity field $\boldsymbol{V}^0$ such as

$$\boldsymbol{V}^0(x, y) = C_1 \begin{pmatrix} \sin(\pi x)\cos(\pi y) \\ -\cos(\pi x)\sin(\pi y) \end{pmatrix}, \tag{3.4}$$

where C_1 is a user-defined constant. As shown in Appendix B, the following pressure field has to be imposed

$$P^0(x, y) = \frac{1}{4}\rho^0 C_1^2 \Big[\cos(2\pi x) + \cos(2\pi y) \Big] + C_2, \tag{3.5}$$

where C_2 is an integration constant. Moreover, the following source term has to be added to the total energy conservation equation at each time step

$$\mathcal{S}(x, y) = \frac{\pi}{4}\frac{\rho^0 C_1^3}{\gamma - 1} \Big[\cos(3\pi x)\cos(\pi y) - \cos(3\pi y)\cos(\pi x) \Big]. \tag{3.6}$$

In the case where a GRP procedure is used, one has to adapt the scheme as shown in Appendix B to properly take into account the source term. Initially, the constants are chosen such that $(\rho^0, C_1, C_2) = (1, 1, 1)$.

This test case enables to compute the order of accuracy of the scheme since there is no shock and the analytic solution is known thanks to its stationarity. This test

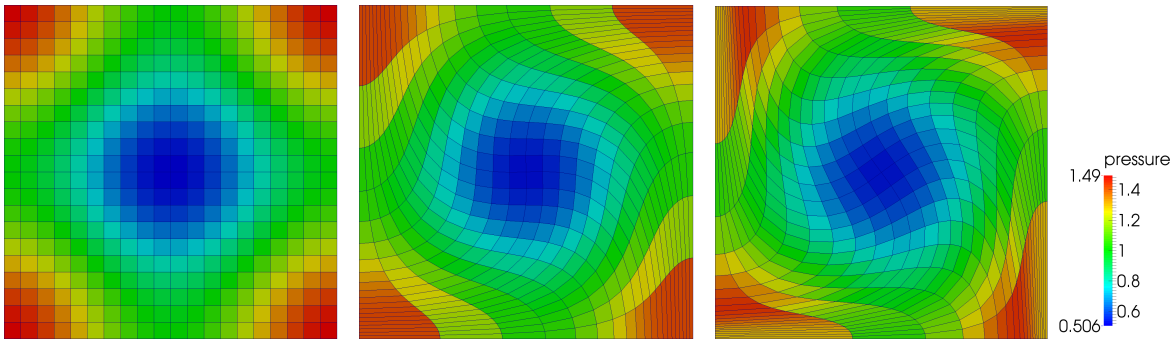

(a) (b) (c)

Figure 3.3 – Taylor-Green vortex - Pressure field and mesh shape at initial time (3.3a), time $t = 0.5$ (3.3b) and time $t = 0.7$ (3.3c) on a $20 \times 20 \times 1$ cells mesh.

case is very difficult for a Lagrangian scheme since the cells are highly distorted, especially at the corners of the domain as shown in Figure 3.3. This Figure shows the pressure field at initial time and at times $t = 0.5$ and $t = 0.7$ in order to evaluate the mesh deformation. In particular, the final time chosen is $t = 0.5$ in order that the mesh is not too deformed and still has a good quality for computing an order of convergence. Indeed, one can see at time $t = 0.7$ that the quality of the solution decreases at the corners of the domain.

The order of convergence is evaluated on the pressure field at time $t = 0.5$ using an unlimited second order procedure. This is possible since the Taylor-Green Vortex is a smooth problem, there is thus no discontinuity which could introduce oscillations. In this way, one can compare the accuracy of both the LS and discrete gradients. The results are shown in Table 3.1. In particular, one can observe a second order accuracy with an order of 1.97 on the finest grid for both gradients with a PC time integration. The GRP procedure introduces some discrepancy between the two possible reconstructions since one can observe a loss of accuracy using LS gradients. This is probably due to the fact that the LS gradients can lose accuracy on highly stretched meshes [97], which is the case for the Taylor-Green vortex at the corners of the domain (see Figure 3.3), and to the fact that these gradients are used to construct the second order in time terms introduced by the GRP procedure. Let however mention that, if the LS gradients do not present the best converging behavior, they produce the lowest errors.

The impact of the limiting procedures is evaluated in Figure 3.4 representing the logarithmic plot of the L_2 error with respect to $1/\Delta x$. The upper straight line of this Figure corresponds to a first order convergence and the lower straight line corresponds to a second order convergence. The CW-limiter is applied to the LS gradients whereas the SP-limiter is applied the Discrete gradients. In particular, one can observe on this plot that the limiting procedure reduces the accuracy of the

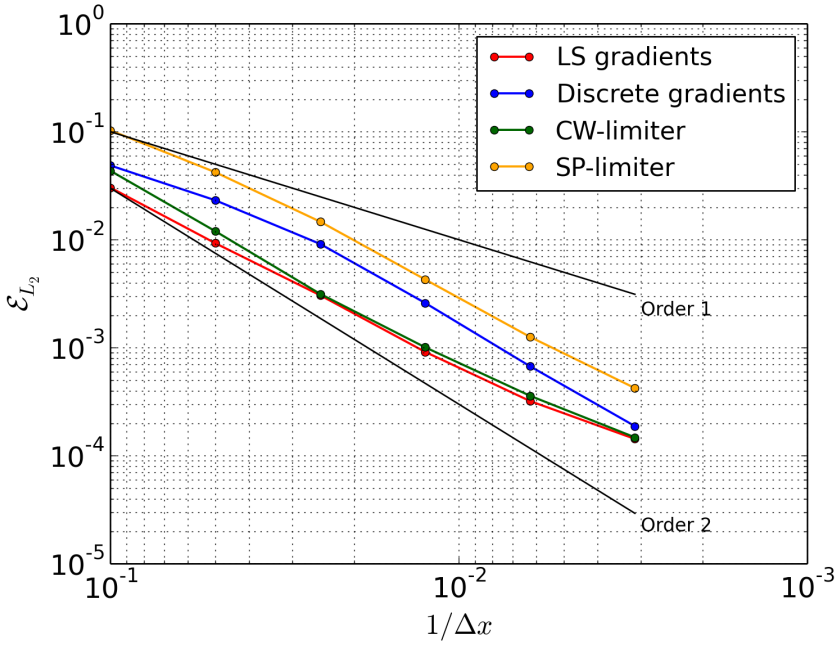

Figure 3.4 – Taylor-Green vortex - L_2 error computed on the pressure field at time $t = 0.5$ with respect to $1/\Delta x$ - Results obtained using a GRP approach - Logarithmic plot (x axis inverted).

solution but does not impact the converging behavior.

The MM-limiter is not studied on this problem since it is designed for 1D radial flows and has no particular reasons to perform well on this 2D problem.

In these Tables, the meshes used are denoted $n \times n$ for reducing the Table size but are in fact $n \times n \times 1$ cells meshes. Moreover, $\mathcal{E}_{L_p}$ and $\mathcal{O}_{L_p}$, $p \in \{1, 2, \infty\}$ denote respectively the global error and order of convergence in L_p norm. These errors are computed as

$$\mathcal{E}_{L_1} = \frac{1}{v_\omega} \sum_c v_c |\Delta P_c|, \quad \mathcal{E}_{L_2} = \sqrt{\frac{1}{v_\omega} \sum_c v_c |\Delta P_c|^2}, \quad \text{and} \quad \mathcal{E}_{L_\infty} = \max_c |\Delta P_c|, \tag{3.7}$$

where $v_\omega = \sum_c v_c$ is the total volume of the domain and v_c the volume of cell ω_c. Moreover, $\Delta P_c = P_c^{num} - P_c^{exact}$ is the difference in cell c between the numerical approximation (computed by the scheme) and the exact value of pressure (obtained from relation (3.5)) in cell ω_c. The corresponding order of convergence $\mathcal{O}_{L_p}$ is then computed as

$$\mathcal{O}_{L_p} = \frac{\log(\mathcal{E}^a_{L_p}) - \log(\mathcal{E}^b_{L_p})}{\log(\Delta x^a) - \log(\Delta x^b)}, \tag{3.8}$$

where $\mathcal{E}^a_{L_p}$ and $\mathcal{E}^b_{L_p}$ are the L_p-errors computed on two meshes of characteristic length Δx^a and Δx^b. Here the meshes are Cartesian thus $\Delta x^a = \Delta y^a$.

Predictor-Corrector - Least Squares gradients

Mesh	$\mathcal{E}_{L_1}$	$\mathcal{O}_{L_1}$	$\mathcal{E}_{L_2}$	$\mathcal{O}_{L_2}$	$\mathcal{E}_{L_\infty}$	$\mathcal{O}_{L_\infty}$
10×10	2.34×10^{-2}	-	3.02×10^{-2}	-	6.91×10^{-2}	-
20×20	6.22×10^{-3}	1.91	9.50×10^{-3}	1.67	3.08×10^{-2}	1.16
40×40	2.17×10^{-3}	1.52	3.22×10^{-3}	1.56	1.24×10^{-2}	1.30
80×80	6.48×10^{-4}	1.74	9.05×10^{-4}	1.83	3.62×10^{-3}	1.78
160×160	1.72×10^{-4}	1.91	2.35×10^{-4}	1.95	9.46×10^{-4}	1.94
320×320	4.39×10^{-5}	1.97	5.94×10^{-5}	1.98	2.40×10^{-4}	1.98

(a)

Predictor-Corrector - Discrete gradients

Mesh	$\mathcal{E}_{L_1}$	$\mathcal{O}_{L_1}$	$\mathcal{E}_{L_2}$	$\mathcal{O}_{L_2}$	$\mathcal{E}_{L_\infty}$	$\mathcal{O}_{L_\infty}$
10×10	3.72×10^{-2}	-	4.96×10^{-2}	-	1.17×10^{-1}	-
20×20	2.11×10^{-3}	0.82	2.37×10^{-3}	1.06	4.64×10^{-2}	1.33
40×40	8.29×10^{-3}	1.35	9.61×10^{-3}	1.30	1.99×10^{-2}	1.22
80×80	2.39×10^{-3}	1.79	2.83×10^{-3}	1.76	7.46×10^{-3}	1.42
160×160	6.21×10^{-4}	1.94	7.45×10^{-4}	1.92	2.19×10^{-3}	1.76
320×320	1.57×10^{-4}	1.98	1.89×10^{-4}	1.98	5.69×10^{-4}	1.95

(b)

GRP - Least Squares gradients

Mesh	$\mathcal{E}_{L_1}$	$\mathcal{O}_{L_1}$	$\mathcal{E}_{L_2}$	$\mathcal{O}_{L_2}$	$\mathcal{E}_{L_\infty}$	$\mathcal{O}_{L_\infty}$
10×10	2.32×10^{-2}	-	3.04×10^{-2}	-	6.73×10^{-2}	-
20×20	6.05×10^{-3}	1.94	9.29×10^{-3}	1.70	2.83×10^{-2}	1.25
40×40	2.10×10^{-3}	1.52	3.06×10^{-3}	1.60	1.23×10^{-2}	1.20
80×80	6.88×10^{-4}	1.61	9.16×10^{-4}	1.74	3.64×10^{-3}	1.76
160×160	2.48×10^{-4}	1.47	3.21×10^{-4}	1.51	9.65×10^{-4}	1.91
320×320	1.17×10^{-4}	1.08	1.43×10^{-4}	1.16	4.03×10^{-4}	1.26

(c)

GRP - Discrete gradients

Mesh	$\mathcal{E}_{L_1}$	$\mathcal{O}_{L_1}$	$\mathcal{E}_{L_2}$	$\mathcal{O}_{L_2}$	$\mathcal{E}_{L_\infty}$	$\mathcal{O}_{L_\infty}$
10×10	3.63×10^{-2}	-	4.87×10^{-2}	-	1.15×10^{-1}	-
20×20	2.06×10^{-2}	0.82	2.32×10^{-2}	1.07	4.56×10^{-2}	1.34
40×40	7.86×10^{-3}	1.39	9.14×10^{-3}	1.34	1.99×10^{-2}	1.19
80×80	2.19×10^{-3}	1.84	2.60×10^{-3}	1.81	7.41×10^{-3}	1.43
160×160	5.57×10^{-4}	1.97	6.74×10^{-4}	1.95	2.18×10^{-3}	1.76
320×320	1.50×10^{-4}	1.88	1.88×10^{-4}	1.84	5.64×10^{-4}	1.93

(d)

Table 3.1 – Taylor-Green vortex - Table of convergence of the pressure field at final time $t = 0.5$ - Unlimited LS gradients with a PC time integration (3.1a), unlimited discrete gradients with a PC time integration (3.1b) - Unlimited LS gradients with a GRP time integration (3.1c), unlimited discrete gradients with a GRP time integration (3.1d).

3.3 Saltzmann test case

The Saltzmann test case (see [42] for the original 2D test case and [26] for its extension to 3D) is used to evaluate the sensitivity of the Lagrangian scheme to the mesh. It simulates the propagation of a piston driven shock wave in the computational domain $(x, y, z) \in [0; 1] \times [0; 0.1] \times [0; 0.1]$ distorted as proposed in [26] (refer to Figure 3.5)

$$\begin{cases} \tilde{x} = x + (0.1 - z)(1 - 20y)\sin(x\pi), & \text{if} \quad 0 \leq y \leq 0.05, \\ \tilde{x} = x + z(20y - 1)\sin(x\pi), & \text{if} \quad 0.05 \leq y \leq 0.1, \\ \tilde{y} = y, \\ \tilde{z} = z. \end{cases} \tag{3.9}$$

This domain is filled with a monoatomic gas such that $(\rho^0, P^0, \boldsymbol{V}^0) = (1, 10^{-6}, \boldsymbol{0})$. The compression is ensured by a velocity condition $\boldsymbol{V}^b = 1\boldsymbol{e}_x$ imposed on the plane initially at the position $x = 0$. All the other boundaries of the domain are symmetry boundary conditions. The solution is plotted at time $t = 0.7$, before the shock reaches the wall $x = 1$.

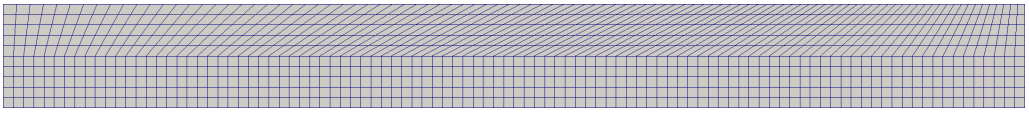

(a)

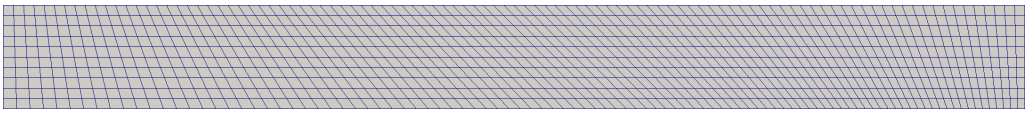

(b)

Figure 3.5 – Saltzmann problem - Initial perturbed mesh in the $(O, \boldsymbol{z})$ plane (3.5a) and $(O, \boldsymbol{y})$ plane (3.5b).

The second order results are shown in Figures 3.6 and 3.7 using the SP-limiter. The results obtained with the CW-limiter are not shown since they are very similar on this test case. In particular, one can observe that the shock is almost planar and that the density field behind the shock presents a good uniformity. Classically, 3D computations of this problem stop around time $t = 0.75$ due to the strong mesh deformations [28, 88, 95]. In the present study, we show that the problem can be computed at latter times since the mesh remains rather well aligned with the $\boldsymbol{x}$ direction. In particular, the solution at time $t = 0.9$ is shown in Figure 3.7 and a zoom on the mesh is shown in Figure 3.8. At his time, the shock has bounced twice against the wall. The results are still satisfactory at this late time. However, the mesh deformation prevents from going further in the computations, particularly due to the pinched cells at the corners of the domain. Similar results are observed in [22].

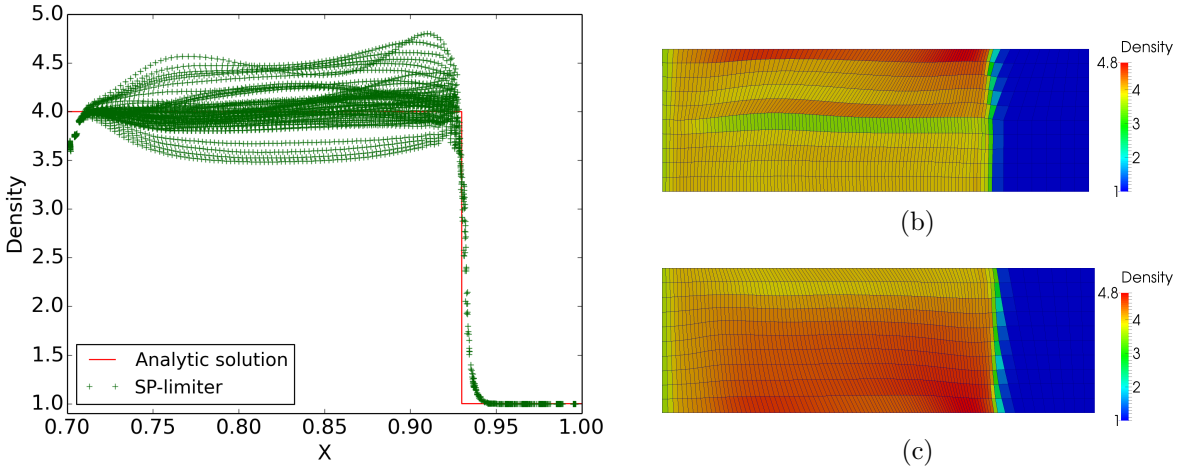

(a) (b) (c)

Figure 3.6 – Saltzmann problem - Second order solution obtained with the SP-limiter - Scatter plot of the x-density (3.6a), density field in the $(O, \boldsymbol{z})$ plane (3.6b) and in the $(O, \boldsymbol{y})$ plane (3.6c) at time $t = 0.7$ on a $100 \times 10 \times 10$ cells mesh.

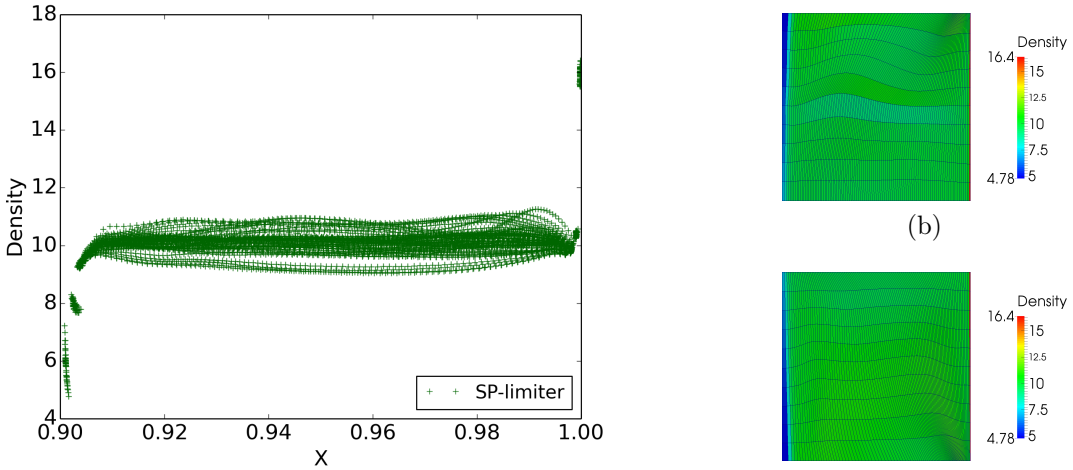

(a) (b) (c)

Figure 3.7 – Saltzmann problem - Second order solution obtained with the SP-limiter - Scatter plot of the x-density (3.7a), density field in the $(O, \boldsymbol{z})$ plane (3.7b) and in the $(O, \boldsymbol{y})$ plane (3.7c) at time $t = 0.9$ on a $100 \times 10 \times 10$ cells mesh.

3.4 Noh problem

The Noh problem [104] models the implosion of a unit cube $(x, y, z) \in [0; 1]^3$ filled with a monoatomic gas which has a centripetal velocity. More precisely, the gas is such that $(\rho^0, P^0, \boldsymbol{V}^0) = (1, 10^{-6}, -\boldsymbol{e}_r)$ where $\boldsymbol{e}_r$ is the radial vector. This flow creates a spherical shock of infinite strength at the space origin that propagates in the radial direction. In particular, the solutions are plotted at final time $t = 0.6$ when the shock is at radius $r = 0.2$. Symmetry boundary conditions are applied

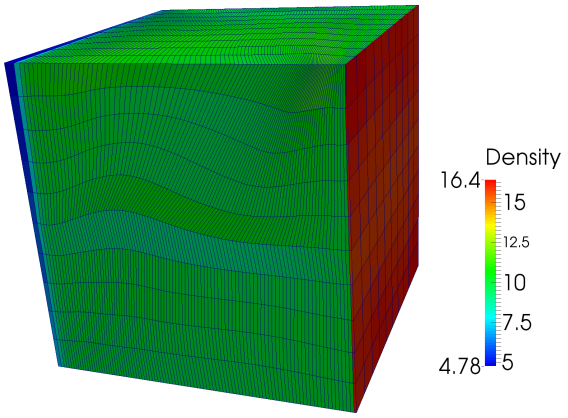

Figure 3.8 – Saltzmann problem - Second order solution obtained with the SP-limiter - Zoom of the mesh at time $t = 0.9$.

to the boundaries holding the origin O whereas the other boundaries are pressure boundary conditions with $P^b = 1 \times 10^{-6}$. This test case is difficult for a Lagrangian scheme since it is a 3D radial problem run on a Cartesian grid. This problem is thus subject to a strong mesh printing.

The first order solution of this problem is shown in Figure 3.9 for a $20 \times 20 \times 20$ cells mesh. The density, the velocity norm, the pressure and the internal energy are plotted with respect to the radius of the cell center. One can observe the wall heating phenomenon which is responsible for the low density and strong internal energy at the origin. A review of this phenomenon can be found in [109]. The first order problem is already difficult since a hourglass mode appears at 45° in the three Cartesian planes when the mesh is refined (refer to Figures 3.9e and 3.9f). This instability is due to the nodal solver itself and has also been observed in [127]. In particular, it is shown in this paper that using the Dukowicz solver [40] enables to remove these oscillations. The Dukowicz solver is not used in this study since the oscillations disappear when the scheme is extended to second order. However, there is no clear explanation why the first order scheme presents this flaw and not the second order one.

The CW-limiter (refer to the Algorithm in Section 2.5) does not provide satisfactory results on this problem. The Figure 3.10 shows the solutions obtained by limiting the velocity field in three different basis: the Cartesian basis, denoted $\mathcal{B}_C$, the basis of eigenvectors of tensor $\mathbb{D}_c$, denoted $\mathcal{B}_D$, and the basis of eigenvectors of tensor $\mathbb{N}_c$, denoted $\mathcal{B}_N$ (refer to Section 2.2). In particular, one can observe overshoots appearing behind the shock. These overshoots are lethal for the numerical solution since they are amplified when the mesh is refined. Moreover, the deformation of the mesh behind the shock is not in accordance with the radial flow. Nonetheless, the density fields are identical in the three planes $(O, \boldsymbol{x})$, $(O, \boldsymbol{y})$ and $(O, \boldsymbol{z})$ and have a symmetry at 45°.

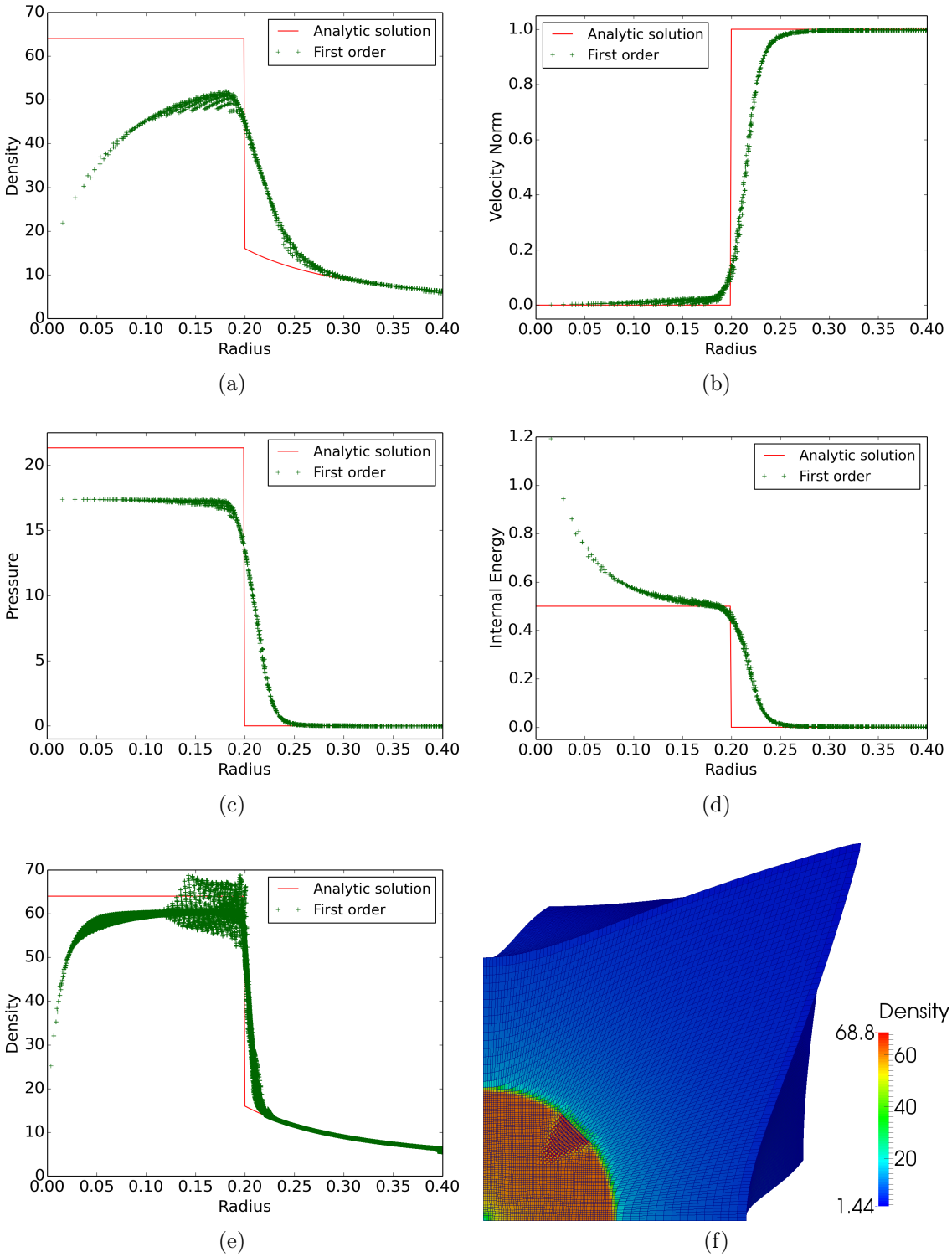

Figure 3.9 – Noh test case - First order solution - Scatter plots of the radial density (3.9a), velocity norm (3.9b), pressure (3.9c) and internal energy (3.9d) at time $t = 0.6$ on a $20 \times 20 \times 20$ cells mesh - Scatter plot of the radial density (3.9e) and density field (3.9f) at time $t = 0.6$ on a $80 \times 80 \times 80$ cells mesh.

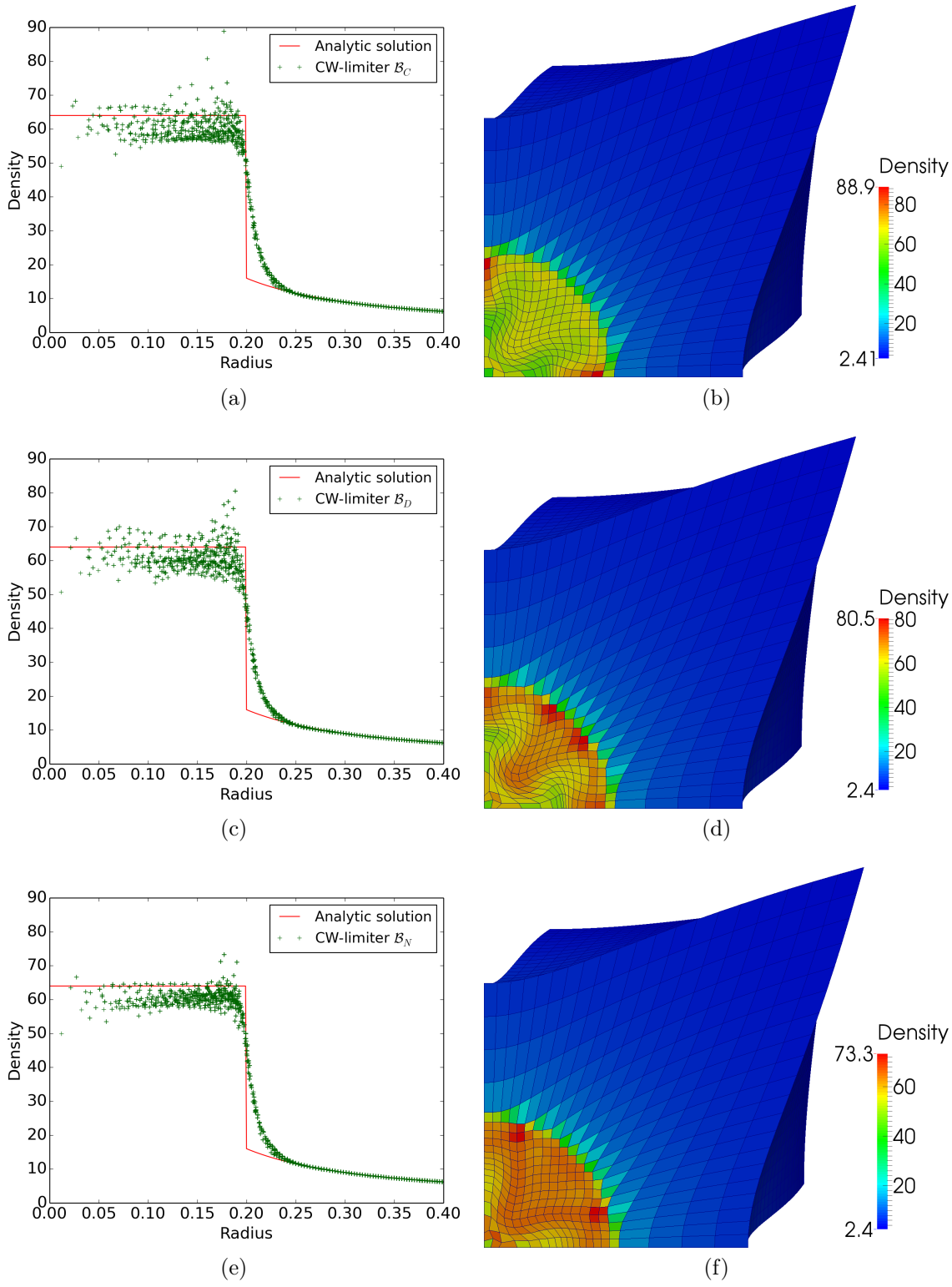

Figure 3.10 – Noh test case - Second order solution obtained with the CW-limiter - Scatter plot of the radial density and density field at time $t = 0.6$ on a $20 \times 20 \times 20$ cells mesh - Component-wise limiting in the basis $\mathcal{B}_C$ (3.10a, 3.10b), the basis $\mathcal{B}_D$ (3.10c, 3.10d) and the basis $\mathcal{B}_N$ (3.10e, 3.10f).

The SP-limiter enables to completely remove the overshoots on the $20 \times 20 \times 20$ cells mesh (refer to Figures 3.11a and 3.11b). In fact, the solution obtained with this limiter is very similar to the first order one with a higher maximum density (58 against 52 at first order). It is now possible to perform a convergence analysis (refer to Figure 3.11). However, this analysis also shows that the SP-limiter reaches its limits when the mesh is strongly refined. Indeed, one can observe strong overshoots behind the shock for a $80 \times 80 \times 80$ cells mesh (refer to Figure 3.11e).

The MM-limiter shows its strength on this radial problem (refer to Figure 3.12). The solution obtained on the $20 \times 20 \times 20$ cells mesh (refer to Figures 3.12a) is similar to the one provided by the SP-limiter. The behavior of the MM-limiter is however better when the mesh is refined. Indeed, the solution on the $80 \times 80 \times 80$ cells mesh (refer to Figures 3.12e) presents no overshoot with a maximum density of 63.6 against 64 for the expected value. Moreover the symmetry of the flow behind the shock is very well preserved, even on this refined mesh. Finally, one can remark that the hourglass mode observable at first order (refer to Figure 3.9f) is no longer present at second order on the same mesh.

3.5 Sedov problem

The Sedov test case [73] simulates the propagation of a spherical shock wave within the computational domain $(x, y, z) \in [0; 1.2]^3$. This domain is filled with a diatomic gas such that $(\rho^0, P^0, \boldsymbol{V}^0) = (1, 10^{-6}, \boldsymbol{0})$. The shock wave is initialized by imposing the pressure $P_o = (\gamma - 1)\varepsilon^0/v^0$ in the cells containing the space origin, where v^0 is the cell volume and $\varepsilon^0 = 0.106384$ is the initial specific internal energy. Symmetry boundary conditions are applied on all the boundaries of the domain. With this initialization, the diverging spherical shock is characterized by a shock located at radius $R = 1$ at time $t = 1$ with a maximum density of $\rho^{shock} = 6$, as in [95].

The first order density solution is shown in Figure 3.13 on a $20 \times 20 \times 20$ cells mesh. In particular one can notice node crossing along the Cartesian axis and non-convex cells at 45° (refer to Figure 3.13b). As for the Noh problem, only the $(O, \boldsymbol{x})$ plane is shown here but the mesh shape is identical in the two others Cartesian planes. The solution presents nonetheless a good shock timing and a good symmetry (refer to Figure 3.13a). In particular, the symmetry preservation on this test case can be evaluated by the width of the scatter plot around the analytic solution. Let mention that the two aforementioned flaws do not appear with the 2D EUCCLHYD scheme [92, 93] and seem thus to be characteristic of the 3D configuration.

At second order, the solutions obtained with the CW- or SP-limiter present the same node crossing. Only the solution obtained with the SP-limiter is shown in Figure 3.14 since both limiters provide similar results. In particular, one can observe that the solution is very similar to the first order one with a higher shock density. As for the previous test case, the MM-limiter provides very good results on

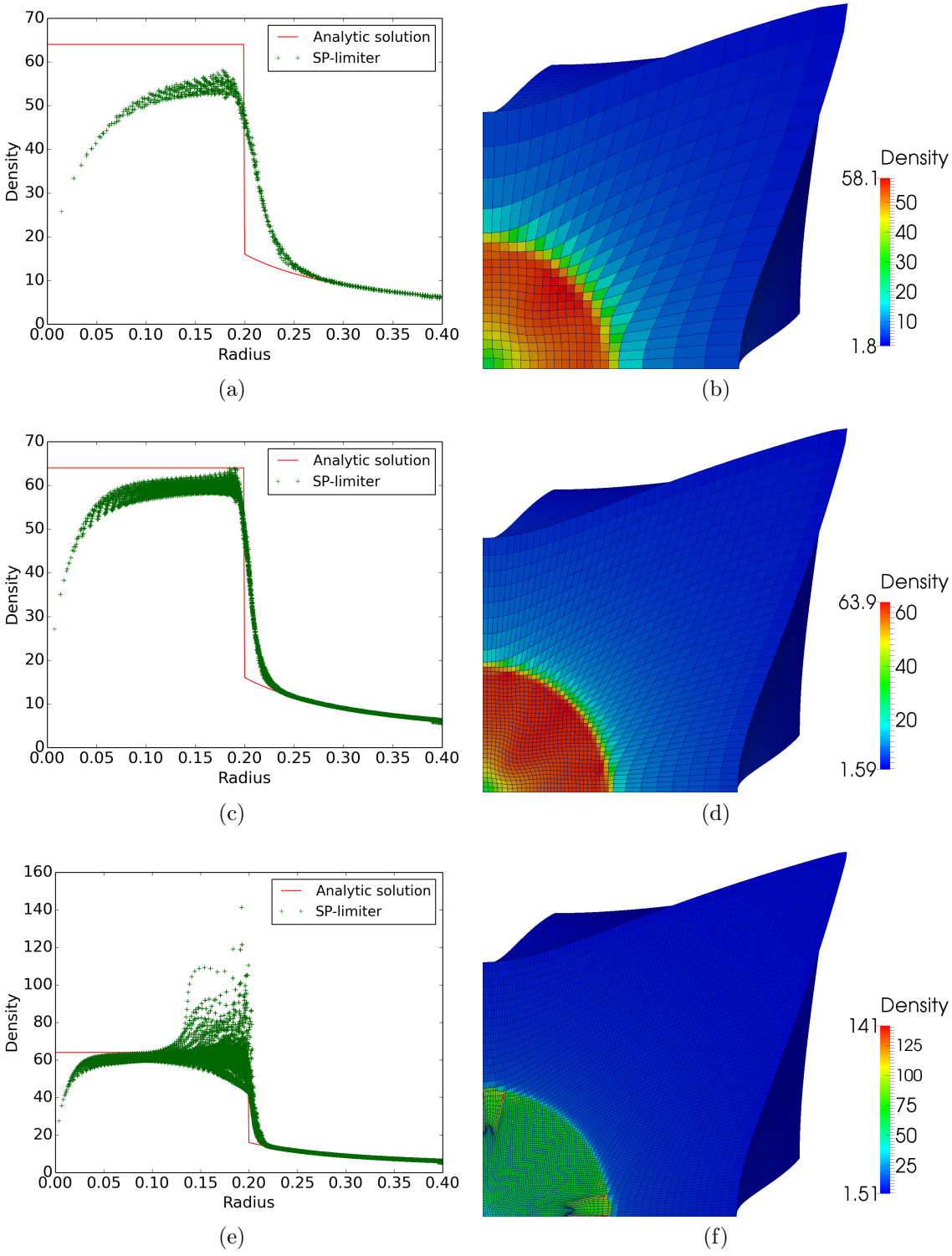

Figure 3.11 – Noh problem - Second order solution using the SP-limiter - Scatter plot of the radial density and density field at time $t = 0.6$ on $20 \times 20 \times 20$ (3.11a, 3.11b), $40 \times 40 \times 40$ (3.11c, 3.11d) and $80 \times 80 \times 80$ (3.11e, 3.11f) cells meshes.

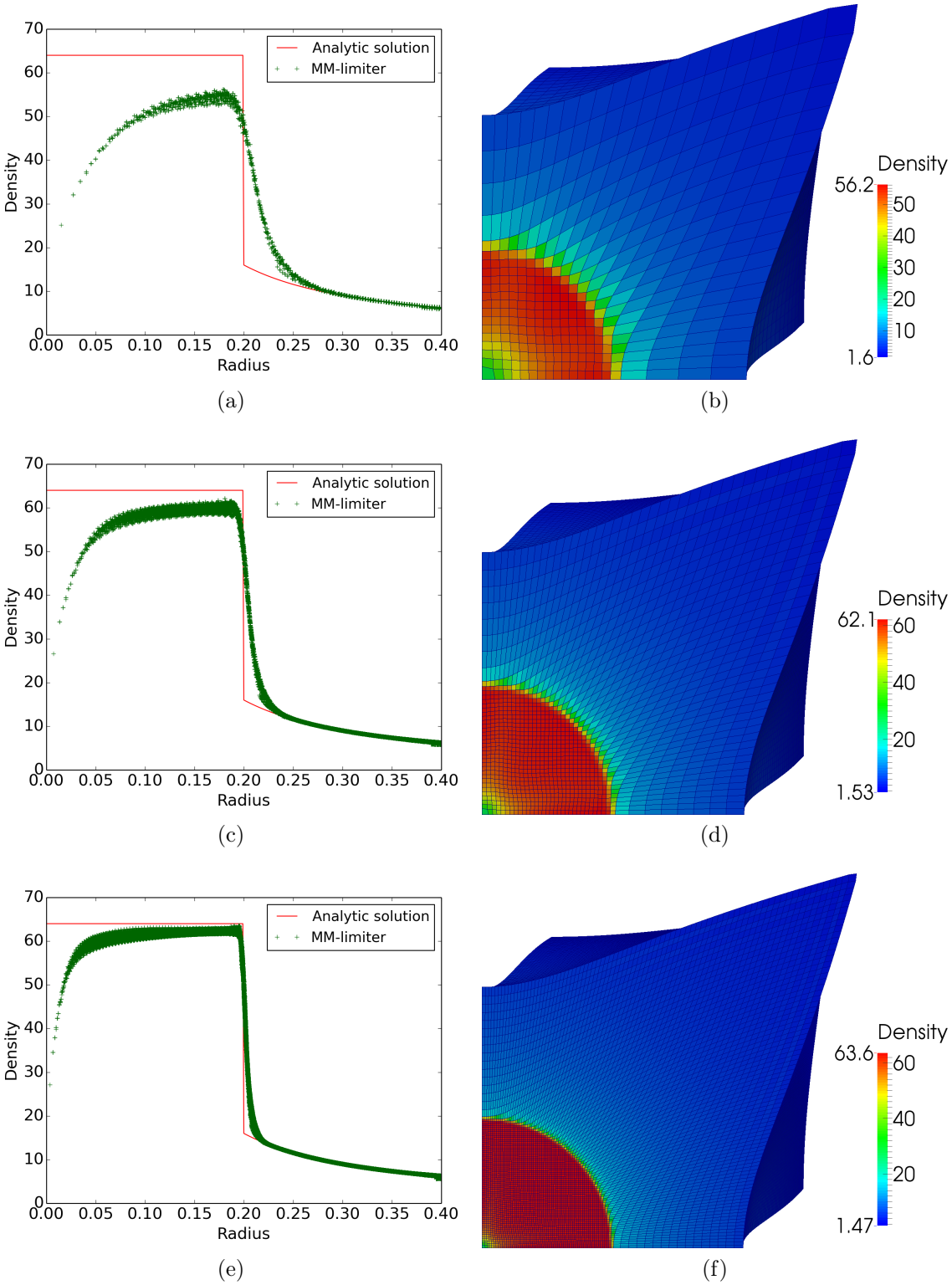

Figure 3.12 – Noh problem - Second order solution using the MM-limiter - Scatter plot of the radial density and density field at time $t = 0.6$ on $20 \times 20 \times 20$ (3.12a, 3.12b), $40 \times 40 \times 40$ (3.12c, 3.12d) and $80 \times 80 \times 80$ (3.12e, 3.12f) cells meshes.

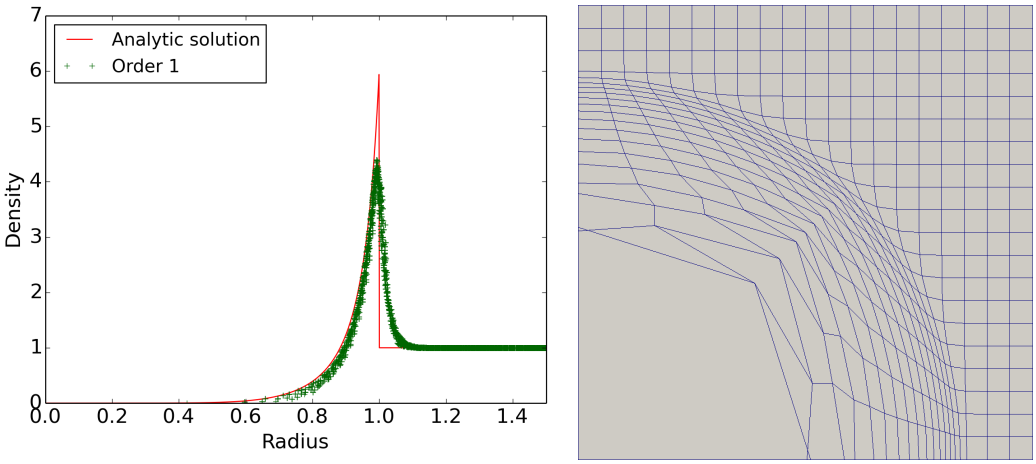

(a) (b)

Figure 3.13 – Sedov problem - First order solution - Scatter plot of the radial density (3.13a) and 3D mesh (3.13b) in the $(O, \boldsymbol{x})$ plane at time $t = 1$ on a $20 \times 20 \times 20$ cells mesh.

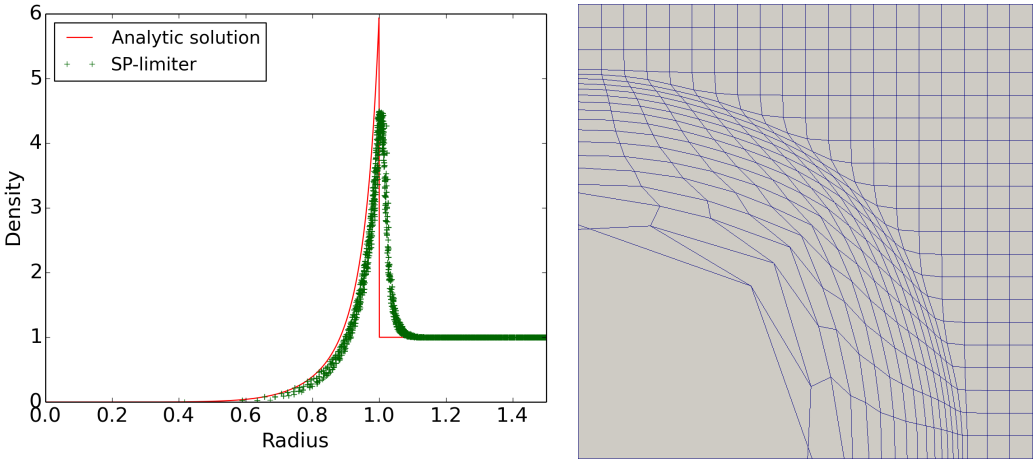

(a) (b)

Figure 3.14 – Sedov problem - SP-limiter - Scatter plot of the radial density and 3D mesh in the $(O, \boldsymbol{x})$ plane at time $t = 1$ on $20 \times 20 \times 20$ (3.14a, 3.14b) cells meshes.

this radial problem (refer to Figure 3.15). The node crossing along the Cartesian axis is removed and the solution shows a good converging behavior. Moreover, one can notice that the cells in the Cartesian plane are all convex when using this limiter whereas a bowtie-shaped hourglass mode appears with the CW- and SP-limiters.

3.6 Kidder implosion

The Kidder test case [75] simulates the isentropic compression of a spherical shell of inner radius $r_{inn} = 0.9$ and outer radius $r_{out} = 1$. Here, we use the set-up

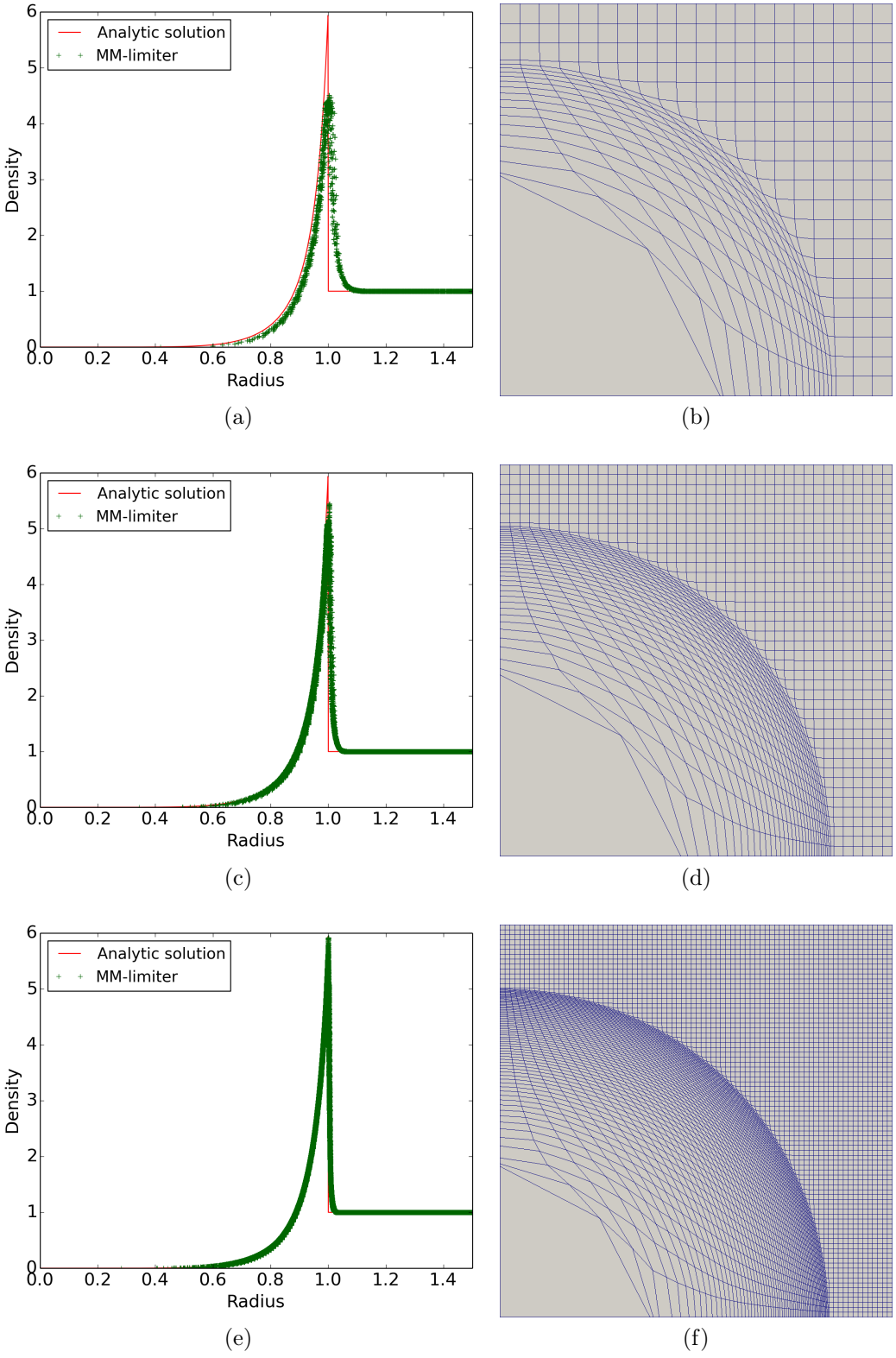

(a) (b)

(c) (d)

(e) (f)

Figure 3.15 – Sedov problem - MM-limiter - Scatter plot of the radial density and 3D mesh in the $(O, \boldsymbol{x})$ plane at time $t = 1$ on $20 \times 20 \times 20$ (3.15a, 3.15b), $40 \times 40 \times 40$ (3.15c, 3.15d) and $80 \times 80 \times 80$ (3.15e, 3.15f) cells meshes.

proposed in [93]. The shell is filled with a perfect monoatomic gas such as

$$\begin{aligned}
\rho^0(r) &= \left(\frac{r_{out}^2 - r^2}{r_{out}^2 - r_{inn}^2}\rho_{inn}^{\gamma-1} + \frac{r^2 - r_{inn}^2}{r_{out}^2 - r_{inn}^2}\rho_{out}^{\gamma-1}\right)^{\frac{1}{\gamma-1}}, \\
P^0(r) &= \left(\rho^0(r)\right)^{\gamma}, \\
\boldsymbol{V}^0(r) &= 0,
\end{aligned} \tag{3.10}$$

where the initial density at the inner interface of the shell is set to $\rho_{inn} = 1$ and at the outer interface $\rho_{out} = 2$. This flow is an isentropic compression since one has $\eta = P/\rho^{\gamma} = 1$. In particular, a node initially at radius r is known to be at position $R(r,t) = h(t)r$ at time t, where

$$h(t) = \sqrt{1 - \left(\frac{t}{t_{foc}}\right)^2}, \tag{3.11}$$

is the homothety rate. Moreover, t_{foc} is the focalisation time computed as

$$t_{foc} = \sqrt{\left(\frac{\gamma - 1}{2}\right)\frac{r_{out}^2 - r_{inn}^2}{a_{out}^2 - a_{inn}^2}}. \tag{3.12}$$

In this last relation a_{inn} and a_{out} are the initial speed of sound at the inner and outer radii as defined in relation (3.2). In particular, one finds $t_{foc} \simeq 0.254345$. This focalisation time is the time when the shell is reduced to a single point, it is thus not possible to use it as the final time for the computations. In the sequel, the times $\tau_1 = \frac{\sqrt{3}}{2}t_{foc}(\simeq 0.220263)$ and $\tau_2 = 0.99t_{foc}(\simeq 0.251801)$ are considered, where τ_1 corresponds to a compression of the shell by a factor $1/2$ as proposed in [28]. In particular, it is much more difficult to obtain the solution at time τ_2 because of the mesh printing. Indeed, this compression test case presents an exponential growth rate of the mesh defects as shown in [93]. It is possible, in the 2D framework, to have perfectly equi-angular zoning of the cylindrical shell and thus to study the growth of small mesh defects. The task is almost impossible in 3D since such perfectly equi-angular meshes cannot exist. The mesh necessarily presents defects, such as the triple point observable in Figure 3.16, that are amplified by the compression and lead to jets as shown in Figures 3.17a-3.17b.

The domain studied is a eighth of spherical shell meshed as shown in Figure 3.16. One can remark that this mesh is composed by three identically deformed cubes. In particular, the node at the center of this shell, i.e. the node shared by the three cubes, is called triple point since it has only three neighboring cells. In this study, such a mesh is referred to as the number of cells along the radius times the number of cells between $\theta = 0$ and $\theta = \pi$. For example, in Figure 3.16, one can observe a 10×40 cells mesh. Moreover, symmetry boundary conditions are applied to the three planar faces of the eighth of shell and the analytic pressure solution is used to

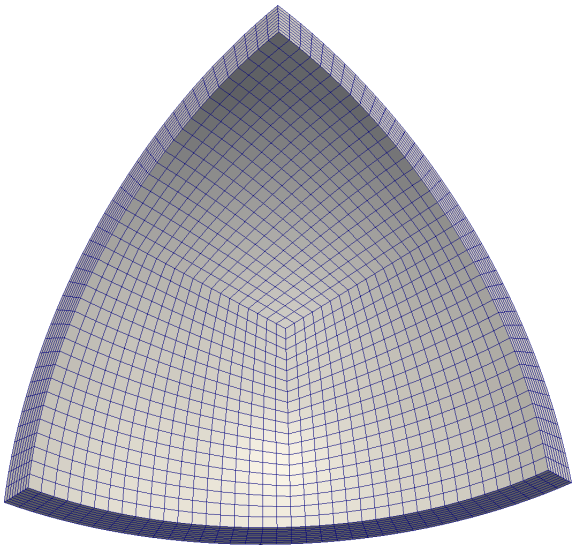

Figure 3.16 – Kidder test case - Example of mesh used for the computation - Eighth of spherical shell - Case of a 10×40 cells mesh.

define the pressure boundary conditions applied to the inner and outer faces. One writes

$$P^b_{inn} = P^0(r_{inn})h(t)^{-\frac{2\gamma}{\gamma-1}}, \tag{3.13}$$

$$P^b_{out} = P^0(r_{out})h(t)^{-\frac{2\gamma}{\gamma-1}}. \tag{3.14}$$

Let emphasize the difficulty of this test case. First, the mesh is not symmetric because of the triple point. This leads to mesh printing which breaks the radial symmetry of the flow. Second, the Kidder problem is known to present an exponential growth of the perturbation at the outer face of the shell [93]. In this way, the stability of the solution at late times is not ensured.

The first order solution is shown in Figure 3.17 on a 10×40 cells mesh at initial time, time τ_1 and time τ_2. One can observe in Figures 3.17a-3.17b the jet appearing at the outer face of the shell at time τ_2. This jet appears at the triple point because of the mesh printing since the mesh is not perfectly equi-angular symmetric. This problem is well known and this is why the final time is set to time τ_1 when the mesh printing is still low and not visible on the mesh. The scatter plot of the radial density at time τ_1 is rarely shown [14, 22, 28, 125] but is interesting for evaluating the ability of the scheme to preserve spherical symmetry. In particular, one can observe in Figure 3.17c that the solution has a good spherical symmetry with points slightly spread around the analytic solution. Finally, the inner and outer radii of the shell are plotted in Figure 3.17d. Only the points on the Cartesian axis and the triple points are used for this Figure. In particular, one can observe that the numerical solution is in good accordance with the analytic one and that the jet is not yet observable.

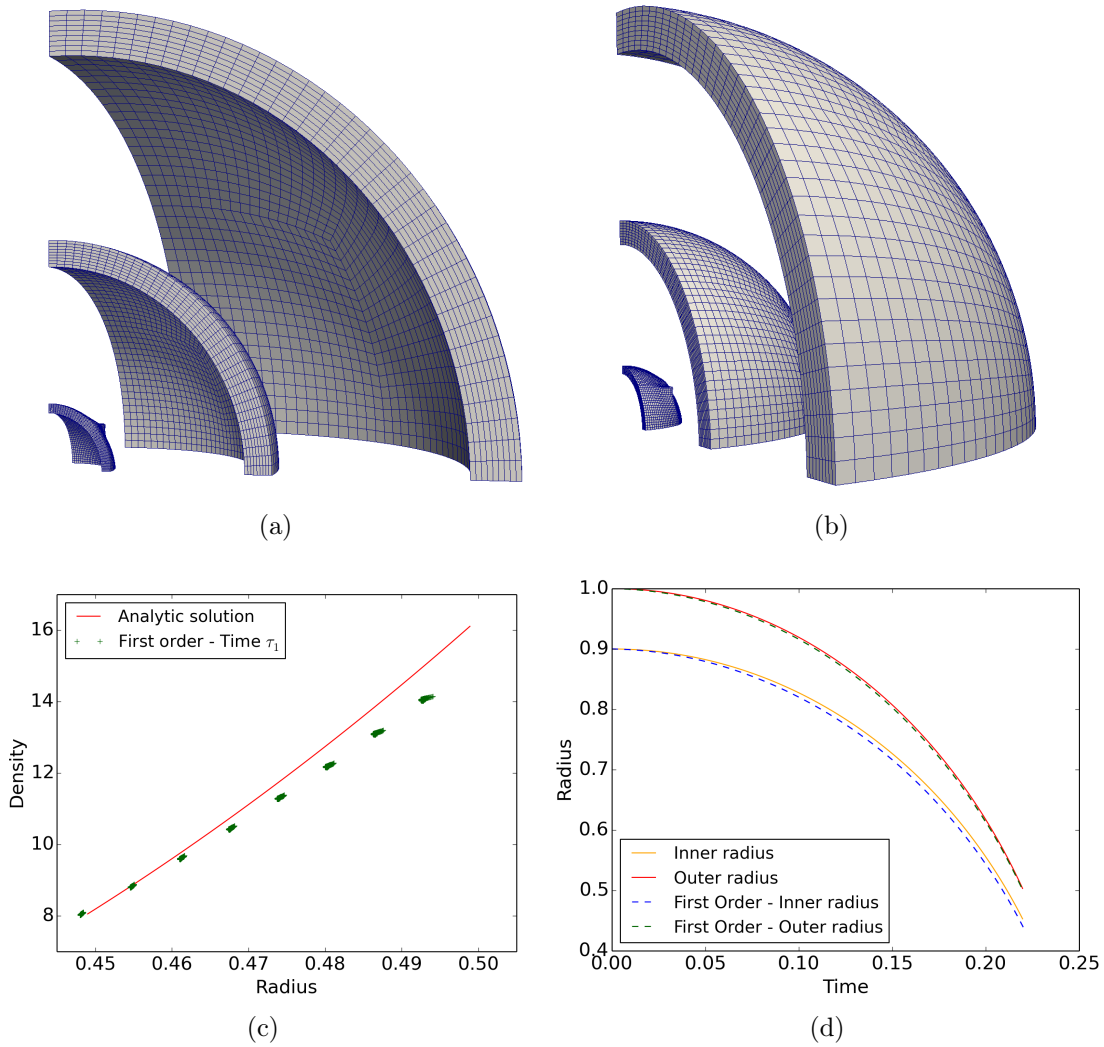

Figure 3.17 – Kidder test case - First order solution - Meshes at initial time, at time $\tau_1 = \frac{\sqrt{3}}{2} t_{foc}$ and time $\tau_2 = 0.99 t_{foc}$ (from right to left) (3.17a-3.17b) - Scatter plot of the radial density at time τ_1 (3.17c) on a 10×40 cells mesh - Plot of the inner and outer radius of the shell with respect to time (3.17d) - One can observe the formation of jet at the triple point.

The second order solution of this problem is difficult to obtained since the scheme presents less dissipation than at first order. Using the CW- or SP-limiter amplifies the mesh printing leading to an early jet on the outer face or oscillations at the inner face respectively (refer to Figure 3.18). The solution is thus studied using the MM-limiter. One can refer to Figure 3.19c for the scatter plot of the radial density and to Figure 3.19d for plot of the inner and outer radii with respect to time. In particular, one can observe in Figure 3.19c that the mesh printing is stronger than at first order. Indeed, the group of points are more spread than at first order. However the density in the cells is closer to the analytic solution. One can also observe

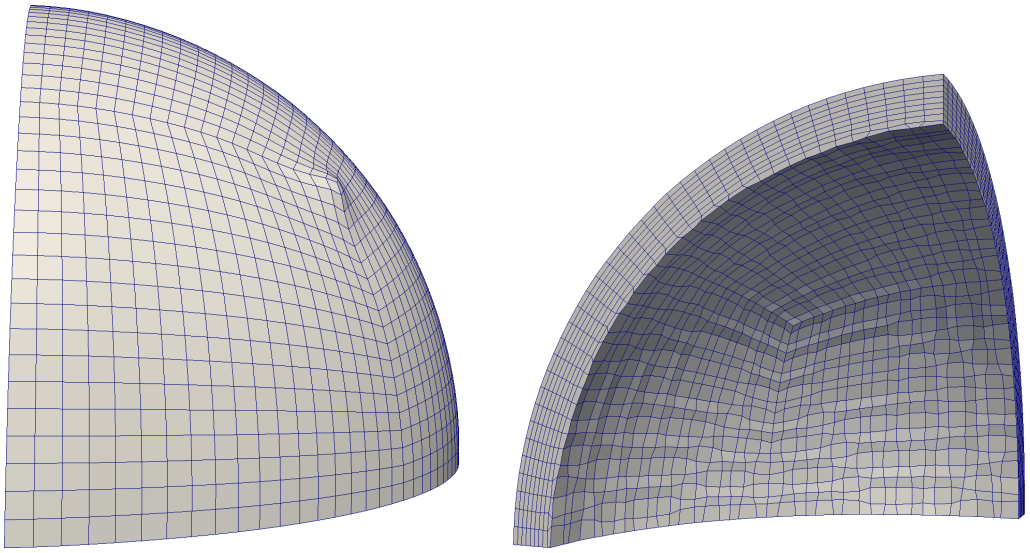

(a) (b)

Figure 3.18 – Kidder test case - Second order solution at time $\tau_1 = \frac{\sqrt{3}}{2} t_{foc}$ on a 10×40 cells mesh - Early jet appearing at the outer face when using the CW-limiter (3.18a) - Oscillations at the inner face when using the SP-limiter (3.18b).

that the positions of the inner and outer radii of the shell are improved at second order since the numerical and analytic solution match perfectly. Finally, one can also observe in this Figure that the jet has not yet appeared.

Conclusion

In this Chapter we have studied the behavior of the second order cell-centered Lagrangian scheme developed in Chapters 1 and 2. The results obtained on classic Lagrangian test cases enable to validate and highlight the good properties of the limiting procedures introduced in Chapter 2. First, the Sod problem enables to isolate the impact of the gradient reconstruction as well as the monotonicity stencil on the solution stability. In particular, it appears that the extended monotonicity stencil leads to a smooth solution with both the LS and discrete gradients whereas the LS gradients leads to spurious oscillations when the monotonicity is verified at the cell nodes. Then, the second order accuracy of the scheme is validated on the Taylor-Green Vortex. In particular, both the LS and the discrete gradients lead to an order of 1.97 using a PC time integration. This order is reduced when the LS gradients are combined with the GRP procedure but is preserved when the GRP procedure is combined with discrete gradients. The Saltzmann problem presents no particular difficulties. The results are shown with the SP-limiter and the solution is evaluated at time 0.9 after two bounce of the shock against the walls. The solution at this late time is still acceptable, however it is difficult to go further because of pinched cells. The Noh problem introduces severe defaults in the solutions. A loss of symmetry and strong overshoots are observable with the CW-limiter using three different basis. The SP-limiter enables to recover the symmetry as well as the

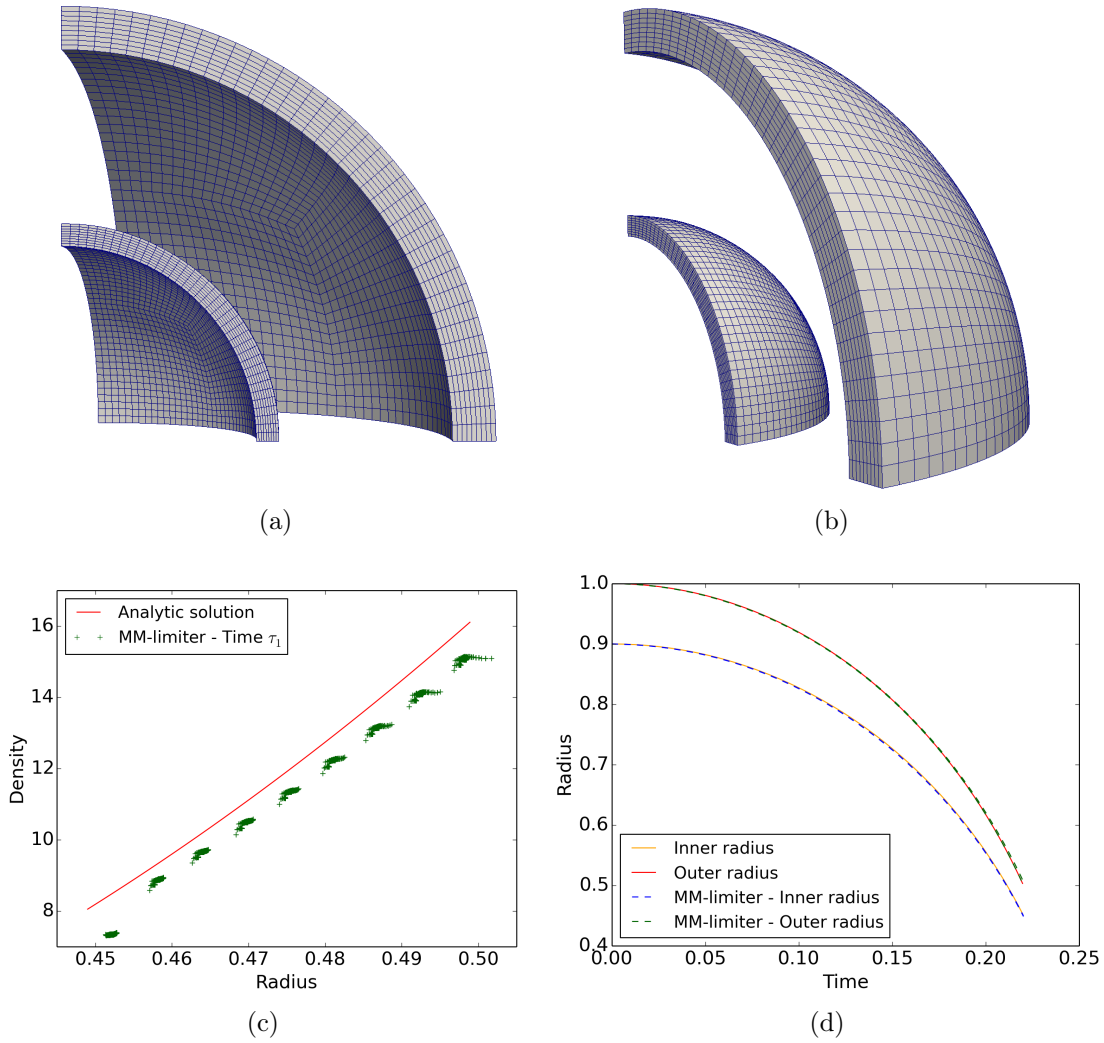

Figure 3.19 – Kidder test case - Second order solution using the MM-limiter - Mesh at initial time and time $\tau_1 = \frac{\sqrt{3}}{2} t_{foc}$ (from right to left) (3.19a-3.19b) - Scatter plot of the radial density at time τ_1 (3.19c) on a 10×40 cells mesh - Plot of the inner and outer radius of the shell with respect to time (3.19d).

monotonicity on coarse meshes, however, overshoots reappear on strongly refined meshes. The MM-limiter enables to remove the overshoots appearing on this difficult problem and to finish the convergence study. The CW- and SP-limiter fail to give a good solution on the Sedov problem since they preserve the node crossing and the bowtie-shaped hourglass mode appearing at first order. The MM-limiter enables to remove these two flaws and leads to a good convergence of the solution towards the analytic solution. Finally, the difficult problem of the Kidder compression is presented. Only the MM-limiter presents a solution which is not degraded by the mesh printing. In particular, the shell inner and outer radii are better tracked with this limiter. As shown by Vilar and Maire in [124], a high order approximation of the geometry could help reducing this mesh printing but this track is not followed

in this study. As a conclusion on the different limiter tested in this Chapter, one can summarize as follows:

- the SP-limiter is shown to be a good improvement of the CW-limiter. In particular, its extended monotonicity stencil and its velocity limiting procedure enable to improve the monotonicity and the symmetry of the solution on 3D problems.
- the MM-limiter is a good candidate to compute the solution of flows characterized by a spherical symmetry. In particular, it enables to deal with the difficult mesh printing problem without resorting to a high order geometry.

In the next Chapter, the MM-limiter is used to study the development of Rayleigh-Taylor Instability (RTI) in supernova remnants. In Chapter 4, the scheme presented so far is extended to the modeling of the Hyperelasticity system.

Chapter 4

Application to astrophysics

The Celia Laboratory is interested in High Energy Density Physics (HEDP) problems such as Inertial Confinement Fusion (ICF) and laboratory astrophysics. Hydrodynamic instabilities are common in such flows since the fluids (or solids) are subject to high mechanical and temperature constraints. For example, one can observe Rayleigh-Taylor Instability (RTI) when a light fluid pushes a heavier fluid, or a Kelvin-Helmholtz instability in the case of a shearing flow between two fluids of different density. In this Chapter, it is proposed to study the development of RTI in a plerion (supernova remnants blown-up by a central pulsar) as done in [54]. This test case corresponds to a shell of gas expanded by an internal pressure (the pulsar wind) which can lead to RTI if the inner interface of the shell is not regular [63, 74]. In particular, the RTI is responsible for the Rayleigh-Taylor fingers observable in the Crab nebula (refer to Figure 4.1). In the case of an ICF experiment, RTI appears at the interface between the shell of the ICF target and the inner fluid because of manufacturing defaults in the target or asymmetry in the irradiation. This instability degrades the compression and prevents the nuclear fusion reactions to happen. In this sense, it is important to understand how this instability grows with respect to space and time in order to better control ICF experiments. Analytic studies, based on self-similar solutions, have been carried out on the RTI phenomenon to provide accurate models [13, 71, 108]. The Chapter is structured as follows. The expansion of the plerion is first studied without perturbation to verify that the analytic solution is recovered. Then, perturbations of the inner interface are introduced by use of spherical harmonics functions. The 3D scheme is first compared to the 2D-axisymmetric CHIC Code [18] in order to validate it on a 2D-axisymmetric flow before proceeding with 3D studies. In particular, the impact of the azimuthal mode m on the perturbation growth is studied at the end of this Chapter.

4.1 Plerion test case

The following plerion test case models the blown-up of a spherical shell by a central pressure as proposed in [108]. The shell, of inner radius $r_{inn} = 0.9$ and outer radius $r_{out} = 1$, is filled with a perfect monoatomic gas. The initial state of the shell

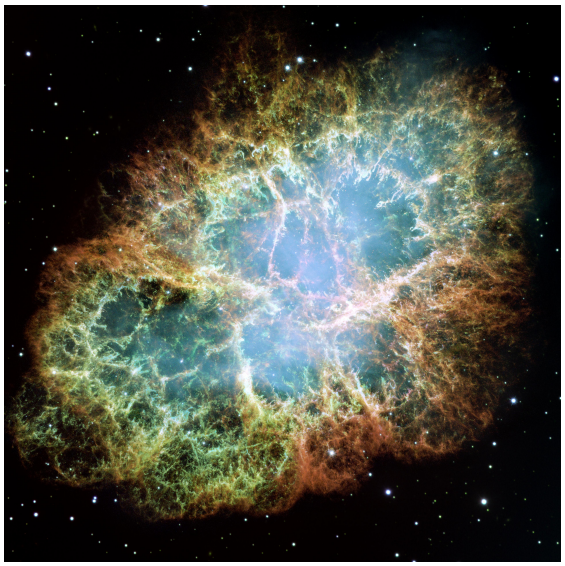

Figure 4.1 – Photo of the Crab nebula taken by the Hubble telescope (2005).

is very similar to the Kidder problem and is given by

$$\begin{aligned} \rho^0(r) &= \left(\frac{r_{out}^2 - r^2}{r_{out}^2 - r_{inn}^2} \rho_{inn}^{\gamma-1} \right)^{\frac{1}{\gamma-1}}, \\ P^0(r) &= K \rho^0(r)^\gamma, \\ \boldsymbol{V}^0(r) &= \frac{\beta r}{\tau} \boldsymbol{e}_r. \end{aligned} \tag{4.1}$$

In this system, $\rho_{inn} = 1$ is the initial density at the inner interface of the shell, β is a constant defining the initial radial velocity magnitude. Finally, the constant K is defined as

$$K = \left(\frac{\gamma - 1}{\gamma} \right) \frac{r_{out}^2 - r_{inn}^2}{2\tau^2}, \tag{4.2}$$

where $\tau = 1$ is a characteristic time. In the present study, $\beta = 0$. The pressure boundary condition applied to the inner interface and modelling the central pulsar wind is defined by

$$P^b(t) = P^0(r_{inn}) h(t)^{-\frac{2\gamma}{\gamma-1}}, \tag{4.3}$$

where $h(t)$ is the scaling function defined as

$$h(t) = \sqrt{\left(1 + \beta \frac{t}{\tau}\right)^2 + \left(\frac{t}{\tau}\right)^2}. \tag{4.4}$$

This scaling function also enables to express the position $R(r,t)$ at time t of a point initially at radius r as

$$R(r,t) = h(t) r. \tag{4.5}$$

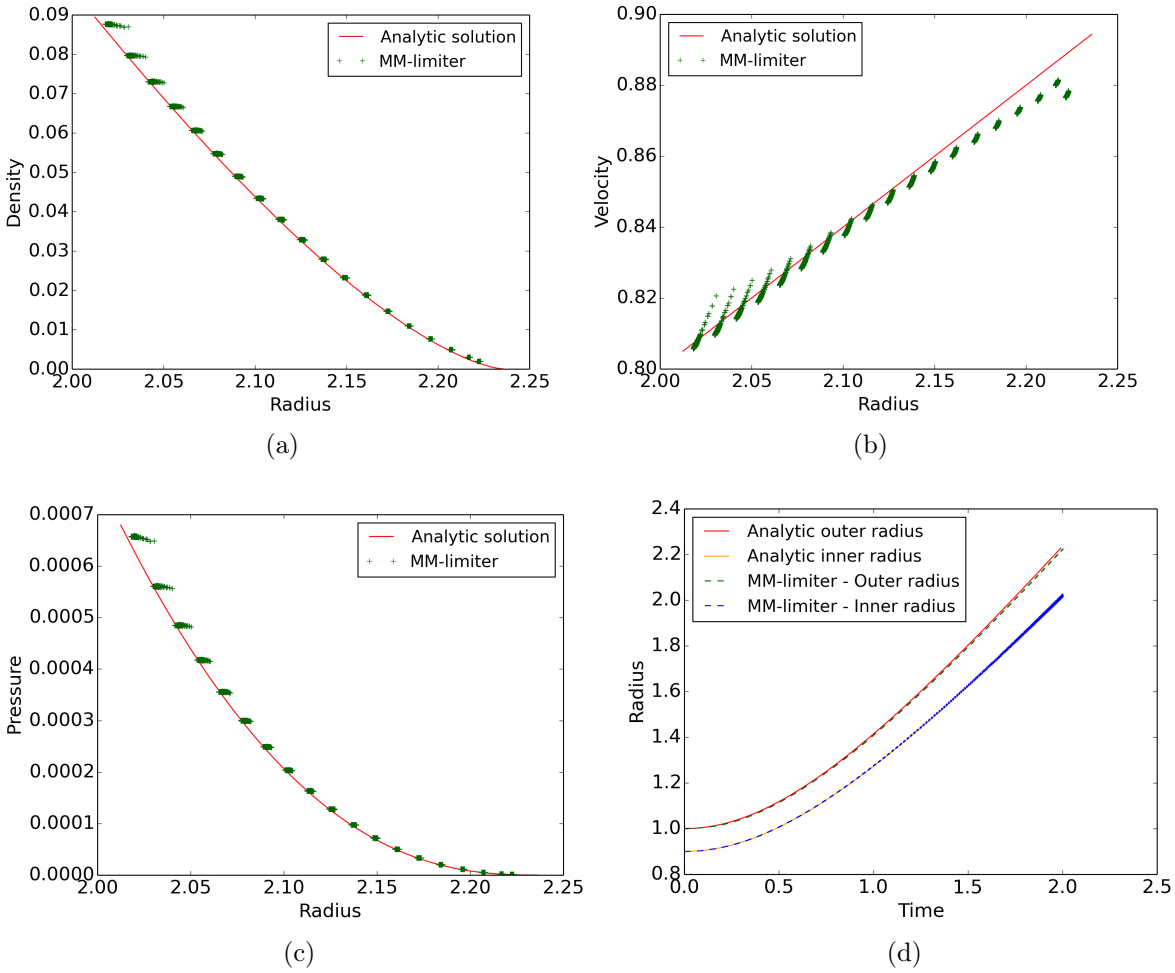

Figure 4.2 – Plerion test case - Second order solution using the MM-limiter - Scatter plot of the radial density (4.2a), velocity (4.2b) and pressure (4.2c). Inner and outer radii with respect to time (4.2d). Solutions at time $t = 2\tau$ on a 20×40 cells mesh.

The analytic solution at time t of this problem is given by

$$\begin{aligned} \rho(r,t) &= h(t)^{-\frac{2}{\gamma-1}} \left(\frac{r_{out}^2 - r^2}{r_{out}^2 - r_{inn}^2} \rho_{inn}^{\gamma-1} \right)^{\frac{1}{\gamma-1}}, \\ P(r,t) &= K\rho(r,t)^{\gamma}, \\ \boldsymbol{V}(r,t) &= \frac{r}{h(t)^2\tau} \left(\beta + (\beta^2+1)\frac{t}{\tau} \right) \boldsymbol{e}_r. \end{aligned} \tag{4.6}$$

The eighth of shell is discretized with meshes as the one presented in Figure 3.16.

The Figure 4.2 presents the second order solution obtained with the MM-limiter. More precisely, this Figure presents the scatter plots of the radial density (Figure 4.2a), the velocity norm (Figure 4.2b) and the pressure (Figure 4.2c) at final time

$t = 2\tau$. One can observe a good accordance between the analytic and the numerical solutions. The mesh printing is however visible on the radial plots since the points are spread around the analytic solutions. The inner and outer radii are also plotted with respect to time and compared to the formula (4.5) in Figure 4.2d. All the nodes of the inner and outer faces are not plotted in this last Figure. The nodes on the Cartesian axis and the triple point are sufficient to understand the behavior of the interface. In particular, one can observe that the blue line begins to split into two lines. This is due to the triple point which does not move at the same speed than the nodes on the Cartesian axis due to mesh printing.

4.2 Perturbation of the inner interface

Even if mesh printing is already present in the unperturbed plerion test case this section proposes to introduce a spherical harmonics perturbation of the inner interface. This perturbation has indeed a strong amplitude which makes it more preponderant than the mesh printing. Moreover, it enables to study the development of RTI in the case where a light fluid pushes a heavier fluid. Let start with an axisymmetric perturbation in order to compare the results with the 2D-axisymmetric CHIC Code [18]. The theoretical solution describing the amplification factor of this perturbation is taken from [108].

Here, the inner interface of the shell is deformed at initial time by moving the nodes along the radial direction $\boldsymbol{e_r}$ such that

$$r_0^{pert}(\theta,\varphi) = r_0\Big[1 + a_0\ \mathcal{D}(r_0)\ \mathcal{R}e\big\{Y_{l,m}\left(\theta,\varphi\right)\big\}\Big], \tag{4.7}$$

where r_0 and $r_0^{pert}(\theta,\varphi)$ are the node radii respectively before and after the perturbation, a_0 is the perturbation amplitude, $\mathcal{D}(r_0)$ is a damping function and $Y_{l,m}\left(\theta,\varphi\right)$ is the spherical harmonics function of modes l and m. The damping function enables to locate the perturbation at the inner interface. Here the damping is linear thus $\mathcal{D}(r)$ writes

$$\mathcal{D}(r_0) = \frac{r_0 - r_{out}}{r_{inn} - r_{out}}. \tag{4.8}$$

Moreover, the spherical harmonics function writes

$$Y_{l,m}(\theta,\varphi) = (-1)^m\sqrt{\frac{(2l+1)}{4\pi}\frac{(l-m)!}{(l+m)!}}P_{l,m}\big(\cos(\varphi)\big)e^{im\theta}, \tag{4.9}$$

where

$$P_{l,m}(x) = (-1)^m\left[1-x^2\right]^{\frac{m}{2}}\frac{d^mP_l(x)}{dx^m}, \tag{4.10}$$

and $P_l(x)$ is the l^{th} Legendre polynomial. These last polynomials are evaluated thanks to a Numerical Recipes routine [107].

Remark:
The mesh perturbation is incompressible which means that the cell volume varies due to the mesh deformation, however, the cell density must be invariant.

With such a perturbation, the analytic study [108] predicts a perturbation growth of the form

$$\xi(\theta,\varphi,t) = a_0 Y_{l,m}(\theta,\varphi) h(t) \sum_{j=1}^{4} \Lambda_j e^{\lambda_j g(t)}, \tag{4.11}$$

where $(\lambda_j)_{j=1,4}$ are the four roots of the dispersion equation linking the perturbation growth rate λ to the mode l. In this study, λ is supposed to be independent on the mode m as supposed in [108]. This hypothesis will be discussed in the next section. In particular, for the plerion test case one finds: $\lambda_{1,2} = \pm\sqrt{l+1}$ and $\lambda_{3,4} = \pm i\sqrt{l}$, where i is the imaginary unit.

The constants $(\Lambda_j)_{j=1,4}$ in relation (4.11) are the amplitude of the excited modes corresponding to each root λ_i. These factors are computed as

$$\begin{aligned}
\Lambda_{1,2} &= \frac{-1}{b_1 - b_2}\left[b_2 D_0 - D_1 \pm \frac{\tau}{\sqrt{l+1}}(b_2 V_0 - V_1)\right], \\
\Lambda_{3,4} &= \frac{1}{b_1 - b_2}\left[b_1 D_0 - D_1 \pm i\frac{\tau}{\sqrt{l}}(b_1 V_0 - V_1)\right].
\end{aligned} \tag{4.12}$$

For a geometric perturbation on the inner interface only, these constants are chosen such as: $D_0 = 1$, $D_1 = 0$ and $V_0 = V_1 = 0$. This leads to

$$\begin{aligned}
\Lambda_{1,2} &= \frac{-b_2}{b_1 - b_2} = \Lambda_I, \\
\Lambda_{3,4} &= \frac{b_1}{b_1 - b_2} = \Lambda_{II},
\end{aligned} \tag{4.13}$$

where the constants $b_1 \simeq 0.098477$ and $b_2 \simeq 7.402737$ are numerical approximated from the eigenmodes displacement equation taken from [108]. Finally, imposing

$$g(t) = \operatorname{atan}\left(\beta + (\beta^2+1)\frac{t}{\tau}\right) - \operatorname{atan}(\beta), \tag{4.14}$$

and using the coefficients (4.13), equation (4.11) is simplified into

$$\xi(\theta,\varphi,t) = a_0 Y_{l,m}(\theta,\varphi) h(t) \left[\Lambda_I \cosh\left(g(t)\sqrt{l+1}\right) + \Lambda_{II} \cos\left(g(t)\sqrt{l}\right)\right]. \tag{4.15}$$

Numerically, the amplification factor of the perturbation is evaluated as follows

$$\xi^{num}(\theta,\varphi,t) = \frac{r^{pert}(\theta,\varphi,t) - r(\theta,\varphi,t)}{r_0^{pert}(\theta,\varphi) - r_0(\theta,\varphi)}. \tag{4.16}$$

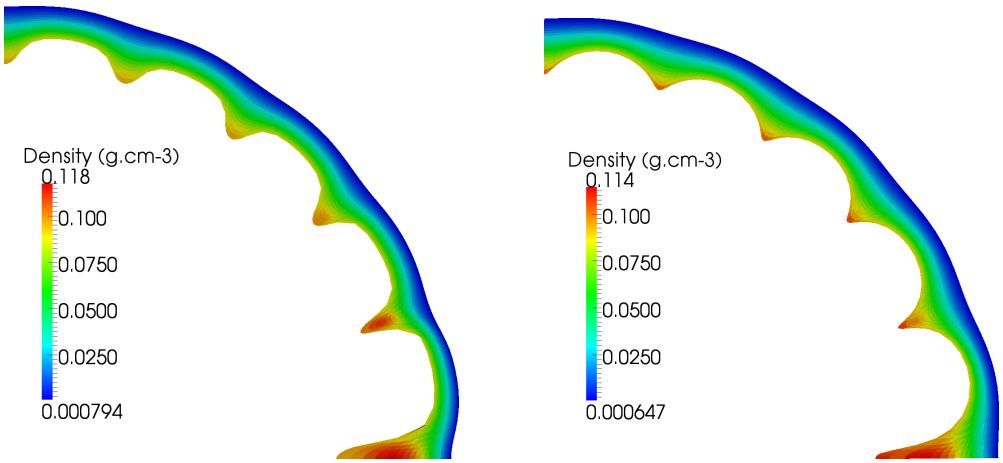

(a) (b)

Figure 4.3 – Plerion test case - Axi-symmetric perturbation with $a_0 = 4 \times 10^{-3}$, $l = 20$ and $m = 0$ - Comparison between the 2D-axisymmetric CHIC Code (4.3a) and the 3D scheme (4.3b) - Slice in the plane $(O, \boldsymbol{y})$ for a 20×80 cells mesh.

This result is comparable to the normalized analytic solution

$$\frac{\xi(\theta, \varphi, t)}{a_0 Y_{l,m}(\theta, \varphi)} = h(t) \left[\Lambda_I \cosh\left(g(t)\sqrt{l+1}\right) + \Lambda_{II} \cos\left(g(t)\sqrt{l}\right) \right]. \tag{4.17}$$

This last expression is independent on (θ, φ) thus $\xi^{num}(\theta, \varphi, t)$ can be evaluated at any point of the inner face. However, there exists (θ, φ) such that $\xi(\theta, \varphi, t) = 0$ thus the amplification factor cannot be measured at any point. For an axi-symmetric perturbation as the one presented in Figures 4.3 and 4.4, the perturbation is measured at the point of the z-axis that also belongs to the inner face.

The results shown in Figure 4.3 are obtained using the MM-limiter on a 20×40 cells mesh. The perturbation magnitude is set to $a_0 = 4 \times 10^{-3}$ and the modes are chosen such that $l = 20$ and $m = 0$. In particular, the perturbation amplitude is strong in order to have qualitatively comparable results. The slices made in the plane $(O, \boldsymbol{y})$ show a good accordance for both the density field and the mesh shape at final time $t = 2\tau$. Moreover, the 3D scheme shows a very good accordance with the CHIC Code with respect to the amplification factor of the perturbation. One can indeed observe that the curves overlap in Figure 4.4. These two Figures completely validate the 3D scheme since the same results than a 2D-axisymmetric code are found. The numerical results are quite far from the analytic one for two main reasons. First, the mesh is quite coarse and the solution is thus not converged. Second, the perturbation magnitude is strong. The RTI is thus in its non-linear regime where the perturbation growth starts to saturate whereas the analytic solution supposes a linear regime.

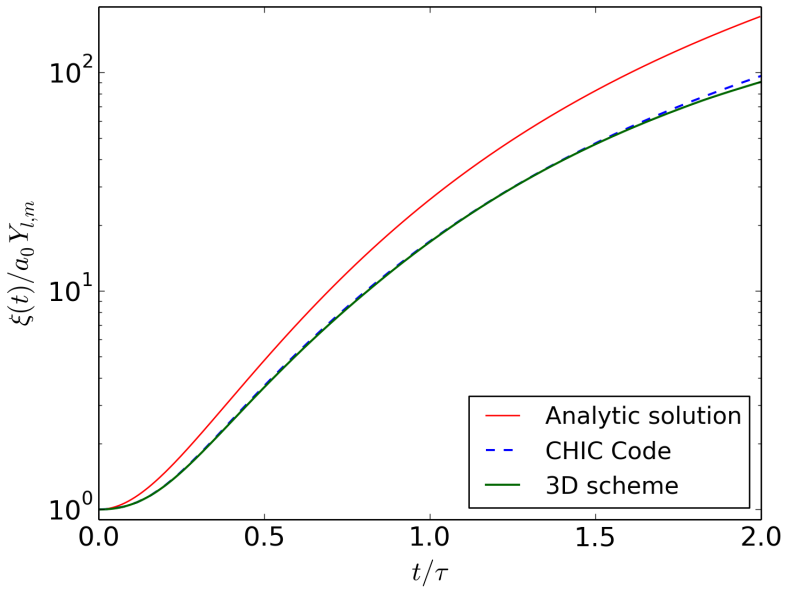

Figure 4.4 – Plerion test case - Amplification factor of the perturbation with respect to time with $a_0 = 4 \times 10^{-3}$, $l = 20$ and $m = 0$ (Logarithmic plot) - Comparison between the 3D scheme (dashed line) and the CHIC code (crosses) on a 20×80 cells mesh.

4.3 Impact of the azimuthal mode m on the perturbation growth

The 3D scheme has proven its ability to handle plerion flows as well as 2D axisymmetric perturbations. Consequently it is now used to perform 3D perturbations. In particular, this study aims at numerically verify the hypothesis stating that the azimuthal mode m has no impact on the perturbation growth. The following (l, m) modes are considered: $(20, 0)$, $(20, 1)$, $(20, 2)$, $(20, 3)$, $(20, 4)$, $(20, 5)$, $(20, 10)$, $(20, 15)$ and $(20, 20)$. The perturbation is now evaluated from the inner face area of the shell. Indeed, as previously said, there exists some points on the inner interface for which the perturbation is null. In this way it is difficult to fix a point and modify the perturbation modes, hoping that this node will always be perturbed. Moreover, the inner face area seems to be a good candidate for evaluating the perturbation growth since it gives a global overview of the perturbation. Strong perturbations with an initial amplitude $a_0 = 4 \times 10^{-3}$ are applied to a 20×40 cells mesh to help visualize the spherical harmonics patterns (refer to Figure 4.7). The analytic computation of the inner face area is cumbersome and complex [78]. A simplifying assumption is thus made to approximate its growth with respect to time. Since the area of a sphere of radius R is $\mathcal{A}_R = 4\pi R^2$ and the perturbation growth at one point of the face evolves as $\xi(t)$, the perturbation growth of the whole face is supposed to evolve as $\xi^2(t)$. This is a rough approximation but it is in good accordance with the numerical results shown in Figure 4.5. One can also observe in this Figure that all the modes provide very similar amplification factors. Numerically, the perturbation

growth is evaluated as

$$(\xi^2)^{num} = \frac{\mathcal{A}^{pert}(t) - \mathcal{A}(t)}{\mathcal{A}^{pert}(0) - \mathcal{A}(0)}, \tag{4.18}$$

where $\mathcal{A}^{pert}(t)$ is the perturbed area measured at time t and $\mathcal{A}(t)$ the unperturbed area at the same time. In this way, the hypothesis stating that the amplification factor does not depend on the m mode is numerically validated.

One can go further in the analysis. The Figure 4.6 shows the internal face area with respect to the perturbation modes. One can notice that introducing a l mode increases the inner face area (blue line) compared to the unperturbed case (red line). Introducing the azimuthal mode m gives an area between the two previous one. However, changing this mode has no impact on the resulting area (green lines).

Conclusion
This study enables to numerically validate the hypothesis stating that the azimuthal mode m has no impact on the growth rate of an RTI perturbation based on spherical harmonics functions. Besides, it is also shown that the area of the perturbed inner face is independent of the mode m and always lower than the area of the axi-symmetric perturbation. Let recall, that the analytic solutions came from the linear theory. In this way, these results are valid only for the early stages of the RTI development since more complex non-linear behavior appear later on.

As a future work on the plerion test case, a spectral decomposition of the inner face on the spherical harmonics functions would be interesting in order to study the evolution of multi-modal perturbations during the RTI development. Moreover, additional physics could be studied such as the magnetic field in order to describe more realistic plerion flows, see for example the recent work in [106].

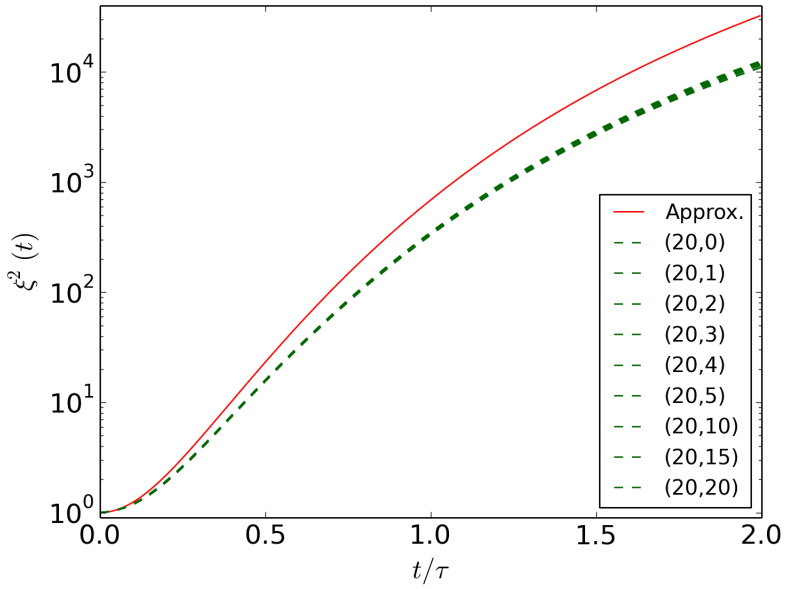

Figure 4.5 – Perturbed plerion test case - Amplification factor of the inner face area with respect to time (Logarithmic plot) - Impact of the azimuthal mode m - Perturbations with $a_0 = 4 \times 10^{-3}$, $l = 20$ and $m = 0, 1, 2, 3, 4, 5, 10, 15, 20$ on a 20×80 cells mesh

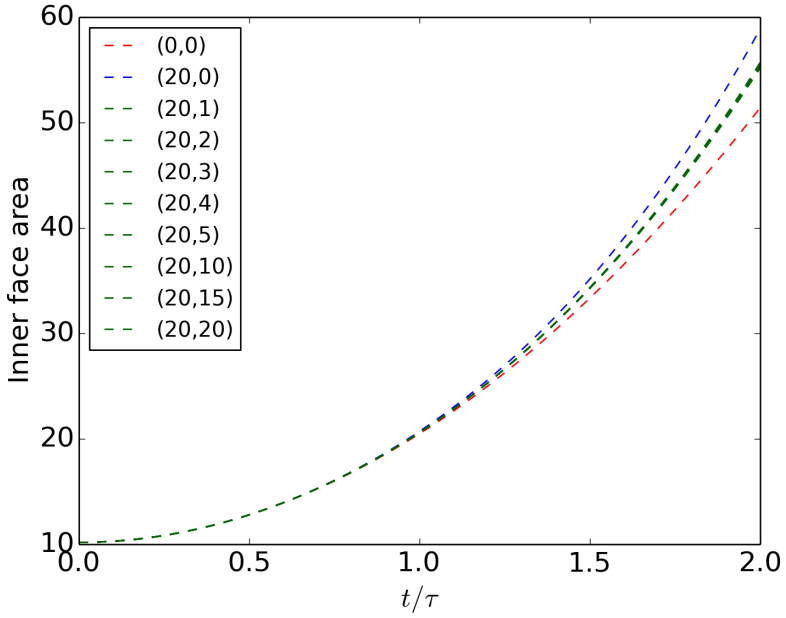

Figure 4.6 – Perturbed plerion test case - Inner face area with respect to time (Logarithmic plot) - Impact of the azimuthal mode m - Perturbations with $a_0 = 4 \times 10^{-3}$, $l = 20$ and $m = 0, 1, 2, 3, 4, 5, 10, 15, 20$ on a 20×80 cells mesh.

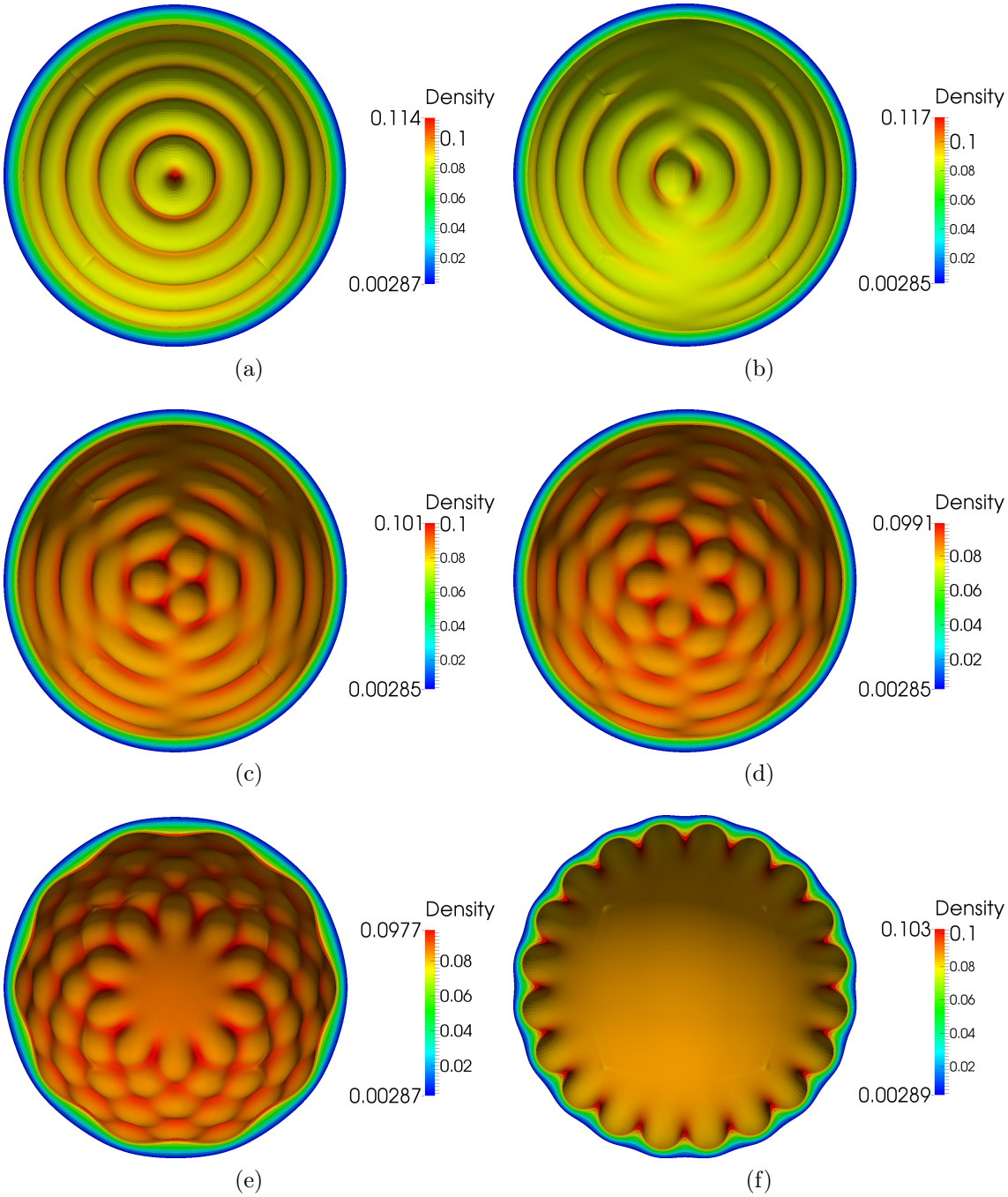

Figure 4.7 – Perturbed plerion test case - Density field and shape of the eighth shell for spherical harmonic perturbations with the following (l, m) modes: $(20, 0)$ (4.7a), $(20, 1)$ (4.7b), $(20, 3)$ (4.7c), $(20, 5)$ (4.7d), $(20, 10)$ (4.7e), $(20, 20)$ (4.7f) - Slices in the $(O, \boldsymbol{z})$ plane at final time $t = 2\tau$ on a 10×120 cells mesh.

Chapter 5

Lagrangian hyperelasticity

5.1 Introduction

In this Chapter, the cell-centered Lagrangian scheme developed in Chapters 1 and 2 is extended to the hyperelasticity system. The simulation of the elastic and elastic-plastic response of a solid material is of great interest for mechanical applications such as impact problems, metal forging, geophysics, biology, etc. Historically, the simulation of solid motion has been principally performed using the Finite Element formalism. However, from the seminal works of Wilkins [132] and Godunov [57] Finite Volume Lagrangian schemes have been designed to model solids. The Lagrangian formalism is natural for the simulation of deforming solids since the computational grid follows the solid motion. This enables, for example, the natural tracking of free-surface boundaries and multi-material interfaces. Two principal models are used for the description of elastic materials under large deformations, namely the hypoelastic and hyperelastic models.

In the hypoelastic approach proposed by Wilkins in [132], the spherical part of the Cauchy stress tensor, which corresponds to the hydrodynamic pressure, is described by an equation of state whereas the deviatoric part is described by an evolution equation. This equation introduces the Jaumann derivative of the deviatoric part in order to ensure the frame-indifference of the scheme. This property, also called objectivity, ensures that the constitutive law does not depend on the frame of reference. In this sense, a change of observer must not impact the behavior of the solid. Numerical schemes have been successfully applied to the hypoelastic model, see for example [39, 67, 120]. However, this model is known to have inherent drawbacks. First, the choice of the objective derivative is not restricted to the Jaumann rate and the deviatoric part of the stress tensor can be computed differently. Besides, the Jaumann rate introduces non-conservative terms which renders questionable the mathematical derivation of numerical schemes [51]. Finally, the hypoelastic model produces entropy even on reversible process. Despite these theoretical drawbacks, the hypoelastic approach is successfully used in numerous studies. In [21, 96, 111, 112], it is proposed to solve the hypoelastic model using cell-centered Finite Volume Lagrangian schemes. As detailed in the introduction of Chapter 1,

these schemes locate all the variables at the cell centers and propose a nodal solver, based on approximate Riemann solver, to compute the nodes velocity and move the computational grid. In particular, the nodal solvers proposed by Després et al. [34] and Maire et al. [93] enable the computation of a nodal velocity which guarantees the global conservation of total energy and momentum as well as the respect of the Second Law of thermodynamics.

The hyperelastic approach was proposed by Godunov [57, 58, 59]. In this model, the constitutive law derives from the Coleman-Noll procedure [61] which ensures the frame-indifference and the thermodynamic consistency by construction. This procedure enables to define the Cauchy stress tensor as the derivative of the free energy with respect to the deformation. In particular, the hyperelastic model is not subject to the theoretical drawbacks of the hypoelastic model which provides a strong mathematical basis for designing numerical schemes. In particular, Ndanou et al. proved the hyperbolicity of the system [103]. One can refer to [44, 51, 64, 99] for studies using Eulerian schemes and [3, 4, 62, 76, 77, 80, 114] for studies involving Lagrangian schemes. In [76, 77], it is proposed to extend the GLACE scheme to the hyperelasticity system at first order in two-dimensions. In a series of papers [3, 4, 62, 80], Bonet et al. proposed different Finite Volume schemes: a vertex-centered scheme using the Jameson-Schmidt-Turkel (JST) algorithm and an upwind cell-centered scheme based on a mixed approach. An important work is also devoted to enforce the conservation of angular momentum. Both procedures are tested in 3D on numerous test cases and show very good results.

Going back to the Finite Element formalism, let mention the recent work of Scovazzi [114], proposing to solve a mixed form of the hyperelasticity equations tetrahedral meshes using a Variational MultiScale (VMS) procedure for stabilization. Let also mention the recent work of Favrie and Gavrilyuk [45] in which it is proposed to derive a hypoelastic model from a hyperelastic one in order to remove the classical theoretical drawbacks. Finally, let mention the work of Boscheri et al. [15] proposing a cell-centered high-order Discontinuous Galerkin (DG) scheme for modelling the Godunov-Peshkov-Romenski (GPR) approach.

The current study is the 3D extension of the work of Kluth et al. [76, 77] using the EUCCLHYD scheme proposed by Maire et al. [93]. Some differences can be noted since in [77], the authors propose to evaluate the deformation gradient between times t^n and t^{n+1} in order to obtain a scheme compatible with an Arbitrary Lagrangian-Eulerian (ALE) procedure. In the current study, the deformations are evaluated in the actual framework using the left Cauchy-Green tensor leading to an updated Lagrangian formalism. The second order extension of the scheme is proposed by mean of a Generalized Riemann Problem (GRP) [10] and the SP-limiter introduced in Chapter 2.

The Chapter is structured as follows: the hyperelastic approach is detailed in Section 5.2. In particular, the complete Coleman-Noll procedure is detailed in order

to construct the constitutive law in such a way that the frame-indifference as well as the Second Law of thermodynamics are respected. Then, the Section 5.3 shows the system discretization using a cell-centered Finite Volume Lagrangian scheme. The second order extension of this scheme is proposed in Section 5.4. Finally, the scheme is validated on several test cases in Section 5.5. Both problems with infinitesimal displacements and large deformations are considered.

5.2 The hyperelastic model

This first section presents the complete derivation of the hyperelasticity model. The interested reader is referred to [61] for more details. In particular, we concentrate on hyperelastic isotropic materials which enable the use of simplifying assumptions.

5.2.1 Kinematics of the solid

Let $\omega(t)$ be a domain of an elastic solid deforming with time in the $\mathbb{R}^3$ space. It represents the position, at time $t \in \mathbb{R}^+$, of a solid initially contained in Ω at $t = 0$. In this way, one has $\Omega = \omega(0)$. The spatial domain $\omega(t)$ is called the actual, or current, configuration of the solid whereas Ω is called the reference or initial configuration. Let define the function $\boldsymbol{\phi}(\boldsymbol{X}, t)$ mapping the reference configuration onto the current configuration as

$$\begin{aligned} \boldsymbol{X} \mapsto \boldsymbol{\phi}(\boldsymbol{X}, t) = &\quad \boldsymbol{x}, \quad \boldsymbol{x} \in \omega(t), \boldsymbol{X} \in \Omega, \\ \boldsymbol{\phi}(\boldsymbol{X}, 0) = &\quad \boldsymbol{X}. \end{aligned} \tag{5.1}$$

This mapping represents the motion of the solid with respect to time. In particular, it is supposed to be bijective in order that the solid does not penetrate itself. In this last relation, the points $\boldsymbol{x}$ are called spatial points and $\boldsymbol{X}$ are the material points. They are also respectively called Eulerian and Lagrangian coordinates.

The mapping $\boldsymbol{\phi}$ enables to follow the deformation of the solid during its motion. In particular, one has to differentiate an entity in the reference configuration from its counterpart in the current configuration. For this purpose, let use a capital letter to represent this entity in the reference configuration and a small letter to represent its counterpart. See for example the unit outward normal $\boldsymbol{N}$ of the boundary $\partial\Omega$ in Figure 5.1.

The Jacobian of the mapping $\boldsymbol{\phi}$ is referred to as the deformation gradient. This tensor is denoted $\mathbb{F}$ and represents the deformation of the solid during its motion. This tensor writes as

$$\mathbb{F} = \nabla_{\boldsymbol{X}} \boldsymbol{x} = \frac{\partial \boldsymbol{x}}{\partial \boldsymbol{X}}. \tag{5.2}$$

The determinant of $\mathbb{F}$ is denoted $J = \det(\mathbb{F})$. It represents the variation of volume during the motion thanks to the relation

$$dv = JdV, \tag{5.3}$$

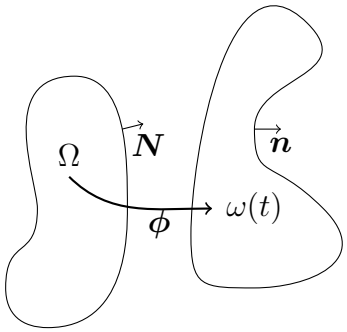

Figure 5.1 – Representation of the solid Ω in the reference configuration and its counterpart $\omega(t)$ in the current configuration. The motion of the solid is represented by the mapping ϕ. The unit outward normal of the boundary $\partial\Omega$ is denoted $\boldsymbol{N}$ whereas the unit outward normal of the boundary $\partial\omega(t)$ is denoted $\boldsymbol{n}$.

where dv is an infinitesimal volume in $\omega(t)$ and dV its counterpart in Ω. In particular, the bijectivity of the mapping $\boldsymbol{\phi}$ ensures that $J > 0$ and thus the volumes are always positive. Finally, time differentiating the relation (5.2), one gets

$$\begin{aligned} \frac{d\mathbb{F}}{dt} &= \frac{\partial}{\partial \boldsymbol{X}}\frac{d\boldsymbol{x}}{dt} = \frac{\partial \boldsymbol{V}}{\partial \boldsymbol{X}} = \frac{\partial \boldsymbol{V}}{\partial \boldsymbol{x}}\frac{\partial \boldsymbol{x}}{\partial \boldsymbol{X}}, \\ &= (\nabla_{\boldsymbol{x}} \boldsymbol{V})\mathbb{F}, \end{aligned} \tag{5.4}$$

where $\boldsymbol{V} = d\boldsymbol{x}/dt$ is the velocity. Classically, the deformation gradient is used to express the hyperelasticity system under the total Lagrangian form as in [76]. In particular, it is possible to express the divergence and gradient operators with respect to the Lagrangian coordinates, i.e. replace $\nabla_{\boldsymbol{x}}$ by $\nabla_{\boldsymbol{X}}$. For example, one has the relation $\nabla_{\boldsymbol{x}} \cdot (\mathbb{T}\boldsymbol{V}) = \nabla_{\boldsymbol{X}} \cdot (\mathbb{P}\boldsymbol{V})$ where $\mathbb{P}$ is the first Piola-Kirchhoff tensor $\mathbb{P} = J\mathbb{T}\mathbb{F}^{-t}$. In this study, only the updated Lagrangian formalism is considered which means that all the differentiation are made with respect to the Eulerian coordinates $\boldsymbol{x}$. In this way, it is possible to simplify the notations and replace $\nabla_{\boldsymbol{x}}$ by ∇. In particular, this notation simplification is possible thanks to the use of the left Cauchy-Green tensor $\mathbb{B}$ instead of the deformation gradient $\mathbb{F}$. This tensor is defined as

$$\mathbb{B} = \mathbb{F}\mathbb{F}^t, \tag{5.5}$$

and represents the deformation of an infinitesimal length. Indeed, considering an infinitesimal length $d\boldsymbol{x}$ in the current configuration and its counterpart $d\boldsymbol{X}$ in the reference configuration, one has

$$d\boldsymbol{X} = \mathbb{F}^{-1} d\boldsymbol{x}, \tag{5.6}$$

hence

$$d\boldsymbol{X} \cdot d\boldsymbol{X} = \mathbb{F}^{-t}\mathbb{F}^{-1} d\boldsymbol{x} \cdot d\boldsymbol{x} = \mathbb{B}^{-1} d\boldsymbol{x} \cdot d\boldsymbol{x}. \tag{5.7}$$

In particular, the scalar J becomes

$$J = \sqrt{\det(\mathbb{B})}, \tag{5.8}$$

and the time derivative of $\mathbb{B}$ is computed as

$$\begin{aligned}\frac{d\mathbb{B}}{dt} &= \frac{d\mathbb{F}}{dt}\mathbb{F}^t + \mathbb{F}\left(\frac{d\mathbb{F}}{dt}\right)^t, \\ &= (\nabla \boldsymbol{V})\mathbb{F}\mathbb{F}^t + \mathbb{F}\mathbb{F}^t(\nabla \boldsymbol{V})^t, \\ &= (\nabla \boldsymbol{V})\mathbb{B} + \mathbb{B}(\nabla \boldsymbol{V})^t.\end{aligned} \tag{5.9}$$

This particular form of $d\mathbb{B}/dt$ is called the Oldroyd rate which is frame-indifferent [61].

5.2.2 Conservation laws

The system of conservation laws describing an elastic material is the system of Euler equations (1.1) with the Cauchy stress tensor $\mathbb{T}$ instead of the scalar pressure P. In particular, this tensor is symmetric, i.e. $\mathbb{T} = \mathbb{T}^t$ which ensures the conservation of angular momentum [61]. Denoting by ρ the solid density, $\boldsymbol{V}$ its velocity and E its total energy, the Eulerian form of this system writes as

$$\begin{aligned}&\frac{\partial \rho}{\partial t} + \nabla \cdot \big(\rho \boldsymbol{V}\big) = 0, \\ &\frac{\partial (\rho \boldsymbol{V})}{\partial t} + \nabla \cdot \big(\rho \boldsymbol{V} \otimes \boldsymbol{V} + \mathbb{T}\big) = \boldsymbol{0}, \\ &\frac{\partial (\rho E)}{\partial t} + \nabla \cdot \big((\rho E + \mathbb{T})\boldsymbol{V}\big) = 0.\end{aligned} \tag{5.10}$$

These equations respectively represent the conservation of mass, momentum and total energy. In the same way as in Chapter 1, the updated Lagrangian form of this system is written

$$\begin{aligned}&\rho \frac{d}{dt}\left(\frac{1}{\rho}\right) - \nabla \cdot \boldsymbol{V} = 0, \\ &\rho \frac{d\boldsymbol{V}}{dt} - \nabla \cdot \mathbb{T} = \boldsymbol{0}, \\ &\rho \frac{dE}{dt} - \nabla \cdot (\mathbb{T}\boldsymbol{V}) = 0,\end{aligned} \tag{5.11}$$

and the internal energy writes $\varepsilon = E - \frac{1}{2}\boldsymbol{V}^2$. Finally, the following equation is added to the system

$$\frac{d\mathbb{B}}{dt} = (\nabla \boldsymbol{V})\mathbb{B} + \mathbb{B}(\nabla \boldsymbol{V})^t. \tag{5.12}$$

In order to close the system, the thermodynamic variables and the Cauchy stress tensor have to be related. This is achieved by use of the Coleman-Noll procedure described in the next section.

5.2.3 Constitutive law modeling

The constitutive law dictates the behavior of the solid by linking the stress to the strain. Here it is proposed to define the stress $\mathbb{T}$ as a function of the deformations.

An important prerequisite is to impose the constitutive law to be *frame-indifferent* in such a way that the solid behavior is not impacted under a change of observer. This condition is also called the objectivity condition. In combination with a thermodynamic consistency criterion, the constitutive law modeling is referred to as the Coleman-Noll procedure [61].

Frame-indifference - Definitions and properties

- A change of frame is generally composed of a translation $\boldsymbol{y}$ and a rotation $\mathbb{Q}$ and transforms the coordinate $\boldsymbol{x}$ into $\boldsymbol{x}^*$ such as

$$\boldsymbol{x}^* = \boldsymbol{y} + \mathbb{Q}\boldsymbol{x}. \tag{5.13}$$

- An arbitrary vector field $\boldsymbol{\psi}$ is said to be frame-indifferent if it simply rotates with the frame-rotation $\mathbb{Q}$

$$\boldsymbol{\psi}^* = \boldsymbol{\psi}\mathbb{Q}. \tag{5.14}$$

- An arbitrary tensor field $\mathbb{M}$ is said to be frame-independent if for an arbitrary frame-rotation $\mathbb{Q}$

$$\mathbb{M}^* = \mathbb{Q}\mathbb{M}\mathbb{Q}^t. \tag{5.15}$$

- A scalar field φ is frame-invariant i.e. $\varphi^* = \varphi$.

It is easily proved that the deformation gradient $\mathbb{F}$ is not frame-indifferent. For an arbitrary change of frame (5.13), One has

$$\mathbb{F}^* = \frac{\partial \boldsymbol{x}^*}{\partial \boldsymbol{X}} = \frac{\partial \boldsymbol{y}}{\partial \boldsymbol{X}} + \mathbb{Q}\frac{\partial \boldsymbol{x}}{\partial \boldsymbol{X}} = \mathbb{Q}\mathbb{F}. \tag{5.16}$$

On the other hand, $\mathbb{B}$ is frame-indifferent since

$$\mathbb{B}^* = \mathbb{F}^*(\mathbb{F}^*)^t = \mathbb{Q}\mathbb{F}\mathbb{F}^t\mathbb{Q}^t = \mathbb{Q}\mathbb{B}\mathbb{Q}^t. \tag{5.17}$$

This is why $\mathbb{B}$ is used as a relevant measure of deformation in the constitutive law, i.e. one writes $\varepsilon = \varepsilon(\mathbb{B}, \eta)$ and $\mathbb{T} = \mathbb{T}(\mathbb{B}, \eta)$.

Thermodynamic consistency

The first step of the system closure consists in imposing the Second Law of thermodynamics which enables to express the Cauchy stress tensor as a function of the internal energy. In particular, the Clausius-Duhem inequality [61] writes

$$\rho\frac{d\varepsilon}{dt} - \rho\theta\frac{d\eta}{dt} - \mathbb{T} : \nabla \boldsymbol{V} \leq 0, \tag{5.18}$$

where $\theta > 0$ is the solid temperature and η its entropy. Recalling that a frame-indifferent expression of the internal energy is $\varepsilon = \varepsilon(\mathbb{B}, \eta)$, its material derivative writes

$$\frac{d\varepsilon}{dt} = \left(\frac{\partial \varepsilon}{\partial \mathbb{B}}\right)_{\eta} : \frac{d\mathbb{B}}{dt} + \left(\frac{\partial \varepsilon}{\partial \eta}\right)_{\mathbb{B}} \frac{d\eta}{dt}, \tag{5.19}$$

where $(\partial\varepsilon/\partial\mathbb{B})_\eta$ is a second order tensor such that $(\partial\varepsilon/\partial\mathbb{B})_{i,j} = \partial\varepsilon/\partial\mathbb{B}_{i,j}$. In particular, this tensor is symmetric since $\mathbb{B}$ is symmetric. Substituting relation (5.12) into this equality leads to

$$\frac{d\varepsilon}{dt} = \left(\frac{\partial\varepsilon}{\partial\mathbb{B}}\right)_\eta : (\nabla\boldsymbol{V})\mathbb{B} + \left(\frac{\partial\varepsilon}{\partial\mathbb{B}}\right)_\eta : \mathbb{B}(\nabla\boldsymbol{V}) + \left(\frac{\partial\varepsilon}{\partial\eta}\right)_\mathbb{B} \frac{d\eta}{dt}. \tag{5.20}$$

Using the symmetry of $\mathbb{B}$ and the formulas (D.5)-(D.6), one can simplify this relation into

$$\frac{d\varepsilon}{dt} = 2\left(\frac{\partial\varepsilon}{\partial\mathbb{B}}\right)_\eta \mathbb{B} : \nabla\boldsymbol{V} + \left(\frac{\partial\varepsilon}{\partial\eta}\right)_\mathbb{B} \frac{d\eta}{dt}. \tag{5.21}$$

Then, substituting this last relation into (5.18) leads to

$$\left[2\rho\left(\frac{\partial\varepsilon}{\partial\mathbb{B}}\right)_\eta \mathbb{B} - \mathbb{T}\right] : \nabla\boldsymbol{V} + \rho\left[\left(\frac{\partial\varepsilon}{\partial\eta}\right)_\mathbb{B} - \theta\right]\frac{d\eta}{dt} \leq 0. \tag{5.22}$$

This relation is satisfied for any deformation tensor $\mathbb{B}$ if and only if

$$\theta = \left(\frac{\partial\varepsilon}{\partial\eta}\right)_\mathbb{B}, \quad \text{and} \quad \mathbb{T} = 2\rho\left(\frac{\partial\varepsilon}{\partial\mathbb{B}}\right)_\eta \mathbb{B}. \tag{5.23}$$

In particular, one can observe that $\mathbb{T}$ depends only on $\mathbb{B}$ and that it is symmetric by symmetry of $\mathbb{B}$. This is the advantage of using the left Cauchy-Green tensor $\mathbb{B}$ instead of the right Cauchy-Green tensor $\mathbb{C}$ which is also frame-invariant and for which one finds $\mathbb{T} = 2\rho\mathbb{F}(\partial\varepsilon/\partial\mathbb{C})_\eta\mathbb{F}^t$.

Remark:
An alternative approach consists in using the free energy $\psi = \varepsilon - \theta\eta = \psi(\mathbb{B}, \theta)$ [61].

Internal energy

Let recall that the internal energy is an isotropic scalar function of the symmetric tensor $\mathbb{B}$. Using the theorem of representation of isotropic functions [61], ε is thus function of the three invariants of $\mathbb{B}$. That is to say

$$\varepsilon = \varepsilon\big(i_1(\mathbb{B}), i_2(\mathbb{B}), i_3(\mathbb{B}), \eta\big) \tag{5.24}$$

where the three invariants of a square matrix write as

$$\begin{cases} i_1(\mathbb{B}) = \mathrm{tr}(\mathbb{B}), \\ i_2(\mathbb{B}) = \dfrac{1}{2}\left(\mathrm{tr}(\mathbb{B})^2 - \mathrm{tr}(\mathbb{B}^2)\right), \\ i_3(\mathbb{B}) = \det(\mathbb{B}). \end{cases} \tag{5.25}$$

In particular, from relation (5.8) it comes $i_3(\mathbb{B}) = J^2$.

One can go further and separate the isochoric (shearing) part from the volumic part of the deformation. A deformation is isochoric if it lets the volume unchanged. As said previously, the determinant of the deformation gradient J represents the volume variation. In this way, let define the isochoric part $\bar{\mathbb{F}}$ of the deformation gradient as $\mathbb{F} = J^{\frac{1}{3}}\bar{\mathbb{F}}$ in order that $\det(\bar{\mathbb{F}}) = 1$. As a consequence, the isochoric part $\bar{\mathbb{B}}$ of $\mathbb{B}$ writes as $\mathbb{B} = J^{\frac{2}{3}}\bar{\mathbb{B}}$ such that $\det(\bar{\mathbb{B}}) = 1$.

The internal energy can now be split into a volumic, ε_v, and a shearing part, ε_s, by use of the invariants of $\bar{\mathbb{B}}$. One writes

$$\varepsilon\big(J, \bar{\mathbb{B}}, \eta\big) = \varepsilon_v\big(J, \eta\big) + \varepsilon_s\big(i_1(\bar{\mathbb{B}}), i_2(\bar{\mathbb{B}}), \eta\big), \tag{5.26}$$

where the invariants of $\bar{\mathbb{B}}$ write in function of the invariants of $\mathbb{B}$ as

$$\begin{cases} i_1(\bar{\mathbb{B}}) = J^{-\frac{2}{3}} i_1(\mathbb{B}), \\ i_2(\bar{\mathbb{B}}) = J^{-\frac{4}{3}} i_2(\mathbb{B}), \\ i_3(\bar{\mathbb{B}}) = J^{-2} i_3(\mathbb{B}) = 1. \end{cases} \tag{5.27}$$

In this way, one can write

$$\left(\frac{\partial \varepsilon}{\partial \mathbb{B}}\right)_\eta = \left(\frac{\partial \varepsilon_v}{\partial J}\right)_\eta \frac{\partial J}{\partial \mathbb{B}} + \left(\frac{\partial \varepsilon_s}{\partial i_1(\bar{\mathbb{B}})}\right)_\eta \frac{\partial i_1(\bar{\mathbb{B}})}{\partial \mathbb{B}} + \left(\frac{\partial \varepsilon_s}{\partial i_2(\bar{\mathbb{B}})}\right)_\eta \frac{\partial i_2(\bar{\mathbb{B}})}{\partial \mathbb{B}}, \tag{5.28}$$

where the derivatives of the invariants J, $i_1(\bar{\mathbb{B}})$ and $i_2(\bar{\mathbb{B}})$ with respect to $\mathbb{B}$ express as

$$\begin{aligned} \frac{\partial J}{\partial \mathbb{B}} &= \frac{1}{2} J \mathbb{B}^{-1}, \\ \frac{\partial i_1(\bar{\mathbb{B}})}{\partial \mathbb{B}} &= \bar{\mathbb{B}}_0 \mathbb{B}^{-1}, \\ \frac{\partial i_2(\bar{\mathbb{B}})}{\partial \mathbb{B}} &= -(\bar{\mathbb{B}}^{-1})_0 \mathbb{B}^{-1}. \end{aligned} \tag{5.29}$$

The proof of these formulas are detailed in Appendix C.1. The interested reader is also referred to [61, 76]. In this last relation, $\bar{\mathbb{B}}_0$ is the deviatoric part of $\bar{\mathbb{B}}$ defined as $\bar{\mathbb{B}}_0 = \bar{\mathbb{B}} - \frac{1}{3}\operatorname{tr}(\bar{\mathbb{B}})\,\mathrm{Id}$. Finally, the Cauchy stress tensor (5.23) becomes

$$\mathbb{T} = J\rho \left(\frac{\partial \varepsilon_v}{\partial J}\right)_\eta \mathrm{Id} + 2\rho \left[\left(\frac{\partial \varepsilon_s}{\partial i_1(\bar{\mathbb{B}})}\right)_\eta \bar{\mathbb{B}}_0 - \left(\frac{\partial \varepsilon_s}{\partial i_2(\bar{\mathbb{B}})}\right)_\eta (\bar{\mathbb{B}}^{-1})_0\right]. \tag{5.30}$$

Remark:
Writing the Cauchy stress tensor as $\mathbb{T} = -P\,\mathrm{Id} + \mathbb{T}_0$, where $\mathbb{T}_0$ is its deviatoric part, and knowing that $J\rho = \rho_0$ (where ρ_0 is the density in the reference configuration) enables to recover the classic hydrodynamic pressure P as

$$P = J\rho \left(\frac{\partial \varepsilon_v}{\partial J}\right)_\eta = \rho^2 \left(\frac{\partial \varepsilon_v}{\partial \rho}\right)_\eta. \tag{5.31}$$

In this study, the hyperelastic materials are represented by the compressible Neo-Hookean model [66] which defines the internal energy as

$$\begin{aligned} \varepsilon_v\big(J,\eta\big) &= \frac{\kappa}{4J\rho}\Big[(J-1)^2+\log^2(J)\Big], \\ \varepsilon_s\big(i_1(\bar{\mathbb{B}}),i_2(\bar{\mathbb{B}}),\eta\big) &= \frac{\mu}{2J\rho}\Big[i_1(\bar{\mathbb{B}})-3\Big], \end{aligned} \tag{5.32}$$

where λ and μ are the Lamé coefficients (μ is also called shear modulus) and $\kappa = \lambda + \frac{2}{3}\mu$ is the bulk modulus of the solid. In particular, this last relation (5.32) is used to compute the derivatives of ε_v and ε_s in (5.30).

5.3 Scheme construction

5.3.1 Integral form of the system

In the same way as in Chapter 1, the system (5.11) is written under its integral form to facilitate the development of a Finite Volume scheme. One writes

$$\begin{aligned} &\frac{d}{dt}\int_{\omega(t)} \mathrm{d}v - \int_{\partial\omega(t)} \boldsymbol{V}\cdot\boldsymbol{n}\,\mathrm{d}s = 0, \\ &\frac{d}{dt}\int_{\omega(t)} \rho\boldsymbol{V}\,\mathrm{d}v - \int_{\partial\omega(t)} \mathbb{T}\boldsymbol{n}\,\mathrm{d}s = \boldsymbol{0}, \\ &\frac{d}{dt}\int_{\omega(t)} \rho E\,\mathrm{d}v - \int_{\partial\omega(t)} \mathbb{T}\boldsymbol{V}\cdot\boldsymbol{n}\,\mathrm{d}s = 0, \\ &\frac{d}{dt}\int_{\omega(t)} \rho\mathbb{B}\,\mathrm{d}v = \int_{\omega(t)} \rho\left[(\nabla\boldsymbol{V})\mathbb{B}+\mathbb{B}(\nabla\boldsymbol{V})^t\right]\,\mathrm{d}v, \end{aligned} \tag{5.33}$$

where the first equation of this system is nothing but the Geometric Conservation Law (GCL). Moreover, using the Reynolds transport formula presented in Chapter 1, one recovers the mass conservation condition

$$\frac{d}{dt}\int_{\omega(t)} \rho\,\mathrm{d}v = 0. \tag{5.34}$$

Finally, the following trajectory equation is added to move the grid nodes

$$\begin{cases} \dfrac{d\boldsymbol{x}}{dt} = \boldsymbol{V}, \\ \boldsymbol{x}(t=0) = \boldsymbol{X}. \end{cases} \tag{5.35}$$

5.3.2 Spatial discretization

The system (5.33) is discretized using the Finite Volume cell-centered Lagrangian scheme proposed in Chapter 1. Let briefly recall the main steps of this discretization. The spatial domain $\omega(t)$ is paved with a set of non-overlapping polyhedrons

denoted ω_c such that $\omega(t) = \bigcup_c \omega_c$. The faces f of each cell are split into triangles t_r using their barycenter p_f^* as shown in Figure 1.1.

The GCL compatibility, stating that the volume computed geometrically is identical to the volume computed from the discretized GCL equation (5.33), is ensured by using the discrete divergence operator proposed in Section 1.3.2. In particular, the discrete divergence operator of a vector field is written

$$\mathcal{DIV}_c(\boldsymbol{V}) = \frac{1}{v_c} \sum_{p\in\mathcal{P}(c)} \sum_{f\in\mathcal{F}(c,p)} \boldsymbol{V}_p \cdot s_{pf}\boldsymbol{n}_{pf}, \tag{5.36}$$

the discrete divergence of a tensor field is written

$$\mathcal{DIV}_c(\mathbb{T}) = \frac{1}{v_c} \sum_{p\in\mathcal{P}(c)} \sum_{f\in\mathcal{F}(c,p)} s_{pf}\mathbb{T}_{cfp}\boldsymbol{n}_{pf}, \tag{5.37}$$

and, finally, the discrete gradient of a vector field is written

$$\mathcal{GRAD}_c(\boldsymbol{V}) = \frac{1}{v_c} \sum_{p\in\mathcal{P}(c)} \sum_{f\in\mathcal{F}(c,p)} s_{pf}\boldsymbol{V}_p \otimes \boldsymbol{n}_{pf}. \tag{5.38}$$

In these last relations, v_c is the cell volume, $\boldsymbol{V}_p$ is the velocity of node p and $\mathbb{T}_{cfp}$ is the Cauchy stress tensor at node p on face f relatively to cell c. Finally, the face area vectors $s_{pf}\boldsymbol{n}_{pf}$ are defined by relation (1.46). These face area vectors provide a consistent discretization of the cell boundary $\partial\omega_c$ in the sense that

$$\sum_{p\in\mathcal{P}(c)} \sum_{f\in\mathcal{F}(c,p)} s_{pf}\boldsymbol{n}_{pf} = \boldsymbol{0}. \tag{5.39}$$

5.3.3 Semi-discrete system

Defining mass averaged quantities as in Chapter 1 and using the discrete operators (5.36)-(5.37)-(5.38), the semi-discrete scheme is written

$$\begin{aligned} m_c\frac{d\boldsymbol{V}_c}{dt} &= v_c\mathcal{DIV}_c(\mathbb{T}), \\ m_c\frac{dE_c}{dt} &= v_c\mathcal{DIV}_c(\mathbb{T}\boldsymbol{V}), \\ \frac{d\mathbb{B}_c}{dt} &= \mathcal{GRAD}_c(\boldsymbol{V})\mathbb{B}_c + \mathbb{B}_c\mathcal{GRAD}_c(\boldsymbol{V})^t, \end{aligned} \tag{5.40}$$

where the mass m_c is constant in cell c and the mean left Cauchy-Green tensor is written

$$\mathbb{B}_c = \frac{1}{m_c}\int_{\omega_c} \rho\mathbb{B}\,\mathrm{d}v. \tag{5.41}$$

In particular, by definition of the discrete operators, this system can be equivalently written

$$\begin{aligned} m_c \frac{d\boldsymbol{V}_c}{dt} &= \sum_{p\in\mathcal{P}(c)} \sum_{f\in\mathcal{F}(c,p)} s_{pf} \mathbb{T}_{cfp} \boldsymbol{n}_{pf}, \\ m_c \frac{dE_c}{dt} &= \sum_{p\in\mathcal{P}(c)} \sum_{f\in\mathcal{F}(c,p)} s_{pf} \mathbb{T}_{cfp} \boldsymbol{V}_p \cdot \boldsymbol{n}_{pf}, \\ \frac{d\mathbb{B}_c}{dt} &= \frac{1}{v_c} \sum_{p\in\mathcal{P}(c)} \sum_{f\in\mathcal{F}(c,p)} s_{pf} \left[(\boldsymbol{V}_p \otimes \boldsymbol{n}_{pf}) \mathbb{B}_c + \mathbb{B}_c (\boldsymbol{V}_p \otimes \boldsymbol{n}_{pf})^t \right]. \end{aligned} \tag{5.42}$$

Moreover, the semi-discrete trajectory equation writes

$$\frac{d\boldsymbol{x}_p}{dt} = \boldsymbol{V}_p. \tag{5.43}$$

The last unknowns to be computed are thus the nodal fluxes $\mathbb{T}_{cfp}$ and $\boldsymbol{V}_p$. In the same way as in Chapter 1, a nodal solver is derived from an entropy condition and a momentum conservation condition.

5.3.4 Nodal solver

The nodal fluxes are computed by imposing two criteria: the consistency with the Second Law of thermodynamics and the global conservation of momentum.

Second Law of thermodynamics

Starting from the assumption $\varepsilon = \varepsilon(\eta, \mathbb{B})$, one can easily derive the Gibbs relation

$$\rho\theta \frac{d\eta}{dt} = \rho \frac{d\varepsilon}{dt} - \frac{1}{2} \mathbb{T}\mathbb{B}^{-1} : \frac{d\mathbb{B}}{dt}, \tag{5.44}$$

from the chain rule and the relation (5.23). After integration over the cell c, the Gibbs equation is approximated by

$$m_c \theta_c \frac{d\eta_c}{dt} = m_c \frac{d\varepsilon_c}{dt} - \frac{v_c}{2} \mathbb{T}_c \mathbb{B}_c^{-1} : \frac{d\mathbb{B}_c}{dt}. \tag{5.45}$$

By definition of the internal energy, $\varepsilon_c = E_c - \frac{1}{2}\boldsymbol{V}_c^2$, one gets from the two first equations of system (5.42)

$$m_c \frac{d\varepsilon_c}{dt} = \sum_{p\in\mathcal{P}(c)} \sum_{f\in\mathcal{F}(c,p)} s_{pf} \mathbb{T}_{cfp} \boldsymbol{n}_{pf} \cdot (\boldsymbol{V}_p - \boldsymbol{V}_c). \tag{5.46}$$

Then, from the third equation of system (5.42), it comes straightforwardly

$$v_c \mathbb{T}_c \mathbb{B}_c^{-1} : \frac{d\mathbb{B}_c}{dt} = \sum_{p\in\mathcal{P}(c)} \sum_{f\in\mathcal{F}(c,p)} s_{pf} \mathbb{T}_c \mathbb{B}_c^{-1} : \left[(\boldsymbol{V}_p \otimes \boldsymbol{n}_{pf}) \mathbb{B}_c + \mathbb{B}_c (\boldsymbol{V}_p \otimes \boldsymbol{n}_{pf})^t \right], \tag{5.47}$$

which can be simplified into

$$v_c \mathbb{T}_c \mathbb{B}_c^{-1} : \frac{d\mathbb{B}_c}{dt} = 2 \sum_{p \in \mathcal{P}(c)} \sum_{f \in \mathcal{F}(c,p)} s_{pf} \mathbb{T}_c \boldsymbol{n}_{pf} \cdot \boldsymbol{V}_p, \tag{5.48}$$

by use of relation (D.6) and the symmetry of $\mathbb{B}_c$ and $\mathbb{T}_c$. Finally, the Gibbs relation can be written as

$$m_c \theta_c \frac{d\eta_c}{dt} = \sum_{p \in \mathcal{P}(c)} \sum_{f \in \mathcal{F}(c,p)} s_{pf} (\mathbb{T}_{cfp} - \mathbb{T}_c) \boldsymbol{n}_{pf} \cdot (\boldsymbol{V}_p - \boldsymbol{V}_c). \tag{5.49}$$

The Second Law of thermodynamics imposes the entropy variation to be positive. A sufficient condition to respect this criterion at the semi-discrete level is to choose the nodal fluxes in such a way that the right-hand side term in (5.49) sums only positive terms. This is easily achieved by defining the nodal flux $\mathbb{T}_{cfp}$ as

$$\mathbb{T}_{cfp} = \mathbb{T}_c + [\mathbb{Q}_{cfp}(\boldsymbol{V}_p - \boldsymbol{V}_c)] \otimes \boldsymbol{n}_{pf}, \tag{5.50}$$

where $\mathbb{Q}_{cfp}$ is a definite positive tensor. In this way, using the formula (D.8), one has

$$(\mathbb{T}_{cfp} - \mathbb{T}_c) \boldsymbol{n}_{pf} = \mathbb{Q}_{cfp}(\boldsymbol{V}_p - \boldsymbol{V}_c), \tag{5.51}$$

and

$$m_c \theta_c \frac{d\eta_c}{dt} = \sum_{p \in \mathcal{P}(c)} \sum_{f \in \mathcal{F}(c,p)} s_{pf} \mathbb{Q}_{cfp}(\boldsymbol{V}_p - \boldsymbol{V}_c) \cdot (\boldsymbol{V}_p - \boldsymbol{V}_c) \geq 0, \tag{5.52}$$

since $\mathbb{Q}_{cfp}$ is definite positive. In this study, $\mathbb{Q}_{cfp}$ is defined as the square root of the acoustic tensor [96]. It writes as

$$\mathbb{Q}_{cfp} = \rho_c \left[a_c^L (\boldsymbol{n}_{pf} \otimes \boldsymbol{n}_{pf}) + a_c^T (\mathrm{Id} - \boldsymbol{n}_{pf} \otimes \boldsymbol{n}_{pf}) \right], \tag{5.53}$$

where a_c^L and a_c^T are the velocities of the longitudinal and transverse waves such as

$$a_c^L = \sqrt{\frac{\kappa_c + \frac{4}{3}\mu_c}{\rho_c}}, \quad \text{and} \quad a_c^T = \sqrt{\frac{\mu_c}{\rho_c}}. \tag{5.54}$$

This definition of the matrix $\mathbb{Q}_{cfp}$ can also be found in [76, 77]. In particular, the acoustic tensor can be found by performing a progressive wave study of the Euler system (5.10) (refer to Appendix C.2).

Momentum conservation and nodal velocity

The last step of the nodal solver consists in imposing a momentum balance condition around each node (refer to Chapter 1). Balancing all the forces acting around a node writes as

$$\sum_{c \in \mathcal{C}(p)} \sum_{f \in \mathcal{F}(c,p)} s_{pf} \mathbb{T}_{cfp} \boldsymbol{n}_{pf} = \boldsymbol{0}. \tag{5.55}$$

Then, substituting the relation (5.50) in this last relation leads to

$$\sum_{c\in\mathcal{C}(p)}\sum_{f\in\mathcal{F}(c,p)} s_{pf}\left[\mathbb{T}_c\boldsymbol{n}_{pf}+\mathbb{Q}_{cfp}(\boldsymbol{V}_p-\boldsymbol{V}_c)\right]=\boldsymbol{0}. \tag{5.56}$$

One can then compute the nodal velocity as

$$\boldsymbol{V}_p=\mathbb{M}_p^{-1}\boldsymbol{B}_p, \tag{5.57}$$

where

$$\begin{aligned}\mathbb{M}_p&=\sum_{c\in\mathcal{C}(p)}\sum_{f\in\mathcal{F}(c,p)} s_{pf}\mathbb{Q}_{cfp},\\ \boldsymbol{B}_p&=\sum_{c\in\mathcal{C}(p)}\sum_{f\in\mathcal{F}(c,p)} s_{pf}\left[\mathbb{Q}_{cfp}\boldsymbol{V}_c-\mathbb{T}_c\boldsymbol{n}_{pf}\right].\end{aligned} \tag{5.58}$$

In particular, $\mathbb{M}_p^{-1}$ always exists since the $\mathbb{Q}_{cfp}$ are symmetric definite positive matrices thus the nodal velocity is always computable. Finally, $\mathbb{T}_{cfp}$ is computed from $\boldsymbol{V}_p$ and relation (5.50).

5.3.5 Time step monitoring

The first-order time discretization and the time step monitoring of the hyperelasticity system is very similar to the work done in Chapter 1 and the reader is referred to the Section (refer to Section 1.5). In particular, the first-order time discretization is performed using a classic Explicit Euler integration and the time step is computed from the relation

$$\Delta t^n=\min(C_v\Delta t_v,\quad C_e\Delta t_{CFL},\quad C_m\Delta t^{n-1}). \tag{5.59}$$

In this last relation, one recovers $C_v\Delta t_v$ as the criterion controlling the volume variation with $C_v=0.1$ and $C_m\Delta t^{n-1}$ as the criterion controlling the growth of the time step with $C_m=1.1$. The only difference comes in the CFL criterion $C_e\Delta t_{CFL}$. Indeed, for the hyperelasticity system, two type of waves appear at the interface between two cells: the longitudinal and transverse waves. The CFL criterion is then adapted as

$$\Delta t_{CFL}=\min_c\left\{\frac{\mathcal{L}_c}{a_c^L+a_c^T}\right\}, \tag{5.60}$$

where C_e is the CFL number chosen as $C_e=0.4$ in practice, $\mathcal{L}_c$ is the minimum edge length in cell c and a_c^L and a_c^T are the bulk and shear speed of sound introduced in relation (5.54).

At this point, all the ingredients are present to solve the hyperelasticity system at first order. The complete algorithm is detailed below in the case where an Explicit Euler time discretization is used. The next sections investigate the second order extension in space and time of this cell-centered Lagrangian scheme.

First order algorithm:

- The complete state $\mathcal{U}^n$ is known.
- Computation of the nodal fluxes $\boldsymbol{V}_p^n$ and $\mathbb{T}_{cfp}^n$ from relations (5.57) and (5.50) respectively.
- Computation of the time step Δt from relation (5.60).
- Mesh update from the trajectory equation (5.73).
- Computation of the new velocity $\boldsymbol{V}_c^{n+1}$ and total energy E_c^{n+1} in the cells from

$$\begin{aligned} \boldsymbol{V}_c^{n+1} &= \boldsymbol{V}_c^n + \frac{\Delta t}{m_c} \sum_{p\in\mathcal{P}(c)} \sum_{f\in\mathcal{F}(c,p)} s_{pf}^n \mathbb{T}_{cfp}^n \boldsymbol{n}_{pf}^n, \\ E_c^{n+1} &= E_c^n + \frac{\Delta t}{m_c} \sum_{p\in\mathcal{P}(c)} \sum_{f\in\mathcal{F}(c,p)} s_{pf}^n \mathbb{T}_{cfp}^n \boldsymbol{V}_p^n \cdot \boldsymbol{n}_{pf}^n. \end{aligned} \tag{5.61}$$

- Computation of the new left Cauchy-Green tensor

$$\mathbb{B}_c^{n+1} = \mathbb{B}_c^n - \frac{\Delta t}{v_c^n} \sum_{p\in\mathcal{P}(c)} \sum_{f\in\mathcal{F}(c,p)} s_{pf}^n \left[(\boldsymbol{V}_p^n \otimes \boldsymbol{n}_{pf}^n)\mathbb{B}_c^n + \mathbb{B}_c^n (\boldsymbol{V}_p^n \otimes \boldsymbol{n}_{pf}^n)^t \right]. \tag{5.62}$$

- Determination of the complete final state $\mathcal{U}^{n+1}$:

$$\begin{aligned} &\rho_c^{n+1} = m_c / v_c^{n+1}, \\ &\varepsilon_c^{n+1} = E_c^{n+1} - \frac{1}{2} \left(\boldsymbol{V}_c^{n+1} \right)^2, \\ &T_c^{n+1} \quad \text{from (5.30)}, \\ &(a_c^L)^{n+1} \quad \text{and} \quad (a_c^T)^{n+1} \quad \text{from (5.54)}. \end{aligned} \tag{5.63}$$

5.4 Second order extension

For the second order extension in space of the scheme presented so far, it is proposed to perform a MUSCL procedure as done in Chapter 2 for hydrodynamics.

5.4.1 Linear reconstruction

The velocity and stress field are linearly reconstructed in order to improve the accuracy of the Riemann problem (5.50). These reconstructions write

$$\begin{aligned} \widetilde{\mathbb{T}}_c(\boldsymbol{x}) &= \mathbb{T}_c + \nabla \mathbb{T}_c (\boldsymbol{x} - \boldsymbol{x}_c), \\ \widetilde{\boldsymbol{V}}_c(\boldsymbol{x}) &= \boldsymbol{V}_c + \nabla \boldsymbol{V}_c (\boldsymbol{x} - \boldsymbol{x}_c). \end{aligned} \tag{5.64}$$

In particular, the gradient of stress is a third order tensor. These gradients are approximated by using the discrete operator introduced previously. In particular,

in the case of the velocity field, the gradient writes as

$$\nabla \boldsymbol{V}_c \simeq \mathcal{GRAD}_c(\boldsymbol{V}) = \frac{1}{v_c} \sum_{p \in \mathcal{P}(c)} \sum_{f \in \mathcal{F}(c,p)} s_{pf} \boldsymbol{V}_p \otimes \boldsymbol{n}_{pf}. \tag{5.65}$$

In the case of the Cauchy stress tensor, the gradient is expressed as

$$\nabla \mathbb{T}_c \simeq \mathcal{GRAD}_c(\mathbb{T}) = \frac{1}{v_c} \sum_{p \in \mathcal{P}(c)} \sum_{f \in \mathcal{F}(c,p)} s_{pf} \mathbb{T}_{cfp} \otimes \boldsymbol{n}_{pf}, \tag{5.66}$$

where the tensorial product between a vector and a second order tensor is recalled in formula (D.7).

5.4.2 The SP-limiter extended to tensors

In the same way as in Chapter 2, the linearly reconstructed velocity field (5.64) is limited using the SP-limiter in order to avoid spurious oscillations. Concerning the reconstructed tensor field, a classic MUSCL procedure based on the Barth-Jespersen limiter is used. In order to respect the symmetries of the tensor field, a single limiting scalar $\alpha_{\mathbb{T}}$ is applied to the gradient $\nabla \mathbb{T}$ such that

$$\widetilde{\mathbb{T}}_c(\boldsymbol{x})^{lim} = \mathbb{T}_c + \alpha_{\mathbb{T}} \nabla \mathbb{T}_c (\boldsymbol{x} - \boldsymbol{x}_c). \tag{5.67}$$

This scalar is computed as the minimal scalar resulting from the component-wise limiting of the tensor field. Let mention that it is also possible to decompose the stress field as $\mathbb{T} = -P\,\mathrm{Id} + \mathbb{D}$ and to limit the pressure and shearing contribution separately. This is done for example in [110]. In this study, the scalar $\alpha_{\mathbb{T}}$ it is computed as

$$\alpha_{\mathbb{T}} = \min_{i,j}(\alpha_{\mathbb{T},i,j}), \tag{5.68}$$

where

$$\alpha_{\mathbb{T},i,j} = \min_{p}(\alpha_{\mathbb{T},i,j,p}). \tag{5.69}$$

The final value $\alpha_{\mathbb{T},i,j,p}$ is then obtained by using the Barth-Jespersen limiter (2.22) on the $(i,j)^{th}$ component of the Cauchy stress tensor as

$$\alpha_{\mathbb{T},i,j,p} = \begin{cases} \min\left(\dfrac{(\mathbb{T}_c)_{i,j}^{max} - (\mathbb{T}_c)_{i,j}}{(\widetilde{\mathbb{T}}_c(\boldsymbol{x}_p))_{i,j} - (\mathbb{T}_c)_{i,j}},\ 1 \right) & \text{if } (\widetilde{\mathbb{T}}_c(\boldsymbol{x}_p))_{i,j} > (\mathbb{T}_c)_{i,j}, \\ \min\left(\dfrac{(\mathbb{T}_c)_{i,j}^{min} - (\mathbb{T}_c)_{i,j}}{(\widetilde{\mathbb{T}}_c(\boldsymbol{x}_p))_{i,j} - (\mathbb{T}_c)_{i,j}},\ 1 \right) & \text{if } (\widetilde{\mathbb{T}}_c(\boldsymbol{x}_p))_{i,j} < (\mathbb{T}_c)_{i,j}, \\ 1 & \text{if } (\widetilde{\mathbb{T}}_c(\boldsymbol{x}_p))_{i,j} = (\mathbb{T}_c)_{i,j}. \end{cases} \tag{5.70}$$

In this last relation, the values $(\mathbb{T}_c)_{i,j}^{min}$ and $(\mathbb{T}_c)_{i,j}^{max}$ are respectively the minimum and maximum values of the $(i,j)^{th}$ component of the Cauchy stress tensor defined

as

$$
\begin{aligned}
(\mathbb{T}_c)_{i,j}^{min} &= \min\left(\min_{c'\in\mathcal{C}_p(c)}((\mathbb{T}_{c'})_{i,j}), (\mathbb{T}_c)_{i,j}\right), \\
(\mathbb{T}_c)_{i,j}^{max} &= \max\left(\max_{c'\in\mathcal{C}_p(c)}((\mathbb{T}_{c'})_{i,j}), (\mathbb{T}_c)_{i,j}\right),
\end{aligned}
\tag{5.71}
$$

where $\mathcal{C}_p(c)$ is the node-based stencil introduced in Figure 2.1.

Remark:
This limiting procedure is the straightforward extension of the SP-limiter to the case of a tensor field. As a future work, more sophisticated procedure could be investigated.

5.4.3 Second order GRP extension

The second order in time discretization is performed using the Generalized Riemann Problem (GRP) proposed in Chapter 2. Let start from the second-order semi-discrete hyperelasticity system

$$
\begin{aligned}
\frac{d\boldsymbol{x}_p}{dt} &= \boldsymbol{V}_p, \\
m_c\frac{d\boldsymbol{V}_c}{dt} &= \sum_{p\in\mathcal{P}(c)}\sum_{f\in\mathcal{F}(c,p)}\mathbb{T}_{cfp}s_{pf}\boldsymbol{n}_{pf}, \\
m_c\frac{dE_c}{dt} &= \sum_{p\in\mathcal{P}(c)}\sum_{f\in\mathcal{F}(c,p)}\mathbb{T}_{cfp}\boldsymbol{V}_p\cdot s_{pf}\boldsymbol{n}_{pf}.
\end{aligned}
\tag{5.72}
$$

Replacing the double sums by $\sum_p\sum_f$ and performing the same steps as in Chapter 2, one gets

$$
\boldsymbol{x}_p^{n+1} = \boldsymbol{x}_p^n + \Delta t\left[\boldsymbol{V}_p^n + \frac{\Delta t}{2}\left(\frac{d\boldsymbol{V}_p}{dt}\right)^n\right], \tag{5.73}
$$

for the discrete trajectory equation,

$$
\boldsymbol{V}_c^{n+1} = \boldsymbol{V}_c^n + \frac{\Delta t}{m_c}\sum_p\sum_f\left[\mathbb{T}_{cfp}s_{pf}^n\boldsymbol{n}_{pf}^n + \frac{\Delta t}{2}\frac{d}{dt}\left(\mathbb{T}_{cfp}s_{pf}\boldsymbol{n}_{pf}\right)^n\right], \tag{5.74}
$$

for the discrete momentum conservation equation, and

$$
E_c^{n+1} = E_c^n + \frac{\Delta t}{m_c}\sum_p\sum_f\left[\mathbb{T}_{cfp}\boldsymbol{V}_p^n\cdot s_{pf}^n\boldsymbol{n}_{pf}^n + \frac{\Delta t}{2}\frac{d}{dt}\left(\mathbb{T}_{cfp}\boldsymbol{V}_p\cdot s_{pf}\boldsymbol{n}_{pf}\right)^n\right], \tag{5.75}
$$

for the discrete total energy conservation equation. In these equations $\mathbb{T}_{cfp}$ is the second order in space approximation of the nodal stress tensor computed as

$$
\mathbb{T}_{cfp} = \widetilde{\mathbb{T}}_c(\boldsymbol{x}_p^n) + \left[\mathbb{Q}_{cfp}\left(\boldsymbol{V}_p - \widetilde{\boldsymbol{V}}_c(\boldsymbol{x}_p^n)\right)\right]\otimes\boldsymbol{n}_{pf}, \tag{5.76}
$$

and $\boldsymbol{V}_p$ is the corresponding second order in space node velocity computed from (5.57). Using the chain rule, the time derivatives in the right hand-side terms of relations (5.74) and (5.75) can be developed into

$$\frac{d}{dt}\left(\mathbb{T}_{cfp}s_{pf}\boldsymbol{n}_{pf}\right)^n = \mathbb{T}_{cfp}\frac{d}{dt}\left(s_{pf}\boldsymbol{n}_{pf}\right)^n + \left(\frac{d\mathbb{T}_{cfp}}{dt}\right)^n s_{pf}^n\boldsymbol{n}_{pf}^n, \tag{5.77}$$

and

$$\begin{aligned}\frac{d}{dt}\left(\mathbb{T}_{cfp}\boldsymbol{V}_p\cdot s_{pf}\boldsymbol{n}_{pf}\right)^n = \;& \mathbb{T}_{cfp}\boldsymbol{V}_p^n\cdot\frac{d}{dt}\left(s_{pf}\boldsymbol{n}_{pf}\right)^n \\ + \;& \left[\left(\frac{d\mathbb{T}_{cfp}}{dt}\right)^n\boldsymbol{V}_p^n + \mathbb{T}_{cfp}\left(\frac{d\boldsymbol{V}_p}{dt}\right)^n\right]\cdot s_{pf}^n\boldsymbol{n}_{pf}^n.\end{aligned} \tag{5.78}$$

These expressions introduce the time derivative of the face area vectors $s_{pf}^n\boldsymbol{n}_{pf}^n$ which is computed from relation (2.68). They also introduce the time derivatives of the nodal fluxes $\mathbb{T}_{cfp}$ and $\boldsymbol{V}_p$ which require to be dealt with.

Time derivative of the nodal fluxes

The time derivative of the stress flux is obtained by time differentiating the relation (5.76). One gets

$$\begin{aligned}\left(\frac{d\mathbb{T}_{cfp}}{dt}\right)^n = \;& \left(\frac{d\widetilde{\mathbb{T}}_c(\boldsymbol{x}_p)}{dt}\right)^n + \left[\frac{\mathbb{Q}_{cfp}^n}{s_{pf}^n}\left(\left(\frac{d\boldsymbol{V}_p}{dt}\right)^n - \left(\frac{d\widetilde{\boldsymbol{V}}_c(\boldsymbol{x}_p)}{dt}\right)^n\right)\right]\otimes s_{pf}^n\boldsymbol{n}_{pf}^n \\ + \;& \left[\frac{\mathbb{Q}_{cfp}^n}{s_{pf}^n}\left(\boldsymbol{V}_p^n - \widetilde{\boldsymbol{V}}_c(\boldsymbol{x}_p^n)\right)\right]\otimes\frac{d}{dt}\left(s_{pf}\boldsymbol{n}_{pf}\right)^n.\end{aligned} \tag{5.79}$$

In the same way as in Chapter 2, one can prove that it is required to balance the time derivatives of the stress fluxes around each node to globally conserve the momentum. This condition writes as

$$\sum_{c\in\mathcal{C}(p)}\sum_{f\in\mathcal{F}(c,p)}\left[\left(\frac{d\mathbb{T}_{cfp}}{dt}\right)^n s_{pf}^n\boldsymbol{n}_{pf}^n + \mathbb{T}_{cfp}\frac{d}{dt}\left(s_{pf}\boldsymbol{n}_{pf}\right)^n\right] = \boldsymbol{0}. \tag{5.80}$$

Let replace the double sum $\sum_{c\in\mathcal{C}(p)}\sum_{f\in\mathcal{F}(c,p)}$ by $\sum_c\sum_f$ to simplify the notation. Substituting relation (5.79) into (5.80), the time derivative of the node velocity can be written as

$$\begin{aligned}\mathbb{M}_p\left(\frac{d\boldsymbol{V}_p}{dt}\right)^n = \;& -\sum_c\sum_f\left(\frac{d\widetilde{\mathbb{T}}_c(\boldsymbol{x}_p)}{dt}\right)^n s_{pf}^n\boldsymbol{n}_{pf}^n \\ & + \sum_c\sum_f\left(\left[\frac{\mathbb{Q}_{cfp}^n}{s_{pf}^n}\left(\frac{d\widetilde{\boldsymbol{V}}_c(\boldsymbol{x}_p)}{dt}\right)^n\right]\otimes s_{pf}^n\boldsymbol{n}_{pf}^n\right)s_{pf}^n\boldsymbol{n}_{pf}^n \\ & - \sum_c\sum_f\left(\left[\frac{\mathbb{Q}_{cfp}^n}{s_{pf}^n}\left(\boldsymbol{V}_p^n - \widetilde{\boldsymbol{V}}_c(\boldsymbol{x}_p^n)\right)\right]\otimes\frac{d}{dt}\left(s_{pf}\boldsymbol{n}_{pf}\right)^n\right)s_{pf}^n\boldsymbol{n}_{pf}^n \\ & - \sum_c\sum_f\mathbb{T}_{cfp}\frac{d}{dt}\left(s_{pf}\boldsymbol{n}_{pf}\right)^n,\end{aligned} \tag{5.81}$$

where

$$\mathbb{M}_p = \sum_c \sum_f s_{pf} \mathbb{Q}_{cfp}. \tag{5.82}$$

Finally, one has to compute the time derivatives of the cell Cauchy stress tensor $\widetilde{\mathbb{T}}_c(\boldsymbol{x}_p)$ and velocity $\widetilde{\boldsymbol{V}}_c(\boldsymbol{x}_p^n)$.

Time derivatives of the cell stress and cell velocity

Starting from the linear reconstructions (5.64) the time derivatives of the cell stress and velocity write as

$$\begin{aligned} \left(\frac{d\widetilde{\mathbb{T}}_c(\boldsymbol{x}_p)}{dt}\right)^n &= \left(\frac{d\mathbb{T}_c}{dt}\right)^n, \\ \left(\frac{d\widetilde{\boldsymbol{V}}_c(\boldsymbol{x}_p)}{dt}\right)^n &= \left(\frac{d\boldsymbol{V}_c}{dt}\right)^n. \end{aligned} \tag{5.83}$$

Then, from the momentum conservation equation, the time derivative of the cell velocity comes straightforwardly as

$$\left(\frac{d\boldsymbol{V}_c}{dt}\right)^n = \frac{1}{\rho^n} \mathcal{DIV}_c(\mathbb{T})^n. \tag{5.84}$$

In particular, the divergence of the Cauchy stress tensor can be computed from its gradient and the formula (D.12) or from relation (5.37). To compute the time derivative of the Cauchy stress tensor, let start from the constitutive law (5.30) recalled here

$$\mathbb{T}_c = J\rho \left(\frac{\partial \varepsilon_v}{\partial J}\right)_\eta \mathrm{Id} + 2\rho \left[\left(\frac{\partial \varepsilon_s}{\partial i_1(\bar{\mathbb{B}})}\right)_\eta \bar{\mathbb{B}}_0 - \left(\frac{\partial \varepsilon_s}{\partial i_2(\bar{\mathbb{B}})}\right)_\eta (\bar{\mathbb{B}}^{-1})_0\right]. \tag{5.85}$$

In the case of a Neo-Hookean solid, one has

$$\begin{aligned} \left(\frac{\partial \varepsilon_v}{\partial J}\right)_\eta &= \frac{\kappa}{2\rho J}\left[J - 1 + \frac{\log J}{J}\right], \\ \left(\frac{\partial \varepsilon_s}{\partial i_1(\bar{\mathbb{B}})}\right)_\eta &= \frac{\mu}{2\rho J}, \\ \left(\frac{\partial \varepsilon_s}{\partial i_2(\bar{\mathbb{B}})}\right)_\eta &= 0. \end{aligned} \tag{5.86}$$

One can remark that in fact $\mathbb{T}_c = \mathbb{T}(\mathbb{B}_c)$ since $\varepsilon_c = \varepsilon(\mathbb{B}_c)$ and $J = \sqrt{\det(\mathbb{B})}$. In this way, the time derivative of the Cauchy stress tensor can be computed as

$$\left(\frac{d\mathbb{T}_c}{dt}\right)^n = \left(\frac{\partial \mathbb{T}_c}{\partial \mathbb{B}}\right)^n \left(\frac{d\mathbb{B}_c}{dt}\right)^n, \tag{5.87}$$

where $(d\mathbb{B}_c/dt)^n$ is computed from relation (5.42). The fourth-order order tensor $(\partial\mathbb{T}_c/\partial\mathbb{B})^n$ requires some more steps. First, using the relations (5.86), the tensor $\mathbb{T}_c$ can be rewritten as

$$\mathbb{T}_c = \frac{\kappa}{2}\left[J - 1 + \frac{\log J}{J}\right]\mathrm{Id} + \mu J^{-\frac{5}{3}}\mathbb{B}_0. \tag{5.88}$$

Then, differentiating with respect to $\mathbb{B}$ leads to

$$\frac{\partial\mathbb{T}}{\partial\mathbb{B}} = \frac{\kappa}{2}\left[\left(\frac{\partial J}{\partial\mathbb{B}}\right) + \frac{\partial}{\partial\mathbb{B}}\left(\frac{\log J}{J}\right)\right]\otimes\mathrm{Id} + \mu\left(\frac{\partial J^{-\frac{5}{3}}}{\partial\mathbb{B}}\right)\otimes\mathbb{B}_0 + \mu J^{-\frac{5}{3}}\left(\frac{\partial\mathbb{B}_0}{\partial\mathbb{B}}\right). \tag{5.89}$$

Using now the relation (5.29) and the chain rule, one gets

$$\begin{aligned}
\left(\frac{\partial J}{\partial\mathbb{B}}\right) &= \frac{1}{2}J\mathbb{B}^{-1}, \\
\frac{\partial}{\partial\mathbb{B}}\left(\frac{\log J}{J}\right) &= \frac{(1-\log J)\mathbb{B}^{-1}}{2J}, \\
\left(\frac{\partial J^{-\frac{5}{3}}}{\partial\mathbb{B}}\right) &= -\frac{5}{6}J^{-\frac{5}{3}}\mathbb{B}^{-1}.
\end{aligned} \tag{5.90}$$

Finally, by definition of $\mathbb{B}_0$ it comes [61]

$$\left(\frac{\partial\mathbb{B}_0}{\partial\mathbb{B}}\right) = \frac{2}{3}\mathbb{I}, \tag{5.91}$$

where $\mathbb{I}$ is the fourth order identity tensor. Gathering all these terms into (5.89) leads finally to

$$\left(\frac{\partial\mathbb{T}_c}{\partial\mathbb{B}}\right)^n = \frac{\kappa}{4J}\left[1 + J^2 - \log J\right]\mathbb{B}^{-1}\otimes\mathrm{Id} + \mu J^{-\frac{5}{3}}\left[\frac{2}{3}\mathbb{I} - \frac{5}{6}\mathbb{B}^{-1}\otimes\mathbb{B}_0\right]. \tag{5.92}$$

Manipulating fourth order tensors is not convenient, by use of the relation (D.11), one can write the more simple form

$$\begin{aligned}
\left(\frac{\partial\mathbb{T}_c}{dt}\right)^n = &\quad \frac{\kappa}{4J}\left[1 + J^2 - \log J\right]\mathrm{tr}\left(\frac{d\mathbb{B}}{dt}\right)^n\mathbb{B}^{-1} \\
&+ \frac{2\mu}{3}J^{-\frac{5}{3}}\left(\frac{d\mathbb{B}}{dt}\right)^n \\
&- \frac{5\mu}{6}J^{-\frac{5}{3}}\,\mathrm{tr}\left(\mathbb{B}_0^t\left(\frac{d\mathbb{B}}{dt}\right)^n\right)\mathbb{B}^{-1}.
\end{aligned} \tag{5.93}$$

Now that $d\mathbb{T}_c/dt$ and $d\boldsymbol{V}_c/dt$ are known, one can compute relation (5.79). Finally, using then relation (5.81), it is possible to compute (5.74) and (5.75).

Time integration of the left Cauchy-Green tensor

Finally, let investigate the time integration of relation (5.12) recalled as

$$\frac{d\mathbb{B}_c}{dt} = \frac{1}{v_c}\sum_p\sum_f s_{pf}\left[(\boldsymbol{V}_p\otimes\boldsymbol{n}_{pf})\mathbb{B}_c + \mathbb{B}_c(\boldsymbol{V}_p\otimes\boldsymbol{n}_{pf})^t\right]. \tag{5.94}$$

The GRP procedure leads to

$$\begin{aligned}\mathbb{B}_c^{n+1} - \mathbb{B}_c^n &= \frac{\Delta t}{v_c}\sum_p\sum_f s_{pf}^n\left[(\boldsymbol{V}_p^n\otimes\boldsymbol{n}_{pf}^n)\mathbb{B}_c^n + \mathbb{B}_c^n(\boldsymbol{V}_p^n\otimes\boldsymbol{n}_{pf}^n)^t\right]\\ &+ \frac{\Delta t^2}{2v_c}\sum_p\sum_f\frac{d}{dt}\left(\left[\boldsymbol{V}_p^n\otimes(s_{pf}^n\boldsymbol{n}_{pf}^n)\right]\mathbb{B}_c^n + \mathbb{B}_c^n\left[\boldsymbol{V}_p^n\otimes(s_{pf}^n\boldsymbol{n}_{pf}^n)\right]^t\right)^n.\end{aligned} \tag{5.95}$$

Using the chain rule, the time derivative of the flux can be developed as

$$\begin{aligned}&\frac{d}{dt}\left(\left[\boldsymbol{V}_p^n\otimes(s_{pf}^n\boldsymbol{n}_{pf}^n)\right]\mathbb{B}_c^n + \mathbb{B}_c^n\left[\boldsymbol{V}_p^n\otimes(s_{pf}^n\boldsymbol{n}_{pf}^n)\right]^t\right)^n =\\ &\qquad\left[\boldsymbol{V}_p^n\otimes(s_{pf}^n\boldsymbol{n}_{pf}^n)\right]\frac{d\mathbb{B}_c^n}{dt} + \frac{d\mathbb{B}_c^n}{dt}\left[\boldsymbol{V}_p^n\otimes(s_{pf}^n\boldsymbol{n}_{pf}^n)\right]^t\\ &\qquad+\left(\left[\frac{d\boldsymbol{V}_p^n}{dt}\otimes(s_{pf}^n\boldsymbol{n}_{pf}^n)\right] + \left[\boldsymbol{V}_p^n\otimes\frac{ds_{pf}^n\boldsymbol{n}_{pf}^n}{dt}\right]\right)\mathbb{B}_c^n\\ &\qquad+\mathbb{B}_c^n\left(\left[\frac{d\boldsymbol{V}_p^n}{dt}\otimes(s_{pf}^n\boldsymbol{n}_{pf}^n)\right]^t + \left[\boldsymbol{V}_p^n\otimes\frac{ds_{pf}^n\boldsymbol{n}_{pf}^n}{dt}\right]^t\right)\end{aligned} \tag{5.96}$$

where $d\mathbb{B}_c^n/dt$ is evaluated thanks to relation (5.12). In this way, all the unknown can be computed and the GRP procedure is complete.

Second order GRP algorithm:

- The complete state $\mathcal{U}^n$ is known.
- Spatial reconstruction using the SP-limiter:
  - Computation of the cell gradients using the discrete operators (5.65)-(5.66),
  - Gradients limiting using the SP-limiter extended to tensors introduced in Section 5.4.2.
- Second order in time nodal solver:
  - determination of the second order fluxes: $\boldsymbol{V}_p^n$ and $\widetilde{\mathbb{T}}_{cfp}(\boldsymbol{x}_p^n)$ from (5.57)-(5.50) and the linearly reconstructed fields $\widetilde{\mathbb{T}}_c$ and $\widetilde{\boldsymbol{V}}_c$,
  - determination of $\mathbb{B}_c^n$ and $d\mathbb{B}_c^n/dt$ at second order using (5.12),
  - determination of the cell derivatives $\left(d\widetilde{\mathbb{T}}_c(\boldsymbol{x}_p)/dt\right)^n$ and $\left(d\widetilde{\boldsymbol{V}}_c(\boldsymbol{x}_p)/dt\right)^n$ from (5.83),
  - determination of the geometry derivative $(ds_{pf}\boldsymbol{n}_{pf}/dt)^n$ from (2.68),

- determination of the nodal velocity derivative $(d\boldsymbol{V}_p/dt)^n$ from (5.81),
- determination of the nodal pressure derivative $(dP_{cfp}/dt)^n$ from (5.79).

◦ Computation of the time step Δt from relation (5.60).

◦ Mesh update from the trajectory equation (5.73).

◦ Computation of the new velocity $\boldsymbol{V}_c^{n+1}$ (5.74) and total energy E_c^{n+1} (5.75) in the cells.

◦ Determination of the complete final state $\mathcal{U}^{n+1}$ from the relations in (5.63).

5.5 Validation on test cases

The robustness of the proposed scheme is assessed against three numerical test cases. The hyperelastic model is known to degenerate onto the linear elastic model in the case of infinitesimal displacements. This property is verified with the two first test cases, namely the 1D pile driving and the Blake problem. Moreover, the good behavior of the scheme is tested on elastic problems with large deformations, namely the Elastic vibration of a Beryllium plate and the twisting column.

5.5.1 1D pile driving

This test case is taken from [80] and simulates the propagation of a shock wave in a 1D steel pile. The pile geometry is parallelepipedic of length $L = 10$ m and unit square cross section: $(x, y, z) \in [0; 10] \times [-0.5; 0.5] \times [-0.5; 0.5]$. The face $x = 0$ is embedded in a wall modeled by a zero-velocity boundary condition. The shock is initialized by a stress boundary condition $\mathbb{T}^b$ applied at $x = L$ and such that $\mathbb{T}^b = \mathbb{T}^b_{x,x} = -5 \times 10^7$ Pa. All the other faces of the pile are free-surface boundary conditions such that $\mathbb{T}^b\boldsymbol{n} = \boldsymbol{0}$. The Young's modulus of the solid is $E = 200 \times 10^9$ Pa, its Poisson's ratio $\nu = 0$ and its initial density $\rho^0 = 8000$ kg.m^{-3}. The stress at the wall is plotted with respect to time until final time $t_f = 8 \times 10^{-3}$ s. As explained in [80], the shock reaches the wall at time $t = 2 \times 10^{-3}$ s where its strength is doubled up to $\mathbb{T}^{max}_{x,x} = -1 \times 10^8$ Pa.

Figure 5.2 shows the stress $\mathbb{T}_{x,x}$ at the wall provided by the second order scheme on $(100 \times 4 \times 4)$, $(200 \times 4 \times 4)$ and $(400 \times 4 \times 4)$ cells meshes. These solutions are compared to the first order solution on a $(100 \times 4 \times 4)$ cells mesh and to the analytic solution. In particular, a good accordance is observed between the analytic solution and the numerical approximations for both shock timing and shock strength. One can observe the natural diffusion of the scheme with a shock more diffused at time $t = 6 \times 10^{-3}$ s than at time $t = 2 \times 10^{-3}$ s. Moreover, the numerical solution is shown to converge towards the analytic one as the mesh is refined. In the same way as in Chapter 3, this 1D problem is run on a 3D mesh in order to prove that no 3D motion is created by the scheme.

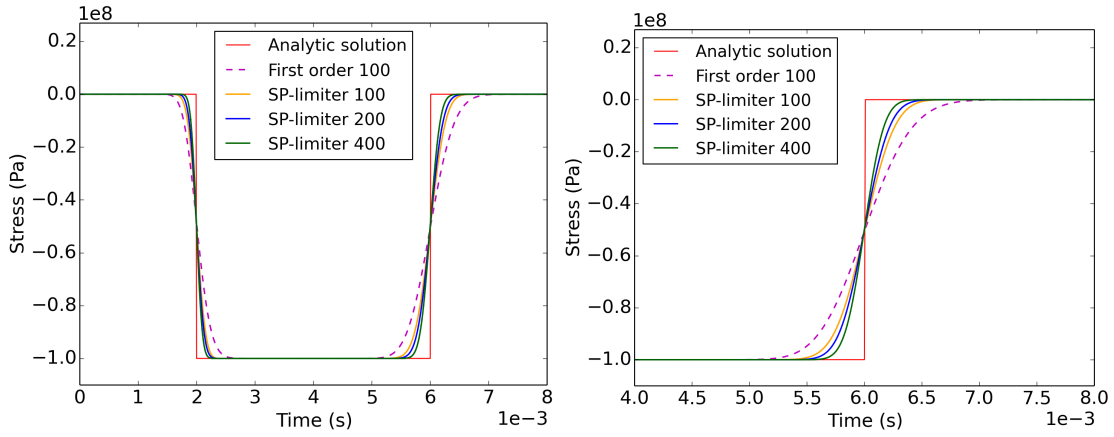

(a) (b)

Figure 5.2 – 1D pile driving - Stress $\mathbb{T}_{x,x}$ at the wall $x = 0$ with respect to time until final time $t_f = 8 \times 10^{-3}$ s (5.2a) - Zoom between $t = 4 \times 10^{-3}$ s and t_f (5.2b) - Second order solutions on $(100 \times 4 \times 4)$, $(200 \times 4 \times 4)$ and $(400 \times 4 \times 4)$ cells meshes.

5.5.2 Blake problem

The Blake Problem is a spherical problem derived from the small strain linear elasticity theory [72]. In particular, the domain considered is a shell of inner radius $r_{inn} = 0.1$ m and outer radius $r_{out} = 1$ m. The shell material is isotropic and has the following parameters: initial density $\rho^0 = 3000$ kg.m^{-3}, Young's modulus $E = 62.5 \times 10^9$ Pa, Poisson's ratio $\nu = 0.25$. A driving pressure is applied to the inner face of the shell such that $\mathbb{T}^b_{r,r} = -10^6$ Pa whereas the outer face is a free-surface boundary condition i.e. $\mathbb{T}^b \boldsymbol{n} = \mathbf{0}$. In practice, for computational time reasons, the domain is not a complete shell as the one shown in Figure 5.3a but a needle-like domain of 1° aperture angle (refer to Figure 5.3b). All the boundary faces introduced by this geometrical simplification are then symmetry boundary conditions.

The radial pressure (5.31) and the radial stress are plotted at final time $t_f = 1.6 \times 10^{-4}$ s in Figures 5.4a and 5.4b for $(1000 \times 3 \times 3)$, $(2000 \times 3 \times 3)$ and $(4000 \times 3 \times 3)$ cells meshes. These solutions are compared to the analytic solution as well as the first order solution on a $(1000 \times 3 \times 3)$ cells mesh. In particular, the numerical solution is shown to converge towards the analytic solution as the mesh is refined. The radial stress is also plotted in Figures 5.4c and 5.4d for the same meshes. One can observe on Figure 5.4c that the radial stress is well approximated by the numerical solution with a good shock timing. However, a zoom around the shock (refer to Figure 5.4d) shows an underestimated stress behind the shock.

5.5.3 Elastic vibration of a Beryllium plate

This test case, also studied in [3, 111], simulates the oscillations of a 3D $(x, y, z) \in [-0.03; 0.03] \times [-0.005; 0.005] \times [-0.005; 0.005]$ plate centered at the space origin and

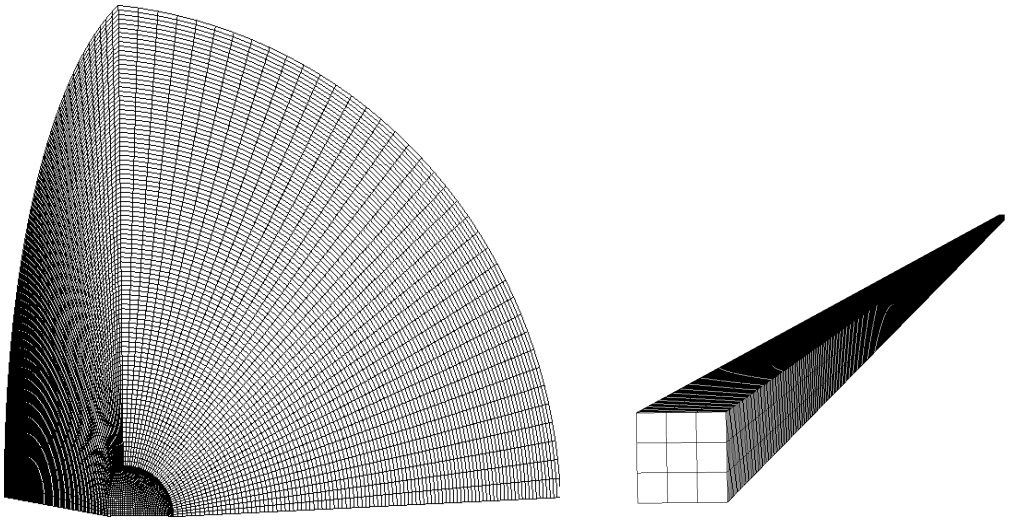

(a) (b)

Figure 5.3 – Blake Problem - Mesh of a 8^{th} of shell with 100 cells along the radius and 40 between $\theta = [0, \frac{\pi}{2}]$ (5.3a) - Mesh of a needle, used in practice, with 500 cells along the radius and 3 between $\theta = [0, 1°]$ (5.3b).

initially perturbed by the velocity field $\boldsymbol{V}_0 = (0, V_y, 0)$, where

$$V_y(x) = A\omega\Big[g_1\big[\sinh(k_x) + \sin(k_x)\big] + g_2\big[\cosh(k_x) + \cos(k_x)\big]\Big]. \tag{5.97}$$

Denoting the plate length $L = 0.06$ m and its square section $l = 0.01$ m, one has $k_x = \Omega(x + L/2)$ with $\Omega = 78.834$ m^{-1}. The other constants are defined as

$$A = 4.3369 \times 10^{-5} \text{ m}, \;\; \omega = 2.3597 \times 10^{5} \text{ s}^{-1}, \;\; g_1 = 56.6368, \;\; g_2 = 57.6455. \tag{5.98}$$

The plate is made of Beryllium which admits the following constants: initial density $\rho^0 = 1845$ kg.m^{-3}, Young's modulus $E = 3.1827 \times 10^{11}$ Pa and Poisson's ratio $\nu = 0.0539$. Symmetry boundary conditions are applied on the plate faces of normal $\boldsymbol{e}_z$. All the other faces are free boundary conditions. The oscillations of the plate are modeled until final time $t_f = 3 \times 10^{-5}$ s. The numerical solution is compared to an approximation of the analytic solution. This approximation is the first bending mode of a 2D beam with no boundary condition. In particular, the theory supposes that the beam is infinite in the y direction which is not the case here since symmetry boundary condition are used. The numerical results are thus expected to be different from the approximation.

This test case highlights the strong dissipation of the first order scheme since the oscillation amplitude quickly decrease with time. However, one can prove that a non negligible part of this dissipation is linked to the shearing part of the acoustic tensor (5.53), namely the part holding the a_c^T velocity which drastically changes the results if present (refer to Figure 5.5). This phenomenon was also noticed by Kluth et al. in [77] and was controlled by reducing the magnitude of the shearing contribution.

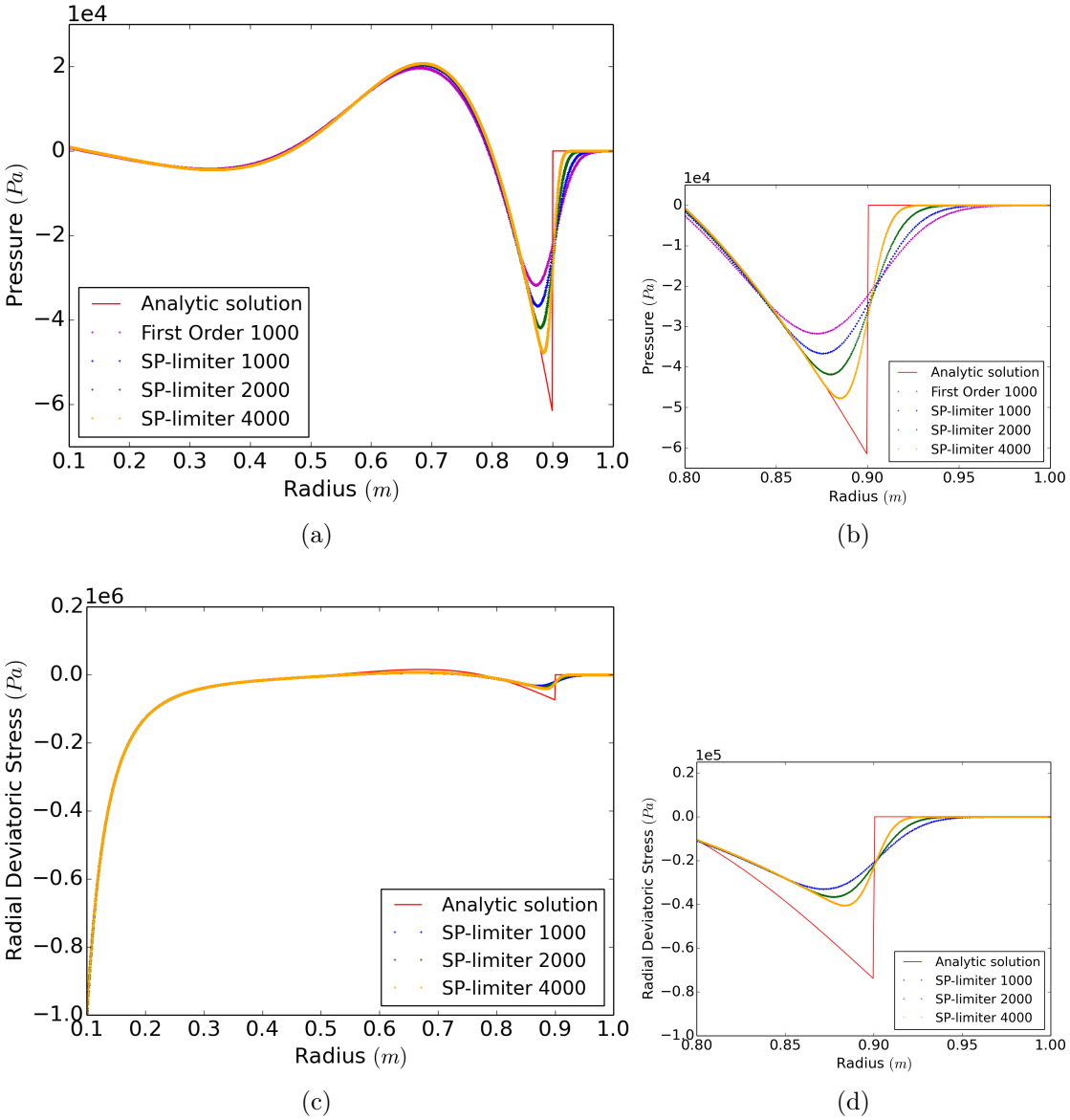

Figure 5.4 – Blake Problem - Convergence of the second order solution towards the analytic solution - Radial pressure (5.4a) and radial stress (5.4c) at time $t_f = 1.6 \times 10^{-4}$ s on $(1000 \times 3 \times 3)$, $(2000 \times 3 \times 3)$ and $(4000 \times 3 \times 3)$ cells meshes - Zoom around the shock (5.4b) and (5.4d) respectively.

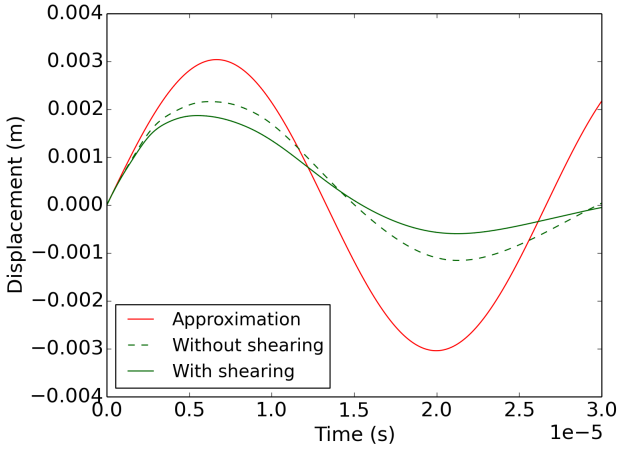

Figure 5.5 – Oscillating plate - First order scheme - Impact of the shearing part of the acoustic tensor - Vertical displacement of the z-axis with respect to time until final time $t_f = 3 \times 10^{-5}$ s on a $(100 \times 24 \times 2)$ cells mesh.

In [111], the shearing contribution is also neglected. In the sequel, the complete acoustic tensor is considered.

The convergence of the second order solution is studied in Figure 5.6. In this Figure, the vertical displacement of the z-axis is plotted with respect to time on $(100 \times 24 \times 2)$, $(200 \times 48 \times 2)$ and $(400 \times 96 \times 2)$ cells meshes and is compared to the 2D approximation. This displacement corresponds to the y-position over time of the nodes on the z-axis. One can observe that the second order extension of the scheme is significantly less dissipative than the first order one. Moreover, the results show a good accordance with the 2D approximation in terms of oscillation amplitude. One can however observe that the oscillation period is longer for the 3D numerical solution than for the 2D approximation. This is probably due to the 3D effects, such as the shearing part of the acoustic tensor as shown in Figure 5.5, that are not taken into account in the 2D theory. Let mention that a similar period of about 3×10^{-5} s can be found in [3, 111]. Finally, as noticed by Aguirre et al. [3] and also observable in [111], higher oscillation modes appear around $t = 0.5 \times 10^{-5}$ s as the mesh is refined. The mesh is plotted in Figure 5.7 at different instants to show the deformation of the beam during the motion.

5.5.4 Twisting column

The twisting column test case simulates the twisting of an elastic rubber-like material [3, 55, 114]. The column is parallelepipedic such that $(x, y, z) \in [-0.5; 0.5] \times [-0.5; 0.5] \times [0; 6]$. The rubber-like material is characterized by an initial density $\rho^0 = 1100$ kg.m^{-3}, Young's modulus $E = 1.7 \times 10^7$ Pa and Poisson's ratio $\nu = 0.45$. The face $z = 0$ of the beam is embedded in a wall which corresponds to a null-velocity boundary condition. All the other faces of the beam hold stress-free boundary

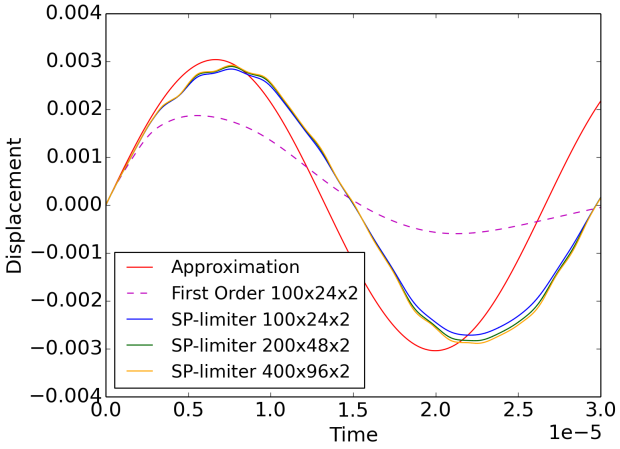

Figure 5.6 – Oscillating plate - Convergence of the second order solution towards the 2D analytic solution - Vertical displacement of the z-axis with respect to time until final time $t_f = 3 \times 10^{-5}$ s on $(100 \times 24 \times 2)$, $(200 \times 48 \times 2)$ and $(400 \times 96 \times 2)$ cells meshes.

conditions. To initialize the torsion, the following velocity field is applied to the beam

$$\boldsymbol{V}(\boldsymbol{x}, 0) = 100 \sin\left(\frac{\pi y}{2L}\right) (y, -x, 0)^t, \qquad z \in [0, 6], \tag{5.99}$$

where $L = 6$ m is the beam height.

The expected motion of the beam can be roughly described as follows: the beam turns counter-clockwise until $t = 0.1$ s approximately. Then the elasticity stops the rotation and the beam returns to its initial configuration around $t = 0.2$ s. Finally, the beam, driven by its inertia, turns clockwise until time $t = 0.3$ s. The period of the resulting twisting oscillation depends on the material property, of course, but also on the scheme dissipation. In particular, one can show that the first order cell-centered Lagrangian scheme is so dissipative that the beam cannot twist and is almost returned to its initial configuration at time $t = 0.1$ s (refer to Figure 5.8a). The second order extension helps reducing the dissipation and leads to better results (refer to Figure 5.8b). Let mention that the limiting is deactivated for this test case since there is no shock. To show the improvement of the solution due to the mesh refinement, the solutions are studied on $(6 \times 6 \times 36)$, $(12 \times 12 \times 72)$ and $(24 \times 24 \times 144)$ cells meshes. In particular, on can observe in Figure 5.9 that the beam makes three turns at time $t = 0.1$ s on the more refined mesh which makes the results comparable to the solutions obtained in [3, 55, 114]. However, the scheme dissipation is still important and the solution at time $t = 0.3$ s for the same mesh presents less turns that in the aforementioned works (refer to Figure 5.10 that describes the history of the rotation).

Conclusion

In this Chapter, we have extended the cell-centered Lagrangian scheme developed

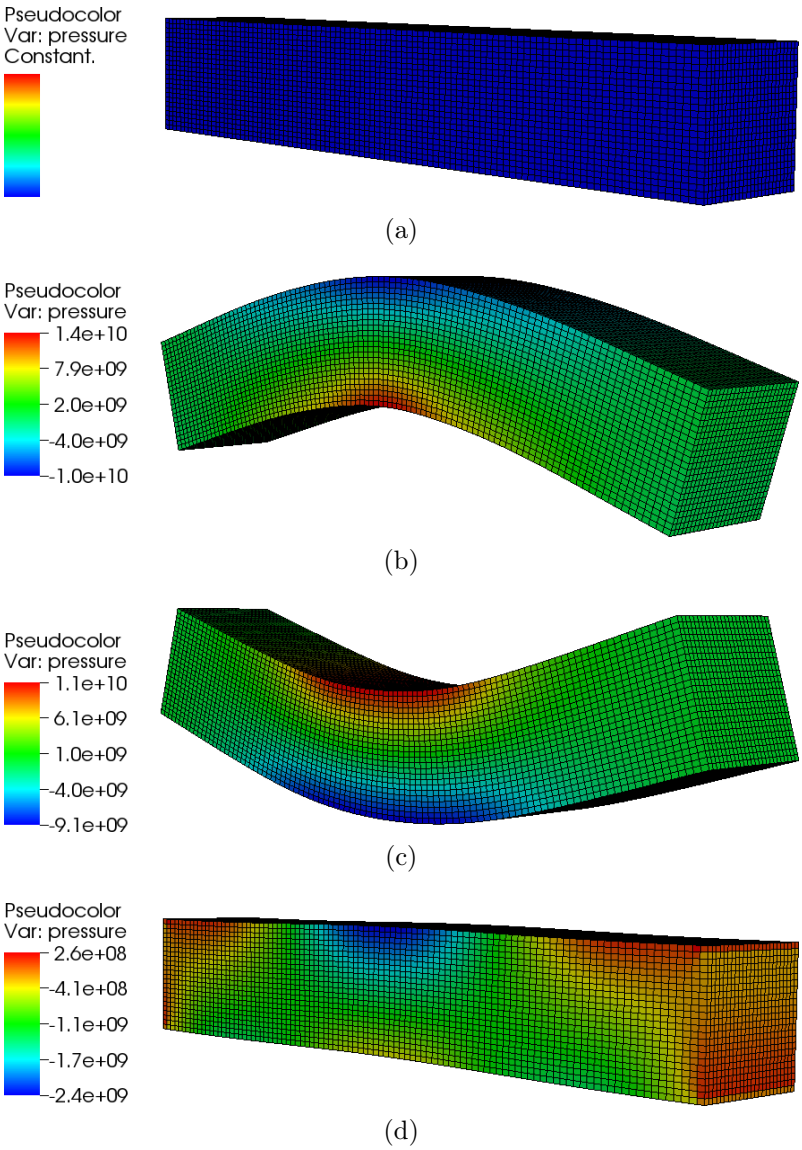

Figure 5.7 – Oscillating plate - Shape of the beam at different instants: initial time (5.7a), $t = 0.1$ (5.7b), $t = 0.2$ (5.7c) and final time $t = 0.3$ (5.7d) - Mesh colored with the pressure field.

throughout Chapters 1 and 2 to the hyperelasticity system. This system is closed by a constitutive law constructed by mean of a Coleman-Noll procedure ensuring the thermodynamic consistency and the frame-indifference. In particular, the Second Law of thermodynamics is imposed by the Gibbs relation which expresses the Cauchy stress tensor as the derivative of the internal energy with respect to the left Cauchy-Green stress tensor $\mathbb{B}$. Concerning the frame-indifference, it is ensured by expressing the internal energy as a function of the invariants of $\mathbb{B}$. This particular form of the internal energy enables then the use of the compressible Neo-Hookean model. The system of equations is discretized using the discrete operators introduced in Chapter 1. The nodal solver is build on a momentum conservation condition in the dual cells as well as an entropy criterion. The second order extension in space of this scheme is performed using a MUSCL procedure. The reconstruction step uses the discrete gradients introduced by the spatial discretization and the limiting step is ensured by the SP-limiter (refer to Chapter 2) extended to tensor fields in a component-wise manner. The second order in time discretization is performed by a GRP procedure which is fully detailed in the particular case of a Neo-Hookean solid. The scheme is finally validated on different test cases introducing small as well as large deformations. In the small deformations regime, the hyperelasticity system degenerates onto the elasticity system. The scheme is proved to behave in the same way since good shock timing and amplitude are found on the 1D steel pile and the 3D spherical Blake problems. On large deformation problems, the first order scheme is proved to be strongly dissipative due to the shearing introduced by the square root of the acoustic tensor used in the nodal solver. Hopefully, the second order extension enables to drastically reduce this flaw. In particular, the scheme is assessed against the difficult problems of oscillating and twisting beams for which results are comparable to the literature.

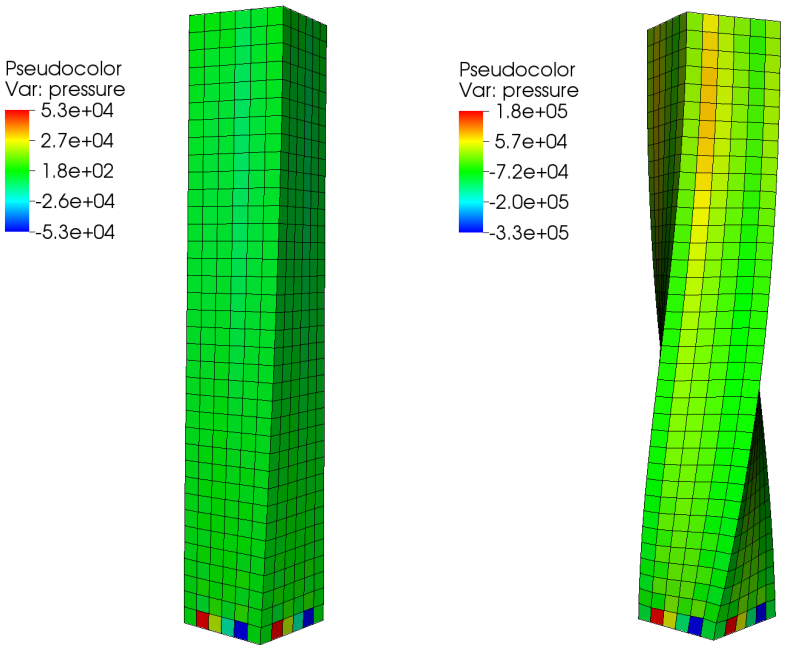

(a) (b)

Figure 5.8 – Twisting column - First (5.8a) and Second order (5.8b) solutions - Beam shape and pressure field at time $t = 0.1$ s on a $(6 \times 6 \times 36)$ cells meshes.

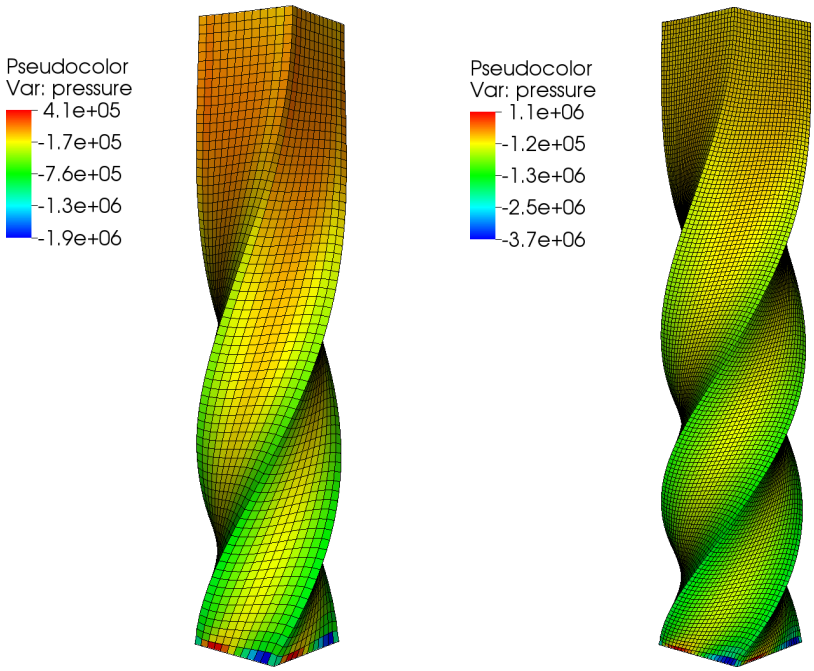

(a) (b)

Figure 5.9 – Twisting column - Second order solutions - Beam shape and pressure field at time $t = 0.1$ s on $(12 \times 12 \times 72)$ (5.9a) and $(24 \times 24 \times 144)$ (5.9b) cells meshes.

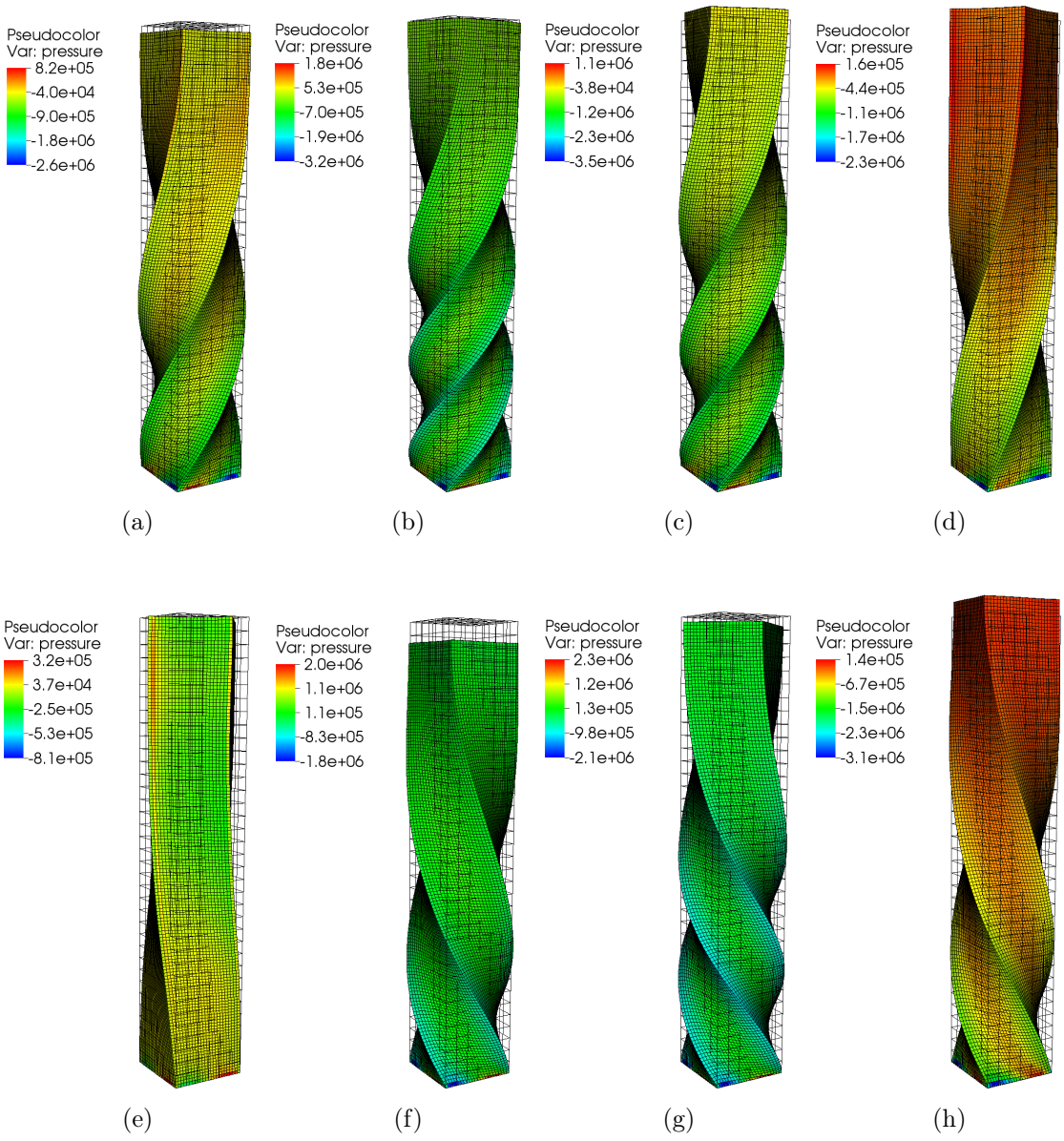

Figure 5.10 – Twisting column - Second order solutions - Beam shape and pressure field at times $t = 0.0375$ s (5.10a), $t = 0.075$ s (5.10b), $t = 0.1125$ s (5.10c), $t = 0.15$ s (5.10d), $t = 0.1875$ s (5.10e), $t = 0.225$ s (5.10f), $t = 0.2625$ s (5.10g) and $t = 0.3$ s (5.10h) on a $(24 \times 24 \times 144)$ cells meshes - Comparison with the shape of a $(6 \times 6 \times 36)$ cells meshes to see the deformation with respect to the initial configuration.

Conclusion

The motivation of this thesis was to develop robust and accurate methods for the 3D extension of the EUCCLHYD scheme and to propose its extension to the modeling of hyperelasticity. The starting point of this thesis was the work [95] in which Maire et Nkonga proposed the 3D extension of the EUCCLHYD scheme, first introduced in [93].

In Chapter 1, a systematic and symmetric discretization of unstructured polyhedral meshes is proposed in order to ensure the important GCL compatibility condition. This discretization decomposes the boundary of the cell into face area vectors that enable the definition of discrete operators which provide a first order approximation of the divergence and gradient operators in the cells. Moreover, the procedure proposed in [126, 127], enabling to compute the time step in such a way that the internal energy remains positive, has been extended to the 3D context.

In chapter 3, the classic 3D extension of the MUSCL procedure, consisting in a component-wise limiting of the fields, is proved to be insufficient. Spurious oscillations are observed on the Sod test case and strong overshoots on the Noh problem. The difficulty comes principally from our incapacity in defining and constructing frame-invariant basis in the 3D space. This is why two new limiting procedures are proposed in Chapter 2. The SP-limiter avoid changes of basis by limiting the velocity gradient with a single scalar which enables to preserve the flow symmetries. Moreover, this limiter uses an extended monotonicity stencil which is proved to remove the spurious oscillations on the Sod problem. For dealing with flows presenting a spherical symmetry, the MM-limiter is proposed. This limiter can be seen as the multi-dimensional extension of the minmod limiter since it computes a limited cell gradient from nodal gradients and the minmod function. In particular, this limiter leads to very stable results on difficult problems with a spherical symmetry and strong mesh printing such as the Noh and Kidder problems. It also enables to remove the non convex cells appearing in the Sedov problem. Finally in Chapter 2, the GRP procedure is detailed for the second order in time discretization. In particular, the terms introduced by the time derivatives of the geometry are taken into account which is not the case in [96].

In Chapter 4, the MM-limiter is used to perform the study of Rayleigh-Taylor Instability (RTI) in supernova remnants blown up by a central pulsar. In this study, the supernova is modeled by a spherical shell and the central pulsar by an inner

pressure boundary condition. The perturbation of the inner face is performed by use of the spherical harmonics function and the numerical results are compared to analytic solutions taken from [108]. The results on a 2D-axisymmetric problem are also compared to the results obtained with the CHIC Code to verify that the 3D and 2D-axisymmetric schemes provide the same results. Finally, full 3D perturbations are implemented in order to numerically validate the assumption stating that the azimuthal mode has no impact on the perturbation growth.

In the last Chapter of this thesis, the extension of the cell-centered Finite Volume scheme to the hyperelasticity system is proposed. This study is the 3D extension of the work [77] with the difference that we are working with the left Cauchy-Green tensor $\mathbb{B}$ instead of the deformation gradient $\mathbb{F}$ which enables to work in a fully updated Lagrangian formalism. The second order extension of this scheme is proposed using a MUSCL procedure combined with a GRP approach. In particular, the SP-limiter is extended to tensor fields in a component-wise manner. Moreover, the complete GRP procedure is detailed in the case of Neo-Hookean compressible solids. The scheme is validated on four test cases introducing small as well as large deformations. In particular, good results are found on the non trivial problems of oscillating and twisting beams.

As a future work, further improvements of the Lagrangian scheme have to be done, especially concerning its robustness. For example, the erratic behavior of the order of convergence on the Taylor-Green vortex when combining the LS gradients with a GRP procedure remains unexplained. One can also refer to the wall heating and mesh printing flaws that are strong in 3D, for example on the Noh and Kidder problems. Moreover, it has been shown that the limiting procedures are often restricted to certain type of flows and reach quickly their limits. It could be interesting to investigate new approaches for the second order extension, maybe procedures alternative to the MUSCL one.

A high order extension of the scheme would also be valuable. In particular for the treatment of spherical problems such as the Kidder implosion. It is indeed shown in [124] that a high order approximation of the flow and the geometry enables to reduce the mesh printing on spherical flows. However, the Finite Volume formalism is not interesting for high-order extensions and it would be more interesting to consider for example a DG formalism as in [14].

The implementation of an Arbitrary Lagrangian-Eulerian (ALE) method would be valuable for treating highly compressible flows such as the Noh problem. Indeed, the natural diffusion introduced by this formalism could help stabilizing the results by reducing the impact of the mesh. Moreover, such a procedure would improve the scheme ability to treat flows with strong vorticity and shearing such as the Kelvin-Helmholtz instability or the triple point problem [50].

An Adaptive Mesh Refinement (AMR) method would also be interesting in order to improve the accuracy of the scheme in certain zones. In fact, the work done on the GCL compatibility in Chapter 1 enables to define discrete operators that can be computed on arbitrary meshes and in particular, on non-conformal meshes. In

this sense, the scheme has already been used at second order on AMR meshes. The next work would then be to verify that the scheme preserves all its good properties on such meshes and to derive a dynamic refinement procedure, based for example on an entropy criterion.

One could also investigate the coupling of this 3D hydrodynamics scheme with the 3D diffusion scheme proposed in [69, 70] to deal with real life applications.

Concerning the modeling of hyperelasticity, the treatment of plasticity effects would be interesting in order to study solids under strong deformations such as high velocity impacts. The same work as in [126, 127] could also be extended to the hyperelasticity system in order to design a time step ensuring the positivity of the internal energy.

Finally, combining all these methods, this Lagrangian scheme would be an interesting starting point for the study of Fluid Structure Interactions (FSI) [46, 47, 118] under a Finite Volume ALE-AMR formalism.

Acknowledgments

This study has been carried out with financial support from the French State, managed by the French National Research Agency (ANR) in the frame of the "Investments for the future" Programme IdEx Bordeaux (ANR-10-IDEX-03-02), Cluster of excellence CPU. It was also supported by the Aquitaine-Poitou-Charentes-Limousin region.

Appendix A

Properties of the discrete operators

The consistency analysis of the GLACE scheme was performed by Després in [32] and is completely valid for the EUCCLHYD scheme. In this Appendix, we aim at showing that the discrete operators (1.51)-(1.53) are exact for linear fields.

A.1 Divergence operator

Let consider the linear vector field $\boldsymbol{\psi} = \mathbb{A}\boldsymbol{x} + \boldsymbol{b}$ in cell c where $\mathbb{A}$ is an arbitrary matrix and $\boldsymbol{b}$ an arbitrary vector. The analytic formula gives $\nabla \cdot \boldsymbol{\psi} = \mathrm{tr}(\mathbb{A})$.

At the discrete level, the value of this linear field at node p is written $\boldsymbol{\psi}_p = \mathbb{A}\boldsymbol{x}_p + \boldsymbol{B}$. Then, using the discrete divergence operator (1.51), the approximation of the divergence of this field is

$$\mathcal{DIV}_c(\boldsymbol{\psi}) = \frac{1}{v_c} \sum_{p \in \mathcal{P}(c)} \sum_{f \in \mathcal{F}(c,p)} S_{pf} (\mathbb{A}\boldsymbol{x}_p + \boldsymbol{b}) \cdot \boldsymbol{n}_{pf}. \tag{A.1}$$

Expanding the term between brackets, one gets

$$\mathcal{DIV}_c(\boldsymbol{\psi}) = \frac{1}{v_c} \sum_{p \in \mathcal{P}(c)} \sum_{f \in \mathcal{F}(c,p)} S_{pf} \left(\mathbb{A}\boldsymbol{x}_p\right) \cdot \boldsymbol{n}_{pf} + \boldsymbol{b} \cdot \left(\frac{1}{v_c} \sum_{p \in \mathcal{P}(c)} \sum_{f \in \mathcal{F}(c,p)} S_{pf} \boldsymbol{n}_{pf} \right). \tag{A.2}$$

Since the cell has a closed contour, then

$$\sum_{p \in \mathcal{P}(c)} \sum_{f \in \mathcal{F}(c,p)} S_{pf} \boldsymbol{n}_{pf} = \boldsymbol{0}. \tag{A.3}$$

Now, using the formula (D.3), the discrete divergence becomes

$$\mathcal{DIV}_c(\boldsymbol{\psi}) = \mathbb{A} : \left(\frac{1}{v_c} \sum_{p \in \mathcal{P}(c)} \sum_{f \in \mathcal{F}(c,p)} S_{pf} \boldsymbol{x}_p \otimes \boldsymbol{n}_{pf} \right). \tag{A.4}$$

With straightforward but cumbersome calculations, it is possible to prove that, for an arbitrary tetrahedron, one has

$$\frac{1}{v_c}\sum_{p\in\mathcal{P}(c)}\sum_{f\in\mathcal{F}(c,p)} S_{pf}\boldsymbol{x}_p\otimes\boldsymbol{n}_{pf} = \mathrm{Id}\,. \tag{A.5}$$

An elegant proof is also proposed in [32]. In particular, if it is true for an arbitrary tetrahedron, it is also true for an arbitrary polyhedron by linearity of the tensorial product. Finally, the discrete divergence writes

$$\mathcal{DIV}_c(\boldsymbol{\psi}) = \mathbb{A} : \mathrm{Id} = \mathrm{tr}(\mathbb{A}). \tag{A.6}$$

A.2 Gradient operator

The same proof can be derived for the discrete gradient operator. Considering a linear scalar field $\varphi = \boldsymbol{a}\cdot\boldsymbol{x} + b$, where $\boldsymbol{a}$ is an arbitrary vector and b an arbitrary scalar, denoting by $\varphi_p = \boldsymbol{a}\cdot\boldsymbol{x}_p + b$ the value of this field at node p, the discrete gradient operator on cell c writes

$$\begin{aligned}\mathcal{GRAD}_c(\varphi) &= \frac{1}{v_c}\sum_{p\in\mathcal{P}(c)}\sum_{f\in\mathcal{F}(c,p)} S_{pf}(\boldsymbol{a}\cdot\boldsymbol{x}_p + b)\boldsymbol{n}_{pf},\\ &= \boldsymbol{a}\left(\frac{1}{v_c}\sum_{p\in\mathcal{P}(c)}\sum_{f\in\mathcal{F}(c,p)} S_{pf}\boldsymbol{x}_p\otimes\boldsymbol{n}_{pf}\right) + b\left(\frac{1}{v_c}\sum_{p\in\mathcal{P}(c)}\sum_{f\in\mathcal{F}(c,p)} S_{pf}\boldsymbol{n}_{pf}\right).\end{aligned} \tag{A.7}$$

Using once again the relations (A.3) and (A.5), one finds the analytic solution

$$\mathcal{GRAD}_c(\boldsymbol{\psi}) = \boldsymbol{a}. \tag{A.8}$$

Finally, for a vector linear field $\boldsymbol{\psi} = \mathbb{A}\boldsymbol{x} + \boldsymbol{b}$ as defined previously, the analytic gradient is $\nabla\boldsymbol{\psi} = \mathbb{A}$ and the discrete gradient operator provides

$$\begin{aligned}\mathcal{GRAD}_c(\boldsymbol{\psi}) &= \frac{1}{v_c}\sum_{p\in\mathcal{P}(c)}\sum_{f\in\mathcal{F}(c,p)} S_{pf}(\mathbb{A}\boldsymbol{x}_p + \boldsymbol{b})\otimes\boldsymbol{n}_{pf},\\ &= \mathbb{A}\left(\frac{1}{v_c}\sum_{p\in\mathcal{P}(c)}\sum_{f\in\mathcal{F}(c,p)} S_{pf}\boldsymbol{x}_p\otimes\boldsymbol{n}_{pf}\right)\\ &+ \boldsymbol{b}\otimes\left(\frac{1}{v_c}\sum_{p\in\mathcal{P}(c)}\sum_{f\in\mathcal{F}(c,p)} S_{pf}\boldsymbol{n}_{pf}\right),\\ &= \mathbb{A}.\end{aligned} \tag{A.9}$$

Appendix B

Source term for the Taylor-Green vortex

B.1 Modification of the total energy conservation equation

This Appendix shows the computation of the pressure and energy source term needed for the initialization of the Taylor-Green vortex. Starting from the Euler equations

$$\begin{aligned}
&\frac{\partial \rho}{\partial t} + \nabla \cdot (\rho \boldsymbol{V}) = 0, \\
&\frac{\partial (\rho \boldsymbol{V})}{\partial t} + \nabla \cdot (\rho \boldsymbol{V} \otimes \boldsymbol{V}) + \nabla P = \boldsymbol{0}, \\
&\frac{\partial (\rho E)}{\partial t} + \nabla \cdot (\rho E \boldsymbol{V}) + \nabla \cdot (P \boldsymbol{V}) = 0,
\end{aligned} \tag{B.1}$$

we search the steady solution of the following velocity perturbation

$$\boldsymbol{V}^0(x, y) = C_1 \begin{pmatrix} \sin(\pi x)\cos(\pi y) \\ -\cos(\pi x)\sin(\pi y) \end{pmatrix}, \tag{B.2}$$

where C_1 is a constant to be chosen. Now, supposing the initial density ρ^0 is constant, the stationary system writes

$$\begin{aligned}
&\rho^0 \nabla \cdot \boldsymbol{V}^0 = 0, \\
&\rho^0 \nabla \cdot (\boldsymbol{V}^0 \otimes \boldsymbol{V}^0) + \nabla P^0 = \boldsymbol{0}, \\
&\rho^0 \nabla \cdot (E^0 \boldsymbol{V}^0) + \nabla \cdot (P^0 \boldsymbol{V}^0) = 0.
\end{aligned} \tag{B.3}$$

It is easily shown that the divergence-free condition imposed by the continuity equation is respected by the velocity field (B.2). Now, substituting this field into the momentum conservation equation leads to

$$\begin{aligned}
\nabla P^0 &= -\rho^0 \nabla \cdot (\boldsymbol{V}^0 \otimes \boldsymbol{V}^0) \\
&= -\rho^0 C_1^2 \begin{pmatrix} \sin^2(\pi x)\cos^2(\pi y) - \frac{1}{4}\sin(2\pi x)\sin(2\pi y) \\ -\frac{1}{4}\sin(2\pi x)\sin(2\pi y) + \cos^2(\pi x)\sin^2(\pi y) \end{pmatrix},
\end{aligned} \tag{B.4}$$

which can be simplified into

$$\nabla P^0 = -\frac{\pi}{2}\rho^0 C_1^2 \begin{pmatrix} \sin(2\pi x) \\ \sin(2\pi y) \end{pmatrix}. \tag{B.5}$$

Integrating the first equation relatively to x gives

$$P^0(x,y) = \frac{1}{4}\rho^0 C_1^2 \cos(2\pi x) + f(y). \tag{B.6}$$

Then, differentiating this result with respect to y enables to identify $f'(y)$ with relation (B.5). One writes

$$f'(y) = -\frac{\pi}{2}\rho^0 C_1^2 \sin(2\pi y), \tag{B.7}$$

and finally the stationary pressure field writes as

$$P^0(x,y) = \frac{1}{4}\rho^0 C_1^2 \Big(\cos(2\pi x) + \cos(2\pi y) \Big) + C_2, \tag{B.8}$$

where C_2 is an integration constant.

One has to verify that the total energy conservation equation is respected by a stationary flow with velocity and pressure fields as (B.2) and (B.8). Thanks to the definition of the internal energy $\varepsilon = E - \frac{1}{2}\boldsymbol{V}^2$ and the Euler equations (B.1), the conservation equation for internal energy expresses as

$$\frac{d(\rho\varepsilon)}{dt} + P\nabla\cdot\boldsymbol{V} = 0. \tag{B.9}$$

In the particular case of the Taylor-Green vortex, we are considering a perfect gas ruled by a gamma gas law, thus $\rho\varepsilon = \frac{1}{\gamma-1}P$ and

$$\begin{aligned} \frac{d(\rho\varepsilon)}{dt} &= \frac{1}{\gamma-1}\frac{dP}{dt}, \\ &= \frac{1}{\gamma-1}\left(\frac{\partial P}{\partial t} + \boldsymbol{V}\cdot\nabla P\right), \\ &= \frac{1}{\gamma-1}\boldsymbol{V}\cdot\nabla P, \end{aligned} \tag{B.10}$$

since the flow is stationary. The flow is also divergence-free, thus $\nabla\cdot\boldsymbol{V} = 0$, and one can write the equivalence

$$\frac{d(\rho\varepsilon)}{dt} + P\nabla\cdot\boldsymbol{V} = \frac{1}{\gamma-1}\boldsymbol{V}\cdot\nabla P. \tag{B.11}$$

One can remark that a source term appears in the internal energy conservation equation. Now, adding the conservation equation of kinetic energy $\frac{1}{2}d(\rho\boldsymbol{V}^2)/dt + \boldsymbol{V}\cdot$

$\nabla P = \mathbf{0}$ to the previous relation leads to the following expression of the conservation of total energy

$$\frac{d(\rho E)}{dt} + \nabla \cdot (P\boldsymbol{V}) = \frac{1}{\gamma - 1}\boldsymbol{V} \cdot \nabla P. \tag{B.12}$$

Finally, writing this relation for the stationary flow $(\rho^0, \boldsymbol{V}^0, P^0, E^0)$ and substituting (B.2) and (B.8) provides

$$\rho^0 \nabla \cdot (E\boldsymbol{V}^0) + \nabla \cdot (P\boldsymbol{V}^0) = \frac{\pi}{4}\frac{\rho^0 C_1^3}{\gamma - 1}\Big[\cos(3\pi x)\cos(\pi y) - \cos(3\pi y)\cos(\pi x)\Big]. \tag{B.13}$$

The right hand-side term of this last equation is thus the quantity to remove at each time step from the total energy conservation equation in order to respect the Euler equations. This source term writes

$$\mathcal{S}_c^n = -\frac{\pi}{4}\frac{1}{\gamma - 1}\Big[\cos(3\pi x_c)\cos(\pi y_c) - \cos(3\pi y_c)\cos(\pi x_c)\Big], \tag{B.14}$$

in the case where $\rho^0 = 1$ and $C_1 = 1$.

B.2 Impact of the source term on the pressure time derivative

The presence of a source term in the total energy conservation equation modifies the expression of dP/dt. Let consider the following form of the Euler system

$$\begin{aligned} &\rho \frac{d}{dt}\left(\frac{1}{\rho}\right) - \nabla \cdot \boldsymbol{V} = 0, \\ &\rho \frac{d\boldsymbol{V}}{dt} + \nabla P = \mathbf{0}, \\ &\rho \frac{dE}{dt} + \nabla \cdot (P\boldsymbol{V}) = \mathcal{S}, \end{aligned} \tag{B.15}$$

where $\mathcal{S}$ is a source term. One can classically write the kinetic and internal energy conservation equations as

$$\rho \frac{d}{dt}\left(\frac{\boldsymbol{V}^2}{2}\right) + \boldsymbol{V} \cdot \nabla P = \mathbf{0}, \tag{B.16}$$

and

$$\rho \frac{d\varepsilon}{dt} + \rho \nabla \cdot \boldsymbol{V} = \mathcal{S}. \tag{B.17}$$

In particular, using the continuity equation, this last relation can be rewritten as

$$\rho \frac{d\varepsilon}{dt} = P \frac{d\rho}{dt} + \mathcal{S}. \tag{B.18}$$

Now, using the chain rule the time derivative of the pressure writes

$$\begin{aligned}\frac{dP}{dt} &= \frac{\partial P}{\partial \rho}\frac{d\rho}{dt} + \frac{\partial P}{\partial \varepsilon}\frac{d\varepsilon}{dt}, \\ &= \left(\frac{\partial P}{\partial \rho} + \frac{P}{\rho}\frac{\partial P}{\partial \varepsilon}\right)\frac{d\rho}{dt} + \frac{\mathcal{S}}{\rho}\frac{\partial P}{\partial \varepsilon}, \\ &= -\rho a^2 \nabla \cdot \boldsymbol{V} + \frac{\mathcal{S}}{\rho}\frac{\partial P}{\partial \varepsilon},\end{aligned} \tag{B.19}$$

where a is the isentropic speed of sound. In the particular case of a perfect gas ruled by the gamma gas law, one can simplify this last relation as

$$\frac{dP}{dt} = -\rho a^2 \nabla \cdot \boldsymbol{V} + (\gamma - 1)\mathcal{S}. \tag{B.20}$$

Appendix C

Proof relative to the hyperelasticity

C.1 Derivative of the invariants of $\bar{\mathbb{B}}$

This section computes the derivatives of the three invariants of the tensor $\bar{\mathbb{B}}$ with respect to $\mathbb{B}$. These proof can be found in [61, 76]. The invariants of $\bar{\mathbb{B}}$ are recalled to write as

$$\begin{cases} i_1(\bar{\mathbb{B}}) = \mathrm{tr}(\bar{\mathbb{B}}), \\ i_2(\bar{\mathbb{B}}) = \dfrac{1}{2}\left(\mathrm{tr}(\bar{\mathbb{B}})^2 - \mathrm{tr}(\bar{\mathbb{B}}^2)\right), \end{cases} \tag{C.1}$$

where $\mathbb{B} = J^{\frac{2}{3}}\bar{\mathbb{B}}$ and $J = \sqrt{\det(\mathbb{B})}$. Using the property

$$\frac{\partial \,\mathrm{tr}(\mathbb{B})}{\partial \mathbb{B}} = \mathrm{Id}, \tag{C.2}$$

one can firstly write

$$\frac{\partial i_1(\bar{\mathbb{B}})}{\partial \bar{\mathbb{B}}} = \mathrm{Id} \quad \text{and} \quad \frac{\partial i_2(\bar{\mathbb{B}})}{\partial \bar{\mathbb{B}}} = i_1(\bar{\mathbb{B}})\,\mathrm{Id} - \bar{\mathbb{B}}. \tag{C.3}$$

• Let compute $\partial J/\partial \mathbb{B}$: by definition, one has

$$\begin{aligned} \frac{\partial J}{\partial \mathbb{B}} &= \frac{\partial \sqrt{\det(\mathbb{B})}}{\partial \mathbb{B}} \\ &= \frac{1}{2}\frac{1}{\sqrt{\det(\mathbb{B})}}\frac{\partial \det(\mathbb{B})}{\partial \mathbb{B}} \qquad \text{(using the chain rule)} \\ &= \frac{1}{2}\frac{\det(\mathbb{B})}{\sqrt{\det(\mathbb{B})}}\mathbb{B}^{-t} \\ &= \frac{1}{2}J\mathbb{B}^{-1} \qquad \text{(by symmetry of } \mathbb{B}) \qquad \square \end{aligned} \tag{C.4}$$

• Let compute $\partial\bar{\mathbb{B}}/\partial\mathbb{B}$:

$$\begin{aligned}
\frac{\partial\bar{\mathbb{B}}}{\partial\mathbb{B}} &= \frac{\partial J^{-\frac{2}{3}}\mathbb{B}}{\partial\mathbb{B}} \qquad \text{(by definition)} \\
&= J^{-\frac{2}{3}}\frac{\partial\mathbb{B}}{\partial\mathbb{B}} - \frac{2}{3}J^{-\frac{5}{3}}\frac{\partial J}{\partial\mathbb{B}}\otimes\mathbb{B} \qquad \text{(using the chain rule)} \\
&= J^{-\frac{2}{3}}\left(\mathbb{III} - \frac{1}{3}\mathbb{B}^{-1}\otimes\mathbb{B}\right) \qquad \text{(by definition of } \partial J/\partial\mathbb{B}) \qquad \square
\end{aligned} \tag{C.5}$$

• Let compute $\partial i_1(\bar{\mathbb{B}})/\partial\mathbb{B}$:

$$\begin{aligned}
\frac{\partial i_1(\bar{\mathbb{B}})}{\partial\mathbb{B}} &= \frac{\partial i_1(\bar{\mathbb{B}})}{\partial\bar{\mathbb{B}}}\frac{\partial\bar{\mathbb{B}}}{\partial\mathbb{B}} \\
&= J^{-\frac{2}{3}}\left(\mathbb{III} - \frac{1}{3}\mathbb{B}^{-1}\otimes\mathbb{B}\right)\mathrm{Id} \qquad \text{(using the previous result)} \\
&= J^{-\frac{2}{3}}\left(\mathrm{Id} - \frac{1}{3}\,\mathrm{tr}(\mathbb{B})\mathbb{B}^{-1}\right) \qquad \text{(using relation (D.10))} \\
&= \bar{\mathbb{B}}_0\mathbb{B}^{-1} \qquad \square
\end{aligned} \tag{C.6}$$

• Let compute $\partial i_2(\bar{\mathbb{B}})/\partial\mathbb{B}$:

$$\begin{aligned}
\frac{\partial i_2(\bar{\mathbb{B}})}{\partial\mathbb{B}} &= \frac{\partial i_2(\bar{\mathbb{B}})}{\partial\bar{\mathbb{B}}}\frac{\partial\bar{\mathbb{B}}}{\partial\mathbb{B}} \\
&= \left[i_1(\bar{\mathbb{B}})\,\mathrm{Id} - \bar{\mathbb{B}}\right]\left[J^{-\frac{2}{3}}\left(\mathbb{III} - \frac{1}{3}\mathbb{B}^{-1}\otimes\mathbb{B}\right)\right] \qquad \text{(using the previous result)} \\
&= i_1(\bar{\mathbb{B}})\bar{\mathbb{B}}_0\mathbb{B}^{-1} - J^{-\frac{2}{3}}\bar{\mathbb{B}} + \frac{1}{3}(\mathbb{B}^{-1}\otimes\bar{\mathbb{B}})\bar{\mathbb{B}} \\
&= i_1(\bar{\mathbb{B}})\bar{\mathbb{B}}_0\mathbb{B}^{-1} - \bar{\mathbb{B}}^2\mathbb{B}^{-1} + \frac{1}{3}\,\mathrm{tr}(\bar{\mathbb{B}}^2)\mathbb{B}^{-1} \\
&= \left[i_1(\bar{\mathbb{B}})\bar{\mathbb{B}}_0 - \left(\bar{\mathbb{B}}^2\right)_0\right]\mathbb{B}^{-1}
\end{aligned} \tag{C.7}$$

Using the Cayley Hamilton theorem, one can prove that $\mathbb{B}$ satisfies

$$\mathbb{B}^{-1} = \bar{\mathbb{B}}^2 - i_1(\bar{\mathbb{B}})\bar{\mathbb{B}} + i_2(\bar{\mathbb{B}})\,\mathrm{Id}, \tag{C.8}$$

which leads to

$$(\mathbb{B}^{-1})_0 = i_1(\bar{\mathbb{B}})\bar{\mathbb{B}}_0 - \left(\bar{\mathbb{B}}^2\right)_0. \tag{C.9}$$

Finally, one gets

$$\frac{\partial i_2(\bar{\mathbb{B}})}{\partial\mathbb{B}} = -(\bar{\mathbb{B}}^{-1})_0\mathbb{B}^{-1}. \qquad \square \tag{C.10}$$

C.2 Progressive wave study

Considering an isotropic elastic material under the small deformations hypothesis, the Cauchy stress tensor writes as

$$\mathbb{T} = 2\mu\mathbb{E} + \lambda\,\mathrm{tr}(\mathbb{E})\,\mathrm{Id}, \tag{C.11}$$

where $\mathbb{E}$ is the deformation tensor, defined as

$$\mathbb{E} = \frac{1}{2}\left[\nabla \boldsymbol{U} + (\nabla \boldsymbol{U})^t\right], \tag{C.12}$$

and $\boldsymbol{U} = \boldsymbol{x} - \boldsymbol{X}$ is the displacement between the reference and current configurations. In this way, the Cauchy stress tensor can be written equivalently as

$$\mathbb{T} = \mu\left[\nabla \boldsymbol{U} + (\nabla \boldsymbol{U})^t\right] + \lambda(\nabla \cdot \boldsymbol{U})\,\mathrm{Id}\,. \tag{C.13}$$

Substituting this expression of $\mathbb{T}$ into the momentum conservation equation

$$\rho\frac{\partial \boldsymbol{V}}{\partial t} - \nabla \cdot \mathbb{T} = \boldsymbol{0}, \tag{C.14}$$

and knowing that $\partial \boldsymbol{U}/\partial t = \boldsymbol{V}$ leads to

$$\rho\frac{\partial^2 \boldsymbol{U}}{\partial t^2} - \mu\left[\nabla \cdot (\nabla \boldsymbol{U}) + \nabla \cdot (\nabla \boldsymbol{U})^t)\right] + \lambda\nabla \cdot (\nabla \cdot \boldsymbol{U})\,\mathrm{Id} = \boldsymbol{0}. \tag{C.15}$$

Using now the formulas

$$\nabla \cdot (\nabla \boldsymbol{U}) = \Delta \boldsymbol{U}, \quad \text{and} \quad \nabla \cdot ((\nabla \boldsymbol{U})^t) = \nabla \cdot ((\nabla \cdot \boldsymbol{U})\,\mathrm{Id}) = \nabla(\nabla \cdot \boldsymbol{U}), \tag{C.16}$$

this equation becomes

$$\rho\frac{\partial^2 \boldsymbol{U}}{\partial t^2} - \mu\Delta \boldsymbol{U} + (\lambda + \mu)\nabla(\nabla \cdot \boldsymbol{U}) = \boldsymbol{0}. \tag{C.17}$$

Let suppose that the solution $\boldsymbol{U}$ of (C.17) is a progressive wave. This solution writes

$$\boldsymbol{U} = \boldsymbol{U}(\boldsymbol{x} \cdot \boldsymbol{\zeta} - ct) = \boldsymbol{U}(\xi), \tag{C.18}$$

where $\boldsymbol{\zeta}$ is the propagation direction of the wave, c its velocity and ξ is introduced to simplify the notations. In particular, using the change of variable $\xi \mapsto \boldsymbol{x} \cdot \boldsymbol{\zeta} - ct$, the equation (C.17) becomes

$$\rho c^2 \boldsymbol{U}'' - \mu \boldsymbol{U}'' - (\lambda + \mu)(\boldsymbol{\zeta} \otimes \boldsymbol{\zeta})\boldsymbol{U}'' = \boldsymbol{0}. \tag{C.19}$$

Adding now $\boldsymbol{0} = \mu(\boldsymbol{\zeta} \otimes \boldsymbol{\zeta})\boldsymbol{U}'' - \mu(\boldsymbol{\zeta} \otimes \boldsymbol{\zeta})\boldsymbol{U}''$, this relation can finally be written as

$$\left[\rho c^2 - \mu(\mathrm{Id} - (\boldsymbol{\zeta} \otimes \boldsymbol{\zeta})) + (\lambda + 2\mu)(\boldsymbol{\zeta} \otimes \boldsymbol{\zeta})\right]\boldsymbol{U}'' = \boldsymbol{0}. \tag{C.20}$$

This last relation is in fact an eigenvalue problem written as

$$\left[c^2 - \mathbb{K}(\boldsymbol{\zeta})\right]\boldsymbol{U}'' = \boldsymbol{0}, \tag{C.21}$$

with

$$\mathbb{K}(\boldsymbol{\zeta}) = \left(\frac{\mu}{\rho}\right)[\mathrm{Id} - (\boldsymbol{\zeta} \otimes \boldsymbol{\zeta})] + \left(\frac{\lambda + 2\mu}{\rho}\right)(\boldsymbol{\zeta} \otimes \boldsymbol{\zeta}). \tag{C.22}$$

$\mathbb{K}(\boldsymbol{\zeta})$ is called the acoustic tensor. In this way, one can define $\mathbb{Q}_{cfp}$ the square root of the acoustic tensor such that

$$\mathbb{Q}_{cfp}^2 = \mathbb{K}(\boldsymbol{n}_{pf}). \tag{C.23}$$

In particular, it is easily shown that $\alpha_1 = (\lambda + 2\mu)/\rho$ is an eigenvalue of this tensor of associated eigenvector $\boldsymbol{\zeta}$. Moreover, $\alpha_2 = \mu/\rho$ is the other eigenvalue, of multiplicity two and its associated eigenvectors are two orthogonal vectors in the plane orthogonal to $\boldsymbol{\zeta}$.

Appendix D

Algebraic form

D.1 Useful algebraic relations

This Appendix gathers some useful algebraic relations that are used throughout the manuscript. One can also refer to [61]. Let $\mathbb{M}$, $\mathbb{N}$ and $\mathbb{K}$ be second order tensors, $\boldsymbol{a} = (a_1, a_2, a_3)$, $\boldsymbol{b} = (b_1, b_2, b_3)$ and $\boldsymbol{c}$ vectors in the $\mathbb{R}^3$ space, $\mathbb{I}$ the fourth-order identity tensor, then one has the following formula:

$$(\boldsymbol{a} \cdot \boldsymbol{b})\boldsymbol{c} = (\boldsymbol{c} \otimes \boldsymbol{a})\boldsymbol{b} \tag{D.1}$$

$$\boldsymbol{a} \otimes \boldsymbol{b} = \begin{pmatrix} a_1 b_1 & a_1 b_2 & a_1 b_3 \\ a_2 b_1 & a_2 b_2 & a_2 b_3 \\ a_3 b_1 & a_3 b_2 & a_3 b_3 \end{pmatrix} \tag{D.2}$$

$$(\mathbb{M}\boldsymbol{a}) \cdot \boldsymbol{b} = \mathbb{M} : (\boldsymbol{b} \otimes \boldsymbol{a}) \tag{D.3}$$

$$\mathbb{M} : \mathbb{N} = \mathrm{tr}(\mathbb{M}^t \mathbb{N}) \tag{D.4}$$

$$\mathbb{M} : (\boldsymbol{a} \otimes \boldsymbol{b}) = \mathbb{M}\boldsymbol{b} \cdot \boldsymbol{a} = \mathbb{M}^t \boldsymbol{a} \cdot \boldsymbol{b} \tag{D.5}$$

$$\mathrm{tr}(\mathbb{K}\mathbb{M}\mathbb{K}^{-1}) = \mathrm{tr}(\mathbb{M}), \text{ since } \mathrm{tr}(\mathbb{M}\mathbb{N}) = \mathrm{tr}(\mathbb{N}\mathbb{M}) \tag{D.6}$$

$$(\mathbb{M} \otimes \boldsymbol{a})_{i,j,k} = \mathbb{M}_{i,j} \boldsymbol{a}_k \tag{D.7}$$

$$(\mathbb{M} \otimes \boldsymbol{a})\boldsymbol{b} = \mathbb{M}(\boldsymbol{a} \cdot \boldsymbol{b}), \text{ thus } (\mathbb{M} \otimes \boldsymbol{a})\boldsymbol{a} = \mathbb{M} \text{ if } \boldsymbol{a}^2 = 1 \tag{D.8}$$

$$\mathbb{M}(\boldsymbol{a} \otimes \boldsymbol{b}) = (\mathbb{M}\boldsymbol{a}) \otimes \boldsymbol{b} \tag{D.9}$$

$$(\mathbb{M} \otimes \mathbb{N})\,\mathbb{I} = \mathrm{tr}(\mathbb{N})\mathbb{M} \tag{D.10}$$

$$(\mathbb{M} \otimes \mathbb{N})\mathbb{K} = (\mathbb{N} : \mathbb{K})\mathbb{M} = \mathrm{tr}(\mathbb{N}^t\mathbb{K})\mathbb{M} \tag{D.11}$$

$$(\nabla \cdot \mathbb{M}) = \frac{\partial \mathbb{M}_{i,j}}{\partial x_i}\boldsymbol{e}_j \tag{D.12}$$

D.2 Change of basis

Let $\mathbb{B}_\xi = (\boldsymbol{\xi}_1|\boldsymbol{\xi}_2|\boldsymbol{\xi}_3)$ be the change of basis from the Cartesian basis to the basis $\mathcal{B}_{\boldsymbol{\xi}} = (\boldsymbol{\xi}_1, \boldsymbol{\xi}_2, \boldsymbol{\xi}_3)$. Then for an arbitrary vector $\boldsymbol{a}$ and an arbitrary tensor $\mathbb{M}$ expressed in the Cartesian basis, their counterparts $\boldsymbol{a}_\xi$ and $\mathbb{M}_\xi$ in the $\mathcal{B}_{\boldsymbol{\xi}}$ basis write

$$\boldsymbol{a}_\xi = \mathbb{B}_\xi^t\boldsymbol{a}, \quad \text{and} \quad \mathbb{M}_\xi = \mathbb{B}_\xi^t\mathbb{M}\mathbb{B}_\xi. \tag{D.13}$$

D.3 Symmetric positive definite matrix

Let prove that a second order tensor $\mathbb{M}$ under the from

$$\mathbb{M} = \boldsymbol{n} \otimes \boldsymbol{n}, \tag{D.14}$$

with $\boldsymbol{n}$ an arbitrary vector, is necessarily symmetric positive definite (SPD).

Proof: The symmetry is obvious by definition of the tensorial product (D.2). Moreover, a matrix is said positive definite if for any vector $\boldsymbol{x}$, one has

$$\boldsymbol{x}^t\mathbb{M}\boldsymbol{x} \geq 0. \tag{D.15}$$

By definition of $\mathbb{M}$ and use of formula (D.1), one has

$$\begin{aligned} \boldsymbol{x}^t\mathbb{M}\boldsymbol{x} &= \boldsymbol{x}^t(\boldsymbol{n} \otimes \boldsymbol{n})\boldsymbol{x}, \\ &= [(\boldsymbol{n} \cdot \boldsymbol{x})\boldsymbol{n}] \cdot \boldsymbol{x}, \\ &= (\boldsymbol{n} \cdot \boldsymbol{x})^2 \geq 0. \qquad \square \end{aligned} \tag{D.16}$$

Moreover, the sum of two SDP matrices is itself a SDP matrix.

Bibliography

[1] R. Abgrall, R. Loubère, and J. Ovadia. A Lagrangian Discontinuous Galerkin-type method on unstructured meshes to solve hydrodynamics problems. *Int. J. Numer. Meth. Fluids*, 44:645–663, 2004.

[2] F.L. Adessio, J.R. Baumgardner, J.K. Dukowicz, N.L. Johnson, B.A. Kashiwa, R.M. Rauenzahn, and C. Zemach. Caveat: a computer code for fluid dynamics problems with large distortion and internal slip. *Technical report, Lawrence Livermore National Laboratory*, 1992.

[3] M. Aguirre, A.J. Gil, J. Bonet, and A.A. Carreno. A vertex centered Finite Volume Jameson-Schmidt-Turkel (JST) algorithm for a mixed conservation formulation in solid. *J. Comput. Phys.*, 259:672–699, 2014.

[4] M. Aguirre, A.J. Gil, J. Bonet, and C.H. Lee. An upwind vertex centered Finite Volume solver for Lagrangian solid dynamics. *J. Comput. Phys.*, 300:387–422, 2015.

[5] A.J. Barlow. A compatible finite element multi-material ALE hydrodynamics algorithm. *Int. J. Numer. Meth. Fluids*, 56:953–964, 2008.

[6] A.J. Barlow, D. Burton, and M. Shashkov. Compatible, energy and symmetry preserving 2D Lagrangian hydrodynamics in rz-cylindrical coordinates. *Procedia Computer Science*, 1:1893–1901, 2012.

[7] A.J. Barlow and P.L. Roe. A cell-centered Lagrangian Godunov scheme for shock hydrodynamics. *Computers and Fluids*, 46:133–136, 2011.

[8] T.J. Barth. Numerical methods for conservation laws on structured and unstructured meshes. *Technical report, VKI Lecture Series*, 2003.

[9] T.J. Barth and D.C. Jespersen. The design and application of upwind schemes on unstructured meshes. *AIAA Paper, 27th Aerospace Sciences Meeting, Reno, Nevada*, 89-0366, 1989.

[10] M. Ben-Artzi and J. Falcovitz. A second-order Godunov-type scheme for compressible fluid dynamics. *J. Comput. Phys.*, 55:1–32, 1984.

[11] D.J. Benson. Computational methods in Lagrangian and Eulerian hydrocodes. *Comput. Methods Appl. Mech. Engrg.*, 99:235–394, 1992.

[12] M. Berger, M. Aftosmis, and S. Murman. Analysis of slope limiters on irregular grids. *AIAA Paper, 43th Aerospace Sciences Meeting, Reno, Nevada*, 43, 2005.

[13] I.B. Bernstein and D.L. Book. Rayleigh-Taylor Instability of self-similar spherical expansion. *The Astrophysical Journal*, 225:633, 1978.

[14] W. Boscheri and M. Dumbser. A direct Arbitrary-Lagrangian-Eulerian ADER-WENO finite volume scheme on unstructured tetrahedral meshes for conservative and non-conservative hyperbolic systems in 3D. *J. Comput. Phys.*, 275:484–523, 2014.

[15] W. Boscheri, M. Dumbser, and R. Loubère. Cell centered direct Arbitrary-Lagrangian-Eulerian ADER-WENO finite volume schemes for nonlinear hyperelasticity. *Computers and Fluids*, 134-135:111–129, 2016.

[16] W. Boscheri, M. Dumbser, and O. Zanotti. High order cell-centered Lagrangian-type Finite Volume schemes with time-accurate local time stepping on unstructured triangular meshes. *J. Comput. Phys.*, 291:120–150, 2015.

[17] J. Breil. *Numerical methods for Lagrangian ans Arbitrary-Lagrangian-Eulerian hydrodynamics.Contribution to the simulation of High-Energy-Density-Physics problems.* Habilitation à diriger des recherches, Bordeaux University, 2016.

[18] J. Breil, S. Galera, and P.-H. Maire. Multi-material ALE computation in Inertial Confinement Fusion code CHIC. *Computers and Fluids*, 46:161–167, 2011.

[19] D. Burton. Conservation of energy, momentum and angular momentum in Lagrangian staggered-grid hydrodynamics. *Technical report, Lawrence Livermore National Laboratory*, 1990.

[20] D.E. Burton. Multidimensional discretization of conservation laws for unstructured polyhedral grids. *Technical report, Lawrence Livermore National Laboratory*, UCRL-JC-118306, 1994.

[21] D.E. Burton, T.C. Carney, N.R. Morgan, S.K. Sambasivan, and M.A. Kenamond. A cell-centered Lagrangian Godunov-like method for solid dynamics. *Computers and Fluids*, 83:33–47, 2013.

[22] D.E. Burton, N.R. Morgan, T.C. Carney, and M.A. Kenamond. Reduction of dissipation in Lagrange cell-centered hydrodynamics (CCH) through corner gradient reconstruction (CGR). *J. Comput. Phys.*, 299:229–280, 2015.

[23] J. Campbell and M. Shashkov. A tensor artificial viscosity using a mimetic Finite Difference algorithm. *J. Comput. Phys.*, 172:739–765, 2001.

[24] E. Caramana and M. Shashkov. Elimination of artificial grid distortion and hourglass-type motions by means of Lagrangian subzonal masses and pressures. *J. Comput. Phys.*, 142:521–561, 1998.

[25] E.J. Caramana, D.E. Burton, M.J. Shashkov, and P.P. Whalen. The construction of compatible hydrodynamics algorithms utilizing conservation of total energy. *J. Comput. Phys.*, 146:227–262, 1998.

[26] E.J. Caramana, C.L. Rousculp, and D.E. Burton. A compatible, energy and symmetry preserving Lagrangian Hydrodynamics algorithm in three-dimensional Cartesian geometry. *J. Comput. Phys.*, 157:89–119, 2000.

[27] E.J. Caramana, M.J. Shashkov, and P.P. Whalen. Formulations of artificial viscosity for multi-dimensional shock wave computations. *J. Comput. Phys.*, 144:70–97, 1998.

[28] G. Carré, S. Del Pino, B. Després, and E. Labourasse. A cell-centered Lagrangian hydrodynamics scheme on general unstructured meshes in arbitrary dimension. *J. Comput. Phys.*, 228:5160–5183, 2009.

[29] J. Cheng and C.-W. Shu. Positivity-preserving Lagrangian scheme for multi-material compressible flow. *J. Comput. Phys.*, 257:143–168, 2014.

[30] R. Courant, K.O. Friedrichs, and H. Lewy. On the partial difference equations of mathematical physics. *IBM J.*, 11:215–234, 1967.

[31] J.-A. Desideri and A. Dervieux. Compressible flow solvers using unstructured grids. *Von Karman Institute Lectures series*, pages 1–115, 1988-05.

[32] B. Després. Weak consistency of the cell centered Lagrangian GLACE scheme on general meshes in any dimension. *Technical Report Lab. JLL-UPMC*, R09052, 2009.

[33] B. Després and E. Labourasse. Stabilization of cell-centered compressible Lagrangian methods using subzonal entropy. *J. Comput. Phys.*, 231:6559–6595, 2012.

[34] B. Després and C. Mazeran. Lagrangian gas dynamics in dimension two and Lagrangian systems. *Arch. Ration. Mech. Anal.*, 178:327–372, 2005.

[35] V. Dobrev, Tz. Kolev, R. Rieben, and V. Tomov. Multi-material closure model for high-order finite element Lagrangian hydrodynamics. *Int. J. Numer. Meth. Fluids*, page DOI: 10.1002/fld.4236, 2016.

[36] V.A. Dobrev, T.E. Ellis, T.V. Kolev, and R.N. Rieben. High-order curvilinear finite elements for axisymmetric Lagrangian hydrodynamics. *Comput. and Fluids*, 83:58–69, 2013.

[37] V.A. Dobrev, T.E. Ellis, T.V. Kolev, and R.N. Curvilinear finite elements for Lagrangian hydrodynamics. *Int. J. Numer. Meth. Fluids*, 65:1295–1310, 2011.

[38] V.A. Dobrev, T.V. Kolev, and R.N. Rieben. High-order curvilinear finite element methods for Lagrangian hydrodynamics. *SIAM J. Sci. Comput.*, 34:606–641, 2012.

[39] V.A. Dobrev, T.V. Kolev, and R.N. Rieben. High order curvilinear Finite Elements for elastic-plastic Lagrangian dynamics. *J. Comput. Phys.*, 257:1062–1080, 2014.

[40] J.K. Dukowicz. A general, non-iterative Riemann solver for Godunov's method. *J. Comput. Phys.*, 61:119–137, 1985.

[41] J.K. Dukowicz. Efficient volume computation for three-dimensional hexahedral cells. *J. Comput. Phys.*, 74:493–496, 1988.

[42] J.K. Dukowicz and B. Meltz. Vorticity errors in multidimensional Lagrangian codes. *J. Comput. Phys.*, 99:115–134, 1992.

[43] M. Dumbser. Arbitrary-Lagrangian-Eulerian ADER-WENO finite volume schemes with time-accurate local time stepping for hyperbolic conservation laws. *Comput. Methods Appl. Mech. Engrg.*, 280:57–83, 2014.

[44] N. Favrie and S. Gavrilyuk. Diffuse interface model for compressible fluid - Compressible elastic-plastic solid interaction. *J. Comput. Phys.*, 231:2695–2723, 2012.

[45] N. Favrie and S. Gavrilyuk. A wellposed hypoelastic model derived from a hyperelastic one. *HAL*, pages https://hal.archives–ouvertes.fr/hal–01164353, 2015.

[46] M.A. Fernandez and P. Le Tallec. Linear stability analysis in fluid-structure interaction with transpiration. Part I: Formulation and mathematical analysis. *Comput. Methods Appl. Mech. Engrg.*, 192:4805–4835, 2003.

[47] M.A. Fernandez and P. Le Tallec. Linear stability analysis in fluid-structure interaction with transpiration. Part II: Numerical analysis and applications. *Comput. Methods Appl. Mech. Engrg.*, 192:4837–4873, 2003.

[48] L. Fezoui and B. Stoufflet. A class of implicit upwind schemes for Euler simulations with unstructured meshes. *J. Comput. Phys.*, 84:174–206, 1989.

[49] D. Fridrich, R. Liska, and B. Wendroff. Some cell-centered Lagrangian Lax-Wendroff HLL hybrid schemes. *Submitted to J. Comput. Phys.*, 2016.

[50] S. Galera, P.-H. Maire, and J. Breil. A two-dimensional unstructured cell-centered multi-material ALE scheme using VOF interface reconstruction. *J. Comput. Phys.*, 229:5755–5787, 2010.

[51] S.L. Gavrilyuk, N. Favrie, and R. Saurel. Modelling wave dynamics of compressible elastic materials. *J. Comput. Phys.*, 227:2941–2969, 2008.

[52] G. Georges, J. Breil, and P.-H. Maire. A 3D symmetric cell-centered Lagrangian scheme based on a multi-dimensional minmod limiter. *Proceedings of the ECCOMAS conference at Barcelona http://www.wccm-eccm-ecfd2014.org/frontal/Ebook.asp*, pages 5965–5976, 2014.

[53] G. Georges, J. Breil, and P.H. Maire. A 3D GCL compatible cell-centered Lagrangian scheme for solving gas dynamics equations. *J. Comput. Phys.*, 305:921–941, 2016.

[54] G. Georges, J. Breil, X. Ribeyre, and E. Le Bel. A 3D cell-centered Lagrangian scheme applied to the simulation of 3D non-stationary Rayleigh-Taylor Instability in supernova remnants. *High Energy Density Physics*, 17:151–156, 2015.

[55] A.J. Gil, C.H. Lee, J. Bonet, and M. Aguirre. A stabilized Petrov-Galerkin formulation for linear tetrahedral elements in compressible, nearly incompressible and truly incompressible fast dynamics. *Computer Methods in Applied Mechanics and Engineering*, 276:659–690, 2014.

[56] S.K. Godunov. A difference scheme for numerical computation of discontinuous solution of hydrodynamics equations. *Math. Sib.*, 47, 1959.

[57] S.K. Godunov and E.I. Romenski. Nonstationary equations of nonlinear elasticity theory in Eulerian coordinates. *Journal of Applied Mechanics and Technical Physics*, 13:868–884, 1972.

[58] S.K. Godunov and E.I. Romenski. Thermodynamics, conservation laws and symmetric forms of differential equations in mechanics of continuous media. *Computational Fluid Dynamics Review*, 95:19–31, 1995.

[59] S.K. Godunov and E.I. Romenski. Elements of continuum mechanics and conservation laws. *Kluwer Academic/Plenum Publishers*, 2003.

[60] S.K. Godunov, A. Zabrodine, M. Ivanov, A. Kraiko, and G. Prokopov. Résolution numérique des problèmes multi-dimensionnels de la dynamique des gaz. *Mir*, 1979.

[61] M.E. Gurtin, E Fried., and L. Anand. The mechanics and thermodynamics of continua. *Cambridge University Press*, 2009.

[62] J. Haider, C.H. Lee, A.J. Gil, and J. Bonet. A first order hyperbolic framework for large strain computational solid dynamics: An upwind cell centred Total Lagrangian scheme. *Int. J. Numer. Meth. Engng.*, page doi: 10.1002/nme.5293, 2016.

[63] J.J. Hester, J.M. Stone, P.A. Scowen, B.I. Jun, J.S. Gallacher, M.L. Norman, G.E. Ballester, C.J. Burrows, S. Casertano, J.T. Clarke, D. Crisp, R.E. Griffiths, J.G. Hoessel, J.A. Holtzman, J. Krist, J.R. Mould, R. Sankrit, K.R. Stapelfeldt, J.T. Trauger, A. Watson, and J.A. Westphal. WFPC2 studies of the Crab Nebula III. Magnetic Rayleigh-Taylor Instabilities and the origin of the filaments. *The Astrophysical Journal*, 456:225, 1996.

[64] D.J. Hill, D. pullin, M. Ortiz, and D. Meiron. An Eulerian hybrid WENO centered-difference solver for elastic-plastic solids. *J. Comput. Phys.*, 229:9503–9072, 2010.

[65] P. Hoch and E. Labourasse. A frame invariant and maximum principle enforcing second-order extension for cell-centered ALE schemes based on local convex hull preservation. *Int. J. Numer. Meth. Fluids*, 76:1043–1063, 2014.

[66] C.O. Horgan and G. Saccomandi. Constitutive models for compressible nonlinearly elastic materials with limiting chain extensibility. *Journal of Elasticity*, 77:123–138, 2004.

[67] B.P. Howell and G.J. Ball. A free-Lagrange augmented Godunov method for the simulation of elastic-plastic solids. *J. Comput. Phys.*, 175:128–167, 2002.

[68] M.E. Hubbard. Multidimensional slope limiters for MUSCL-type finite volume schemes on unstructured grids. *J. Comput. Phys.*, 155:54–74, 1999.

[69] P. Jacq. *Finite Volume methods on unstructured grids for solving anisotropic heat transfer and compressible Navier-Stokes equations*. Phd thesis, Bordeaux University, 2014.

[70] P. Jacq, P.-H. Maire, and R. Abgrall. A nominally second-order cell-centered finite volume scheme for simulating three-dimensional anisotropic diffusion equations on unstructured grids. *CiCP*, 16:841–891, 2014.

[71] B.I. Jun. Interaction of a pulsar wind with the expanding supernova remnant. *The Astrophysical Journal*, 499:282–293, 1998.

[72] J.R. Kamm and L.A. Ankeny. Analysis of the Blake Problem with RAGE. *Los Alamos National Laboratory Report*, LA-UR-09-01255, 2009.

[73] J.R. Kamm and F.X. Timmes. On efficient generation of numerically robust Sedov solutions. *Technical report, Los Alamos National Laboratory*, LA-UR-07-2849, 2007.

[74] C.F. Kennel and F.V Coroniti. Confinement of the Crab pulsar's wind by its supernova remnant. *The Astrophysical Journal*, 283:694–709, 1984.

[75] R.E. Kidder. Laser-driven compression of hollow shells: Power requirements and stability limitations. *Nuclear Fusion*, 1:3–14, 1976.

[76] G. Kluth. *Analyse mathématique et numérique de systèmes hyperélastiques et introduction de la plasticité*. Phd thesis, Université Pierre et Marie Curie, 2008.

[77] G. Kluth and B. Després. Discretization of hyperelasticity on unstructured mesh with a cell-centered lagrangian scheme. *J. Comput. Phys.*, 229:9092–9118, 2010.

[78] J.A. Koch. Volume and surface area of a spherical harmonic surface approximation to a NIF implosion core defined by HGXI/GXD images from the equator and pole. *LLNL-TR-510411*, 2011.

[79] T.V. Kolev and R.N. Rieben. A tensor artificial viscosity using a finite element approach. *J. Comput. Phys.*, 228:8336–8366, 2009.

[80] C.H. Lee, A.J. Gil, and J. bonet. Development of a cell centered upwind Finite Volume algorithm for a new conservation law formulation in structural dynamics. *Computers and Structures*, 118:13–38, 2013.

[81] B. Van Leer. Towards the ultimate conservative difference scheme. II. Monotonicity and conservation combined in a second-order scheme. *J. Comput. Phys.*, 14:361–370, 1974.

[82] B. Van Leer. Towards the ultimate conservative difference scheme. V. A second-order sequel to Godunov's method. *J. Comput. Phys.*, 32:101–136, 1979.

[83] R.J. Leveque. Finite Volume methods for Hyperbolic problems. *Cambridge Texts in applied mathematics*, 2011.

[84] Z. Li, X. Yu, and Z. Jia. The cell-centered discontinuous Galerkin method for Lagrangian compressible Euler equations in two-dimensions. *Computers and Fluids*, 96:152–164, 2014.

[85] K. Lipnikov and M.L. Shashkov. A framework for developing a mimetic tensor artificial viscosity for Lagrangian hydrocodes on arbitrary polygonal meshes. *J. Comput. Phys.*, 229:7911–7941, 2010.

[86] R. Loubère. *Une méthode particulaire Lagrangienne de type Galerkin Discontinu - Application à la mécanique des fluides et l'interaction Laser/Plasma.* Phd thesis, Bordeaux University, 2002.

[87] R. Loubère, P.-H. Maire, and P. Vachal. Staggered Lagrangian hydrodynamics based on cell-centered Riemann solver. *Commun. Comput. Phys.*, 10:940–978, 2010.

[88] R. Loubère, P.-H. Maire, and P. Vachal. 3D staggered Lagrangian hydrodynamics scheme with cell-centered Riemann solver-based artificial viscosity. *Int. J. Numer. Meth. Fluids*, 72:22–42, 2013.

[89] R. Loubère, J. Ovadia, and R. Abgrall. A Lagrangian Discontinuous Galerkin-type method on unstructured meshes to solve hydrodynamics problems. *Int. J. Numer. Meth. Fluids*, 44:645–663, 2004.

[90] G. Luttwak and J. Falcovitz. Slope limiting for vectors: A novel vector limiting algorithm. *Int. J. Numer. Meth. Fluids*, 65:1365–1375, 2011.

[91] P.-H. Maire. A high-order cell-centered Lagrangian scheme for two-dimensional compressible fluid flows on unstructured meshes. *J. Comput. Phys.*, 228:2391–2425, 2009.

[92] P.-H. Maire. *Contribution to the numerical modeling of Inertial Confinement Fusion*. Habilitation à diriger des recherches, Bordeaux University, 2011, available at https://tel.archives-ouvertes.fr/tel-00589758/.

[93] P.-H. Maire, R. Abgrall, J. Breil, and J. Ovadia. A cell-centered Lagrangian scheme for two-dimensional compressible flows problems. *SIAM J. Sci. Comput.*, 29:1781–1824, 2007.

[94] P.-H. Maire and J. Breil. A second-order cell-centered Lagrangian scheme for two-dimensional compressible flow problems. *Int. J. Numer. Meth. Fluids*, 56:1417–1423, 2007.

[95] P.-H. Maire and B. Nkonga. Multi-scale Godunov-type method for cell-centered discrete Lagrangian hydrodynamics. *J. Comput. Phys.*, 228:799–821, 2009.

[96] P.H. Maire, R. Abgrall, J. Breil, R. Loubère, and B. Rebourcet. A nominally second-order cell-centered Lagrangian scheme for simulating elastic-plastic flows on two-dimensional unstructured grids. *J. Comput. Phys.*, 235:626–665, 2013.

[97] D.J. Mavriplis. Revisiting the Least-Squares procedure for gradient reconstruction on unstructured meshes. *AIAA*, page 3986, 2003.

[98] C. Mazeran. *Sur la structure mathématique et l'approximation numérique de l'hydrodynamique Lagrangienne bidimensionnelle*. Phd thesis, Bordeaux University, 2007.

[99] G.H. Miller and P. Colella. A high-order Eulerian Godunov method for elastic-plastic flow in solids. *J. Comput. Phys.*, 167:131–176, 2001.

[100] B. Mirtich. Fast and accurate computation of polyhedral mass properties. *Journal of Graphics Tools*, 1:31–50, 1996.

[101] N.R. Morgan, K.N. Lipnikov, D.E. Burton, and M.A. Kenamond. A Lagrangian staggered grid Godunov-like approach for hydrodynamics. *J. Comput. Phys.*, 259:568–597, 2014.

[102] N.R. Morgan, J.I. Waltz, D.E. Burton, M.R. Charest, T.R. Canfield, and J.G. Wohlbier. A point-centered arbitrary Lagrangian Eulerian hydrodynamic approach for tetrahedral meshes. *J. Comput. Phys.*, 290:239–273, 2015.

[103] S. Ndanou, N. Favrie, and S. Gavrilyuk. Criterion of hyperbolicity in hyperelasticity in the case of the stored energy in separable form. *Journal of Elasticity*, 115:1–25, 2014.

[104] W.F. Noh. Errors for calculations of strong shocks using an artificial viscosity and an artificial heat flux. *J. Comput. Phys.*, 72:78–120, 1987.

[105] J.S. Park, S.-H. Yoon, and C. Kim. Multi-dimensional limiting process for hyperbolic conservation laws on unstructured grids. *J. Comput. Phys.*, 229:788–812, 2010.

[106] O. Porth, S. Komissarov, and R. Keppens. Rayleigh-Taylor Instability in magnetohydrodynamic simulations of the Crab nebula. *Mon. Not. R. Astron. Soc.*, 443:547–558, 2014.

[107] W.H. Press, S.A. Teukolsky, W.T. Vetterling, and B.P. Flannery. Numerical recipes: The art of scientific computing. *Cambridge University Press*, 1985.

[108] X. Ribeyre, L. Hallo, T. Tikhonchuk, S. Bouquet, and J. Sanz. Non-stationnary Rayleigh-Taylor Instability in supernova ejecta. *Physics of Plasmas*, 14:112902, 2007.

[109] W.J. Rider. Revisiting wall heating. *J. Comput. Phys.*, 162:395–410, 2000.

[110] S.K. Sambasivan, M.J. Shashkov, and D.E. Burton. Exploration of new limiter schemes for stress tensors in Lagrangian and ALE hydrocodes. *Computers and Fluids*, 83:98–114, 2013.

[111] S.K. Sambasivan, M.J. Shashkov, and D.E. Burton. A finite volume cell-centered Lagrangian hydrodynamics approach for solids in general unstructured grids. *Int. J. Numer. Meth. Fluids*, 72:770–810, 2013.

[112] S.K. Sambasivan, M.L. Shashkov, and D.E. Burton. A cell-centered Lagrangian finite volume approach for computing elasto-plastic response of solids in cylindrical axisymmetric geometries. *J. Comput. Phys.*, 237:251–288, 2013.

[113] G. Scovazzi. Lagrangian shock hydrodynamics on tetrahedral meshes: A stable and accurate variational multiscale approach. *J. Comput. Phys.*, 231:8029–8069, 2012.

[114] G. Scovazzi, B. Carnes, X. Zeng, and S. Rossi. A simple, stable, and accurate linear tetahedral finite element for transient, nearly, and fully incompressible solid dynamics: a dynamic variational multiscale approach. *Int. J. Numer. Meth. Engng.*, 106:799–839, 2016.

[115] G. Scovazzi, M.A. Christon, T.J.R. Hughes, and J.N. Shadid. Stabilized shock hydroynamics: I. a Lagrangian method. *Comput. Methods Appl. Mech. Engrg.*, 196:923–966, 2007.

[116] G. Scovazzi, J.N. Shadid, E. Love, and W.J. Rider. A conservative nodal variational multiscale method for Lagrangian shock hydrodynamics. *Comput. Methods Appl. Mech. Engrg.*, 199:3059–3100, 2010.

[117] G.A. Sod. A survey of finite difference methods for system of nonlinear conservation laws. *J. Comput. Phys.*, 27:1–31, 1978.

[118] P. Le Tallec, J.-F. Gerbeau, P. Hauret, and M. Vidrascu. Fluid structure interaction problems in large deformation. *C.R. Mecanique*, 333:910–922, 2005.

[119] C. Le Touze, A. Murrone, and H. Guillard. Multislope MUSCL method for general unstructured meshes. *J. Comput. Phys.*, 284:389–418, 2015.

[120] J.A. Trangenstein and P. Colella. A high-order Godunov method for modeling finite deformation in elastic-plastic solids. *Communications on Pure and Applied Mathematics*, XLIV:41–100, 1991.

[121] P. Vachal and B. Wendroff. A symmetry preserving dissipative artificial viscosity in an r-z staggered Lagrangian discretization. *J. Comput. Phys.*, 258:118–136, 2014.

[122] P. Vachal and B. Wendroff. On preservation of symmetry in r-z staggered Lagrangian schemes. *J. Comput. Phys.*, 207:496–507, 2016.

[123] V. Venkatakrishnan. Convergence to steady solutions of the Euler equations on unstructured grids with limiters. *J. Comput. Phys.*, 118:120–130, 1995.

[124] F. Vilar. *A high-order Discontinuous Galerkin discretization for solving two-dimensional Lagrangian hydrodynamics*. Phd thesis, Bordeaux University, 2012.

[125] F. Vilar, P.-H. Maire, and R. Abgrall. A discontinuous Galerkin discretization for solving the two-dimensional gas dynamics equations written under total Lagrangian formulation on general unstructured grids. *J. Comput. Phys.*, 276:188–234, 2014.

[126] F. Vilar, C.-W. Shu, and P.-H. Maire. Positivity-preserving cell-centered Lagrangian schemes for multi-material compressible flows: From first-order to high-orders. Part I: The one-dimensional case. *J. Comput. Phys.*, 312:385–415, 2016.

[127] F. Vilar, C.-W. Shu, and P.-H. Maire. Positivity-preserving cell-centered Lagrangian schemes for multi-material compressible flows: From first-order to high-orders. Part II: The two-dimensional case. *J. Comput. Phys.*, 312:416–442, 2016.

[128] J. von Neumann and R.D. Richtmyer. A method for the numerical calculations of hydrodynamical shocks. *J. Appl. Phys.*, 21:232–238, 1950.

[129] J. Waltz, N.R. Morgan, T.R. Canfield, M.R.J. Charest, and J.G. Wohlbier. A nodal Godunov method for Lagrangian shock hydrodynamics on unstructured tetrahedral grids. *Int. J. Numer. Meth. Fluids*, 76:129–146, 2014.

[130] C.R. Weber, D.S. Clark, A.W. Cook, D.C. Eder, S.W. Haan, B.A. Hammel, D.E. Hinkel, O.S. Jones, M.M. Marinak, J.L. Milovich, P.K. Patel, H.F. Robey, J.D. Salmonson, S.M. Sepke, and C.A. Thomas. 3D hydrodynamics of the deceleration stage in ICF. *LLNL-JRNL-664615*, 2014.

[131] B. Wendroff. A compact artificial viscosity equivalent to a tensor viscosity. *J. Comput. Phys.*, 229:6673–6675, 2010.

[132] M.L. Wilkins. Calculation of elastic plastic flow. *Methods Comput. Phys.*, 3:211–263, 1964.